Estimating Leaf Area Index In Savanna Vegetation Using Remote Sensing And Inverse Modelling

Paul Bowyer

University of Salford,
Built and Human Environment Research Institute (BuHu)
School of Environment and Life Sciences

Submitted in Partial Fulfilment of the Requirements of the Degree of Doctor of Philosophy, 2005

Contents

List of Tables

List of Figures

Acknowledgements

First, I would like to thank my supervisors, Dr. Nigel Trodd, and Professor Mark Danson, for their help and guidance. I owe a special thanks to Mark, for, not only has he been my PhD supervisor, but also a good boss over the last few years. Similarly, I would like to thank Professor Phil Craig, who has been an enthusiastic and understanding boss over the past year. Next, I would like to thank Jaime Nickeson at the NASA Goddard space flight centre, and the whole of the SAFARI 2000 collaborators, for the fruitful exchange of data sets, without which much of this work would not have been possible. Thanks also to the following people for supplying models, which have been used in this research: Dr. Peter North, Dr. Stephane Jacquemoud, and Dr. Fred Huemmrich. Karen Anderson is warmly thanked, for her assistance with the loan of the ASD. I owe a big thank you to Mr Ed Sherratt, who went beyond the call in helping construct the goniometer, and for help in the field, thanks to Paul Walker also in this regard. I would also like to thank Dr. Kevin Sanderson, Dr. Clare Rowland, and Dr. Alistair Graham for the sound advice over the years. My parents deserve a vote of thanks for their sense of humour, and emotional support. Finally, I need to thank my girlfriend Hanne for her patience in putting up with me, and for giving me the inspiration to write up this research.

List of Acronyms and Abbreviations

6S	Second Simulation of the Satellite Signal in the Solar Spectrum
ANN	Artificial Neural Network
ASD	Analytical Spectral Devices
AVHRR	Advanced Very High Resolution Radiometer
BRDF	Bidirectional Reflectance Distribution Function
CAB	Congo Air Boundary
CHRIS/PROBA	Compact High Resolution Imaging Spectrometer/Project for On-Board Autonomy
CRM	Canopy Reflectance Model
CV	Coefficient of Variation
DN	Digital Number
EFAST	Extended Fourier Amplitude Sensitivity Test
EGO	European Goniometric Facility
ELADP	Ellipsoidal Leaf Angle Distribution Parameter
ENSO	El-Nino Southern Oscillation
EO	Earth Observation
ETM+	Enhanced Thematic Mapper
fcover	Fractional vegetation cover
FLIGHT	Forest LIGHT
FLIGHT 1-D	Forest LIGHT turbid medium
FPAR	Fraction of Absorbed Photosynthetically Active Radiation
FWHM	Full Width Half Maximum
GEMI	Global Environmental Monitoring Index
GeoSAIL	Geometric-Optical Scattering by Arbitrarily Inclined Leaves
GIFOV	Ground Instantaneous Field of View
GO	Geometric-Optical
IFC	Intensive Field Campaign
IFOV	Instantaneous Field Of View
IGBP	International Geosphere Biosphere Program
ITCZ	Inter-Tropical Convergence Zone
LAD	Leaf Angle Distribution
LAI	Leaf Area Index
LitAI	Litter Area Index
LOPEX93	Leaf Optical Properties Experiment
LUT	Look Up Table
MISR	Multi-angle Imaging Spectro-Radiometer
MOD09A1	MODIS 8 day 500m surface reflectance product
MOD15A2	MODIS 8 day 1km LAI/FPAR product
MODIS	MODerate resolution Imaging Spectrometer
NDVI	Normalised Difference Vegetation Index
NIR	Near InfraRed
PAI	Plant Area Index
PAR	Photosynthetically Active Radiation
PDF	Probability Density Function
POLDER	POLarisation and Directionality of the Earth's Reflectance
PROGeoSAIL	PROSPECT and GeoSAIL

PROSAIL	PROSPECT and SAIL
PROSPECT	PROpriétés SPECTral
RAA	Relative Azimuth Angle
RAMI	Radiation Transfer Model Intercomparison
RMSE	Root Mean Squared Error
RRMSE	Relative Root Mean Squared Error
RT	Radiative Transfer
S/N	Signal to Noise ratio
SA	Sensitivity Analysis
SAA	Solar Azimuth Angle
SAFARI 2000	Southern African Regional science Initiative 2000
SAIL	Scattering by Arbitrarily Inclined Leaves
SAVI	Soil Adjusted Vegetation Index
SWIR	Short Wave InfraRed
SZA	Solar Zenith Angle
TM	Turbid Medium
VAA	View Azimuth Angle
VI	Vegetation Index
VIS	Visible wavelengths
VZA	View Zenith Angle
WAI	Woody Area Index
WMA	Wildlife Management Area
WMO	World Meteorological Organisation

Abstract

Leaf area index (LAI), defined as the one sided green leaf area per unit ground area, is a key parameter in ecosystem process models. Owing to the large area of the earth's surface that they occupy, savanna ecosystems represent the third largest terrestrial carbon sink. There is considerable uncertainty however, as to the functioning of these ecosystems, particularly as they respond to land cover changes. Consequently, ecosystem process models constitute one of the best methods available for investigating the effect this may have on terrestrial carbon cycling. If these models are to be used over large areas however, they need to be parameterised.

This thesis develops a methodology to estimate LAI in savanna ecosystems, using remotely sensed earth observation (EO) data, laboratory bidirectional reflectance measurements (BRDF), physically based canopy reflectance models (CRMs), and artificial neural networks (ANN). First, the scattering behaviour of Kalahari soils was characterised, by making laboratory BRDF measurements. Soils were shown to be highly non-Lambertian. These measurements were then used to parameterise three different CRMs. Modelled reflectances were assessed with respect to Landsat ETM+ and Terra-MODIS reflectances. Results showed that a 1-D turbid medium provided the closest fit to the measurements. A series of model sensitivity analyses (SA) were performed, and it was shown that reflectance in the red and short-wave infrared displayed greatest sensitivity to LAI, sensitivity in the near-infrared was negligible. Model inversions were performed with ANN and different waveband combinations, and LAI was estimated. The results showed that LAI could be estimated with high accuracy, an RMSE of 0.31, and 0.18, from ETM+ and MODIS measurements, respectively. These results were promising, and with further improvements to models, coupled with more accurate input data, will see the use of EO data play an increasingly important role in understanding the functioning of these savanna ecosystems.

1 Introduction

1.1 Research context

Savannas may be loosely defined as tropical ecosystems with a continuous layer of grasses and a discontinuous layer of shrubs and/or trees, which may be rare or even absent under certain circumstances, or they may be represented almost entirely by shrubs (Solbrig 1991). Savannas occupy approximately 25 per cent of the Earth's total land surface (Matthews 1983), and approximately 40 per cent of the surface of the tropics, some 23 million km^2 (Cole 1986). Moreover, more than one-fifth of the world's population live in or around savanna areas (Frost *et al.* 1986). Savanna ecosystems are therefore, one of the most important terrestrial ecosystems in the world, yet, are the least well understood. They are subject to significant and increasing land use pressure from the communities that inhabit them, most often in the form of subsistence agriculture and commercial cattle grazing. This, combined with natural climatic variability has meant that savanna ecosystems have witnessed some of the most significant land transformations over the last century (Archer *et al.* 1995), specifically, a relative increase in the abundance of woody plant species at the expense of the grasses, termed 'bush' or 'woody encroachment' (Schlesinger *et al.* 1990, Archer 1994, Scholes and Archer 1997, Laliberte *et al.* 2004). This is important since woody and grass materials contribute differently to biogeochemical processes and energy transfer between the earth surface and the atmosphere (Pielke and Avissar 1990, Sellers *et al.* 1997, Asner *et al.* 1998a, Hibbard *et al.* 2001).

Given the large areas that they cover, savanna ecosystems represent the third largest sink of terrestrial carbon, after tropical and boreal forests, sequestering 0.39 Gigatonnes of carbon per year (Grace 2004). Consequently, savanna ecosystems play a significant role in the global carbon cycle (Schimel *et al.* 2001, Wofsy 2001). In the context of global climate change, there exists considerable uncertainty as to the effect

of changes in savanna structure and function (House *et al.* 2004), with some researchers attributing increases in carbon sequestration (therefore a sink) to woody plant invasion (e.g. Pacala *et al.* 2001), while others suggest a reduction in carbon stored on land (therefore a source) because of the effect that changes above ground, have on processes below ground, such that more carbon is lost from the soil than is stored in the plant (Jackson *et al.* 2002). Information on these carbon sinks or stores may be obtained through the use of ecosystem process models (Running & Coughlan 1988, Potter *et al.* 1993, Melillo *et al.* 1995, Prentice *et al.* 2000). These models require various biophysical parameters of vegetation as input to drive the model, including the leaf area index (LAI), fraction of photosynthetically absorbed radiation (FPAR), and ground vegetation cover (fcover). Clearly, for these models to be applied over large areas information about these biophysical parameters is also required over large areas. Additionally, incorporating LAI into climate models has been shown to lead to improved simulations of near-surface climate (Buermann *et al.* 2001). Satellite remote sensing data therefore provides an excellent means of providing information on these biophysical parameters, over large areas and repeatedly.

The extraction or retrieval of biophysical parameters from remotely sensed earth observation (EO) data, has developed from relatively simple empirically based vegetation index (VI) approaches to the use of more physically based canopy reflectance models (CRM), inverted using an advanced optimisation routine (Goel 1988, Myneni & Williams 1994, Myneni *et al.* 1995a, Kimes *et al.* 2000). The VI approach is limited in its generality, since the relationships are often site- and time-specific, and subject to the confounding influences of variable soil backgrounds and standing litter, especially in low LAI semi-arid ecosystems (Huete 1988, van Leeuwen & Huete 1996, North 2002). Consequently, accurate results may not be achievable (Gobron *et al.* 1997). The use of a CRM inversion represents a more powerful means to estimate LAI than the VI approach since it is based on fewer hypotheses and more physical principles. Higher accuracy, and greater generality is therefore to be expected from a physically based CRM inversion.

1.2 Research aim

The aim of this research is to develop a methodology to estimate LAI in savanna vegetation, through the inversion of a CRM with an artificial neural network (ANN), and Landsat Enhanced Thematic Mapper (ETM+) and Terra-Moderate resolution Imaging Spectrometer (MODIS) surface reflectances. This is based on studies at seven field plots in the Kgalagadi district of Botswana, where there is a semi-arid climate, and a range of different savanna vegetation types. While the MODIS LAI/FPAR product has been providing data since February 2000 (Privette *et al.* 2001), these are at the 1km spatial resolution. Additionally, the MODIS LAI product relies solely on the use of red and near infra-red (NIR) reflectances, which is likely to be a sub-optimal waveband set in savanna vegetation which are largely found against bright soil backgrounds, such that there is low contrast between vegetation and soil. Exploiting more wavebands of the MODIS sensor and using a different inversion method may lead to the generation of more accurate LAI estimates. In addition, high spatial resolution estimates of LAI obtained from ETM+ data may be extendible to the archive of Landsat TM data, thus permitting historical analysis.

The use and application of remotely sensed EO data to obtain quantitative estimates of savanna vegetation have been relatively limited. Studies have generally looked at:

- Relationships between spectral data and vegetation (Graetz & Gentle 1982, Choudhury & Tucker 1987, Prince & Astle 1986, Prince & Tucker, 1986, Ringrose & Matheson 1987, 1991, Duncan *et al.* 1993, Palmer & van Rooyen 1998, Schmidt & Karnieli 2000).
- Community type differentiation (Kremer & Running 1993, Trodd & Dougill 1998, Chopping *et al.* 2002, Lu *et al.* 2003),
- Spectral mixture models to obtain estimates of the relative proportions of vegetation in the landscape (Smith *et al.* 1990, van Leeuwen *et al.* 1997, Drake *et al.* 1999, Elmore *et al.* 2000).
- Canopy cover estimation using VI or simple spectral relationships (Musick 1984, Graetz *et al.* 1988, Yang & Prince 2000).

Only relatively recently have quantitative estimates of vegetation been obtained from model inversion work. Edwards *et al.* (1999) inverted a geometric-optical model with AVHRR data to estimate fractional cover in Jordan. Qi *et al.* (2000), developed a method to estimate LAI from Landsat Thematic Mapper (TM) and Advanced Very High Resolution Radiometer (AVHRR) data over semi-arid field sites in the USA and Niger, respectively, using LAI-VI relationships developed from model simulations. North (2002), performed a modelling study highlighting the difficulty in estimating LAI in semi-arid vegetation from VI, spectral mixture models, and CRM inversion, when there is variation in fcover and standing litter. The first study to present results of a complete CRM inversion in a semi-arid area, was that of Chopping *et al.* (2003). They use airborne multiple-view angle (MVA) data, to estimate LAI and canopy dimensions, over desert grasslands in the USA, with variable accuracy, over mixed vegetation communities high accuracy was reported, while over grasslands results were poor. The research presented in this thesis therefore represents the first attempt to invert a CRM against satellite measurements to estimate LAI at resolutions less than 1km, in semi-arid savanna vegetation.

1.3 Thesis structure

The next chapter of this thesis provides a review of the way in which biophysical parameters may be extracted from remotely sensed EO data, by using canopy reflectance models and their inversion. The chapter begins with a consideration of the remote sensing system and how vegetation and soils interact with solar radiation. Next the concept of canopy reflectance modelling is introduced and the forward and inverse problems are stated. The chapter then goes on to review the broad range of canopy reflectance models and the key inversion methods, and states the research objectives.

Chapter 3 provides an overview of the physical geography of the study area, describes the general characteristics of the field plots, and describes the pre-processing techniques used to obtain measurements of the surface reflectance from the Landsat ETM+ and Terra-MODIS data sets.

Chapter 4 describes the fieldwork and measurements that were made in order to parameterise the CRM in the work of chapter 6. The chapter provides an overview

of the sampling framework and methods that were used to make the measurements. A detailed discussion of the issues involved with making accurate field LAI measurements is presented.

Chapter 5 describes a laboratory experiment, where spectral directional reflectance measurements were made with a goniometer and ASD FR spectroradiometer, in order to characterise the scattering properties of the Kalahari soils, found at the field plots.

Chapter 6 describes an experiment where three different CRM are run in forward mode, in order to determine the accuracy with which the models simulate reflected radiance. Model simulations were assessed with respect to the ETM+ and MODIS data recorded at each of the field plots.

Chapter 7 describes a series of model sensitivity analysis (SA) experiments. Local and global SA techniques are first compared, then the effect of the probability density function (PDF) used for model parameters is investigated. Finally, the sensitivity of reflectance to variation in LAI is quantified for the measured conditions at the field plots.

Chapter 8 is the inversion chapter where artificial neural networks are used to invert the PROSAIL model to estimate LAI. The chapter starts with an experiment investigating the effect of network architecture and resistance to noise. Then various waveband combinations and inputs to the ANN are experimented with in order to determine the optimal waveband set for providing accurate LAI estimates. Finally a comparison is made between the LAI estimates obtained using the methods developed in this research with the MODIS LAI product.

Chapter 9 is the discussion and conclusions chapter where the results of the research are summarised, future research directions are discussed, and the main conclusions from this research are drawn.

2 Literature review

2.1 Introduction

This chapter presents a review of the literature on the remote sensing of vegetation, canopy reflectance models, and the inversion methods which may be used to estimate biophysical parameters by inverting measurements against a model. The chapter begins by outlining the remote sensing system, and the various factors which influence the reflected radiance. Next, the forward and inverse problems of canopy reflectance are described. Then the canopy reflectance models are presented, and the principal inversion methods are discussed, before finishing with a summary and research objectives.

2.2 Remote sensing of vegetation

Radiation reflected from the earth's surface contains information that can be related to the physical features of the surface, over which remotely sensed observations are made. This information resides in five different domains or signatures: the spectral (λ), spatial (x,y), directional (θ,ϕ) (zenith and azimuth angles of the solar source and sensor), temporal (t), and polarised (p) (Gerstl 1990). Formally this relationship R, between measured reflectance ρ, and the domains of information may be represented as:

$$\rho = R(\lambda,x,y,\theta,\phi,t,p) \tag{2.1}$$

Historically, much research effort has been spent exploiting the spectral (e.g. Tucker 1979, Jacquemoud & Baret 1990), spatial (e.g. Woodcock *et al.* 1988a,b), and temporal (e.g. Myneni *et al.* 1997, Zhou *et al.* 2003) domains of information. The polarised domain has received relatively little attention owing to the lack of sensors which record such information such as the short-lived POLDER I and II instruments (Deschamps *et al.* 1994). Similarly, the directional domain has been under-utilised until relatively recently. However, with the recognition that information in this

domain contains unique information (Barnsley *et al.* 1997), which can now be exploited with new sensors such as the Multi-angle Imaging Spectro-Radiometer (MISR), and the Compact High Resolution Imaging Spectrometer (CHRIS), this area is likely to witness sustained growth over the coming years. This is especially so given the clear utility of directional data for sampling the hot spot (the peak in reflectance when the solar and sensor geometries are in the same plane and zenith angle) which contains key information about the nature of clumping within crowns (Breon *et al.* 2002, Lacaze *et al.* 2002, Chen *et al.* 2003).

These domains will all be affected by the canopy over which reflectance measurements are made, such that Goel (1989) developed the following functional relationship between the reflectance of the vegetation canopy, and the five information domains:

$$\rho = R(\lambda,x,y,\theta,\phi,t,p;C) \tag{2.2}$$

Where C represents the various characteristics of the vegetation canopy and the soil background against which it is set. In order to obtain information about the vegetation canopy a model is constructed which relates the vegetation characteristics to the measured reflectance. This is the forward mode of a model. If one is to obtain estimates of the vegetation canopy characteristics from the measured reflectance this relationship in equation 2.2 needs to be inverted. This formulation does not consider the effect of the atmosphere which will affect all airborne and satellite measurements.

2.3 Factors affecting canopy reflectance

This section reviews the factors affecting measurements of canopy reflectance made at the top of the atmosphere. These factors include the spectral and structural properties of the vegetation, scattering from the soil and the effect of the atmosphere. Each of these is now considered in turn.

2.3.1 Spectral properties of vegetation

Radiant flux incident on a vegetation element (leaves, stems) is subject to two processes: scattering and absorption. Scattering is made up of reflectance and transmittance. The main regions of absorption in the leaf are found in the visible

(VIS) and shortwave infra-red (SWIR) wavelengths (Figure 2.1). In the visible, absorption by chlorophyll$_{a+b}$ and other photosynthetic pigments is strongest in the blue and red wavelengths, while less strong in the green wavelengths. Reflectance and transmittance are consequently low in the visible (Gates *et al.* 1965). In the SWIR absorption is due to the presence of water in the leaf, with there being three main water absorption features of increasing depth at 1450nm, 1900nm, and 2500nm (Gates *et al.* 1965, Danson *et al.* 1992). Consequently, reflectance and transmittance is relatively low in these regions, while higher outside of these (Figure 2.1). In the near infra-red (NIR), there are only minor water absorption features at 970nm and 1200nm, such that reflectance and transmittance is typically high. This high reflectance is a result of discontinuities in the cellular ultrastructure (cell wall, air spaces), such that there is marked refraction and high reflectance (Wooley 1971). When there is little or no water in the plant, reflectance and transmittance in the SWIR is controlled by the same process.

Scattering from leaf and stem surfaces is controlled by the presence of hairs and thorns on the leaf surface, and the degree of waxiness of the leaf cuticle (Grant 1987). Scattering is therefore largely non-Lambertian, apart from at near-normal incidence angles, where scattering is approximately Lambertian.

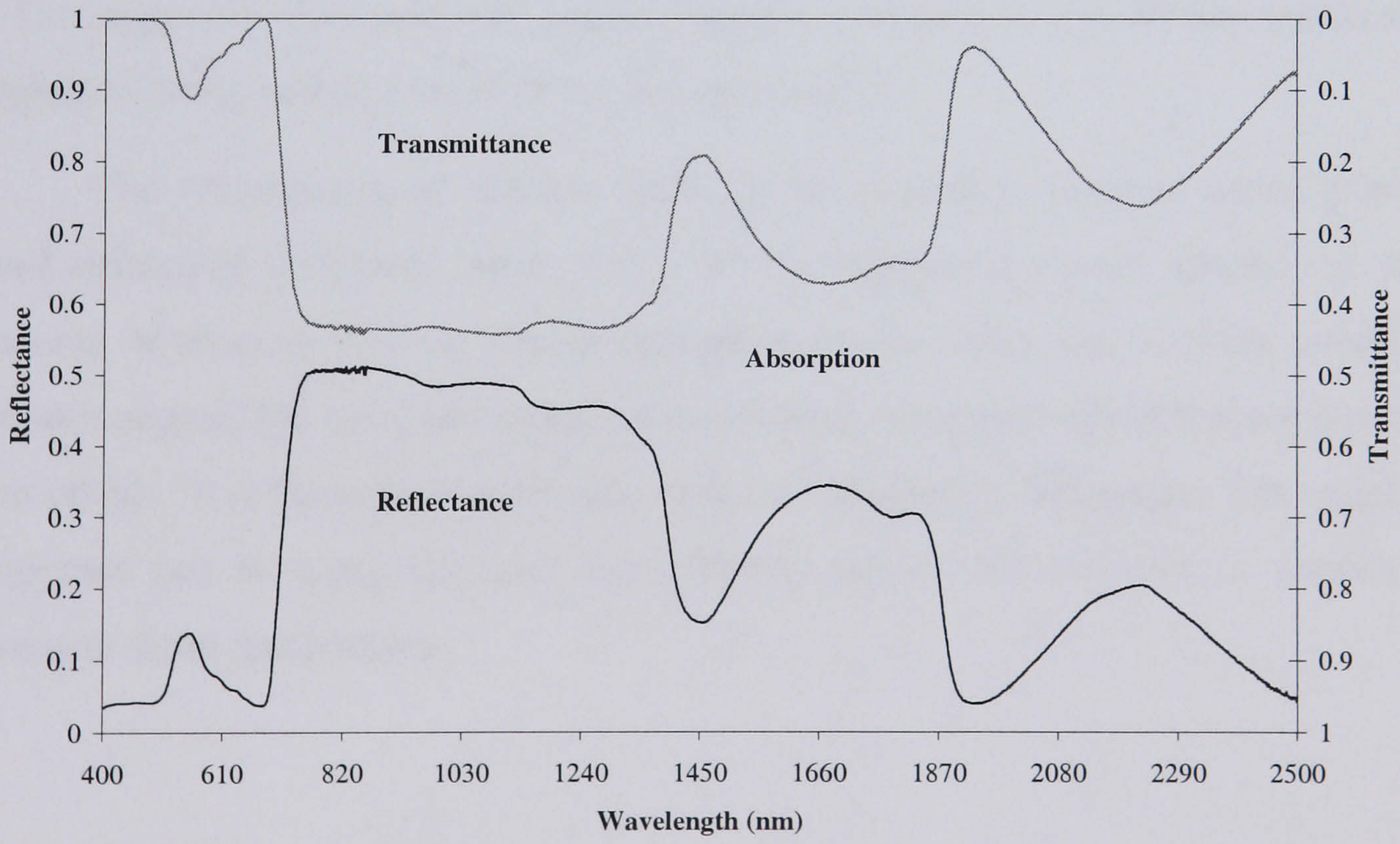

Figure 2.1 Leaf reflectance, transmittance, and absorption of clover (*Trifolium latense*) measured during the LOPEX93 experiment (Hosgood *et al.* 1994).

2.3.2 Structural properties of vegetation

Canopy reflectance is a composite of scattering and absorption at the individual vegetation elements and also the 3-D structure of the plant canopy. The way in which the plant 3-D structure affects canopy reflectance are many and varied, but the central mechanism is through the introduction of shadow onto the surfaces (Myneni *et al.* 1989, Myneni and Ross 1991).

Aspects of the plant 3-D structure which affect canopy reflectance are considered at the stand scale, where the vertical size and shape, and spatial distribution of the plant crowns on the soil surface will be the main factor in generating shadow (Li & Strahler 1992, Rautiainen *et al.* 2004); at the crown level, leaf clumping, leaf inclination angle, and the leaf area index (LAI) will be the main factors governing the amount of mutual shading and the amount of soil background which is visible (Lacaze *et al.* 2002). The combination of the LAI and leaf inclination angle, gives the fractional vegetation cover. The effect of the leaf inclination angle in determining canopy reflectance is illustrated in Figure 2.2, where leaf 1 which is almost perpendicular to the direct sunlight, is well lit, while leaf 2, which is almost parallel with the direct beam, is dimly lit. The viewer at A, with the sun behind her will see the bright leaves represented by leaf 1 well, but not much of the dimly lit leaf 2. The viewer at B will see the dimly lit leaf 2 well, but much less of the well lit leaf 1. Consequently, the scene will appear brighter to viewer A than B, this difference in brightness being solely a result of the leaf geometry.

The introduction of shadow leads to the vegetated surfaces being generally non-Lambertian reflectors, since for a given vegetation cover, greater or lesser amounts of shadow will be visible depending on the solar and viewing zenith and azimuth angles, and therefore radiation is reflected more strongly in certain directions than others. It is through a knowledge of these reflectance differences that vegetation properties can be extracted from the remotely sensed observations, if models can represent these mechanisms.

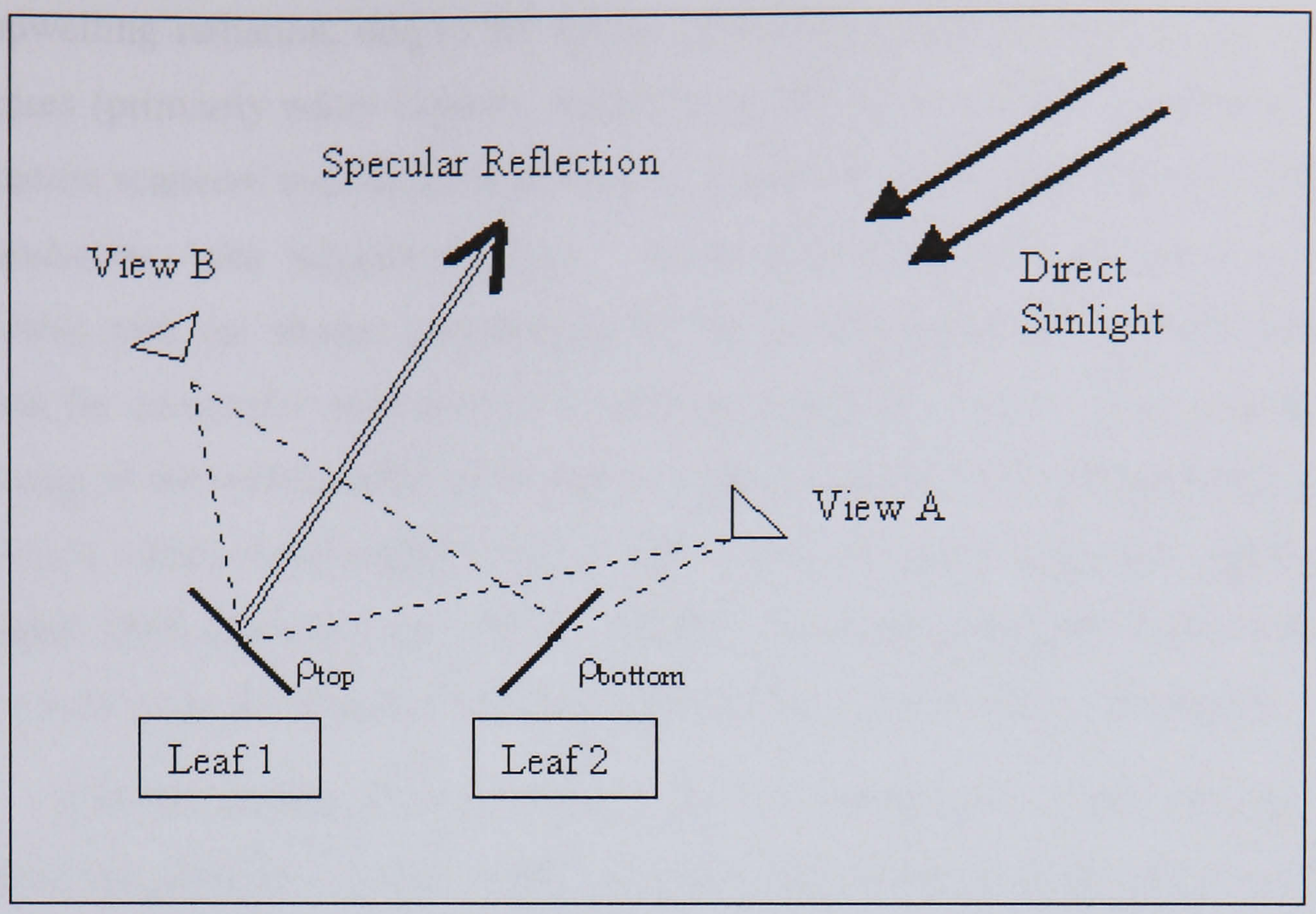

Figure 2.2 Illustration of the leaf geometry, and how it contributes to canopy reflectance (adapted from Norman *et al*. 1985).

2.3.3 Scattering from soil

Soil surfaces absorb and reflect incident radiation, there is very little transmittance. Soil reflectance depends largely on the surface roughness, in addition to the particle size distribution, soil moisture, organic content, soil mineralogy and colour (Irons *et al*. 1989). Soils are generally highly non-Lambertian reflectors, particularly where the surface roughness is pronounced, such as is the case with sandy and stony soils (Cierniewski 1987, Cierniewski & Verbrugge 1997). Reflectance over these soils tends to be dominated by backscatter, because of the shadowing effects introduced by the roughness. For clay and loamy soils, reflectance tends to be dominated by specular reflection. The soil surface will exert a strong influence in the low LAI, low vegetation cover typical in semi-arid ecosystems, such that they need to be characterised well (Pinty *et al*. 1998).

2.3.4 The atmospheric effect

Satellite measurements of reflected solar radiation are inevitably modulated by the path through the atmosphere. The atmosphere exerts an effect on both downwelling

and upwelling radiation, due to the action of scattering and absorption, by aerosols and gases (primarily water vapour), respectively (Kaufman 1989). In addition, there is radiation scattered into the field of view of a satellite sensor from adjacent pixels in the landscape - the adjacency effect. These atmospheric effects are wavelength dependent with the shorter wavelengths of the visible region being more seriously affected by molecular and aerosol scattering (Rayleigh, Mie). This results in a smoothing of the surface reflectance signal, with atmospheric scattering adding to path radiance at visible wavelengths, while at NIR attenuating the signal, due to absorption (Kaufman 1989, Myneni *et al.* 1995a). Clearly, if estimates of land surface variables such as LAI are to be obtained, this atmospheric effect needs to be corrected for.

Various models exist to correct for the atmospheric effect ranging from histogram equalisation (Richter 1996), invariant object correction (Moran *et al.* 1992), and dark object subtraction methods (Teillet & Fedosejevs, 1995, Kaufman *et al.* 2000), or a combination of these (Liang *et al.* 2001, 2002). These methods are all subject to a limitation of not accounting for all known atmospheric effects, from the adjacency effect (particularly important for high spatial resolution sensors such as ETM+), to aerosol scattering, and the limitation of finding dark targets, especially over semi-arid vegetation. An alternative to these methods is to use a model of atmospheric scattering such as MODTRAN (Berk *et al.* 1998), or 6S (Vermote *et al.* 1997a), however these models can be difficult to parameterise with measurements of aerosol optical thickness, and water vapour content, such that 'standard' atmospheres are normally assumed. Some researchers have tried to circumvent this problem by making estimates from top of the atmosphere radiances, by coupling models of the land and atmospheric systems together (Fourty & Baret 1997, Fang & Liang 2003).

Clearly, the atmospheric correction of satellite measurements of reflected radiation presents a serious impediment to the generation of high quality surface reflectance products. This is a critical issue for remote sensing studies, since the quality of the surface variables obtained from model inversions will depend to a large extent on the quality of the reflectance data. Lyapustin & Privette (1999), have shown the importance of accurate atmospheric correction with respect to estimating surface albedo.

2.4 The bi-directional reflectance distribution function (BRDF)

The preceding sections have talked about Lambertian and non-Lambertian reflection at various points, a Lambertian reflector reflects light equally in all directions, and is said to be isotropic, whereas a non-Lambertian reflector reflects light differently in different directions, and is said to be anisotropic. This phenomenon is represented formally by the bidirectional reflectance distribution function (BRDF) (Nicodemus 1970, Martonchik *et al.* 2000). The BRDF describes the scattering of a parallel beam of light from one direction in the hemisphere into another direction in the hemisphere, and hence is bi-directional. This is given formally, ignoring any spectral dependence, as:

$$\text{BRDF}\,(\theta_i,\ \phi_i;\ \theta_r,\ \phi_r) = \frac{dL_r(\theta_i, \phi_i\ ;\ \theta_r\ ,\ \phi_r)}{dE_i(\theta_i, \phi_i\ )}\ (\text{sr}^{-1}) \qquad (2.3)$$

where $\theta_i,\ \phi_i;\ \theta_r,\ \phi_r$ are the zenith and azimuth angles of the direction of illumination and reflection, respectively. dE_i (W m^{-2}) is the irradiance from the illumination direction, and dL_r (W m^{-2} sr^{-1}) is the radiance reflected into the differential solid angle at $\theta_r,\ \phi_r$. This measurement configuration is shown in Figure 2.3. Because the irradiance and radiances are defined in terms of differential solid angles, strictly speaking the BRDF cannot be measured. Instead, the BRDF is assumed retrievable with some level of uncertainty from radiance measurements made over a small solid angle, and thus represents a limited case of biconical reflectance. Figure 2.4 shows a typical surface reflectance feature taken in the principal plane of the viewing hemisphere. This shows the peak in reflectance at the hot-spot when the solar source and sensor lie in the same zenithal and azimuthal planes. This peak in reflectance is due to the sensor viewing the minimal amount of shadow (Hapke 1986, Hapke *et al.* 1996). The dark spot represents the viewing direction where maximal shadow area is visible due to the vertical structure of the surface.

It is important to state that the BRDF only involves information from the spectral and directional domains, and these are the information domains which will be exploited in this thesis to obtain measurements of LAI.

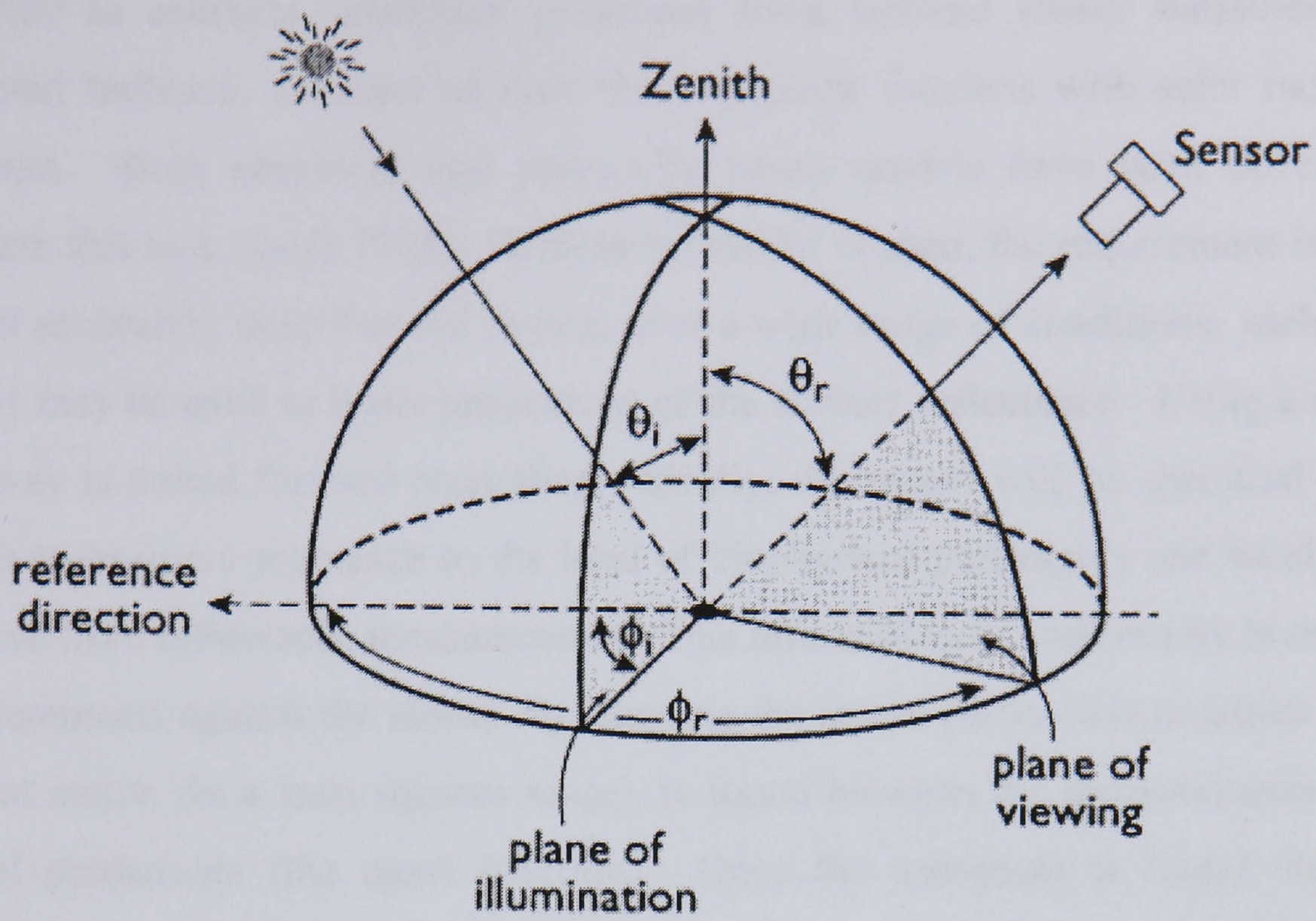

Figure 2.3 Measurement configuration for the surface BRDF (Source: www 2.1).

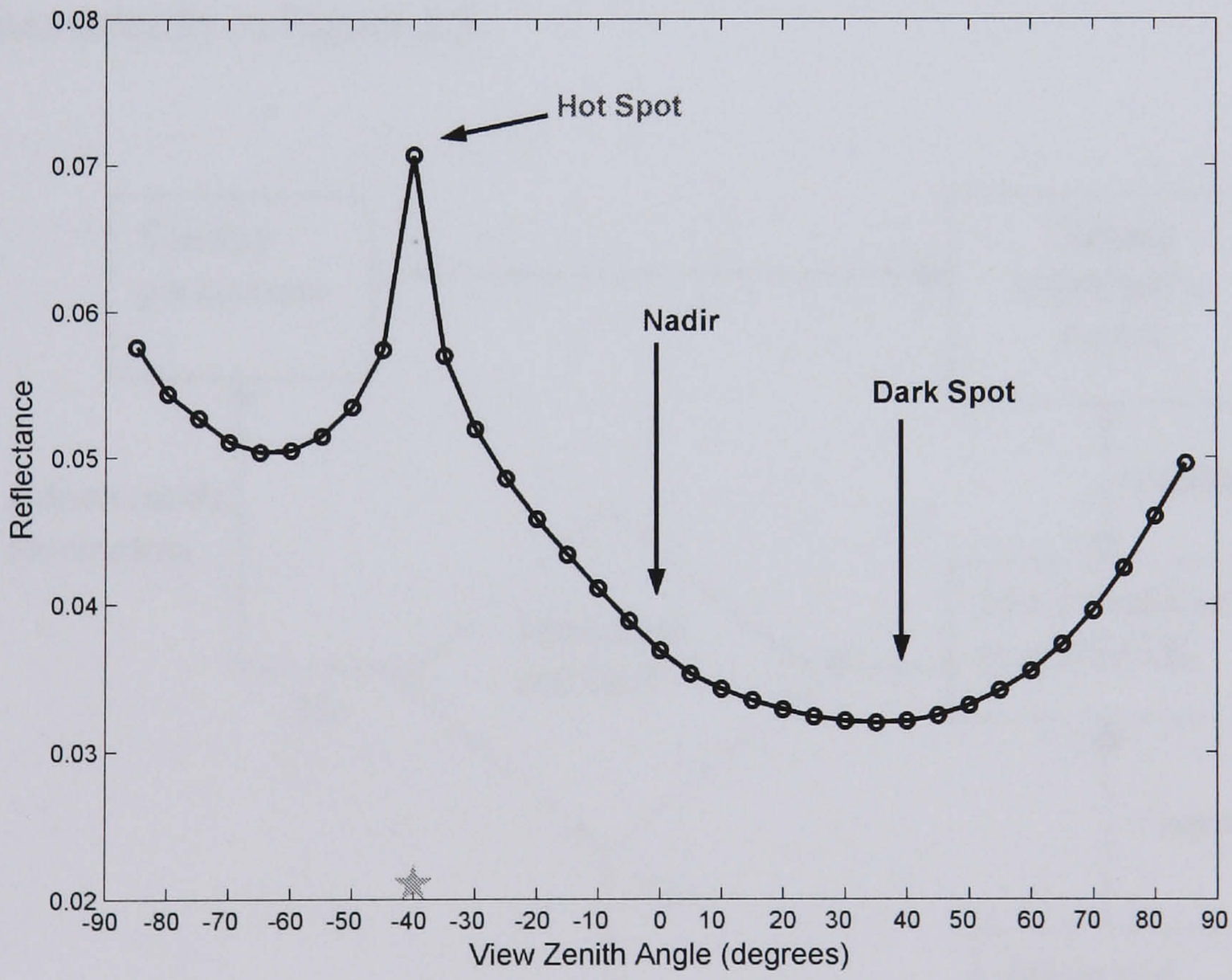

Figure 2.4 Hot spot surface reflectance features observable in the solar principal plane (adapted from www 2.2). The star at 40 degrees backscatter is the sun.

2.5 Canopy reflectance modelling: forward and inverse problems

In order to estimate vegetation properties from satellite sensor measurements of reflected radiance, a model of how the vegetation interacts with solar radiation is required. Both empirical and physically based models have been developed to perform this task (Goel 1988). Whichever model is used, the requirement is that the model accurately describes the system over a wide range of conditions, such that the model may be used to make predictions of the surface reflectance. Using a model in this way is called forward modelling. Ideally, the model will be specified in terms which have direct relevance to the kind of biophysical parameters one would like to retrieve from reflectance measurements. This information is retrieved by inverting the measurements against the model, by allowing the model parameters to adjust until the closest match (in a least squares sense), is found between the measurements and the model predictions (the merit function). Once the minimum is found, the model parameters which gave the predicted reflectance, are considered those of the surface over which the measurement of surface reflectance was made. This process is called inverting the model, or the inverse problem. The forward and inverse problems are shown schematically in Figure 2.5.

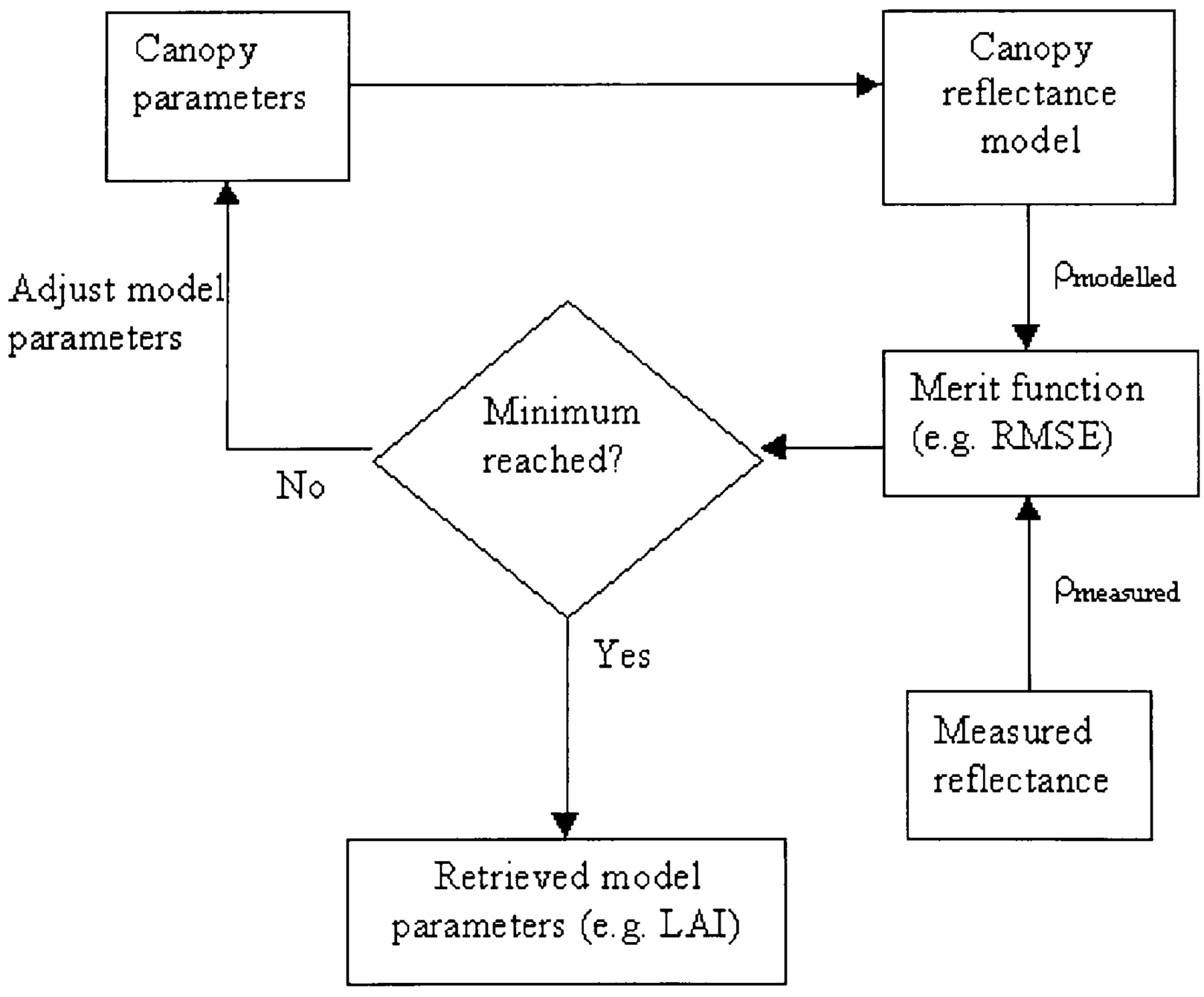

Figure 2.5 Schematic overview of the forward and inverse problems

Strictly speaking, the inverse problem can only be solved if it is well posed, that is, that a solution exists, the solution is unique, and depends continuously on the data (Combal *et al.* 2002a). If one of these statements does not hold, then the problem is defined to be ill-posed. The inverse problem in remote sensing, is inherently ill-posed, since it is not unique - there may be more than one set of canopy parameters for the same solution (difference between measured and modelled reflectances). In order to obtain stable and reliable estimates from model inversion, therefore requires the use of prior information (Li *et al.* 2001), which can take the form of a knowledge of the likely range and distribution of the model parameters, or an estimate of the uncertainty associated with the reflectance measurements, and the pertinence of the model to the architecture of the canopy.

Numerous models of canopy reflectance have been developed (Goel 1988, Strahler 1997), and there are various methods available to invert the models (Kimes *et al.* 2000). The next section of the literature review deals with each of these in turn.

2.6 Canopy reflectance models

There are two main types of canopy reflectance model, which are either based on sound physical principles - the physically based models, or statistical relationships between vegetation and reflectance - the empirical models.

2.6.1 Empirical models

The main type of empirical model used are the well known vegetation indices (VIs). Such models attempt to establish statistical relationships (usually a regression) between measurements of some property of the vegetation made on the ground, and measurements of reflectance in two or more wavebands, such as the commonly used red/NIR combination in the normalised difference vegetation index (Tucker 1979, Verstraete *et al.* 1996, Verstraete & Pinty 1996). Many studies have used a vegetation index approach because their simplistic nature and ease of computation, make them suitable for studies at a range of spatial scales (e.g. Malthus *et al.* 1993, Fassnacht *et al.* 1997, Turner *et al.* 1999, Huete *et al.* 2002, Zhou *et al.* 2003, Lee *et al.* 2004, Walthall *et al.* 2004).

Given the statistical nature of the relationships however, they are subject to many limiting factors. The most serious limitation for their application is that, VIs effectively develop a model between the vegetation property of interest and reflectance, under the assumption that the only factor accounting for variation in the reflectance is variation in that vegetation property (Verstraete & Pinty 1996). This is rarely the case, and as such makes generalisation across landscapes difficult (Turner *et al.* 1999). The central problem of VIs is that they are data dependent, such that they are inflexible, and cannot easily account for perturbations caused by variable soil backgrounds (Huete & Jackson 1987, Huete 1988), the presence of standing litter (van Leeuwen & Huete 1996), and variation in solar and view zenith angles (Gemmel & McDonald 2000). These factors are all significant in semi-arid ecosystems. Furthermore, the demands of labour intensive field work to establish the relationships are considerable (Cohen *et al.* 2003), and the relationships are site- and time-specific.

Moreover, in semi arid ecosystems, where vegetation cover is low, the effect of the soil background is strong, such that the inflexibility inherent in the VI approach is likely to render the accurate quantitative estimation of LAI very difficult. This is supported by theoretical studies. Baret and Guyot (1991), investigated the effects of canopy geometry and soil optical properties on four VIs for estimating LAI and absorbed photosynthetically active radiation (APAR). They found that the NDVI is the most susceptible to variation in soil optical properties, and suggest caution in using a vegetation index approach for assessments of LAI where vegetation cover is low. Leprieur *et al.* (1994, 1996), also investigated the potential of various vegetation indices for estimating LAI and fractional vegetation cover from AVHRR data in semi-arid ecosystems. They report that the effects of a bright soil and variable atmosphere inhibit the accuracy of estimates obtained from the vegetation indices, with the NDVI being most sensitive to these effects, as compared to SAVI and GEMI which take more effective account of the soil and atmosphere respectively. Clearly, despite their simplicity and computational efficiency, the utility of a VI approach would appear to be of limited worth in estimating LAI in these or any other semi arid ecosystems, over large areas, and through time.

2.6.2 Physically based models

Physically based models have been developed based on one of three different theories: radiative transfer, average transmittance, and geometric-optics (Goel 1988, Goel & Thompson 2000). These physical models consider surface scattering and volume scattering (Strahler 1997). Goel (1988), proposed that physically based models fall into one of four categories: 1) turbid medium, 2) geometric-optical, 3) hybrid and, 4) computer simulation models. This is still largely applicable today, and these model types are reviewed below, together with a section on semi-empirical models.

2.6.2.1 Turbid medium models

This type of model approximates the canopy as an infinitely extended plane-parallel scattering medium, made up of randomly distributed scattering phytoelements (leaves) (Myneni *et al.* 1989, Qin & Liang 2000). The phytoelements are assumed small relative to the height of the canopy, optical and structural properties are described by volume averages, such that the spatial location and orientation of phytoelements within the canopy is not considered. As a result turbid medium (TM) models cannot model the hot spot phenomenon (Hapke 1986). This representation of the canopy is depicted in Figure 2.6. Owing to their plane-parallel nature TM models are best suited to homogeneous canopies such as agricultural fields, and grasslands. Where the canopy departs from this assumption, and there is horizontal structure in the canopy such as forests, then inferior results are to be expected.

These models range in complexity from the relatively simple Suits model (Suits 1972), and SAIL model (Verhoef 1984), to the DISORD model of Myneni *et al.* (1992). TM models have been successfully inverted to give LAI in a range of environments and are the most commonly used owing to their simplicity and suitability for inversion. The Suits model was first inverted by Goel & Strebel (1983) and Goel & Thompson (1984a). The Suits model represents the orientation of the phytoelements as being either vertical or horizontal, such that in the nadir direction an unrealistic 'V' shaped BRDF is observed. Verhoef (1984), extended the Suits model by modelling the phytoelements as being arbitrarily inclined, which removed the anomalous 'V' shape about nadir. The scattering by arbitrarily inclined leaves (SAIL) model was thus developed. This model has been inverted by Goel & Thompson (1984b,c) to estimate LAI over crops. More recently, the SAIL model has been

inverted by Braswell *et al*. (1996), and Meroni *et al*. (2004). This model is used in the work presented in chapters 6, 7, and 8 of this thesis.

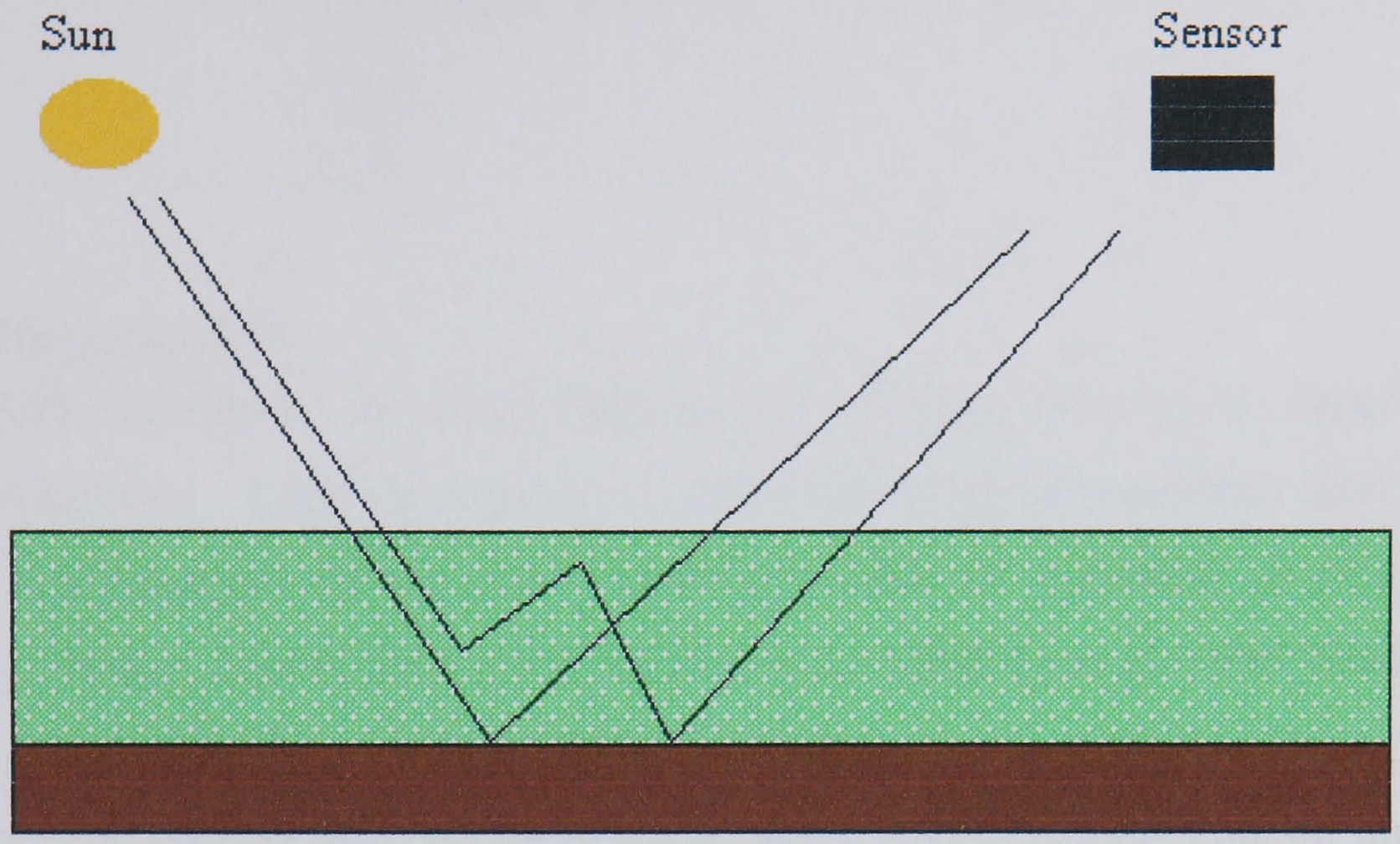

Figure 2.6 Schematic representation of the turbid-medium canopy (adapted from Gerstl & Borel 1992).

2.6.2.2 Geometric-optical (GO) models

This type of model represents tree crowns as a set of discrete opaque geometrical primitives (cones, ellipses) distributed over a soil background, and were pioneered by Li & Strahler (1985, 1992), and recently reviewed by Chen *et al*. (2000). Reflectance (R) is calculated as an area weighted sum of four components: sunlit crown (A_C), shadowed crown (A_T), sunlit background (A_G), shadowed background (A_Z), and their reflectances C, T, G, and Z, respectively, as:

$$R = \frac{(A_C C + A_T T + A_G G + A_Z Z)}{A} \qquad (2.4)$$

where A is the total area. Strahler and Jupp (1990), extended the GO approach by including a Boolean model so that the tree crowns sat above the soil background, the so-called 'spheroids on sticks' approach. These models consider reflectance variability at the individual tree level, whereas the 4-Scale model (Chen & Leblanc 1997), considers the GO approach at levels of the individual leaf and stand.

These GO models are particularly well suited to discontinuous canopies such as forests, and savanna, and have been successfully inverted to give estimates of tree size and canopy dimensions (Franklin and Strahler 1988, Franklin and Turner 1992, Wu and Strahler 1994) and fractional vegetation cover (Woodcock *et al.* 1997). They do not include LAI as a model parameter and are therefore unsuitable for use in this research.

2.6.2.3 Hybrid models

These models incorporate the turbid medium and GO approaches to the modelling of canopy reflectance. External structure is modelled using GO methods and internal structure is represented by the turbid medium. There are a number of this type of model (e.g. Nilson and Peterson 1991, Rosema *et al.* 1992, Li *et al.* 1995, North 1996, Ni *et al.* 1999, Kuusk & Nilson 2001, Lacaze & Roujean 2001). Owing to the combination of the TM and GO approaches, many hybrid models contain numerous parameters, such that they are difficult to parameterise, and invert. The relatively simple FLIM (Rosema *et al.* 1992), and GeoSAIL models have been inverted however, to estimate LAI over forests with reasonable accuracy (Hu *et al.* 2000, Fang & Liang 2005).

2.6.2.4 Computer simulation models

These models use computer intensive simulation techniques such as Monte Carlo ray tracing (North 1996, Gastellu-Etchegorry *et al.* 1996, Disney *et al.* 2000) and radiosity coupled with computer graphics techniques (Borel *et al.* 1991, Qin & Gerstl 2000). The scene phytoelements are modelled as discrete surfaces, and therefore in contrast to the volume average approach of the TM models, simulate the hot spot effect (Gerstl & Borel 1992). Canopy reflectance is calculated by tracing the interaction of individual photons with the various phytoelements until the photon is scattered out of the scene - in the case of ray-tracing, whereas for the radiosity method all energy emitted or reflected from a surface is accounted for by reflection and absorption by other surfaces in the scene. These models are highly detailed requiring a large number of model parameters and are therefore highly accurate, yet are so computationally

intensive that their suitability for inversion is questionable, although they are suitable for forward modelling.

2.6.2.5 Semi-empirical models

This class of models bridges the gap between the fully fledged physical models and the empirical models (Wanner *et al.* 1995, Rahman *et al.* 1993, Lucht & Roujean 2000, Chopping 2000, Chopping *et al.* 2003, Maignan *et al.* 2004). Scattering is modelled by the use of surface scattering (GO), and volumetric kernels, each having an associated weight. Formally this is represented as:

$$\text{BRDF}(\theta_i, \theta_r, \phi) = f_{iso} + f_{vol}k_{vol}(\theta_i, \theta_r, \phi) + f_{GO}k_{GO}(\theta_i, \theta_r, \phi) \quad (2.5)$$

Where θ_i, θ_r, ϕ are the solar and zenith view angles, and relative azimuth angles respectively, k_{vol} is the volumetric kernel, k_{GO} is the surface scattering kernel, $f_{iso,vol,GO}$ are weights associated with each kernel, and isotropic scattering. The surface and volume scattering kernels are based on approximations to GO and TM approaches, respectively. Upon inversion the three weights are retrieved. These models are strictly only applicable to homogeneous surfaces, only model single scattering, and are not specified in terms which permit direct inversion of biophysical parameters. These models, are quick to run because of their linear nature, such that they have received most application in the normalisation of BRDF data (Weiss & Baret 1999), and in albedo studies (Wanner *et al.* 1997).

2.6.3 Models used in this thesis

The SAIL, GeoSAIL and FLIGHT models were used in the research presented in this thesis. These models were chosen since they represented a wide range of complexity, from the TM treatment of SAIL, to the analytical hybrid GeoSAIL, and numerical (Monte-Carlo ray tracing) FLIGHT. FLIGHT has both a 1-D TM treatment, and a 3-D option, and both these were used in the model simulations of chapter 6. In addition, the PROSPECT model (Jacquemoud & Baret 1990, Jacquemoud *et al.* 1996) was used to simulate leaf reflectance and transmittance.

2.7 Model inversion methods

This section considers the various inversion methods which may be used to invert canopy reflectance models to estimate vegetation properties. As the models used in this thesis are non-linear, the linear or analytical inversion methods are not dealt with. Attention is instead focused on the two most suitable inversion methods for operational applications - artificial neural networks (ANN), and look-up table (LUT), methods (Kimes *et al.* 2000). In addition, the numerical optimisation methods are reviewed since these have been the inversion method of choice over the last 15 years and remain popular today (Pinty *et al.* 1990, Privette *et al.* 1994, Asner *et al.* 1998a, Jacquemoud *et al.* 2000, Combal *et al.* 2002a, Chopping *et al.* 2003, Meroni *et al.* 2004). Genetic algorithms (Fang *et al.* 2003) have also been used to invert canopy reflectance models, however, these too are not suited for operational applications, and so are not reviewed. Firstly, however, some general issues regarding the inversion of a canopy reflectance model are considered.

2.7.1 Inversion preliminaries

Inverting a model to biophysical parameters involves several issues. These include, the number of wavebands available for use and the information they contain with respect to the vegetation, the number of model variables to be estimated, and the sensitivity of the inversion to noise in the data (Goel 1989). The inversion proceeds by finding the minimum between a set of measured and modelled reflectances, as shown in Figure 2.5. In order to define the minimum an error, or merit function is required to express the degree of disagreement between the two, typically this is the sum of the squared error. The merit function (F) may be defined as:

$$F = \sum_{i=1}^{N} w_i(\rho_i - \rho_i') \tag{2.6}$$

where i=1...N is the number of measurements, w_i the weights associated with each measurement, and ρ_i and ρ_i' the measured and modelled reflectances respectively. For both the numerical optimisation, and LUT inversion methods this is the way in which the inverse problem is defined, and the model parameters are adjusted, or the

LUT searched until the minimum is found. Another way of defining the merit function which takes account of the measurement and model uncertainties is:

$$F = \sum_{i=1}^{N} w_i \left(\frac{\rho_i - \rho_i'}{\delta_i} \right) \leq 1 \tag{2.7}$$

where δ_i is the uncertainty of the inversion, which may be wavelength dependent. This is the merit function which is used in the LUT based MODIS LAI/FPAR retrieval (Wang *et al.* 2001), such that multiple solutions are possible. For the ANN inversion, the inverse problem is defined differently. Rather than trying to find the smallest difference between two sets of reflectance data, the ANN method tries to learn the underlying relationship between the spectral reflectance measurements, and the vegetation parameter of interest, such that the error between a modelled and measured biophysical parameter of interest is minimised.

Prior to performing an inversion, it is good practice to perform a model sensitivity analysis (Goel & Strebel 1983, Dawson *et al.* 1993, Bowyer *et al.* 2003). This is a critical issue in the use of physically based models. If one desires to estimate biophysical parameters from a model inversion, then the reflectance measurements must be sensitive to variation in the given parameter. If not it will be very difficult to retrieve that parameter from an inverted model. For example, Privette *et al.* (1996a), developed a derivative weighting scheme which provided more weight to those observations to which the parameter of interest was most sensitive. In this way, the inversion was performed more quickly and with higher accuracy. The accuracy of any inversion will largely be determined by the uncertainties associated with the model and measurements, i.e. a good (accurate) model is needed, together with high quality data.

2.7.2 Numerical optimisation

As stated earlier this has been the method of choice for inverting a canopy reflectance model. The procedure is as outlined above - after an initial guess at the parameter values, the model parameters are adjusted until the minimum error is found between the measured and modelled reflectances. Once this minimum is found, the model

parameters which provide the closest fit to the measurements are considered the surface conditions, and the biophysical parameter is retrieved.

There are three main groups of numerical algorithm: 1) the downhill simplex method e.g. subroutine AMOEBA from Press *et al.* (1986) (Privette *et al.* 1996b), 2) the conjugate direction set method e.g. subroutine POWELL from Press *et al.* (1986) and, 3) the quasi-Newton method e.g. subroutine EO4JAF from Numerical Algorithms Group (NAG) (1990). The selection of an optimisation algorithm is very much a case of trial and error (Privette *et al.* 1994), for the optimal one is known to differ depending on the physical model used (Privette *et al.* 1996a, cf. Iaquinta *et al.* 1997). By far the most common however is the quasi-Newton algorithm subroutine EO4JAF (Pinty *et al.* 1990, Jacquemoud *et al.* 1995, Braswell *et al.* 1996, Iaquinta *et al.* 1997, Asner *et al.* 1998a).

There are a number of issues related to the use of these numerical algorithms to invert a model. It is known that the model results are sensitive to the initial guess at the model parameters, such that the model is restarted 3 or 4 times. The convergence to a global minimum may be slow, and the determination of free and fixed model parameter sets. For example, Privette *et al.* (1996a) were able to retrieve LAI over grasslands with acceptable accuracy when all other model parameters were fixed. When there were two free parameters retrieval of LAI was less successful.

Impressive results have been achieved with these algorithms compared to the LUT and ANN approaches, particularly with respect to estimating noisy data sets (Kimes *et al.* 2002, Combal *et al.* 2002a). However, these algorithms require enormous computing power since the model is run for each pixel in turn, such that they are not suitable for operational applications. Moreover, the computing requirements are such that the method is best suited to relatively simple models, specified by a few parameters. This therefore precludes the use of potentially more accurate models.

2.7.3 Look-up tables

This method precomputes model reflectances from a large range of model parameter value combinations and stores them in a table, which may later be searched. In this way the bulk of the computational expense is performed before an inversion is

attempted, such that complex models may be used to create the reflectance database. The problem is then reduced to searching the table optimally to find the modelled reflectance set which most closely matches the measured reflectance. The speed of the search and therefore inversion, will depend on the coarseness of the database (Kimes *et al.* 2000, Barnsley *et al.* 2000). Gastellu-Etchegorry *et al.* (2003), have recently developed an interpolation procedure which may help reduce the size of the database, and therefore increase the speed of inversion. This LUT method is used to derive LAI and FPAR on board the MODIS/MISR instruments (Knyazikhin *et al.* 1998a,b), and have been used to estimate LAI in agricultural (Weiss *et al.* 2000, Combal *et al.* 2002b), and forest settings (Hu *et al.* 2000).

If the size of the LUT is too large then processing time is likely to be significant. More research is required to determine optimal table sizes and the effect of using coarse tables on estimation accuracy. For this reason, LUT inversions are not performed in this thesis.

2.7.4 Artificial neural networks

Artificial neural networks are highly connected parallel distributed information processing structures, consisting of individual processing elements (more commonly termed nodes or neurons), connected to each other via unidirectional signal channels (Haykin 1999). Various types of neural networks exist, however, in the remote sensing literature, multi-layer perceptron feed-forward networks are most commonly used (Kimes *et al.* 1998). These networks have been shown to provide impressive results in a range of remote sensing applications from classification (Arora & Foody 1997), to biophysical parameter estimation (Smith 1993, Kimes *et al.* 1997, Gong *et al.* 1999, Kimes *et al.* 2002, Fang & Liang 2003, Fang & Liang 2005, Carter-Ingram *et al.* 2005). These networks are composed of three or more layers, the input layer, the hidden layer, and the output layer. Networks can have any number of hidden layers. Within each layer there may be any number of nodes, and the outputs of one layer form the inputs to the next layer. This network architecture, or topology, is illustrated in Figure 2.7.

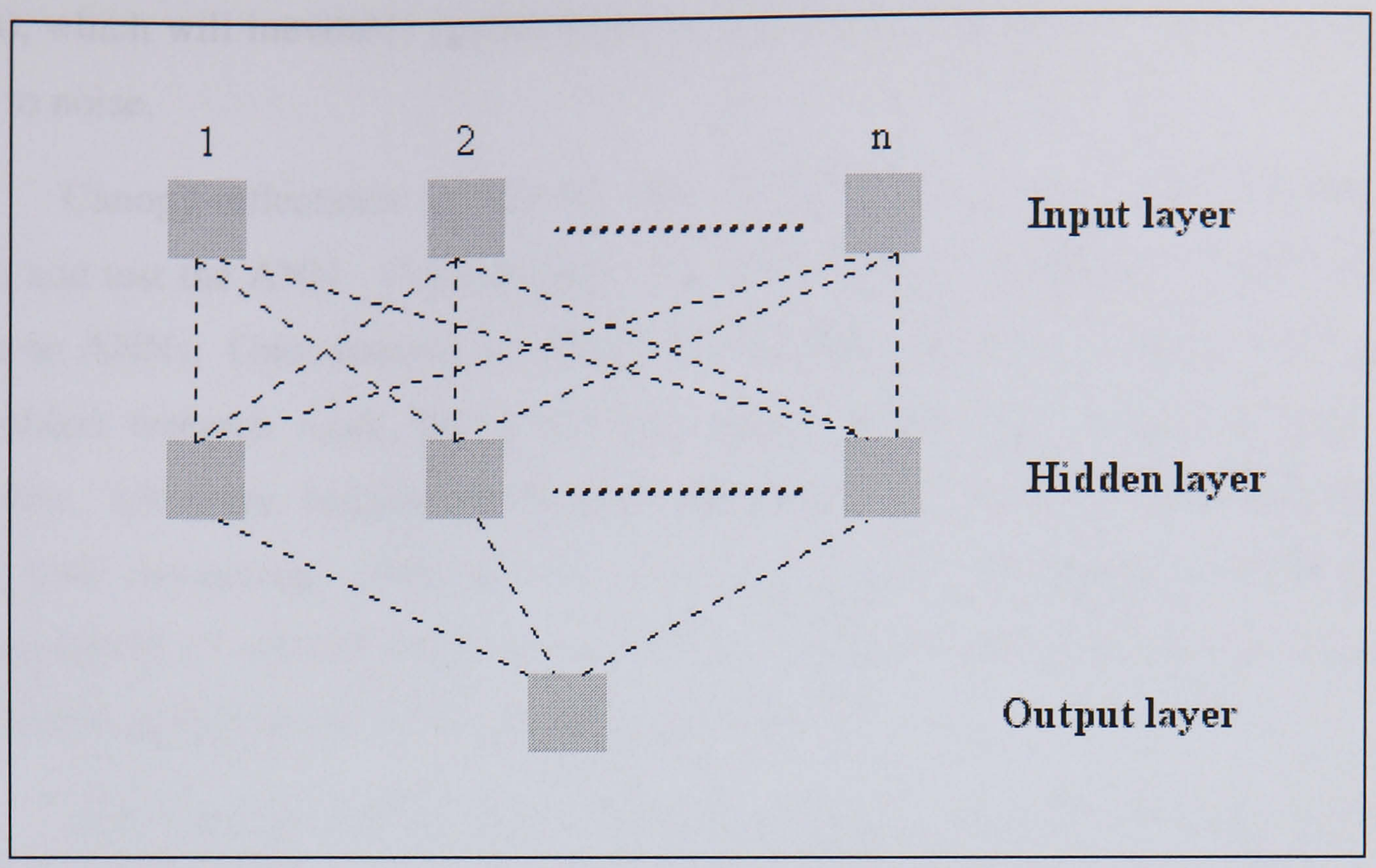

Figure 2.7 Topology of a multi-layer artificial neural network.

An ANN may be trained to learn the underlying relationship between the inputs and outputs. In the case of canopy reflectance model inversion, the inputs are reflectance measurements in one or more wavebands, and the output is the biophysical parameter of interest, in this thesis, the LAI. The node is the central processing unit of the network. Each node receives a signal from nodes in the preceding layer, the inner product of these inputs is taken to give a weight vector, and a bias term is added. The resulting number from this process is then output via a, usually, non-linear activation or transfer function, and fed to the next layer.

Training an ANN proceeds by presenting the network with a set of input patterns, and output targets from which it is to learn the underlying relationship. Training is an iterative process, where learning is achieved by back-propagating the error at each training iteration (Rumelhart *et al.* 1986), and adjusting the weights and biases in such a way that the functional approximation of the network minimises the error goal (difference between network targets and network estimates). If the network can establish a relationship between the inputs and outputs, the network may then be inverted with measurements of reflectance to estimate the LAI. A compromise is to be reached in the training where the network learns the underlying relationship well, but no more, such that the network is able to generalise to unseen measurements (real

data), which will inevitably depart from the data with which the network was trained due to noise.

Canopy reflectance models are used to create the training data with which to train and test the ANN. Consequently, any model of any complexity can be used to train an ANNs. Once trained, an ANN provides rapid inversion results, for example, in related research work, the author inverted 586,000 ETM+ pixels, in only 5.8 seconds. However, because the network training is an iterative process, training is very time consuming. Other factors which detract from the appeal of ANN is the determination of optimal network architecture, which is mainly an heuristic process, and failing to find the global minimum (Bishop 1995).

ANN are used in this thesis to provide estimates of LAI on the basis that they represent the most rapid inversion method at the current time, even when training time is accounted for.

2.8 Summary and research objectives

This review has established the basis upon which vegetation optical and structural properties influence the magnitude and direction of reflected radiance. It is upon this understanding and basis through which biophysical parameters may be estimated from measurements of reflected radiance. The broad range of canopy reflectance models available have been described and discussed, and their suitability for use determined. The various inversion methods were outlined, and the key advantages and disadvantages of each discussed. From this review the following research objectives are stated:

(i) To investigate and characterise the scattering properties of Kalahari soils.

(ii) To compare the performance of different canopy reflectance models in simulating reflected radiation from savanna vegetation, in order to determine the most suitable model.

(iii) To quantify the sources of variability in reflectance data, to determine the sensitivity of reflectance to variation in LAI.

(iv) To investigate the potential of artificial neural networks to accurately estimate LAI.

The next chapter describes the study area and the general characteristics of the field plots used in this thesis.

3 Study Area and Image Processing

3.1 Introduction

The aim of this chapter is to describe the general characteristics of the study area, and introduce some of the wider background, and pre-processing steps taken in the generation of the satellite sensor data sets used in this thesis. The chapter begins with a description of the climate, geomorphology, soils, and vegetation and land use over the study area. This is followed by an introduction to the field sites and plots, and an overview of the SAFARI 2000 international research project (Swap *et al.* 2003), which ran coincident with the research presented in this thesis. After this, the pre-processing methods used to obtain surface reflectance from the Landsat 7 ETM+ and Terra-MODIS sensors are outlined, before finishing with a summary and some conclusions.

3.2 Study area

The study area is situated in the Kgalagadi district, which occupies the south-western corner of the Republic of Botswana. In total there are three field sites where field measurements were made, at which a variable number of study plots were located (Figure 3.1). The most northerly site is at Tshane, where two field plots were sampled; at Mabuasehube, there were also two field plots; while at Tshabong, the most southerly site, a further three field plots were located, for a total of seven field plots. All of these sites are situated within the Kalahari desert, and represent semi-arid savanna vegetation complexes. The three sites are separated by a distance of approximately 200km from north to south, along which there is a significant rainfall gradient, and variation in vegetation and land use type and pressures. The following sections describe in more detail the characteristics of the area.

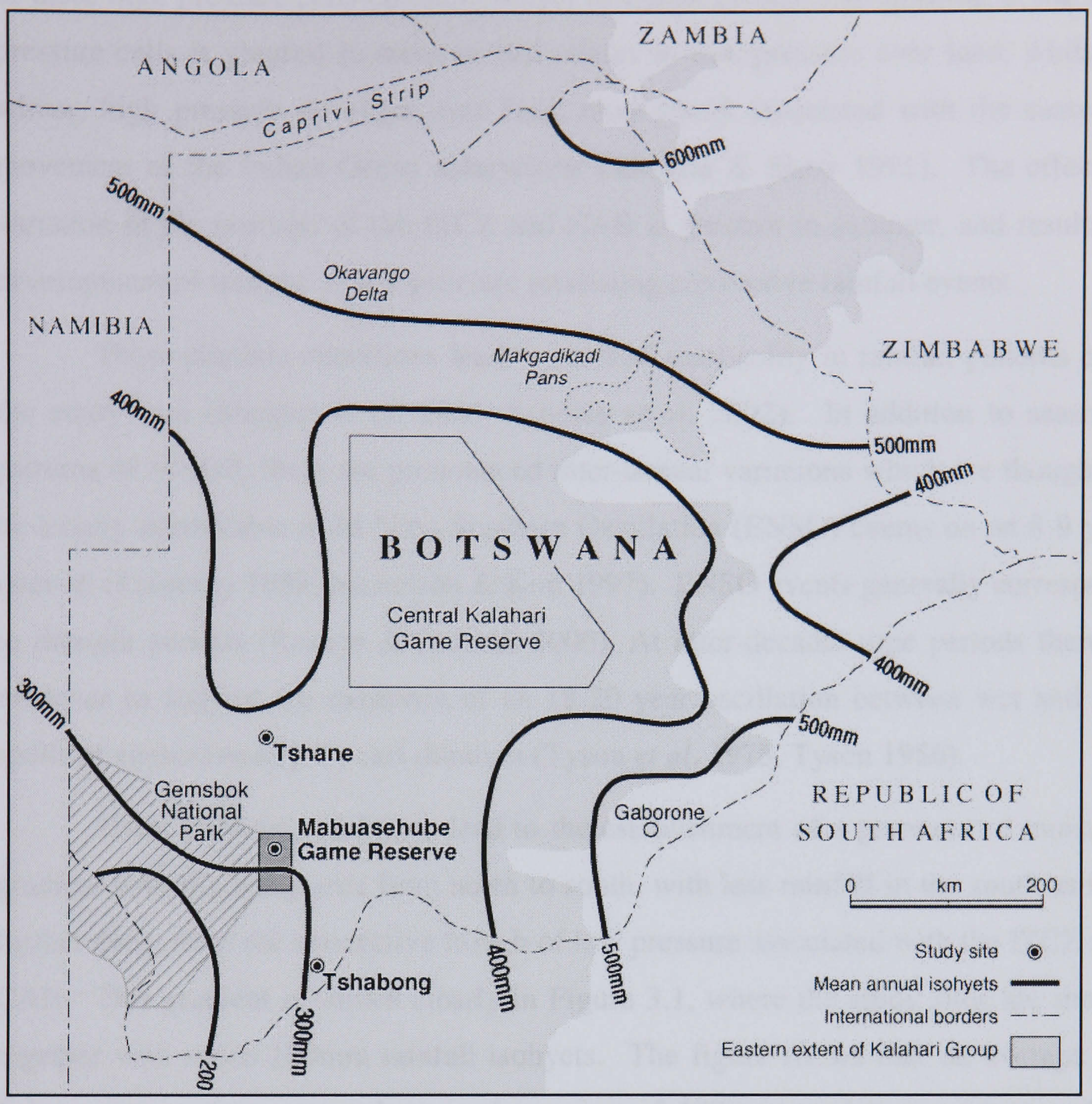

Figure 3.1 Location of the three study sites in south-west Botswana, and 100mm mean rainfall isohyets.

3.2.1 Climate

The synoptic climatology of the study area is dominated by the southern hemisphere descending limb of the Hadley cell, of the general atmospheric circulation (Tyson 1986, Mason & Jury 1997, Tyson & Crimp 1998). Consequently, high pressure anticyclonic circulation patterns characterise the area, in both summer and winter. This general condition is modified by two factors. First, the Southern African land mass creates differential sea-land heating causing the high pressure belt to split into two component cells, the South Atlantic and Indian Ocean anticyclones. Second, variation in the southward movement of the inter-tropical convergence zone (ITCZ), and associated Congo Air Boundary (CAB) in summer, cause variation in the position

of these high pressure cells (Preston-Whyte & Tyson 1989). The splitting of the high pressure cells is greatest in summer and results in low pressure over land, whilst in winter, high pressure develops over land, most likely associated with the eastward movement of the Indian Ocean anticyclone (Thomas & Shaw 1991). The effect of variation in the position of the ITCZ and CAB is greatest in summer, and results in development of troughs of low pressure producing convective rainfall events.

These climatic conditions lead to marked seasonality in rainfall patterns over the study area (Shugart *et al.* 2004, Scholes *et al.* 2002). In addition to seasonal patterns of rainfall, there are pronounced inter-annual variations which are thought to be largely attributable to El-Nino Southern Oscillation (ENSO) events on an 8-9 year interval (Lindesay 1988, Nicholson & Kim 1997). ENSO events generally correspond to drought periods (Reason & Rouault 2000). At inter-decadal time periods there is evidence to suggest the existence of an 18-20 year oscillation between wet and dry spells of approximately 9 years duration (Tyson *et al.* 1975, Tyson 1986).

These climatic conditions lead to the establishment of a pronounced moisture gradient over the study area from north to south, with less rainfall in the south as it is further away from the convective trough of low pressure associated with the ITCZ and CAB. This gradient is shown clearly in Figure 3.1, where the study sites are shown together with mean 100mm rainfall isohyets. The figure shows that on average the Tshane site receives somewhere in the region of 400mm rainfall per annum, while further south at Mabuasehube and Tshabong 300mm of annual rainfall is more typical. In addition to this north-south moisture gradient, the rainfall over the study area is highly concentrated within the summer months, or wet season, from October to April.

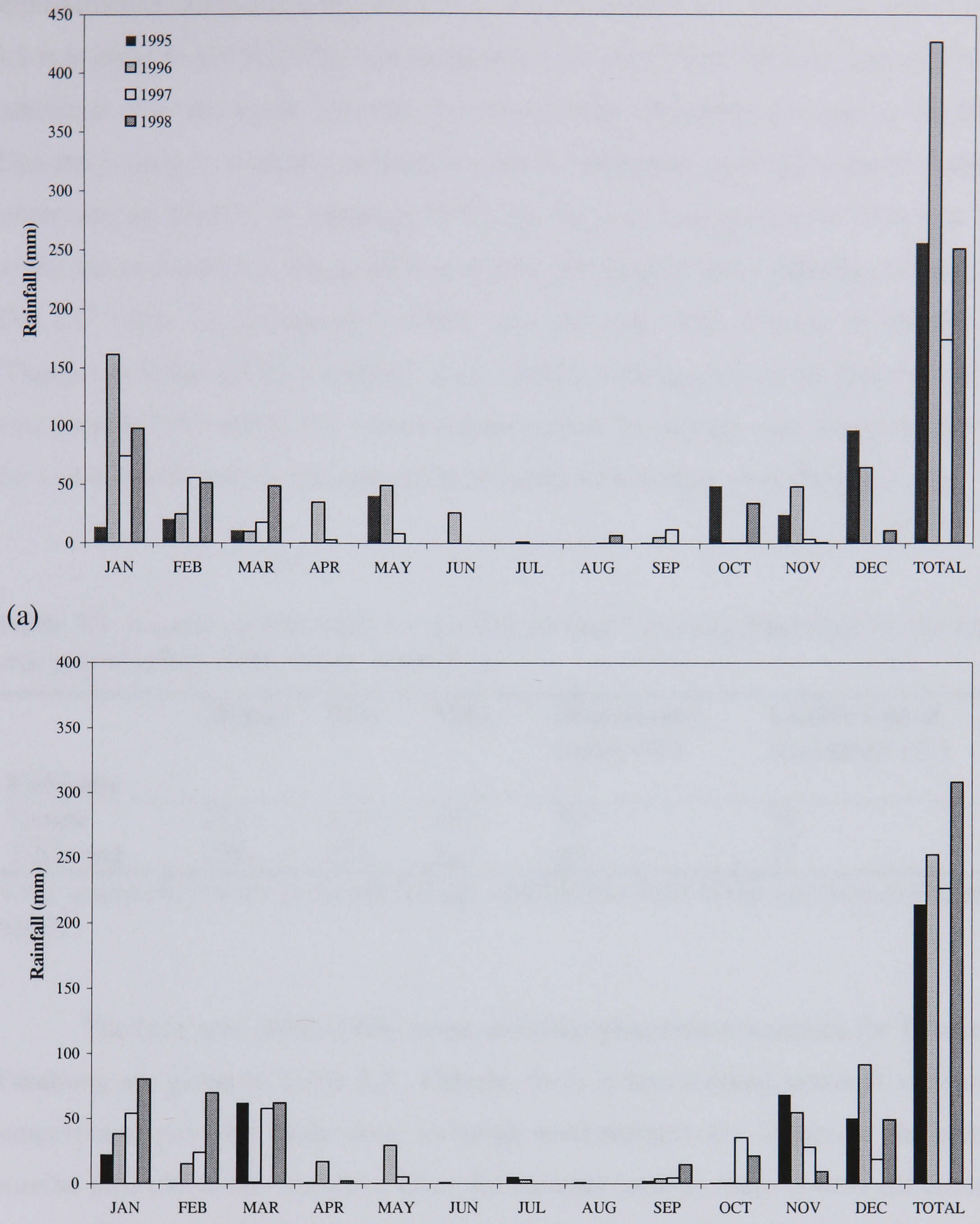

(a)

(b)

Figure 3.2 Monthly and total rainfall at (a) Tshane and (b) Tshabong field sites, for the years 1995-1998. (Data: www 3.1).

These climatic characteristics are illustrated in Figure 3.2 which shows the annual and inter-annual variability in rainfall for the sites at Tshane and Tshabong, over a four year period from 1995-1998. There is no rainfall station at Mabuasehube such that no data were available for this site. These rainfall data were obtained from the International Research Institute for Climate Prediction, at Columbia University, U.S.A. (www 3.1). The data sets are from WMO rainfall stations which are

approximately 20km from the field plots, at both Tshane and Tshabong. From Figure 3.2 it is clear to see both the concentration of the rainfall in the wet season, which is consistent over the years, and also the inter-annual variability throughout the period. This inter-annual variability and seasonality is confirmed with reference to Table 3.1 where the coefficient of variation (CV) for the four year period is 39% and 17%, whilst the seasonality index is 88% and 93%, for Tshane and Tshabong, respectively. The CV value for Tshabong is lower than the long term average of around 40% (Thomas & Shaw 1991), and this is most likely a consequence of the fact that the four year period (1995-1998) fell within a drier period for rainfall over the area, such that the variability is muted. Clearly, there is a semi-arid climate over the study area.

Table 3.1 Annual rainfall totals for the Tshane and Tshabong field sites for the four year period, 1995-1998. (Data: www 3.1).

Field site	Mean	Min	Max	Seasonality index (%)	Coefficient of Variation (%)
Tshane	278	174	427	88	39
Tshabong	250	214	308	93	17

Note: seasonality index is the percentage rainfall that falls in the wet season (October-April).

The four year (1995-1998) mean monthly temperature statistics for Tshane and Tshabong are given in Table 3.2. Clearly, there is less marked seasonal variation in temperature over the study area, although temperatures are higher in the summer months than the winter months. Over the summer months there is little difference in mean daily temperature between sites, temperatures range from 24.8° to 29°, and 22.7° to 29.1° at Tshane and Tshabong, respectively. In the winter months on the other hand, the more southerly site at Tshabong is 2-4° cooler than the most northerly site at Tshane. Data for Mabuasehube is again unavailable, though it is likely that temperatures are somewhere between these values at this site.

A strong diurnal temperature range exists over the study sites, in both summer and winter, however, there is a larger range in winter with mean minimum temperatures being a lot lower than those in summer, which is a reflection of the generally clearer and drier air conditions, permitting night-time re-radiation (Thomas & Shaw 1991). Moreover, there is a larger range in mean minimum and mean

maximum temperature at the Tshabong field site in the winter months, than at Tshane, a result of less solar radiation receipt in the dry season, and longer night-time hours allowing more re-radiation, at this southerly site (Table 3.2). Sub-zero night-time temperatures are commonly experienced in the winter months across the study area.

The study area is also characterised as having high potential evaporation rates. Given the low rainfall and high temperatures, together with low relative humidity, potential evaporation over the south-west Kalahari, exceeds actual evaporation by over six times, thus contributing to the desert like conditions (Tyson & Crimp 1998).

Table 3.2 Mean daily temperature data (°C) for Tshane and Tshabong field sites for the four year period, 1995-1998. (Data: www 3.1).

	Tshane			Tshabong		
Month	**Mean**	**Min**	**Max**	**Mean**	**Min**	**Max**
Jan	29.0	20.6	33.4	28.9	20.2	35.0
Feb	29.0	19.2	33.8	29.1	19.4	35.6
Mar	27.3	18.3	31.9	26.2	17.4	32.8
Apr	24.8	13.9	29.5	22.7	11.8	29.8
May	20.4	9.4	25.8	18.0	6.8	25.5
Jun	18.3	6.0	24.1	14.9	2.9	24.1
Jul	17.8	5.8	23.3	13.8	1.8	21.8
Aug	20.0	7.5	26.4	17.8	5.7	25.8
Sep	25.4	14.1	31.2	22.1	11.6	30.7
Oct	27.8	17.2	33.4	25.1	14.3	32.7
Nov	28.8	19.8	33.2	27.1	17.0	33.4
Dec	28.7	19.4	33.5	28.2	18.2	34.6

3.2.2 Geomorphology

The geomorphology of the study area is dominated by the Kalahari desert (Figure 3.1). The Kalahari desert extends over most of Botswana, and parts of South Africa and Namibia. The Kalahari desert is delimited on climatic grounds, such that the northern (Etosha Pan, Namibia), and southern limits (Orange River, South Africa) extend over semi-arid to arid conditions (Thomas & Shaw 1991). The Kalahari desert is part of a more extensive area which is physiographically and sedimentologically unified, called the Mega Kalahari, extending from ~1° N to 29° S (Thomas & Shaw 1991). The Mega Kalahari formed during the break up of Gondwanaland, about 200 million years ago, when the separation of southern Africa left it with an uplifted

marginal hingeline (which developed into the Great Escarpment of southern Africa), while subsidence led to the formation of the interior basin, which is the Mega Kalahari. Sediments have accumulated here since the Jurassic.

Sedimentation over the millennia has led to the elevated plateau of the Kalahari basin lying at altitudes of ~1000m, with a gently rolling landscape of low relief, mantled largely by unconsolidated Kalahari sand which is between 50 to 100m thick over the study area (Thomas & Shaw 1991). This sand substrate coupled with the low annual rainfall, means that infiltration rates are rapid, and results in there being little if any surface water. It is primarily for this reason that the Kalahari is classed as a desert, despite its abundant vegetation. Other geomorphological features over the study area are frequent pans, where surface water may exist, at least in the wet season (Lancaster 1978, Thomas & Shaw 1991, Shaw & Thomas 1997). Often duricrusts (mainly silcretes and calcretes) are found in combination with these pans. In addition, there are occasional relict linear dune features of moderate elevation, found across the study area.

3.2.3 Soils

The soils over the study area are all developed from Kalahari sands, and display a distinct lack of horizonation, such that it is debatable as to whether they can be considered as soils at all. Nevertheless, the soils are classed as arenosols in the FAO-UNESCO classification used in southern Africa. The soils have poor profile development (though there is some variation in texture with depth in the profile), are moderately acidic, and are generally infertile having very low levels of soil nutrients, and soil organic carbon (Thomas & Shaw 1991, Ringrose *et al.* 1998). In view of this, it is surprising that the vegetation cover is so well developed over the Kalahari.

3.2.4 Vegetation and land use

The vegetation communities over the study area are all savanna complexes. While producing a clear and restrictive definition of savanna is problematic (Cole 1963), because of the large variation in canopy structures encountered, what is common is the existence of a continuous or semi continuous herbaceous layer, together with an

overstorey of woody species, which may be either trees and/or shrubs (Scholes 1997). Savanna may be found with either of these features absent and in varying proportions and conditions, leading to a large range of savanna types, from the wetter more humid savanna woodlands, to the arid desert savanna grasslands (Cole 1986). In southern African savanna, this transition from wood dominated to desert grasslands, trends gradually from Zambia and Zimbabwe in the north east, to the south-west corner of Botswana. This transition is evident at the field sites used in this thesis, where tree dominance and higher cover is largely in evidence at Tshane (where it is wetter), while at the most southerly site Tshabong, there is a general reduction in tree cover and a concomitant increase in shrub cover. These trends are confirmed by others working in the same area (Ringrose 2003, Privette *et al.* 2004, Scholes *et al.* 2002, 2004). It is important to state however, that there is significant variation in savanna structure along this gradient as a result of local variation in soils, geomorphology, and land use practices.

Figure 3.3 shows the physiognomic groupings and vegetation types of Weare & Yalala (1971), across the study area, where it can be seen that all three field sites are on the sandveld (Kalahari sands), and are part of the *Acacia mellifera*, *Acacia leuderitzii*, *Boscia albitrunca* vegetation association. These species dominate the overstorey across the study area and are found together with *Grewia* species. In the understorey, grasses dominate ranging from perennial species of *Aristida*, *Eragrostis*, and *Stipagrostis* where the understorey is in good condition, to annual grasses and forbs where there is disturbance, often associated with overgrazing (van Rooyen & van Rooyen 1998). While the date of the source of this map is now over 30 years old, and vegetation may have changed in this period, from field experience it is considered that the physiognomic groupings and vegetation types are still valid, even if the relative abundance of particular species may have changed.

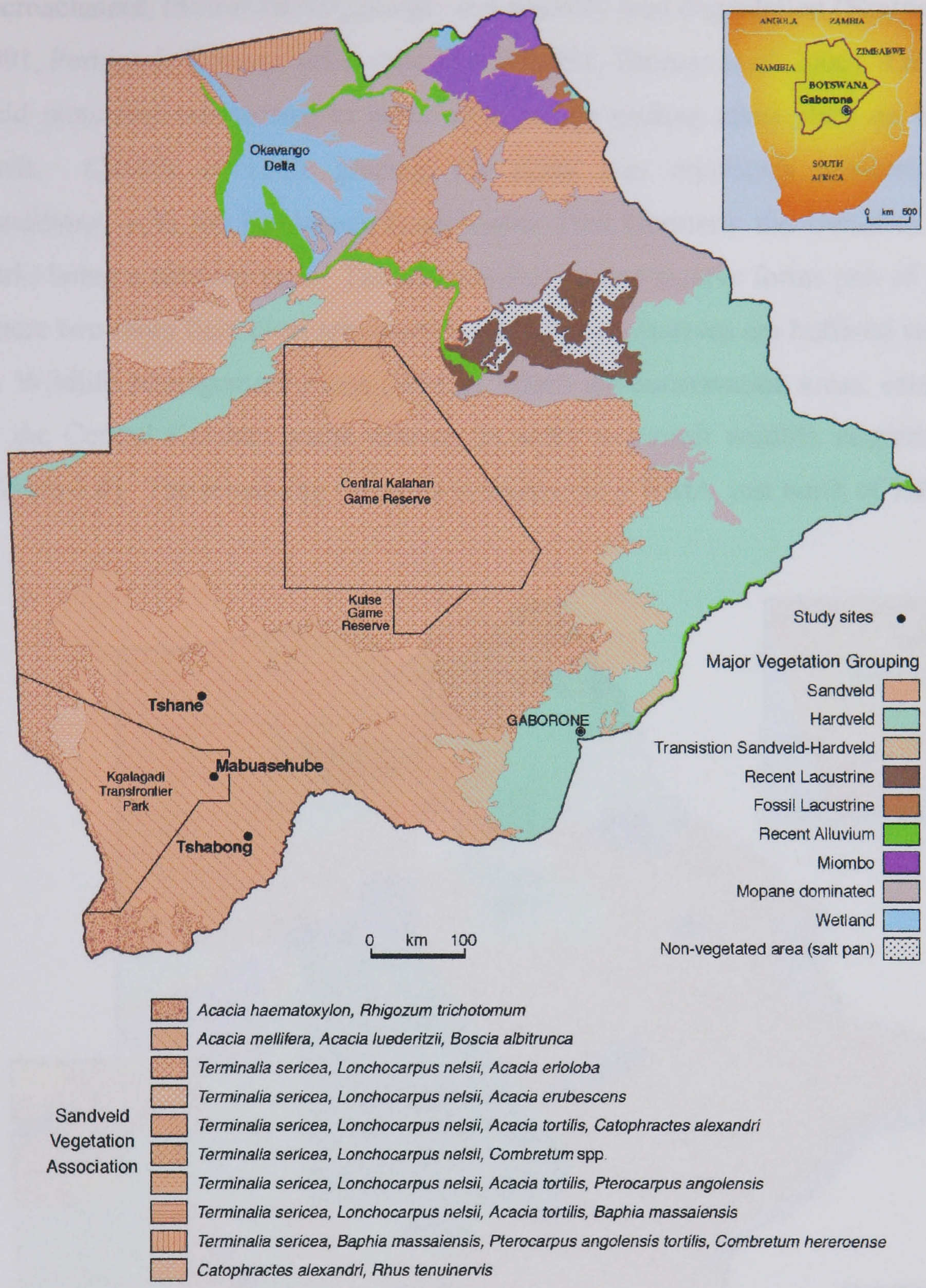

Figure 3.3 Vegetation of the study area (adapted from Weare & Yalala (1971)).

Owing to the remoteness and aridity of the Kalahari in this south-west region of Botswana, the only significant human impact in terms of land use is cattle ranching, both commercial and communal (Dougill *et al.* 1999). The land use over the study is shown in Figure 3.4. This cattle ranching has been associated with the citing of boreholes over large areas of Botswana, which has been reported to lead to an over-concentration of cattle, leading to a reduction in the quality of forage for cattle and, over time, the replacement of these grasses with shrubs, leading to bush

encroachment, environmental change, and possibly land degradation (Skarpe 1990a,b, 1991, Perkins & Thomas 1993, Jeltsch *et al.* 1997, Thomas *et al.* 2000). Of the seven field plots four are located in areas where cattle grazing takes place on communal lands. Outside of cattle grazing, the study area represents relatively pristine conditions, with the Kgalagadi Transfrontier Park (formerly the Gemsbok National Park) being a national park. The Mabuasehube game reserve forms part of this park, where two more field plots are located. These game reserves are buffered on all sides by Wildlife Management Areas (WMA), which are conservation areas, extending up to the Central Kalahari game reserve, in order to permit wildlife migration routes (Figure 3.4). The remaining field plot is situated in a WMA, just north of Tshabong.

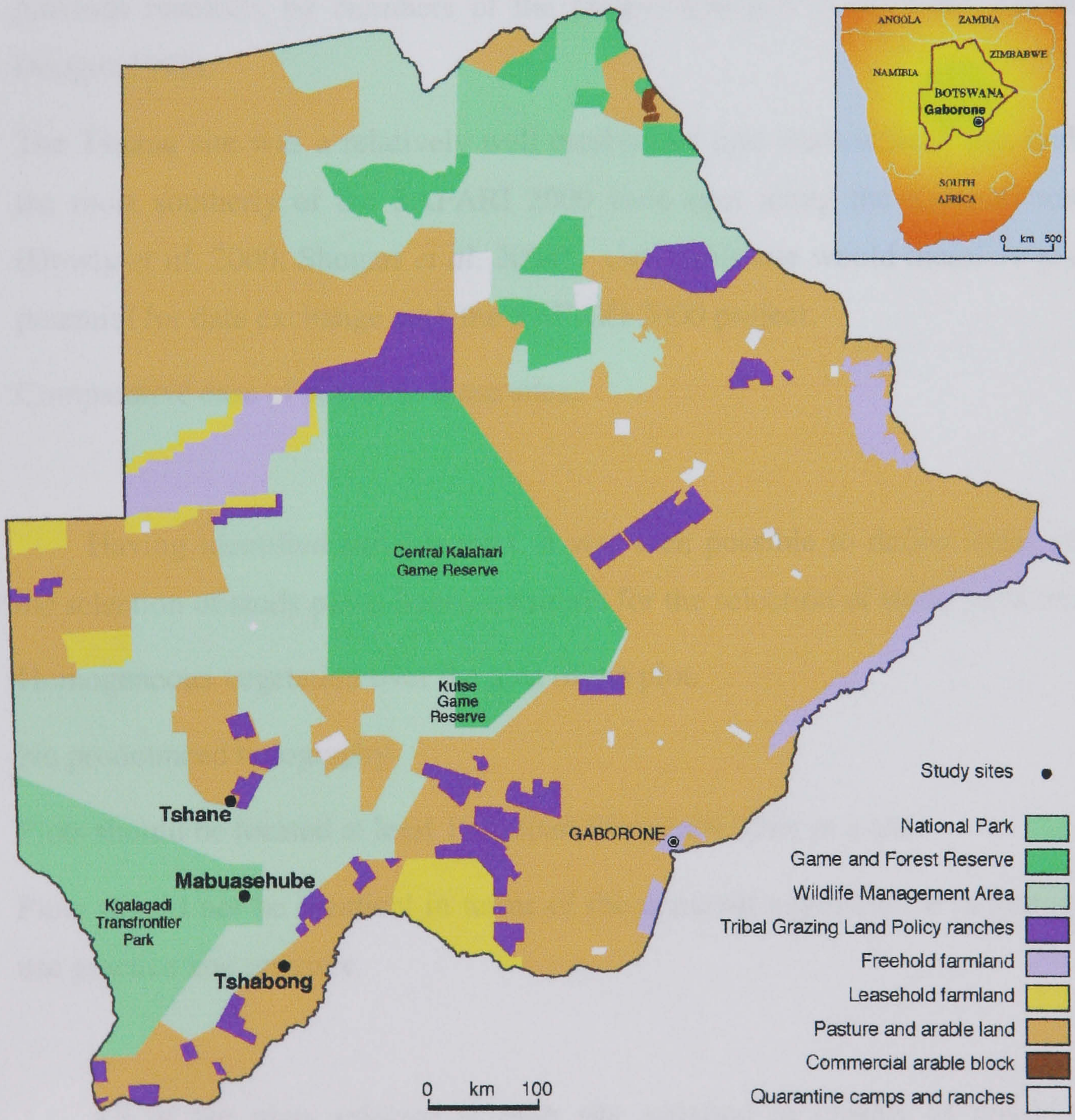

Figure 3.4 Land use over the study area (based on the Republic of Botswana Ministry of Local Government Lands and Housing Map 1996).

3.3 Site and plot selection and description

In order to thoroughly test the physically based plant canopy reflectance models in estimating LAI in savanna ecosystems, it was required that field plots should be located in a range of different savanna vegetation types, congruent with the spatial complexity that is savanna vegetation.

Following a pilot study in the dry season of 2000, it was decided to devote field activity to three sites at Tshane, Mabuasehube, and Tshabong (Figure 3.1). This decision was made for the following reasons:

- These sites offered the desired variation in vegetation type and land use.
- There was an existing knowledge of the Tshabong and Mabuasehube sites from previous research, by members of the project (Dougill *et al.* 1999, Trodd and Dougill 1998).
- The Tshane site was a relatively well established and studied field site, and was the most southerly of the SAFARI 2000 field sites along the Kalahari transect (Dowty *et al.* 2000, Shugart *et al.* 2004). Using this site would therefore provide potential for data exchange with the SAFARI 2000 project.
- Comparative ease of access to these sites.

Having identified suitable sites, it was then possible to define some criteria for the selection of study plots. Specific criteria for the selection of study plots were:

- Homogeneous vegetation over the area of the plot.
- No pronounced topography.
- Plots should be located at least 1km apart from each other at a site.
- Plots should not be identical in terms of the apparent vegetation structure or land use practice and pressure.

All of the plots selected at each site satisfied as closely as possible, the criteria specified. The general characteristics and descriptions of each of the plots are given in Table 3.3.

Table 3.3 General characteristics and description of the field plots.

Site (plot code) and photograph	Geographic co-ordinates (Lat. Long.)	Savanna type	Soil type	Plot description
Tshane plot 1 (T1) 	24.16678 S 21.89017 E	Low tree/shrub savanna	Kalahari sands	*Acacia leuderitzii* and *Acacia mellifera* dominated plot Tree height: 0.87-9.40m LAI: 0.08-3.51 Fractional cover of overstorey vegetation: 16% Fractional cover of understorey vegetation: 17% Light cattle grazing takes place SAFARI 2000 site
Tshane plot 2 (T2) 	24.16473 S 21.88298 E	Low tree/shrub savanna	Kalahari sands	*Acacia leuderitzii* and *Acacia mellifera* dominated plot Tree height: 1.14-9.13m LAI: 0.08-4.45 Fractional cover of overstorey vegetation: 20% Fractional cover of understorey vegetation: 23% Light cattle grazing takes place
Mabuasehube plot 1 (M1) 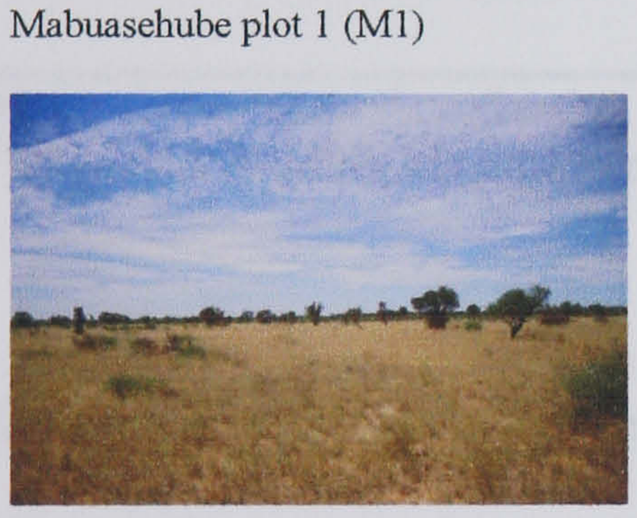	24.91530 S 21.97547 E	Savanna grassland	Kalahari sands	Grass dominated plot Tree height: 0.60-4.41m LAI: 0.01-2.03 Fractional cover of understorey vegetation: 18% Game reserve, light grazing by ungulates
Mabuasehube plot 2 (M2) 	25.00723 S 22.05590 E	Savanna grassland	Kalahari sands	Grass dominated plot Tree height: 0.61-9.08m LAI: 0.05-1.72 Fractional cover of understorey vegetation: 17% Game reserve, light grazing by ungulates
Tshabong plot 1 (TG1) 	25.74133 S 22.31497 E	Shrub savanna	Kalahari sands	*Acacia mellifera* and *Grewia flava* dominated plot Tree height: 1.38-10.38m LAI: 0.10-2.81 Fractional cover of overstorey vegetation: 18% Once intensively grazed, now only very light grazing, little biomass in the understorey

Table 3.3 Continued.

Site (plot code) and photograph	Geographic co-ordinates (Lat. Long.)	Savanna type	Soil type	Plot description
Tshabong plot 2 (TG2) 	25 38 255 S 22 16 711 E	Low tree/shrub savanna	Kalahari sands	*Acacia leuderitzii* and *Grewia flava* dominated plot Tree height: 0.78-8.72m LAI: 0.02-3.59 Fractional cover of overstorey vegetation: 6% Fractional cover of understorey vegetation: 16% Located inside a WMA*, light grazing by ungulates
Tshabong plot 3 (TG3) 	25.63758 S 22.27852 E	Shrub savanna	Kalahari sands	*Acacia mellifera* and *Grewia flava* dominated plot Tree height: 1.55-8.40m LAI: 0.09-5.23 Fractional cover of overstorey vegetation: 8% Once intensively grazed, now only very light grazing, little biomass in the understorey

Note: the savanna classification is based on Cole (1986).
*WMA is a Wildlife Management Area where cattle grazing is not permitted.

3.4 SAFARI 2000 project

The author was able to become an affiliated data partner of the Southern Africa Regional Science Initiative 2000 (SAFARI 2000). SAFARI 2000 was an internationally funded research project, which brought together an international group of researchers, with the aim of developing a better understanding of the southern African regional land-atmosphere system (Dowty *et al.* 2000, Shugart *et al.* 2004). Particular emphasis is given to biogenic, pyrogenic and anthropogenic gaseous emissions, their transport and modification, and how these emissions affect the regional climate and meteorology, and biogeochemistry of ecosystems (Swap *et al.* 2003). To achieve this, SAFARI 2000 integrated remote sensing, computational modelling, airborne and field based studies.

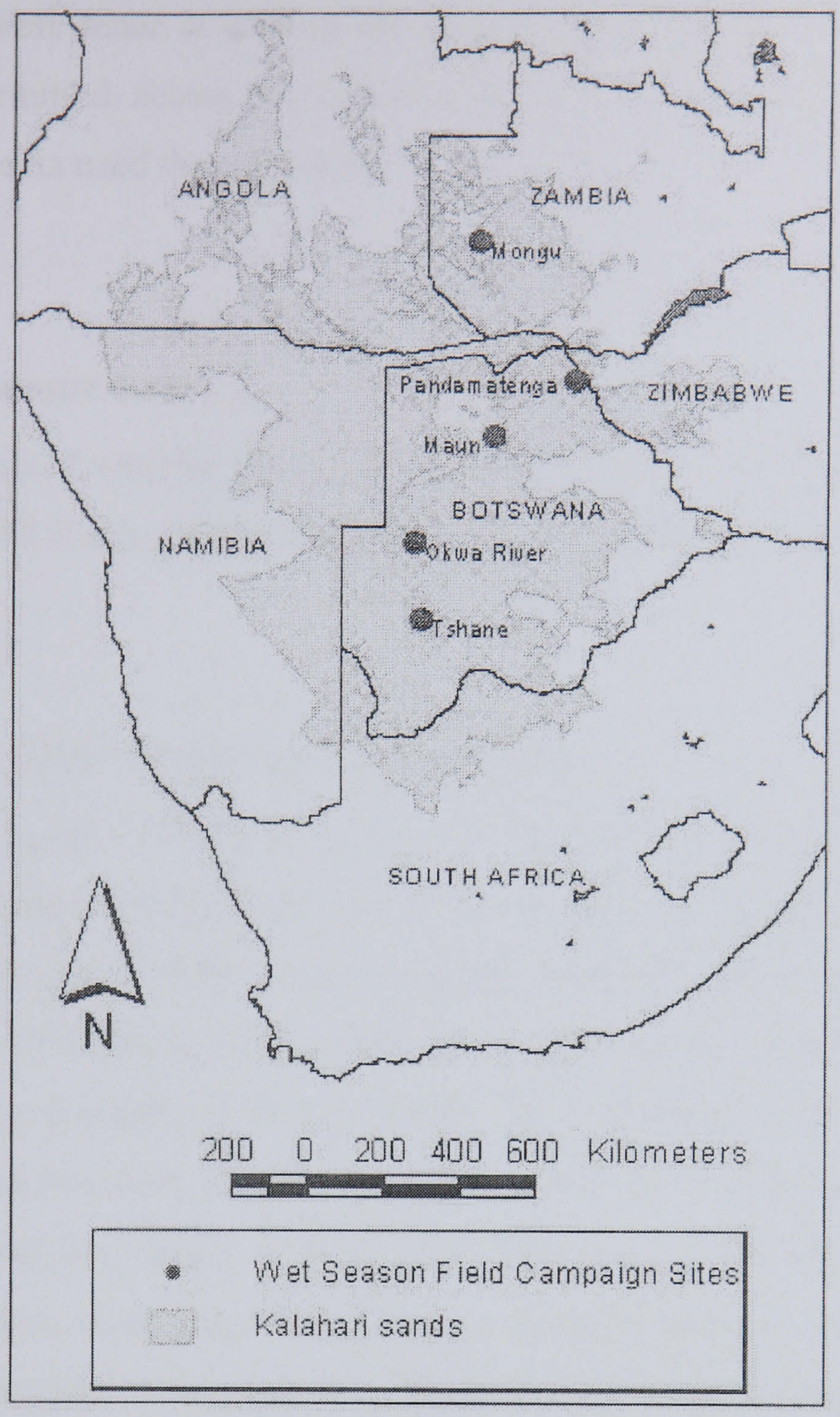

Figure 3.5 Map of the SAFARI 2000 field sites along the Kalahari Transect (*Source*: Dowty *et al*. 2000).

SAFARI 2000 began in mid-1999 and concluded at the end of 2002. A total of four intensive field campaigns (IFCs) were mounted during this period, where ground measurements were made in tandem with airborne and satellite data acquisition. The second of these IFCs took place along a sub-section of the International Geosphere-Biopshere Programme (IGBP) Kalahari Transect (Scholes and Parsons 1997, Scholes *et al*. 2002), in the wet season of 2000. This sub-section of the Kalahari Transect is made up of five field sites, shown in Figure 3.5: one in Zambia at Mongu, and four in Botswana at Pandamatenga, Maun, Okwa River, and Tshane. This transect spans a rainfall gradient of approximately 500mm, with Mongu in the north receiving an average of 880mm per annum and Tshane in the south 365mm. Various ground

measurements were made at each of the sites during this campaign. Membership of this project permitted access to, and sharing of, various data sets, including the Landsat ETM+ data used throughout this thesis.

3.5 Satellite sensor data

Two different sets of satellite sensor data were used in this thesis: Landsat ETM+ and the Terra-MODIS 8-day surface reflectance product (MOD09A1).

3.5.1 Landsat ETM+ imagery and pre-processing

Two level 1-G Landsat ETM+ images were obtained via the SAFARI 2000 project, for use in this thesis (174/078 and 175/077). These two images covered five of the seven field plots, the 174/078 image covered the three plots at Tshabong and was acquired on the 17 February 2001, while the 175/077 image covered the two plots at Tshane, and was acquired on the 28 March 2001. There was no cloud free image available over the two plots at Mabuasehube, to coincide with the field measurements. The nearest cloud free image was not until June 2001, when the vegetation would have been at peak senescence, such that meaningful comparison with this image would not be possible. Consequently, the modelling work in chapter 6 and 8 was performed only for the five plots for which the ETM+ data were available.

Orbital geometric correction was applied to these level 1-G images, since working in this relatively featureless and unspoilt area of the Kalahari means that suitable ground control points (GCPs) are difficult to find. While collecting the field data, an effort was made to collect GCP data, but only two points could confidently be located in the 175/077 image and only one in the 174/078 image. The images therefore relied on the orbital correction applied by the Landsat processing, and is expected to be accurate to within 250 metres (www 3.2). This was checked using the limited GCP data available, and the geometric correction was found to be within this reported accuracy. Given that modelled reflectances are compared against these ETM+ measurements in chapter 6, this lack of precise geometric accuracy is a serious issue, and may lead to large discrepancies. In order to address this issue, an 8x8 pixel area centred on each field plot was extracted and radiometrically calibrated, and

atmospherically corrected to surface reflectance. In this way, there would be 64 different reflectance values to compare against the modelled estimate, and as such at least some of the uncertainty associated with geometric errors has been accounted for.

The images were radiometrically calibrated using the published gains and offsets given in the calibration parameter files (CPF) for each image, and atmospherically corrected using the Second Simulation of the Satellite Signal in the Solar Spectrum (6S), algorithm (Vermote *et al.* 1997a), an improved version of the 5S algorithm (Tanré *et al.* 1990). 6S models the effect of gaseous absorption (primarily O_3, H_2O, O_2, CO_2), and scattering by molecules and aerosols, while the interaction between the two is not considered, except in a statistical way.

To calculate the effect of the atmosphere on the satellite signal, 6S needs inputs of the geometrical conditions (SZA, VZA, RAA), an atmospheric model for gaseous absorption, an aerosol model to calculate scattering effects, target elevation and surface conditions. For all the ETM+ pixels the atmospheric model was given to be tropical, where water and ozone contents in the atmosphere were 4.12g/cm^2 and 0.247cm-atm respectively. The aerosol model was given to be continental, and the aerosol optical thickness was specified from measurements made at Tshane in the wet season of 2000, as part of the SAFARI 2000 project. The value used was 0.1913. It is acknowledged that these data are from a year earlier and as such may not be accurate, however, it was the only information available, and so was used. 6S was run for targets at an elevation of 1000m, so that the temperature and pressure dependence on absorption and scattering was considered. Surface conditions were represented as being patchy but with no directional effect, i.e. a Lambertian surface. After atmospheric correction, all pixels were cloud screened using the method described in Ouaidrari & Vermote (1999), in order to establish data sets of high quality.

3.5.2 Terra-MODIS surface reflectance data and pre-processing

In order to reduce the number of files which would need to be processed and also to increase the likelihood of cloud free images, the MODIS 8-day 500m surface reflectance product (MOD09A1) was downloaded (Vermote & Vermeulen 1999). The MOD09A1 product is atmospherically corrected using data from other MODIS products: MOD04 for aerosols, MOD05 for water vapour, and MOD07 for ozone

(Vermote *et al.* 1997b). Preliminary results indicate that the MODIS surface reflectance product is performing well within the expected uncertainties (Vermote *et al.* 2002).

MODIS data comes in tiles of 10 degrees by 10 degrees, in sinusoidal projection. All data downloaded were version 4 products. The data were first reprojected to a geographic projection, then the various data sets were extracted. For each tile of the MOD09A1 product there are 13 files, 7 surface reflectance for each MODIS channel, 3 geometrical files containing respectively, the SZA, VZA, and RAA of each pixel, a file on the day of year that each pixel was imaged, and 2 quality control files. These data were analysed, and the surface reflectance, SZA, VZA, RAA, and day of year for each field plot was extracted after ensuring the data were not contaminated with cloud or any other contaminant. The MODIS surface reflectances are geometrically corrected and are expected to be accurate to within 150m at nadir (Wolfe *et al.* 2002).

3.6 Summary and conclusions

This chapter has described the general characteristics of the study area, and introduced the seven field plots used in this thesis. The field plots are characterised by:

- Subject to hot and wet summers, with warm and dry winters.
- Rainfall is highly seasonal, with over 80% falling in the summer months.
- All plots are located within the Kalahari desert on Kalahari sands
- Represent a range of savanna vegetation types, and are subject to different land use practices.

In addition, the pre-processing steps and issues associated with the Landsat 7 ETM+ and Terra-MODIS data have been presented. The satellite data were pre-processed to obtain surface reflectance, and these data sets will be used to assess the performance of the modelling work in chapter 6, and to invert the neural networks in chapter 8. While this chapter has described the study area, the next chapter outlines the field measurements which were made during the wet season of 2001, at the seven plots.

4 Field Data Collection

4.1 Introduction

Field measurements of the canopy structure and vegetation surveys were made at the seven field plots between the 28 February and 8 March 2001. The field campaign was undertaken during the latter part of the wet season when it was anticipated that leaf area would be at its maximum. Leaf area being at its maximum would provide the best opportunity for estimating LAI from a canopy reflectance model inversion - the central aim of this thesis. The objectives of the field campaign were:

(i) To establish the probability density functions of key canopy structural variables. These data were required to parameterise the canopy reflectance models in order to perform the experimental modelling work of chapter 6.

(ii) To obtain data on the composition of the vegetation (trees/grass), within the field plots

(iii) To obtain validation data for the inversion work of chapter 8.

Specific measurements that were made during the field campaign were:

- Measurements of the plant area index (PAI), with a SunScan plant canopy analyser.
- Measurements of crown width, crown height, and tree height.
- Measurements of the leaf inclination angle of trees and shrubs.
- Estimates of the canopy coverage (%) of the grass (understorey) and trees/shrubs (overstorey), and the state of the vegetation (fraction green/senescent) within each of the field plots.

This chapter describes the methods used to collect these data. No spectral measurements of the soil or vegetation were made in the field because it was considered too difficult, logistically, to have done so. Soil samples were brought back from the field, and spectral directional measurements were made in the laboratory (chapter 5).

4.2 Plant area index

4.2.1 Sampling framework

A nested sampling framework was adopted to collect the plant area index (PAI) data. One framework was defined on a plot size of 200 by 150 metres, and another was defined on a plot size of 60 by 60 metres, which was centred within the 200 by 150 metre plot (Figure 4.1). Measurements of PAI were made along 200 metre line transects because this represented the most reasonable compromise between transect length, MODIS satellite data spatial resolution, and the time that would be needed to make the measurements, so as to ensure that a sufficient number of plots were studied. This is referred to as the 'MODIS plot'. The 60 by 60 metre plot dimensions were chosen to relate well to the spatial resolution of the Landsat ETM+ imagery, and would allow for potential misregistration of the satellite imagery, given that image registration relied on orbital corrections (Mather 1999). This is referred to as the 'ETM+ plot'.

Within the 200 by 150 metre plot, measurements of PAI were made along five transects A, B, C, D, and E (Figure 4.1). There were three straight line transects (ABC) each of 200 metres in length, each parallel to one another and separated by 75 metres. Measurements were taken at 10 metre intervals, yielding 21 samples per transect. Within the centre of this 200 by 150 metre plot, measurements were taken along two additional straight line transects (DE), which extended from the corners of the 60 by 60 metre plot. These two transects were each of 85 metres in length, measurements were taken every 5 metres, thus yielding 18 samples per transect. Thus, for one plot as a whole there were 99 measurements of PAI.

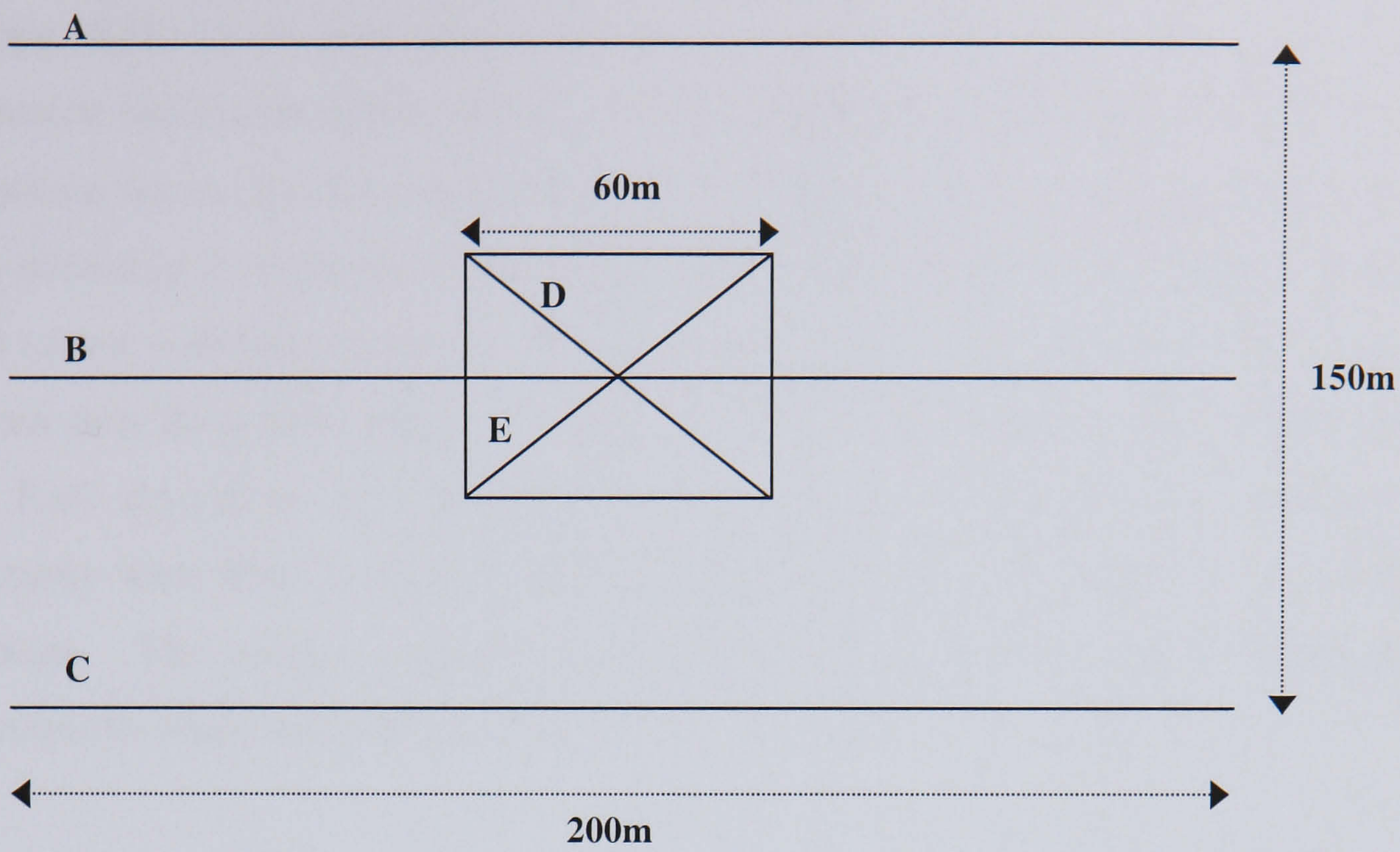

Figure 4.1 Schematic overview of the arrangement and dimensions of the transect measurements of PAI and the central 60 by 60 metre field plot. Measurements along transects A, B, and C were made at 10 metre intervals, and every 5 metres along transects D and E. The central 60 by 60 metre plot served as the focus for measurements of canopy dimensions, vegetation surveys and leaf inclination angle.

4.2.2 Instrumentation

Measurements of PAI were made with a SunScan plant canopy analyser (Delta-T, Cambridge, UK, 1996). This instrument is a line quantum sensor which consists of a 1 metre long probe which has 64 photodiodes evenly spaced along it, sensitive to photosynthetically active radiation (PAR), in the range 400-700nm (Welles 1990). The SunScan probe is connected to a beam fraction sensor (BFS) which records incident PAR above the canopy, whilst the SunScan probe is placed beneath the plant canopy and records the transmitted PAR.

Estimates of PAI are obtained from the SunScan by inverting a simple model of the canopy radiation transmission. The canopy transmission is modelled using the ellipsoidal leaf angle distribution parameter (ELADP) of Campbell (1986), to calculate the canopy extinction coefficient, and Beer's law for direct radiation transmission, as:

$$S_b(L) = S_b(0) \exp(-KL) \qquad (4.1)$$

Where S_b *(0)* is the flux density of direct radiation on a horizontal surface above the canopy, $S_b(L)$ is the flux density below leaf area index, L, and K is the canopy extinction coefficient (Hapke 1986). Wood (1996), integrated Campbell's results over the whole sky to describe the transmission of diffuse radiation through a plant canopy, thus obtaining an estimate of the canopy transmission based on the ratio of direct to total (direct + diffuse) radiation. Wood's model was used to compute the transmission of radiation for a wide range of model parameter combinations (solar zenith angle, leaf PAR absorption, LAI, ELADP, ratio of direct to total radiation). Computable functions were fitted to these model simulations, which are stored in the SunScan software. The canopy transmission measured in the field is used to invert these functions to obtain estimates of PAI.

4.2.3 PAI data collection

PAI is defined as the one sided plant area per unit ground area (m^2/ m^2), and thus represents the sum of: the leaf area index (LAI) - the one sided leaf area per unit ground area (m^2/ m^2), and the wood or litter area index (WAI, LitAI) - the one sided wood or litter area per unit ground area (m^2/ m^2) (Chen *et al.* 1997, Asner *et al.* 1998b, 2000, White *et al.* 2000).

To use the SunScan plant canopy analyser the user inputs some of the model parameters used in the calculation of PAI, to the SunScan software. First, the location, local time (from GMT), and date are given to the SunScan software, and the solar zenith angle - a model parameter - is calculated. Second, a value for the ELADP must be given. Here, the software default was used, an ELADP of 1, representing a spherical leaf angle distribution. Finally, a value must be given for the leaf PAR absorption. Again, the software default was used, and leaf PAR absorption was set to 0.85. These default settings were used since there was no prior information to inform the selection of values. The settings used remained constant for all measurements made with the SunScan, irrespective of plot or canopy type.

The PAI is calculated based on measurements of the transmission of solar radiation in the PAR wavelengths. Above canopy PAR is recorded with the BFS which includes a shadow ring for calculating the ratio of direct to total radiation. The canopy transmission is recorded with the SunScan probe by placing it underneath the

plant canopy (Figure 4.2). The levels of incident PAR above the canopy and transmitted PAR below the canopy are recorded simultaneously, the computable functions in the SunScan software are inverted, and an estimate of PAI is obtained, which is stored on a Psion Workabout ™ handheld computer.

Measurements of PAI were always made with the BFS attached to the SunScan probe, such that data were recorded in 'simultaneous' mode. However, the BFS started to malfunction at Tshabong plot 1. The BFS would occasionally either not record the incident PAR and not give a PAI value and report an error; or instead, always gave the maximum value of 2497.6 μmol m^{-2} s^{-1} PAR, and a nonsense beam fraction value, but a sensible PAI value. This was caused by a temporary short circuit in the communication cables between the BFS and the SunScan probe (Edmund Potter, Delta-T Devices, June 2001, *personal communication*). An example file which illustrates the problem is shown in Figure 4.3. This slowed the data collection because of the time delay for the incident PAR to be recorded correctly, which sometimes took five or six attempts. After a while this problem got worse, with virtually every measurement of incident PAR being recorded as zero.

With this, it was decided to make measurements of PAI in 'sequential' mode, where, first the incident PAR above the canopy was recorded with the SunScan probe, before recording the transmitted PAR beneath the plant canopy. The ratio of direct to total radiation is determined by casting a shadow on the SunScan probe when it is held above the canopy. Data were recorded in 'sequential' mode only at Tshabong plot 3. Fortunately, when measurements were made in this mode, the light conditions were very stable, such that estimates of PAI made in 'sequential' mode were very similar to estimates made when using the instrument in 'simultaneous' mode. To investigate if this difference in data collection mode would bias estimates of PAI, tests were later carried out in Salford. Measurements were made of one plant, both with and without the BFS, and there was no significant difference in PAI found between the two modes of data collection (Student's t-test, $P>0.05$, two-tailed probability).

Figure 4.2 Measurements of PAI with the SunScan plant canopy analyser, at Tshane plot 1. Top, overstorey measurement, showing the SunScan probe and; bottom, understorey measurement, showing the SunScan probe, beam fraction sensor (with shadow ring).

Unfortunately, this malfunction was not always detected because the SunScan software continued to give sensible PAI values. This led to the loss of some data points in the data reduction, since Delta-T recommended that PAI values estimated with incident PAR at 2497.6 μmol m^{-2} s^{-1} should be discarded.

Measurements of PAI were made of both the understorey and overstorey. When measurements of the overstorey were made an 'o' was recorded with the data

value to indicate that the value corresponded to an overstorey measurement (see the 'Notes' column in Figure 4.3). In this way, data were collected on the PAI of both canopy layers of the vegetation, which were needed for the model parameterisation, rather than just having averaged plot values. Measurements were made approximately one hour either side of solar noon to avoid large differences in solar zenith angles. Estimates of PAI obtained from the SunScan are consistent up to solar zenith angles of 60 degrees, beyond which estimates become susceptible to larger errors. This gave a large period of time within which PAI measurements could be made, since the SunScan can be used in most light conditions. Despite this, it was considered good practice to always try and make measurements at around the same time each day. This also made planning the fieldwork more straightforward - everyone involved in the data collection knew when they would be needed, thereby optimising the data collection for all parties concerned.

	A	B	C	D	E	F	G	H	I	J	K	L
1	Created by SunData for Workabout v1.06											
2												
3	Title :	trans200										
4	Location :	TG										
5	Latitude :	25.4S	Longitude	22.2E								
6	07/03/01		Local time is GMT+2 Hrs									
7	SunScan probe v1.01											
8												
9	Ext sensor: BFS		Leaf Angle Distn Parameter:				1	Leaf Absorption:		0.85		
10	Group 1 :											
11												
12	Time	TG2	samp	Trans-	Spread	Incid-	Beam	Zenith	LAI	Notes		
13				mitted		ent	frac	Angle				
14												
15	11:52:30	1	1	1753.1	0.18	2497.6	0.00	23.5	0.4			
16	11:53:26	1	2	1478.3	0.24	2121.6	0.77	23.4	0.6			
17	11:54:02	1	3	585.8	0.64	2497.6	0.00	23.3	2.1	o		
18	11:55:23	1	4	1329.3	0.35	2497.6	0.00	23.1	0.8			
19	11:56:28	1	5	1780.8	0.13	2497.6	0.00	23.0	0.4			
20	12:00:16	1	6	1449.6	0.33	2497.6	0.00	22.6	0.7			
21	12:01:06	1	7	470.1	0.48	2497.6	0.00	22.5	2.4	o		
22	12:02:01	1	8	1568.7	0.28	2497.6	0.00	22.4	0.6			
23	12:03:35	1	9	1822.6	0.09	2138.7	0.75	22.2	0.3			
24	12:04:21	1	10	1682.7	0.14	2114.3	0.75	22.2	0.4			
25	12:06:43	1	11	1454.3	0.31	2131.3	0.75	21.9	0.7			
26	12:07:25	1	12	1767.6	0.16	2163.1	0.76	21.9	0.3			
27	12:08:38	1	13	732.9	0.69	2180.2	0.76	21.8	2.0	o		
28	12:09:34	1	14	182.6	1.01	2179.0	0.77	21.7	4.6	o		
29	12:10:22	1	15	1243.2	0.49	2285.2	0.75	21.6	1.1			
30	12:11:03	1	16	923.3	0.55	2252.2	0.75	21.6	1.6			
31	12:13:05	1	17	1644.0	0.24	2187.5	0.75	21.4	0.5			
32	12:14:20	1	18	1600.8	0.29	2128.9	0.75	21.3	0.5			
33	12:15:40	1	19	1529.3	0.36	2117.9	0.75	21.2	0.6			
34	12:16:27	1	20	1643.0	0.16	2111.8	0.75	21.2	0.4			
35	12:17:16	1	21	1883.3	0.05	2141.1	0.76	21.1	0.2			
36												

TG2A copy

Figure 4.3 Example file output from the SunScan plant canopy analyser, illustrating the problem with the incident PAR readings and fraction of beam (direct) radiation - columns F and G respectively.

4.2.4 PAI data quality assessment

It is pertinent to discuss the accuracy of the data collected with the SunScan plant canopy analysis system, both with respect to the general model assumptions used to derive the functions for estimating PAI, and the particular way in which the instrument was used. First, the SunScan makes the following assumptions about the canopy in the calculation of the PAI:

- The canopy is an infinite, homogeneous horizontal slab
- Foliage elements are distributed randomly in the canopy

The canopies encountered in these semi-arid savanna ecosystems, displayed a range of canopy structures, from the sparse and open to the dense and closed. Most measurements however, were made in the more characteristic sparse and open canopies of the grass understorey, which may be considered homogeneous, while measurements of shrubs and trees, were heterogeneous. Thus, while in some cases the assumption that the canopy is a homogeneous medium may be valid, in other cases this assumption would have been violated. It may be considered that a different optical instrument should have been used, which did not make such an assumption. Of the other optical instruments that could have been used, such as the LAI-2000 (LI-COR, Lincoln, Nebraska), and others (e.g. TRAC, Chen and Cihlar 1995), which rely on the inversion of gap fraction data for estimating PAI, White *et al.* (2000) report very similar estimates of PAI obtained in the Jornada shrublands of New Mexico, U.S.A., when using an LAI-2000 and a ceptometer (which uses a method very similar to the SunScan for deriving estimates of PAI). These Jornada shrublands are similarly composed of sparse open canopies, such that it may be reasonable to assume that similar results would be obtained, if the experiment were to be repeated in the field plots used here. Perhaps the only way to account for the homogeneity assumption, would be to calibrate the SunScan estimates of PAI with destructively sampled estimates, as suggested by Norman and Campbell (1989), and performed by Asner *et al.* (1998b, 2000). This was not done here, however, since it would have been too time consuming to perform for a representative sample of the main shrub and tree species and grasses.

The assumption that the foliage elements are randomly distributed within the canopy is difficult to assess. From field observations and photographs, overall, there does not appear to be non-random or at least no excessive clumping of foliage, such that this assumption may be valid. This assertion is supported by the radiative transfer formulations for various biomes given in Table 1 of Knyazikhin *et al.* (1998a), where foliage dispersion in savanna is stated to exhibit minimal clumping. While the TRAC instrument can measure the gap size distribution from which an estimate of the clumping index can be obtained (Chen and Cihlar 1995), no such instrument was available for use with this work. Various researchers have addressed the issue of non-random or clumped distributions of foliage, as encountered when trying to estimate the PAI from optical instruments (Nilson 1971, Chen *et al.* 1997). Where clumped foliage is present and not accounted for, the estimates of PAI will be underestimated, since more radiation will be transmitted through the canopy than the actual or 'true' PAI value would suggest. In this thesis no correction has been made to the PAI estimates to account for clumping or non-random foliage distribution.

Two further issues regarding the validity of the software settings for the ELADP and leaf absorption need to be addressed. The ELADP was set to 1 representing a spherical LAD (mean leaf angle 57.4 degrees (Wang and Jarvis (1988)), and this value was used irrespective of plot or canopy type. The leaf angle distribution (LAD) of the trees and shrubs was unknown *a priori*, such that a spherical LAD was deemed to be a reasonable representation. This was later confirmed by measurements (mean leaf angles are around 57 degrees, see Table 4.2). The leaf angle distribution of the grasses was also unknown *a priori*, however, it was assumed that the grasses would conform to an erectophile distribution, such that no attempt was made to measure the LAD of the grasses. Clearly, the use of a spherical LAD in the model parameterisation for the SunScan may have been invalid when the PAI of the grass understorey was being measured.

Recently, Wohlfahrt *et al.* (2001), investigated the effect that the type of LAD specified in the model parameterisation (of SunScan and Decagon instruments) had on estimates of PAI. They were able to show that the differences in estimates of PAI were not significant when using a measured versus a spherical LAD when the measured LAD did not deviate from a spherical LAD by more than 27 degrees. It therefore seems likely that the effect of a spherical LAD in deriving estimates of the

PAI of the grass understorey will be a slight underestimation, since more light will be transmitted under an erectophile distribution than a spherical distribution, for a given value of PAI. The software settings on the SunScan could have been updated in the field every time the understorey and overstorey were being measured along the transect. This was not done however, since it was considered that attempting to do so would likely lead to inconsistencies, and therefore random error introduced.

The leaf absorption was set at 0.85 and again was not changed regardless of plot and canopy type. A value of 0.85 for leaf absorption assumes a healthy green leaf. For the measurements of the tree/shrub overstorey this assumption was reasonable. However, for the grass understorey at Mabuasehube plots 1 and 2 this assumption would have been invalid, since both contained a large fraction of standing litter which would not absorb as strongly as a healthy green leaf.

4.2.5 Deriving LAI from PAI data

The discussion so far has concentrated on the measurement of PAI data, when it is the LAI that is required for model parameterisation. The SunScan instrument, like all optical devices used to measure the LAI is based on light interception, such that all the above ground elements of the vegetation (leaves, stems, branches, standing litter) contribute to the interception of light. Consequently, what is measured by the optical instruments is not actually the LAI, but rather the effective PAI, which is the product of the PAI and the clumping index (Chen and Cihlar 1995). It is therefore necessary to correct for two factors in order to obtain estimates of the LAI from the effective PAI: 1) the wood and/or litter area contribution, and, 2) the clumping index (Chen *et al.* 1997, Gower *et al.* 1999). Mathematically:

$$L = (1 - \alpha) L_e / \Omega \qquad (4.2)$$

where L is the LAI, α is the wood and/or litter area to total plant area ratio, L_e is the effective LAI and Ω is the clumping index. As stated in §4.2.4, no correction was made for the clumping index, because the vegetation measured was assumed to be generally randomly distributed, such that the clumping index would be unity.

Corrections were made for the wood and litter area contribution to the PAI (L_t), such that the LAI is obtained from:

$$L = (1 - \alpha) L_t \qquad (4.3)$$

To correct for the wood and/or litter area contribution to the PAI, requires data for the wood area index (WAI) and litter area index (LitAI). No such data were collected in this thesis. Values for the WAI were therefore obtained from the literature. Values for the LitAI were derived using field estimated values of the fraction of green and senescent vegetation (see §4.4), such that if the fraction of senescent was estimated at 50 per cent, the LitAI would be calculated as being 50 per cent of the PAI value (Asner *et al.* 2000).

Published values for PAI and WAI were obtained from Asner (1998b,c) and Asner *et al.* (2000), which relate to measurements of *Prosopis glandulosa* - a fine leaved evergreen shrub, from which a mean value for the WAI:PAI ratio was obtained. These values come from two sites, one a sub-tropical savanna in Texas, the other from the Jornada shrublands of New Mexico, both in the U.S.A. Values from *Prosopis glandulosa* were used since they were considered to bear the closest resemblance to the structure of the various *Acacia* species measured in this study. The mean value was obtained by calculating the ratios for the minimum and maximum values of WAI and PAI from the values in Asner (1998b); and the ratios for the mean plus and minus one standard deviation of WAI and PAI from the values in Asner *et al.* (2000). This resulted in a mean WAI:PAI ratio of 0.22. Values for LAI were then obtained using equation 4.3.

It is important to state that subtracting the whole ratio may lead to an underestimate of the actual LAI, since this assumes that the woody elements are distributed randomly with respect to the leaves in the canopy (Gower *et al.* 1999). If the woody elements are not distributed randomly with respect to the leaves, then the leaves may preferentially shade the woody elements, such that, although the ratio of WAI:PAI may be correct, the actual contribution of the woody elements to light interception, and therefore PAI, may be overestimated. Kucharik *et al.* (1998), showed, using a multi-band vegetation imager (MVI), that the branches play a very

small part in light interception in fully leaved canopies, such that corrections to PAI should be made based on the stem area index alone, and not the total WAI.

Whilst it is clear that for some measurements made in this thesis the subtraction of the complete ratio may overstate the importance of the woody contribution to PAI, and conversely, using the ratio may understate the importance of the woody contribution in other measurements; without any information on the contribution of the woody material, it is difficult to handle the problem any more elegantly.

The measurements of PAI and derived LAI from the transect measurements were also converted to total-area values (of a Landsat ETM+ and MODIS pixel) using the following formula:

$$\text{Total-area componentAI} = \text{componentAI} * \text{Fcov} \tag{4.4}$$

Where componentAI is the PAI, LAI, WAI or LitAI, and Fcov is the fractional cover of vegetation. The total-area PAI, LAI, and WAI/LitAI were all calculated in this way, using the estimates of fractional cover for the overstorey and understorey obtained from the vegetation surveys of section 4.5. The plot total-area LAI (overstorey + understorey pixel LAI) was also calculated.

4.2.6 Spatial dependence of LAI data

Given that measurements of the PAI and therefore derived LAI were made every 10 metres and 5 metres along the transects, it is important to test the adequacy of the sampling framework, in terms of maximising the information content for a minimum number of samples (Curran and Atkinson 1998; Atkinson and Tate 1999). To test whether the LAI data collected exhibited spatial autocorrelation, the Moran's I statistic was calculated (Goodchild 1986). The Moran's I statistic is scaled between +1 and -1, with positive values indicating that data are spatially autocorrelated, and negative values indicating that data are not spatially autocorrelated and independent of one another. Mathematically, the Moran's I is calculated as:

$$I = \left(\frac{n}{\sum_i \sum_j w_{ij}} \right) \left(\frac{\sum_i \sum_j w_{ij} (x_i - \bar{x})(x_j - \bar{x})}{\sum_i (x_i - \bar{x})^2} \right) \quad (4.5)$$

where i and j index the spatial points, of which there are n, $\bar{x}$ is the mean of x and w_{ij} is the weight or degree of connection between points i and j. The Moran's I was calculated for all transects where sufficient data existed.

Overall, the Moran's I was statistically significant in only one case, at Mabuasehube plot 1 transect d, where the calculated value of I was 0.533, indicating reasonably strong spatial autocorrelation. Although the rest of the calculated values of I are not statistically significant, the majority of these I values are either negative or approximately zero, thus suggesting that spatial autocorrelation is not particularly prevalent. Overall therefore, it is unlikely that these data suffer from excessive spatial autocorrelation, and the sampling framework adopted was suitable for maximising the information content for the number of sample measurements.

4.3 Canopy dimensions

Measurements of crown width, tree height, height to crown, and crown height were made for between 10 and 20 individuals of the dominant overstorey tree and shrub species at each plot. Measurements were concentrated within the 60 by 60 metre plot, although measurements were made further a field than this, but still within the bounds of the 200 by 150 metre rectangular plot, when there were insufficient number or uniformity of canopy type within the 60 by 60 metre plot, the idea was to get the naturally occurring range of data values. Measurements of canopy dimensions at Mabuasehube were not made within the actual field plots. This was because the two field plots were both grassland savanna, and so was not possible. Measurements were made elsewhere in the Game Reserve however, because time allowed, and it was considered potentially beneficial to do so. The results of the canopy dimensions measurements made at each of the sites are presented in Table 4.1.

4.3.1 Crown width

Measurements of the crown width were made for the overstorey vegetation of trees and shrubs. Crown width was measured directly using tape measures. If vegetation was clumped as was sometimes the case, then clumps of the same species were treated as one individual. The longest axis was measured first and then a second axis approximately orthogonal to this one was also measured. Crown diameter was then calculated as the average of these two measurements.

Table 4.1 Canopy dimensions by site and species. Mean and standard deviations are given with minimum and maximum values in parentheses. Figures presented are in metres. Measurements at Mabuasehube were not made within the field plots but from elsewhere in the game reserve.

Site / Species	Tree height[1]	Crown height[2]	Height to crown[3]	Crown diameter[4]
Tshane				
Acacia leuderitzii (n=20)	5.28 ± 2.64 (0.87 - 9.40)	4.38 ± 2.55 (0.72 - 9.30)	0.89 ± 0.97 (0.10 - 3.59)	5.33 ± 2.93 (0.95 - 11.10)
Acacia mellifera (n=20)	2.88 ± 0.89 (1.14 - 4.08)	2.62 ± 0.86 (0.98 - 3.94)	0.26 ± 0.15 (0.05 - 0.50)	4.43 ± 1.79 (1.88 - 7.55)
Mabuasehube				
Acacia mellifera (n=12)	1.52 ± 0.67 (0.80 - 3.46)	1.41 ± 0.68 (0.60 - 3.36)	0.11 ± 0.06 (0.00 - 0.20)	2.37 ± 1.08 (1.20 - 4.94)
Grewia flava (n=27)	1.20 ± 0.43 (0.60 - 2.04)	1.08 ± 0.40 (0.45 - 1.82)	0.12 ± 0.09 (0.00 - 0.34)	1.81 ± 0.97 (0.68 - 3.89)
Acacia erioloba (n=37)	4.93 ± 2.89 (0.65 - 11.15)	2.87 ± 1.67 (0.57 - 7.23)	2.06 ± 1.57 (0.05 - 5.09)	3.96 ± 2.36 (0.75 - 9.98)
Boschia albitrunca (n=10)	3.68 ± 0.48 (2.93 - 4.41)	1.98 ± 0.52 (0.85 - 2.55)	1.71 ± 0.51 (0.95 - 2.33)	2.90 ± 0.52 (2.40 - 4.00)
Tshabong				
Acacia leuderitzii (n=18)	5.87 ± 2.71 (1.07 - 10.38)	5.00 ± 2.61 (0.89 - 9.59)	0.88 ± 0.88 (0.00 - 4.00)	6.10 ± 2.98 (1.01 - 11.44)
Acacia mellifera (n=31)	3.11 ± 1.55 (1.38 - 8.40)	2.76 ± 1.47 (1.09 - 7.89)	0.35 ± 0.29 (0.00 - 1.15)	3.78 ± 1.65 (1.02 - 7.78)
Grewia flava (n=37)	2.11 ± 0.58 (0.78 - 2.88)	1.96 ± 0.55 (0.74 - 2.85)	0.15 ± 0.15 (0.00 - 0.46)	3.49 ± 1.56 (1.01 - 7.00)

[1] Distance from the ground to the top of crown.
[2] Difference between tree height and height to crown.
[3] Distance from the ground to the lowest point of the crown.
[4] Calculated as the average of the two principal axes.

4.3.2 Tree/shrub height, height to crown, crown height

Measurements of tree height and height to crown were made by either directly measuring using a tape measure, or using simple trigonometry, where the distance from a point to the centre of the tree/shrub was recorded together with the angle to the top of the canopy. Crown height was calculated by subtracting height to crown from tree height.

4.4 Leaf angle distribution

The leaf angle distribution (LAD) is given by the distribution of inclination and azimuth angles of the leaves (Ross 1981). The leaf inclination angle is generally defined as the angle between the normal to the leaf surface and the vertical; the azimuth angle is that between a horizontal projection of the leaf perpendicular and some direction, usually north (Daughtry 1990). For model parameterisation, the required information is the fractional distribution of leaf area in each angle class (from 0-90 in 10 degree class intervals). de Wit (1965) reports how most leaves display no preferred azimuthal direction, such that it may reasonably be assumed that there is azimuthal symmetry. Therefore, only the leaf inclination angle was measured in order to establish the LAD for a given plant canopy.

In this thesis, the leaf inclination angle was measured for the overstorey vegetation of trees and shrubs, since it was assumed that the grass understorey would conform to an erectophile distribution (de Wit 1965). The leaf inclination angle was measured using a clinometer. Approximately 100 measurements were made at random, on individuals of the most common species at each site, these were: *Acacia leuderitzii*, *Acacia mellifera*, *Acacia erioloba*, and *Grewia flava* (Table 4.2). All measurements made on each species from the different plots were combined in order to increase the sample size from which leaf angle distributions were obtained for each species.

Table 4.2 Summary statistics of leaf angle measurements by site and species totals. Mean and standard deviations are given with range in parentheses. Measurements at Mabuasehube were not made within the field plots but from elsewhere in the game reserve.

Site / Species	Leaf Angle
Tshane	
Acacia mellifera (n=103)	59 ± 15 (23 - 90)
Acacia leuderitzii (n=84)	61 ± 17 (11 - 90)
Mabuasehube	
Acacia erioloba (n=100)	48 ± 17 (0 - 88)
Grewia flava (n=50)	60 ± 19 (5 - 90)
Tshabong	
Acacia leuderitzii (n=100)	52 ± 21 (5 - 90)
Grewia flava (n=204)	57 ± 20 (0 - 90)
Acacia mellifera (n=100)	41 ± 21 (0 - 85)
Species totals	
Acacia leuderitzii (n=184)	56 ± 19 (0 - 90)
Acacia mellifera (n=203)	50 ± 20 (0 - 90)
Acacia erioloba (n=100)	48 ± 17 (0 - 88)
Grewia flava (n=254)	57 ± 19 (0 - 90)

4.5 Vegetation surveys and woody density estimation

Measurements of the fractional cover of woody, herbaceous, soil and litter materials were made within four 30 by 30 metre plot quadrats of the 60 by 60 metre plot. The percentage of each landscape component within each quadrat was estimated visually, from which an average value was calculated for the plot as a whole. In addition, visual estimates were made of the condition of the vegetation, i.e., the fraction of green, bark, and senescent for the plot as a whole.

Estimates of the woody density (number of trees/shrubs per unit area) were made only at Tshabong plot 1, because there was the time to do so. Woody density was recorded in each of the four 30 by 30 metre quadrats that constituted the vegetation survey at this plot, according to a simple frequency count of each species present. No height restriction was imposed for inclusion in the count, however, for a plant to be included in the count it was required to have its roots within the 30 by 30 metre quadrat (Mueller-Dombois and Ellenberg 1974).

4.6 Summary

Measurements of most, if not all, the canopy structural variables were made at each of the field plots. The PAI data were corrected for the WAI contribution to the interception of light, in order to derive estimates of the LAI, or effective LAI. The sampling framework adopted for the measurement of PAI data was shown to be adequate in terms of optimising the information content of the data. The leaf inclination angle data collected allowed transformation and generation of a LAD for each of the species. The estimates of fractional cover allowed calculation of total area LAI. Overall, the design and execution of the field campaign ensured that data of sufficient number and quality were obtained, in order to provide for parameterisation of the canopy reflectance models, and to serve as validation data sets. The next chapter uses the soil samples collected in the field to characterise their BRDF.

5 Characterising Kalahari Soil BRDF

5.1 Introduction

It is well known that soils are generally non-Lambertian or anisotropic scatterers (Coulson *et al.* 1965, Irons *et al.* 1989, 1992, Despan *et al.* 1999). In these semi-arid savanna ecosystems the soil surface represents the largest single fractional component in a pixel. Consequently, the soil reflectance will exert a large influence over the pixel reflectance (Kimes *et al.* 1985, Privette *et al.* 1995, Ni & Li 2000). The vast majority of canopy reflectance models however, represent the soil surface as a Lambertian reflector, and the model simulations in chapter 6 have been performed with a Lambertian soil reflectance. If reflected radiance is to be modelled with higher accuracy it is desirable that something is known about the scattering properties of the soils encountered in these Kalahari field plots. In so doing, the likely impact of this Lambertian assumption, will be determined. This chapter presents the results of a laboratory experiment, where a series of spectral bidirectional and hemispherical measurements were made over soil samples obtained from the field plots. The overall aim of this work was to characterise the scattering properties of the different soils. Specifically, there were two objectives:

(i) Compare the scattering properties of the different soil samples over a range of azimuthal planes.

(ii) Compare spectral bidirectional and hemispherical reflectances, in order to assess the likely impact of a Lambertian assumption on future modelling work.

5.2 Experimental design

Bidirectional and hemispherical reflectance measurements were made over the different soils using an ASD spectrometer. This section outlines the methods used and

experiments conducted, in order to obtain accurate measurements of the soil reflectance.

5.2.1 Soil texture and colour

In order to aid the interpretation of the results, the soil texture and colour was determined. Soil texture is one of the most important properties which determines soil reflectance (Irons *et al.* 1989), and as such it is important to determine the texture of the soils used in this thesis. Having such information will enable better understanding of the reasons for the observed reflectances, and possibly help account for differences observed between samples. In addition, the soil colour may help account for observed differences in the reflectances, therefore the Munsell soil colour code was recorded for each soil sample.

Typically, determination of the particle-size distribution relies on a combination of sieving and sedimentation techniques; sieving to separate the coarse and fine sand particles, and sedimentation to separate the silt and clay particles (Rowell 1994). Particle-size class distinctions are presented in Table 5.1, though one should note that in the U.K., 63 μm is used as the class distinction between fine sand and silt.

Table 5.1 Particle-size class distinctions (Source: Rowell 1994).

Class		Size (mm)
Stones		>2
Fine earth:	Coarse sand	2-0.2 (2000-200 μm)
	Fine sand	0.2-0.06 (200-60 μm)
	Silt	0.06-0.002 (60-2 μm)
	Clay	<0.002 (<2 μm)

Before the particle-size distribution may be determined, the soils are pre-treated. First, any organic matter that may be present is removed (a particle-size analysis is interested only in the mineral particles). Second, the silt and clay particles are dispersed. Here, no systematic attempt was made to remove any organic matter content since this was less than 1% of the weight of the soil. This was determined by

a pilot study which burnt sub-samples of the soils at 350°C overnight then reweighed the soil to determine the loss on ignition, which was less than 1%. Similarly, the weight of material which passed through the 63 μm aperture sieve (the silt and clay), was weighed and was found to be less than 1%. For this reason, the soils were not dispersed before determining the particle-size distribution, and the silt and clay classes were treated as one in the particle-size analysis. The particle-size analysis was therefore performed solely on the basis of dry sieving, and was used to separate and quantify the relative proportions of coarse sand, fine sand, and silt and clay. It is important to state that using dry sieving alone will give the effective particle-size distribution, i.e., that which is found *in situ*, rather than the theoretical particle-size distribution. Given that the spectral measurements were made on samples taken *in situ*, it was desired to have correspondence between the particle-size analysis and the conditions under which the spectral measurements were made. Two sieves were used to obtain the particle-size distribution:

- One with a 250 μm aperture, to separate the coarse sand from the fine sand and silt and clay (actually the distinction between coarse and fine sand is at 200 μm, but 250 μm was the closest sized aperture available (see Table 5.1). The effect of this will be to overestimate the proportion of coarse sand and underestimate the fine sand proportion).
- One with a 63 μm aperture, to separate the fine sand from the silt and clay.

The proportion of each class in the sample was then calculated as a percentage. Particle-size analysis was performed after the spectral measurements had been made.

5.2.2 Laboratory spectroscopic measurements

To augment the field data collected, laboratory bidirectional reflectance distribution (BRDF) measurements were made of Kalahari soils, using an ASD Fieldspec FR spectrometer (Analytical Spectral Devices, Colorado, USA). These data would provide for complete parameterisation of the canopy reflectance models used in the modelling of chapter 6. The methods used to collect these data are described below.

5.2.2.1 Laboratory set-up

In order to make BRDF measurements a goniometer was constructed (Hosgood *et al.* 1999, Sandmeier and Strahler 2000). The goniometer was constructed from wood and is shown in Figure 5.1. The centre of the base of the goniometer was fixed to a table such that the goniometer could pivot through 360 degrees in azimuth. The azimuth planes in which measurements would be made were decided before the construction of the goniometer was completed, such that holes could be drilled at the appropriate spot which would allow fixing of the goniometer base to the table at a particular azimuth angle. The main arch of the goniometer consisted of two pieces of wood cut roughly into hemispheres. On this arch holes were drilled in 10 degree increments in zenith from -80 to +80 degrees (negative angles indicate backscatter direction, and positive angles the forwardscatter direction). The two hemispheres of wood were fixed to the base of the goniometer with space between them to allow the insertion of the supporting arm for the ASD. The supporting arm was made from aluminium and had two holes drilled in it. One was used to fix the base of the arm to the arch of the goniometer, and the other to fix the arm at a given viewing angle. The arm could be moved through 80 degrees back and forward in zenith. The ASD was fixed to the supporting arm with black tape, and the distance between the ASD and the target sample was approximately 15cm (Figure 5.1).

To avoid unwanted reflections, the measurement table, goniometer, supporting arm, and the walls of the spectroscopy laboratory were painted matt black. In addition, a black absorbing curtain surrounded the measurement table and goniometer, such that reflections from other areas of the spectroscopy laboratory (which were not painted black) would be obscured (Figure 5.1).

5.2.2.2 Instrumentation

An ASD fieldspec FR spectrometer was used to make the spectral measurements. The ASD has three spectrometers: one in the visible/near infrared (VNIR), and two in the shortwave-infrared (SWIR). The VNIR spectrometer consists of a 512 channel silicon photodiode array (each channel essentially being a detector) and light is measured simultaneously from 350nm to 1050nm. The two SWIR spectrometers each consist of

a single Indium Gallium Arsenide (InGaAs) detector, which measure light sequentially from 900nm to 1850nm in the first, and from 1700nm to 2500nm in the second detector. The overlap in wavelengths is accounted for by the ASD software. Light energy is obtained via three fibre optic bundles each of which delivers light to the entrance slit of one of the spectrometers. The fibre-optic cable has a conical scan and an instantaneous field of view (IFOV) of approximately 23 degrees. Using the fibre-optic on its own would require relatively large target sample areas (especially at large viewing angles), which, given that measurements were being made in a laboratory was undesirable. Consequently, an 8 degree fore-optic lens was used to restrict the size of the IFOV.

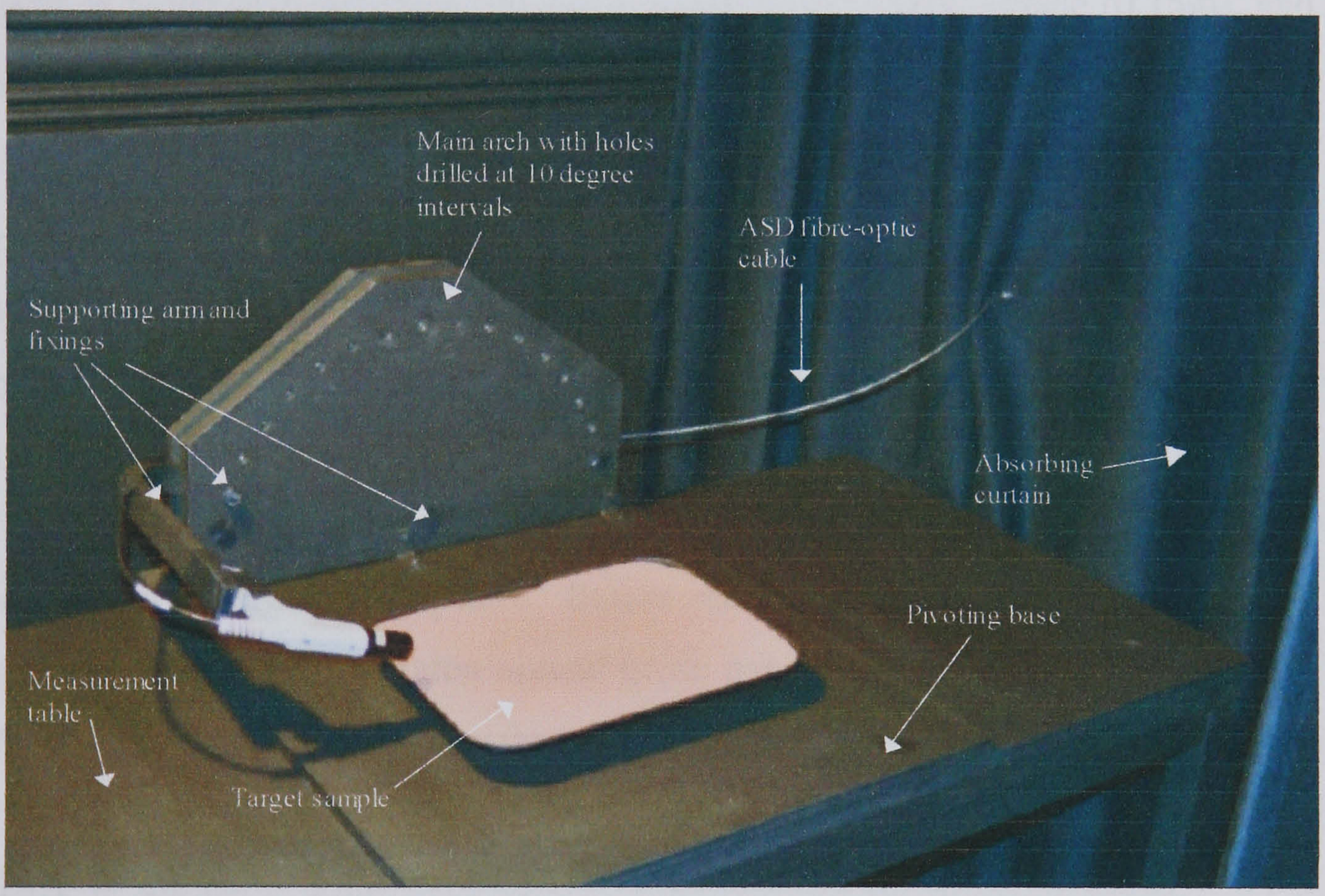

Figure 5.1 Goniometer design and measurement configuration, here, at 70 degrees backscatter.

5.2.2.3 Data collection and processing

A single 1000w tungsten halogen bulb was used as the light source, and the lamp was positioned at an illumination angle (SZA) of 30 degrees. This SZA was chosen to correspond to an expected SZA for a Landsat ETM+/Terra-MODIS overpass in the wet season at the latitudes of the field plots. The configuration of the supporting arm and the ASD with respect to the light source, meant that no hot spot data were collected. The projection of a sensors IFOV to the target surface, is termed the ground

instantaneous field of view (GIFOV) (Walthall *et al.* 2000). The GIFOV for nadir viewing ($GIFOV_0$) and off-nadir viewing angles ($GIFOV_{(\theta v)}$), were calculated using equations 5.1 and 5.2, respectively:

$$GIFOV_0 = (\tan IFOV) * H \tag{5.1}$$

$$GIFOV_{(\theta v)} = H\left[\tan\left(\theta_v + \frac{IFOV}{2}\right) - \tan\left(\theta_v - \frac{IFOV}{2}\right)\right] \tag{5.2}$$

where H is the distance from the ASD sensor to the target surface (0.15m), and θ_v is the view zenith angle.

Having calculated the GIFOV for all view angles in one scattering direction (0 to 80), it was decided to make measurements at 10 degree intervals, from -60 to +60 for all the soil samples, so as to ensure sufficient soil sample area was available to comfortably accommodate the sensor GIFOV. In all cases, measurements were made in seven azimuth planes: the solar principal and orthogonal planes, and at 5, 10, 30, 45, and 70 degrees. Measurements were recorded in raw digital number (DN) mode, with a scan average of 50 spectra. Before each measurement was made the ASD was optimised against a Spectralon optical grade panel (Labsphere, NH, USA). The same Spectralon panel (assumed Lambertian) was used as the reflectance reference (Rollin *et al.* 2000), and the raw DN data were processed to reflectance values by ratioing the BRDF of the target against the BRDF of the Spectralon panel. Because of the signal-to-noise ratio (S/N) the spectra were very noisy at wavelengths shorter than 450nm and longer than 1820nm (a problem with the light source in laboratory studies). Consequently, only wavelengths in the range 450nm to 1820nm were used for further study.

Because of the expectation of the presence of steps in the spectra produced by the ASD (at c.1010nm and c.1820nm), five replicate spectra were saved for each measurement, and the smoothest spectrum of the five (once processed to reflectance) was selected for use (Liang *et al.* 1996). The presence of steps in the spectra is thought to be related to the way in which the fibre-optic bundles are split, in that, each bundle delivers light to the same spectrometer at each scan, such that if the three

bundles view different areas of the target, different amounts of light will be recorded at each spectrometer, thus explaining the presence of steps. The step at 1010nm is also thought to be related to the sensitivity of the silicon detector at these NIR wavelengths (M. Schaepman, *personal communication*, August 2002).

5.2.2.4 Error sources and data quality

When making laboratory (or field) BRDF measurements, error can be introduced in several ways. It is important to attempt to try and quantify the error in the measurements made, so that some faith can be placed in the usefulness of the data sets obtained. Commonly cited sources of error in laboratory BRDF measurements include:

- lamp (or bulb) instability and nonparallelism,
- target variance between successive measurements, and,
- the geometric accuracy of the goniometer (Sandmeier and Strahler 2000).

Sandmeier *et al.* (1998) have shown that the error introduced by lamp instability can be as great as 2.7% relative RMSE (in the 450nm to 1000nm range), for measurements made at the European Goniometric Facility (EGO) on concrete (assumed a temporally invariant target surface), when there is a 59 minute time difference between measurements. They state that by using a direct current (DC) power supply, the errors attributable to lamp instability could be significantly reduced. Meister *et al.* (2000), have been able to show this, and report measurement errors attributable to lamp instability of 0.3% when using a DC power supply for measurements of asphalt and roof-tiles at the EGO. Sandmeier *et al.* (1998) have also shown the effect of target variance. They show that heating of vegetation samples caused by the heat of the lamp, can lead to a relative RMSE of up to 7.8% for repeated measurements of grass taken 2 hours and 55 minutes apart.

To assess the errors that might be introduced in the BRDF measurements made in this thesis, two experiments were conducted. Experiment one was concerned with determining the relative error of successive measurements made over a short and long time period, by taking successive nadir measurements of the Spectralon panel at 30

second intervals for a period of 10 minutes, and at 2 minute intervals for a period of 1 hour and 25 minutes. The second experiment was concerned with determining the repeatability of BRDF measurements made in the principal plane, by making measurements of dry building sand (air dried at room temperature) from -70 to +70 degrees in zenith, then repeating the procedure as soon as the first run of measurements was completed. The time difference between the two measurement runs was approximately 1 hour and 29 minutes, for each corresponding measurement pair. The aim of these two experiments was to investigate the influence of the stability of the lamp on directional measurements made, in order to determine if there is a time period beyond which changes in the lamp become too severe to allow accurate and repeatable measurements to be made.

In both experiments the SZA was fixed at 30 degrees. The error for the nadir measurements over the Spectralon panel was assessed by calculating the relative root mean square error (RRMSE):

$$\mathrm{RRMSE} = \sqrt{\frac{1}{n}\sum_{i=1}^{n}\left(\frac{R_i^* - R_i}{R_i}\right)^2} * 100 \tag{5.3}$$

While for the measurements over dry building sand (processed to reflectance), the root mean squared error (RMSE) was calculated:

$$\mathrm{RMSE} = \sqrt{\frac{1}{n}\sum_{i=1}^{n}\left(R_i^* - R_i\right)^2} \tag{5.4}$$

Where R_i^* is the measured data value to be compared, R_i is the measured or 'true' data, and n is the number of data sets. For the panel measurements of experiment one, the 'true' data value is the first DN number recorded in each wavelength, and subsequent measurements are compared to this value. For the measurements of the dry building sand the 'true' value at each VZA is the reflectance value obtained from the first measurement run, and corresponding values from the second measurement run are compared to these. No attempt was made to investigate the effect of target variance, since the target samples used in this thesis were assumed

to be temporally invariant. The geometric accuracy and precision of repositioning the ASD after successive measurements was also not investigated.

5.2.2.5 Soil BRDF and hemispherical reflectance measurements

To complete the spectral measurements for parameterisation of the canopy reflectance models, samples of soil were brought back from the field. Soil samples were taken from only four of the seven field plots, these were Tshane plot 1 (T1), Mabuasehube plot 2 (M2), and Tshabong plots 1 and 3 (TG1 and TG3). Samples were obtained by taking the top fraction of the soil in a random fashion within the plots. Before spectral measurements were made the soils were sieved in order to separate the small litter fraction from the soil, a sieve with a 4mm aperture was used to achieve this. Any remaining litter was removed by hand. Soil samples, although already dry, were left to air dry in the laboratory in case there was any residual moisture remaining in the samples, doing this ensured the samples would not undergo changes during the measurement time period. The soil samples were placed on a sample tray (which was painted matt black) and were spread out to cover the entire tray area. The soil samples were then levelled off in order to obtain smooth surfaces. Though it may be considered that smoothing the soil surfaces may be unrepresentative of actual field conditions, the soils were prepared in this way because it was the only way of ensuring that surfaces were the same for all samples i.e. reproducible, such that any differences in reflectance would be attributable to different scattering properties of the soil samples, rather than being an artefact of the surface conditions, this was especially important given the small GIFOV of the ASD.

Two sets of reflectance measurements were made on the soil samples: the BRDF measurements were made using the goniometer and ASD with an 8 degree fore-optic lens, while the hemispherical reflectance measurements were made using the ASD together with a contact probe.

5.3 Results and discussion

5.3.1 Soil texture and colour

Table 5.2 presents the results of the particle-size analysis together with the Munsell soil colour code for each sample. Differences in the particle-size distributions for the four different samples are quite pronounced, with there being 20% more coarse sand at Tshane plot 1, and 10% more coarse sand at both of the Tshabong plots than at Mabuasehube plot 2. The coarsest soils are at Tshane plot 1 where the coarse sand class constitutes 65.5% of the sample, while the finest soils are found at Mabuasehube plot 2, where the fine sand class constitutes 55.3% of the sample (Table 5.2). Differences in soil colour are apparent, with the soils at Mabuasehube being the reddest and darkest, while the other three soil samples are of the same hue - a yellowish red, but are lighter at Tshane than at Tshabong.

5.3.2 Error and data quality

Figure 5.2 shows the results of experiment 1 (determining the relative error of successive measurements), where it can be seen that the relative error is less than 2% across the spectral range 450nm to 1820nm, for both measurement time periods. Treating results in the two detectors of the ASD separately, there is a RRMSE of 0.51% and 1.12% in the first detector (450nm to 1010nm), and a RRMSE in the second detector (1011nm to 1820nm) of 0.23% and 0.56%, for the 10 minute and 1 hour 25 minute time intervals respectively. The RRMSE in the second detector is lower than that in the first because of a stronger S/N as shown in Figure 5.2 by the mean DN values of the Spectralon panel. The S/N is lower in the first detector which not only leads to larger RRMSE values, but also introduces a wavelength dependent error when measurements are made over extended periods of time (the 1 hour 25 minute case), a trend not as clearly marked in the second detector (Figure 5.2). Since there was no change in the measurement set up in this experiment (SZA and VZA were constant), and assuming that the panel is temporally invariant, and the ASD reliable, the errors are directly attributable to variations in the light source.

Table 5.2 Particle-size distribution, and Munsell colour code for the four Kalahari soil samples, which the laboratory BRDF work was performed on.

Site	Coarse Sand (%)	Fine Sand (%)	Silt and Clay (%)	Munsell Colour
T1	65.5	34.5	0.0	7.5YR 7/8 (Reddish yellow)
M2	44.2	55.3	0.5	5YR 5/8 (Yellowish red)
TG1	55.0	44.5	0.5	7.5YR 6/8 (Reddish yellow)
TG3	54.2	45.7	0.1	7.5YR 6/8 (Reddish yellow)

Note: T1 is Tshane plot 1, M2 is Mabuasehube plot 2, TG1 and TG3 are Tshabong plots 1 and 3.

Figure 5.3 shows the results of experiment 2 (repeatability of BRDF measurements made on dry building sand), where it can be seen that there is some variability in the repeated measurements, but overall absolute differences in reflectance are observed to be small. Table 5.3 reports the RMSE of the repeated measurements for the two detectors of the ASD. In the first detector (450nm to 1010nm), there is a maximum RMSE of 3.42% at 10 degrees forwardscatter, and a minimum of 0.34% at 50 degrees forwardscatter. Averaging over all view angles the RMSE in the first detector is 1.6%. In the second detector (1011nm to 1820nm), there is a maximum RMSE of 1.83% at 70 degrees forwardscatter and a minimum RMSE of 0.16% at 50 degrees forwardscatter. Averaging over all view angles the RMSE in the second detector is 0.9%. Overall, these results are considered to be acceptable enough in order to have confidence in the quality of the data obtained in the laboratory.

The results of these experiments influenced the design of the measurement procedure. Accordingly, to avoid the introduction of excessive error into the measurements, because of variations in the lamp, BRDF measurements were made within a period of two and a half hours (the same total measurement time period as experiment two), enough time to make full directional sampling in two azimuthal planes.

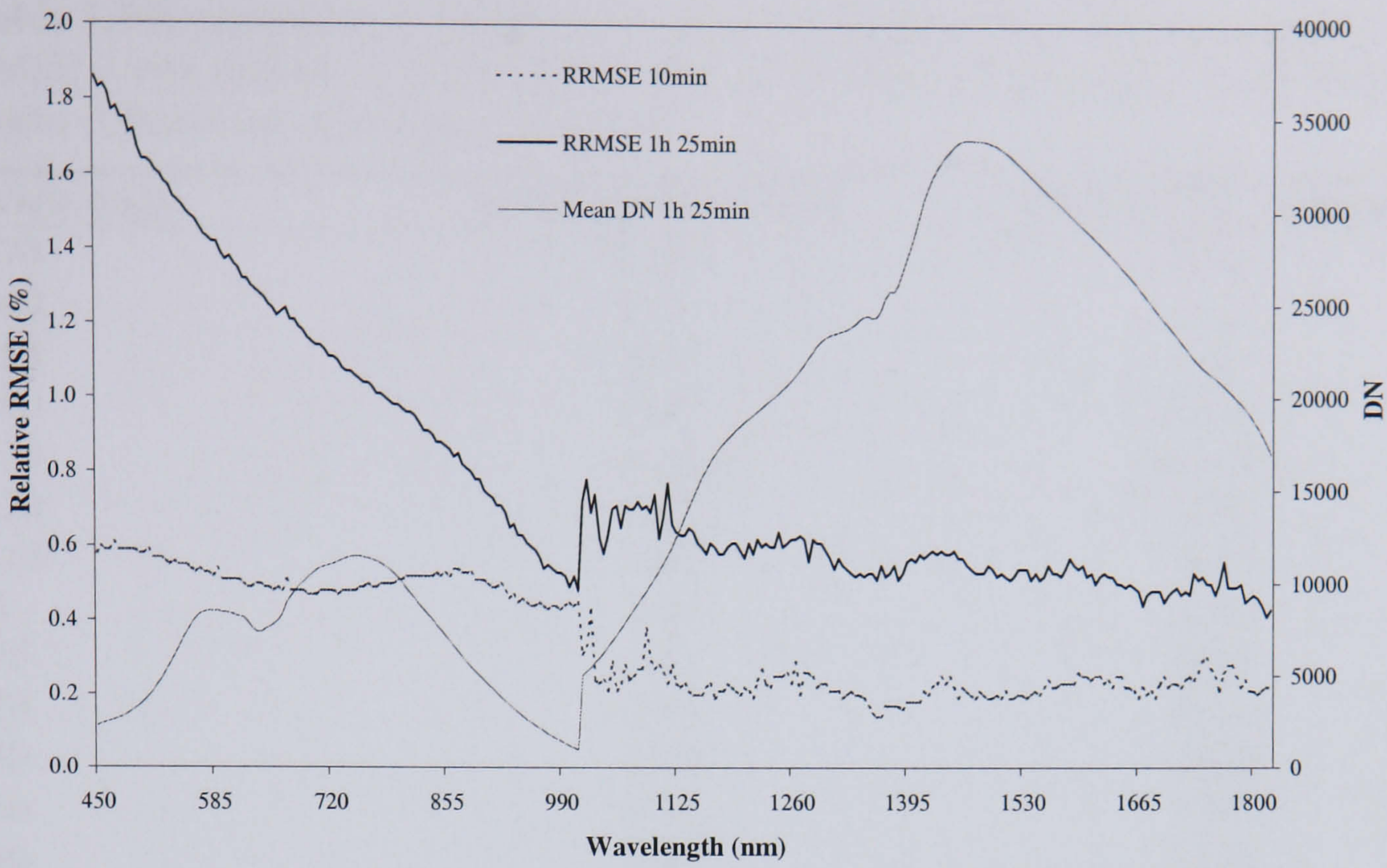

Figure 5.2 Relative RMSE for nadir measurements of a Spectralon panel for different time intervals, with an illumination zenith angle of 30 degrees. The mean DN of the Spectralon panel is also shown.

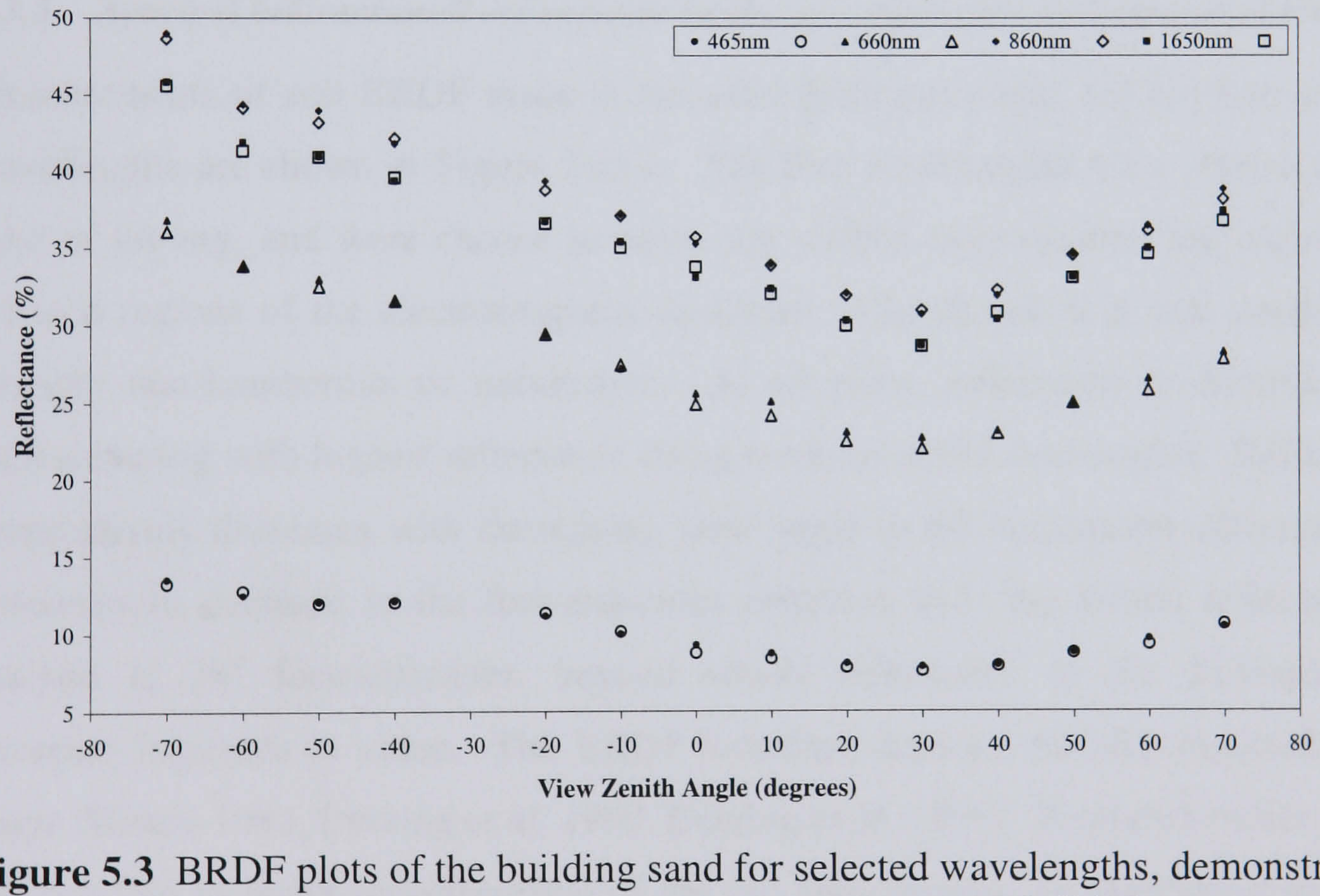

Figure 5.3 BRDF plots of the building sand for selected wavelengths, demonstrating the repeatability of measurements made with the goniometer. Solid shapes represent the first measurement run in the principal plane, the hollow shapes are the values from the measurements made in the second run in the principal plane ~1 hour 29 minutes after the first run. Negative angles indicate the backscatter direction.

Table 5.3 Repeatability of BRDF measurements, taken ~1 hour 29 minutes apart. RMSE is reported in the first two detectors of the ASD, for each view angle. Negative angles indicate the backscatter direction.

View angle	RMSE 450-1010nm	RMSE 1011-1820nm
-70	1.90	0.59
-60	0.58	1.35
-50	1.23	0.57
-40	0.39	0.49
-30	*No data*	*No data*
-20	0.48	0.56
-10	1.03	0.72
0	2.83	1.78
10	3.42	0.99
20	2.45	0.75
30	2.59	0.42
40	0.76	1.70
50	0.34	0.16
60	2.59	0.95
70	1.61	1.83

5.3.3 Spectral bidirectional reflectance in the principal and orthogonal planes

Measurements of soil BRDF made in the solar principal plane, for the five selected wavelengths are shown in Figure 5.4a-e. The five wavelengths were chosen for the sake of brevity, and were chosen to cover the visible, near-infrared and short-wave infrared regions of the electromagnetic spectrum. Clearly, all four soil samples are strongly non-Lambertian or anisotropic. At all plots, reflectance is dominated by backscattering with highest reflectance being recorded at 60° backscatter. Reflectance progressively decreases with decreasing view angle in the backscatter direction, and continues to decrease in the forwardscatter direction until the lowest reflectance is reached at 30° forwardscatter, beyond which reflectance in the forwardscatter direction increases in value. The BRDF therefore displays the well reported bowl-shape (Kimes 1983, Deering *et al.* 1990, Deering *et al.* 1999). As stated earlier, it was not possible to make measurements of the hot spot because of shadowing from the goniometer and instrument. However, measurements of the dark spot, at 30° forwardscatter, are clearly picked up, at all wavelengths and for all soil samples (Figure 5.4a-e). This feature is a result of the spectrometer viewing the maximum shadowed area at this viewing angle. Had hot spot measurements been possible, this would most likely have been the peak reflectance, because of shadow hiding (Hapke 1986, Hapke *et al.* 1996).

Comparing across field plots and wavelength, it is clear that the most striking feature is that the shape of the BRDF for all four field plots is almost identical. All of the soils are very similar anisotropically (measured as a ratio of the highest to lowest value for each sample in each plane), with the difference between the lowest and highest reflectance generally being around 40%, this pattern is repeated across wavelengths. It might be considered that greater anisotropy would be expected at T1 because of the greater fraction of coarse sand at this plot. This is because one would expect larger shadows and therefore a lower reflectance at the dark spot (Li *et al.* 1996). Clearly, there is no evidence to support this, which might be a result of the way in which the soil samples were prepared, they were all smoothed out and so should present very similar surfaces. Another possibility is that the difference in the amount of coarse sand present, is insufficient to translate into a noticeable difference in the reflectance anisotropy.

Although the BRDF shape of the soils is almost identical, and anisotropy similar, differences in magnitude are apparent yet are generally no greater than 5% absolute reflectance, at all wavelengths and viewing angles (Figure 5.4a-e). This is perhaps not surprising given that the soils are all Kalahari sand, and were prepared in the same way i.e. smoothed out before measurements were made. Comparing across wavelengths, the brightest soils are seen at T1, with soils at M2 being the second brightest, whilst at TG1 and TG3 the lowest reflectance is observed. The fact that the soils at T1 are the brightest concurs with the Munsell colours given in Table 5.2, though this is strictly only applicable to the visible wavelengths. With respect to the Munsell colour codes, M2 would be expected to show the lowest reflectance, not the second highest. This may be a result of the order in which measurements were made. The soils from M2 were the last in the series to be measured (over a two week period), by which time repeated use of the goniometer had weakened its structure, such that the geometrical accuracy and stability would most likely have been degraded. In this way greater error may have been introduced into the measurements. This issue notwithstanding, the difference between the TG1 and TG3 and M2 soils was generally less than 1-2% across wavelengths and viewing angles, which is well within the uncertainty in the measurements due to lamp instability (Table 5.3). Again, the differences in colour may not be sufficiently marked to translate into clearly observable differences between these plots.

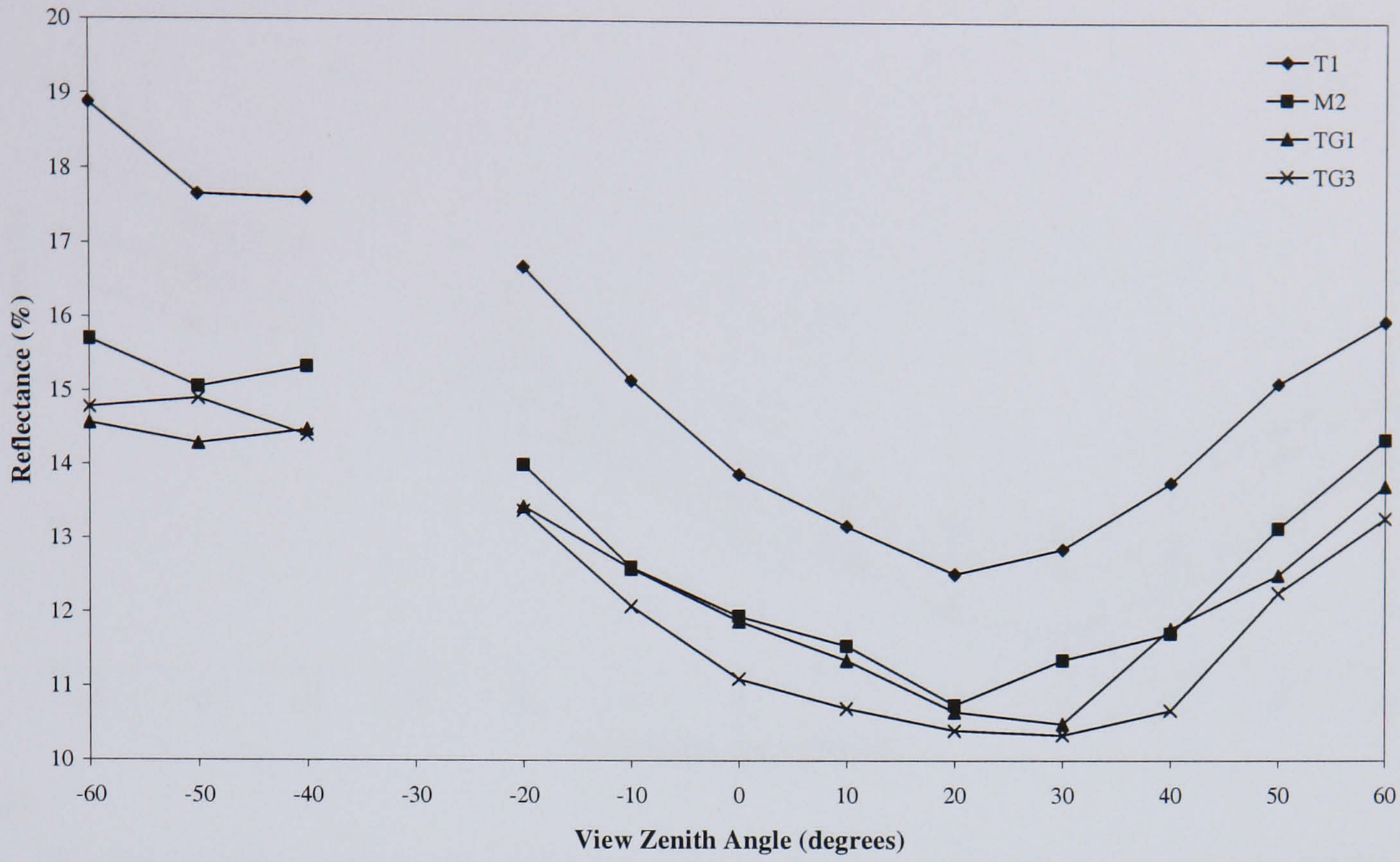

(a)

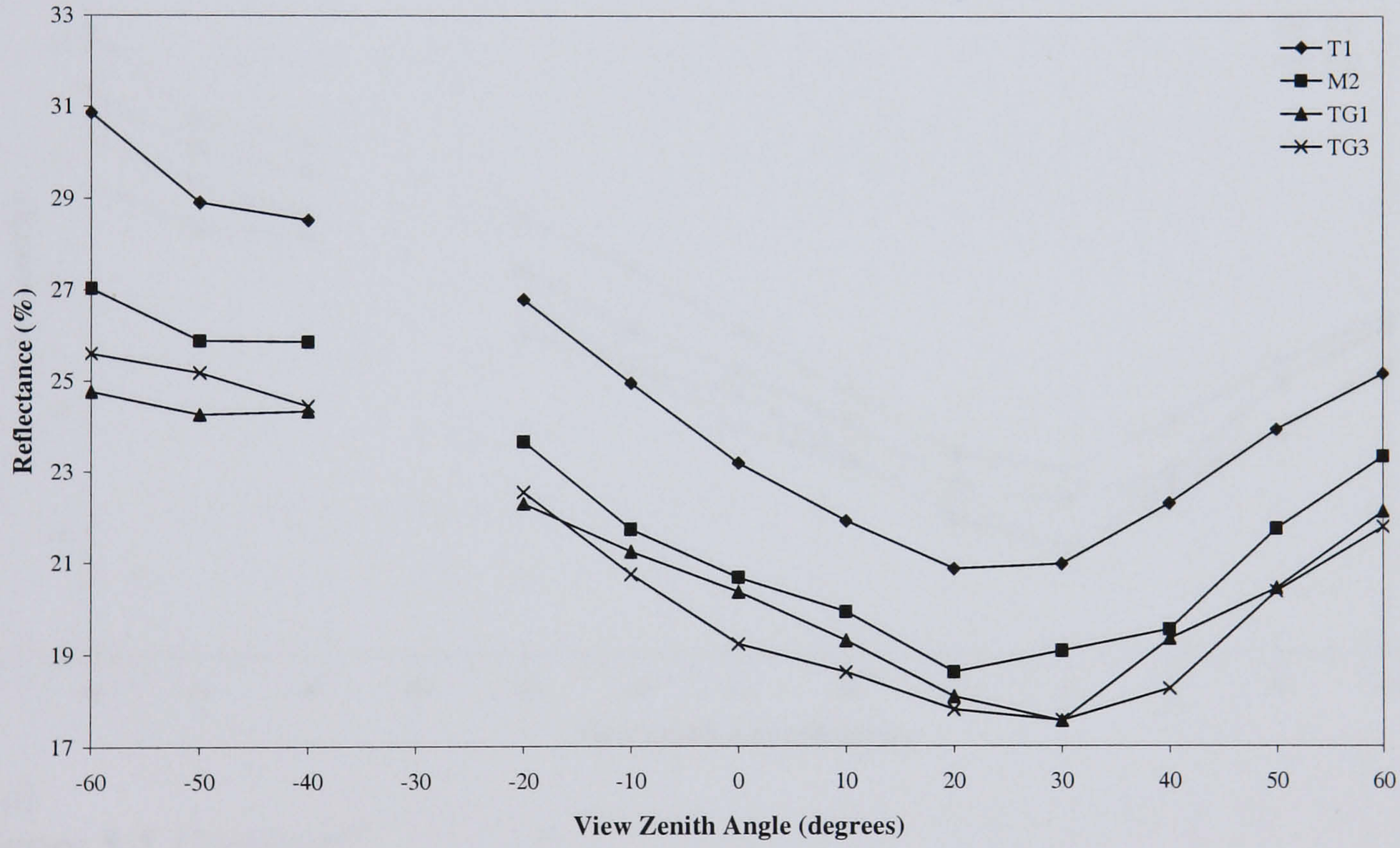

(b)

Figure 5.4 Principal plane spectral bidirectional reflectances for each of the four samples at (a) 465nm, (b) 550nm, (c) 660nm, (d) 860nm, (e) 1650nm. No data were collected in the hot spot at 30 degrees backscatter.

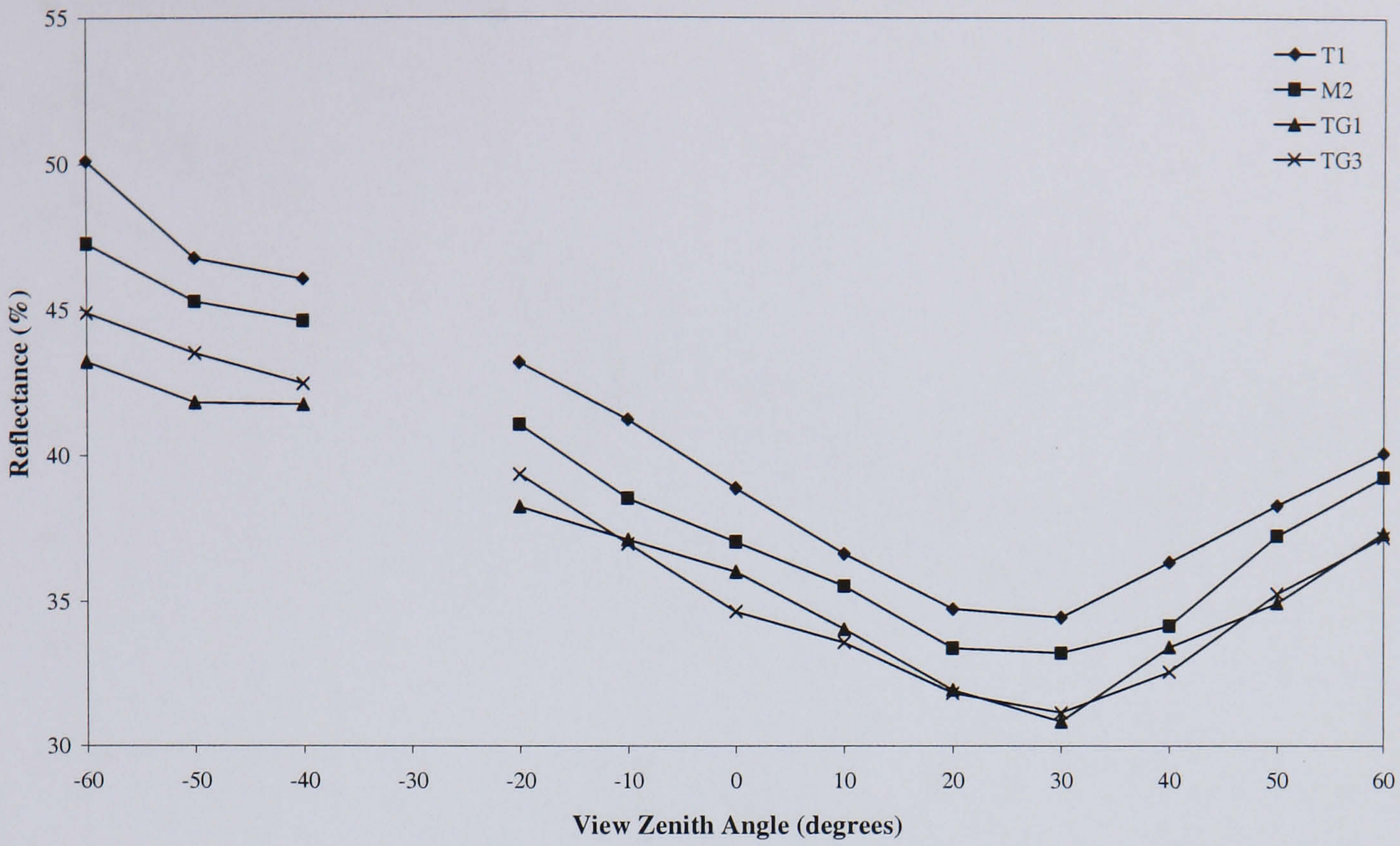

(c)

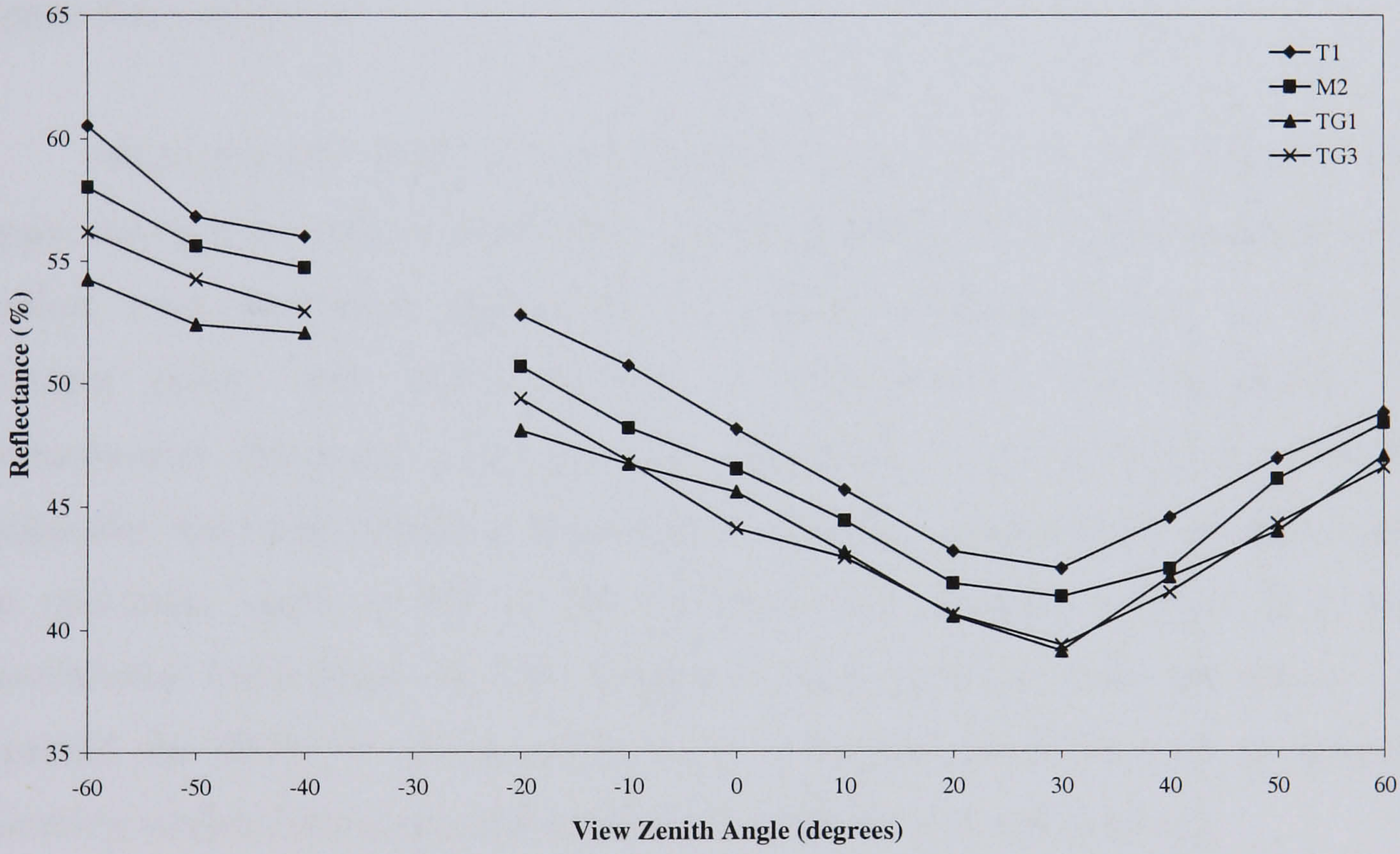

(d)

Figure 5.4 Continued.

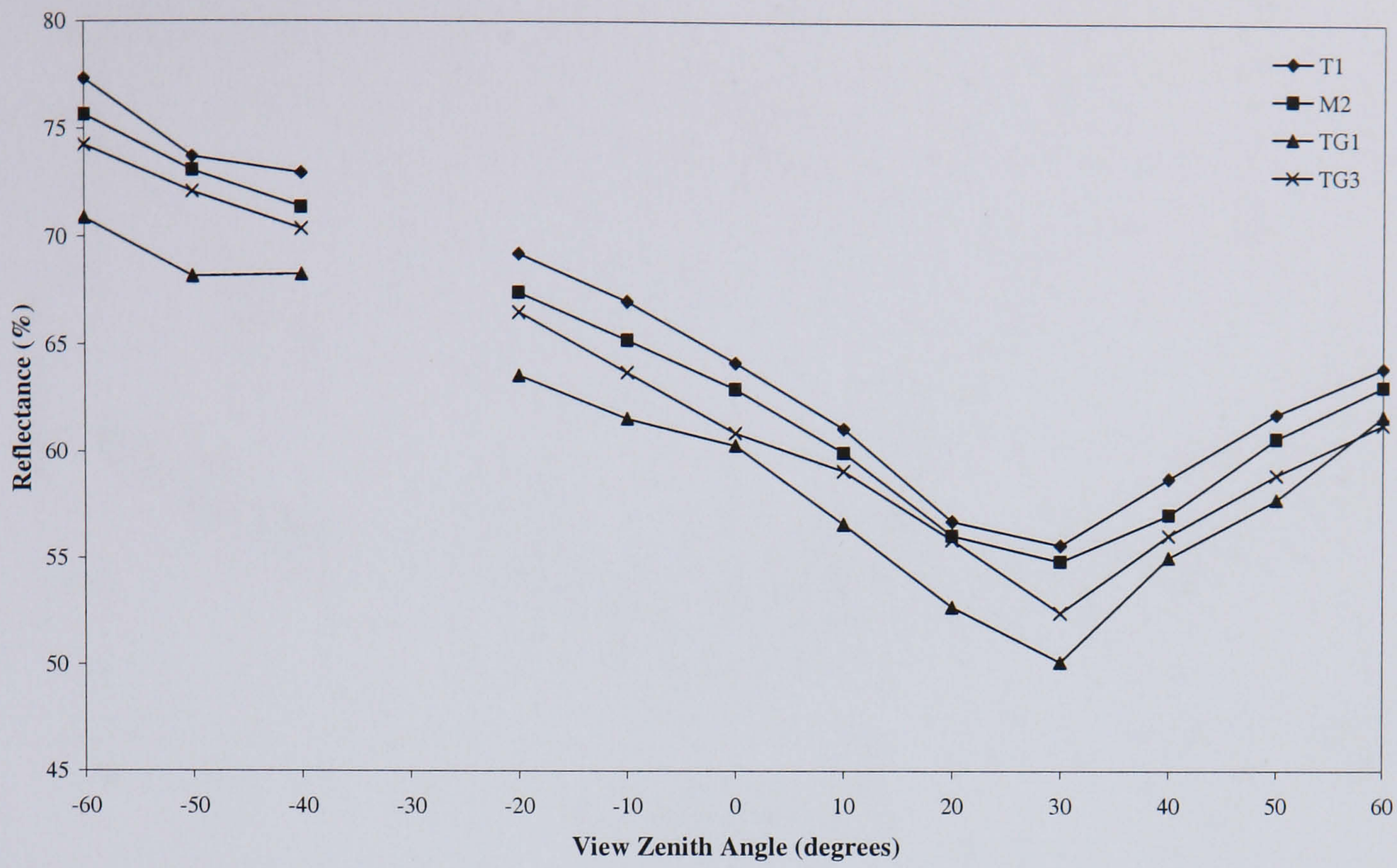

(e)

Figure 5.4 Continued.

Measurements made in the orthogonal plane are shown in Figure 5.5a-e. Again, the soils are seen to be anisotropic and the BRDF very similar in shape to one another, with directional reflectance being more symmetrical than in the solar principal plane, with equal amounts of reflectance in the backscatter and forwardscatter directions. For all soils, reflectance is at its highest in the 60° backscatter direction, reaches a minimum at nadir and progressively increases up to the maximum again at 60° in the forwardscatter direction. There is a more conventional bowl-shape in the orthogonal plane than the principal plane. As expected, the BRDF is less dynamic in the orthogonal plane, because the physical scattering mechanisms (operative in the principal plane) are not as strong.

The same pattern of magnitude differences as was observed in the principal plane is evident in the orthogonal plane, with T1 being the brightest soils followed by M2 and TG1 and TG3, with differences generally being no greater than 5% absolute reflectance, across wavelengths and view angles (Figure 5.5a-e).

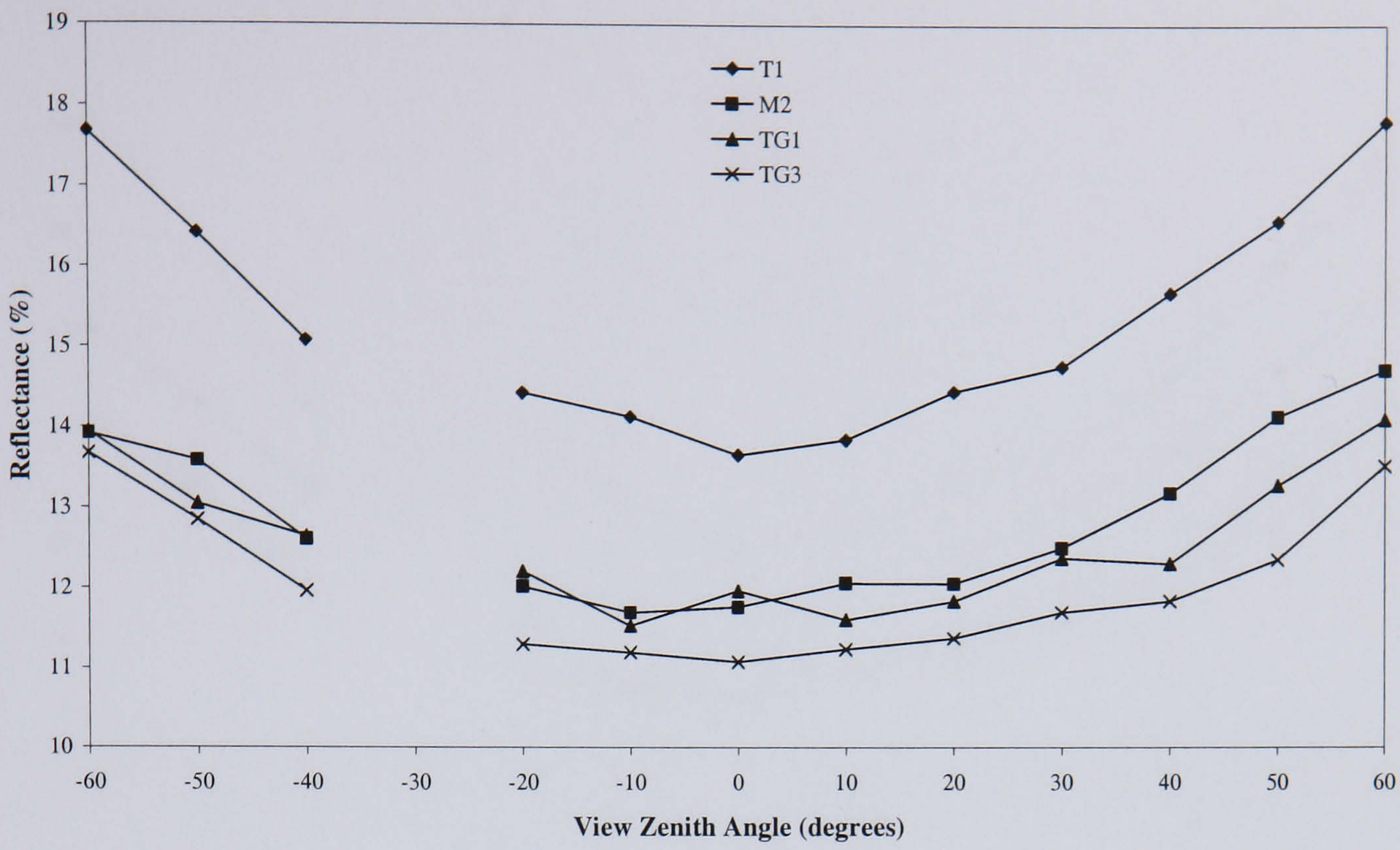

(a)

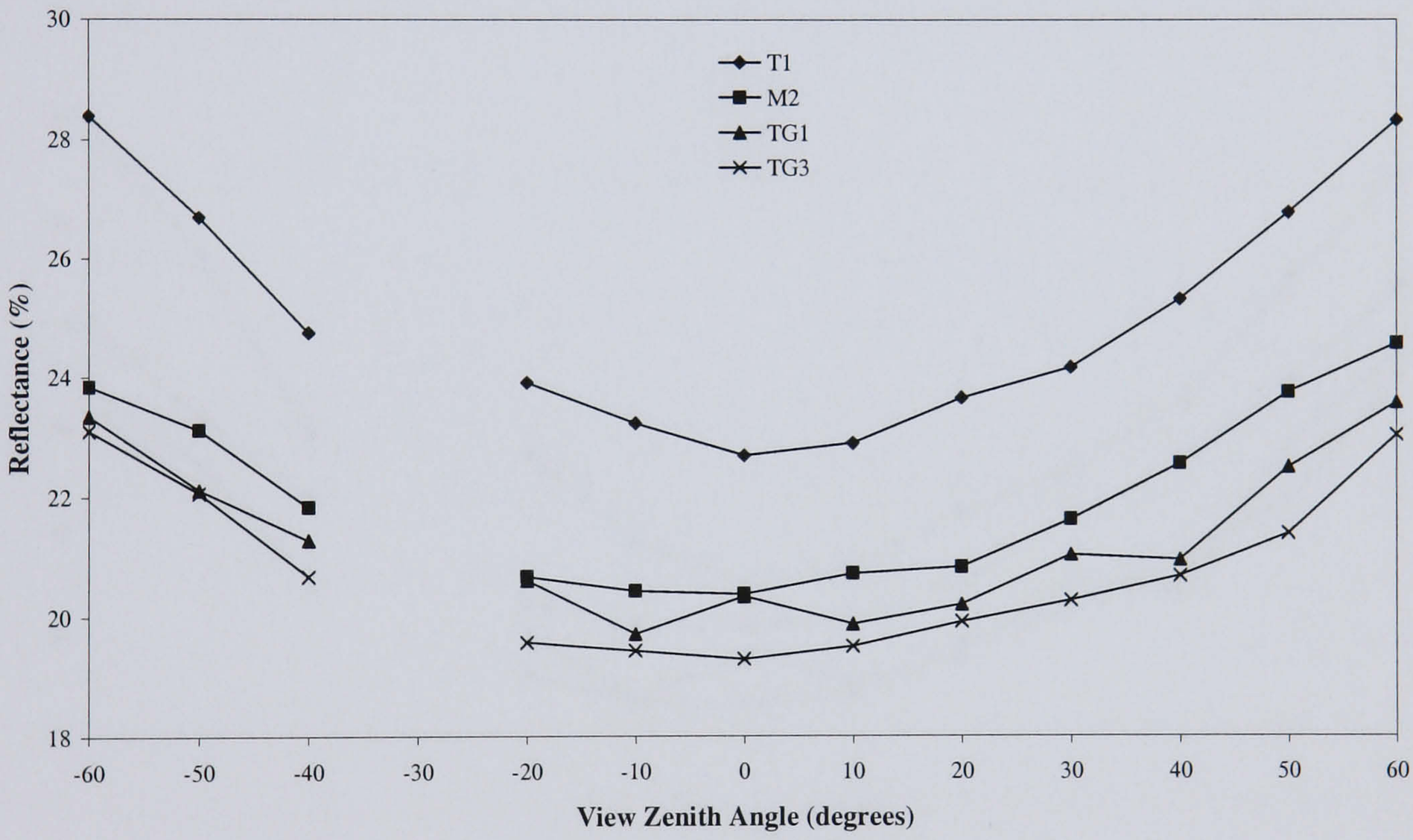

(b)

Figure 5.5 Orthogonal plane spectral bidirectional reflectances for each of the four samples at (a) 465nm, (b) 550nm, (c) 660nm, (d) 860nm, and (e) 1650nm. Hot spot data are not shown for reasons of consistency with the principal plane plots.

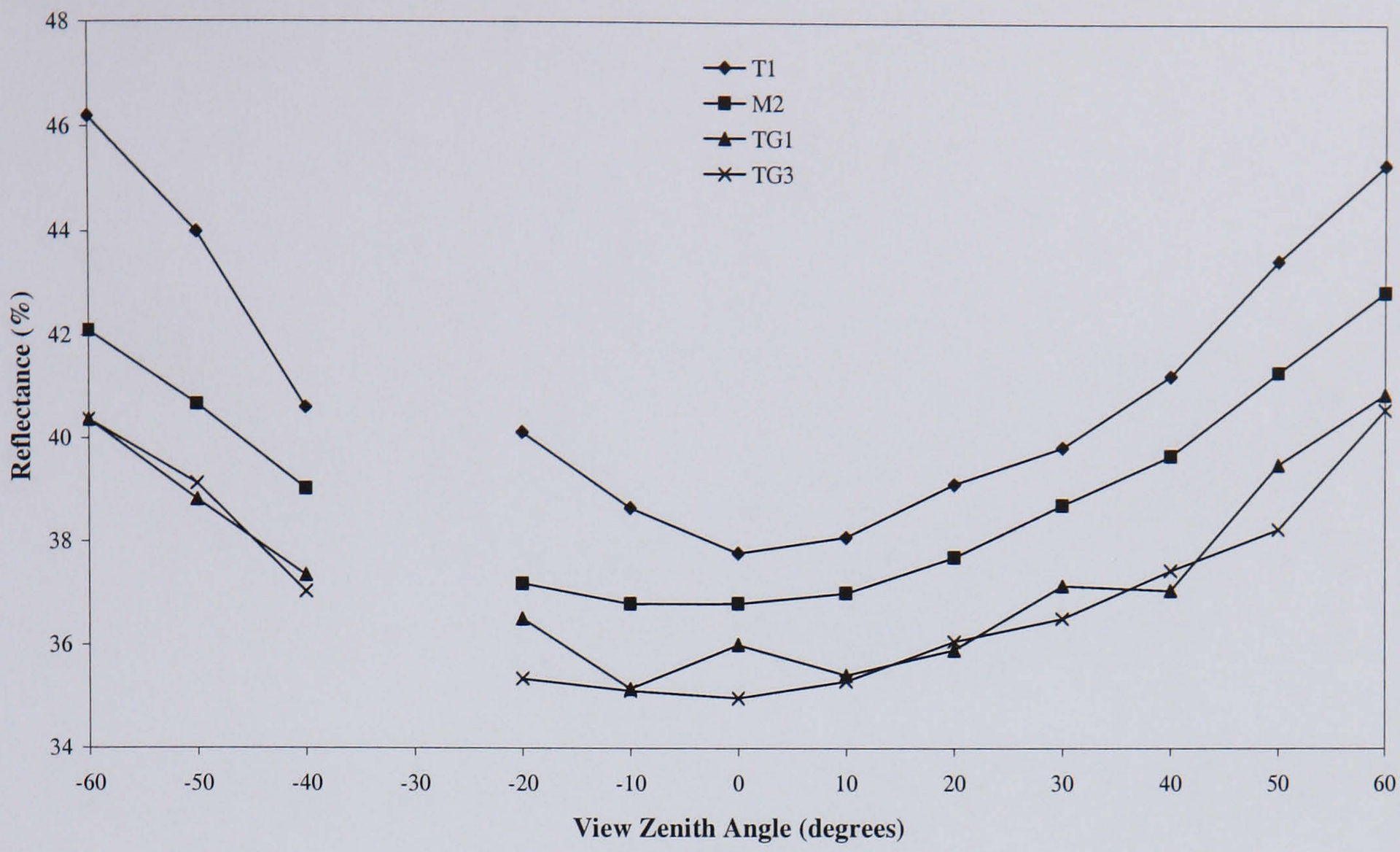

(c)

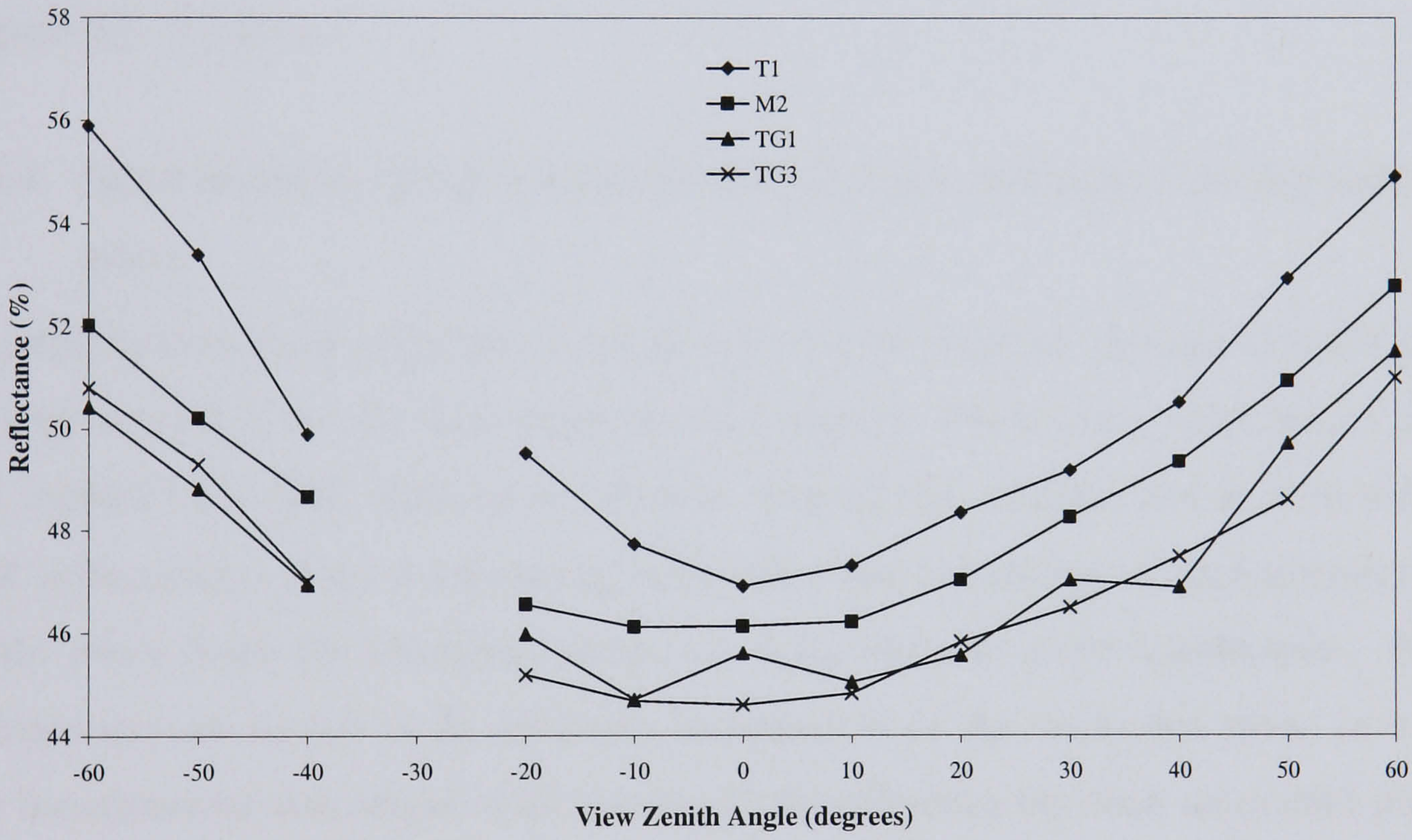

(d)

Figure 5.5 Continued.

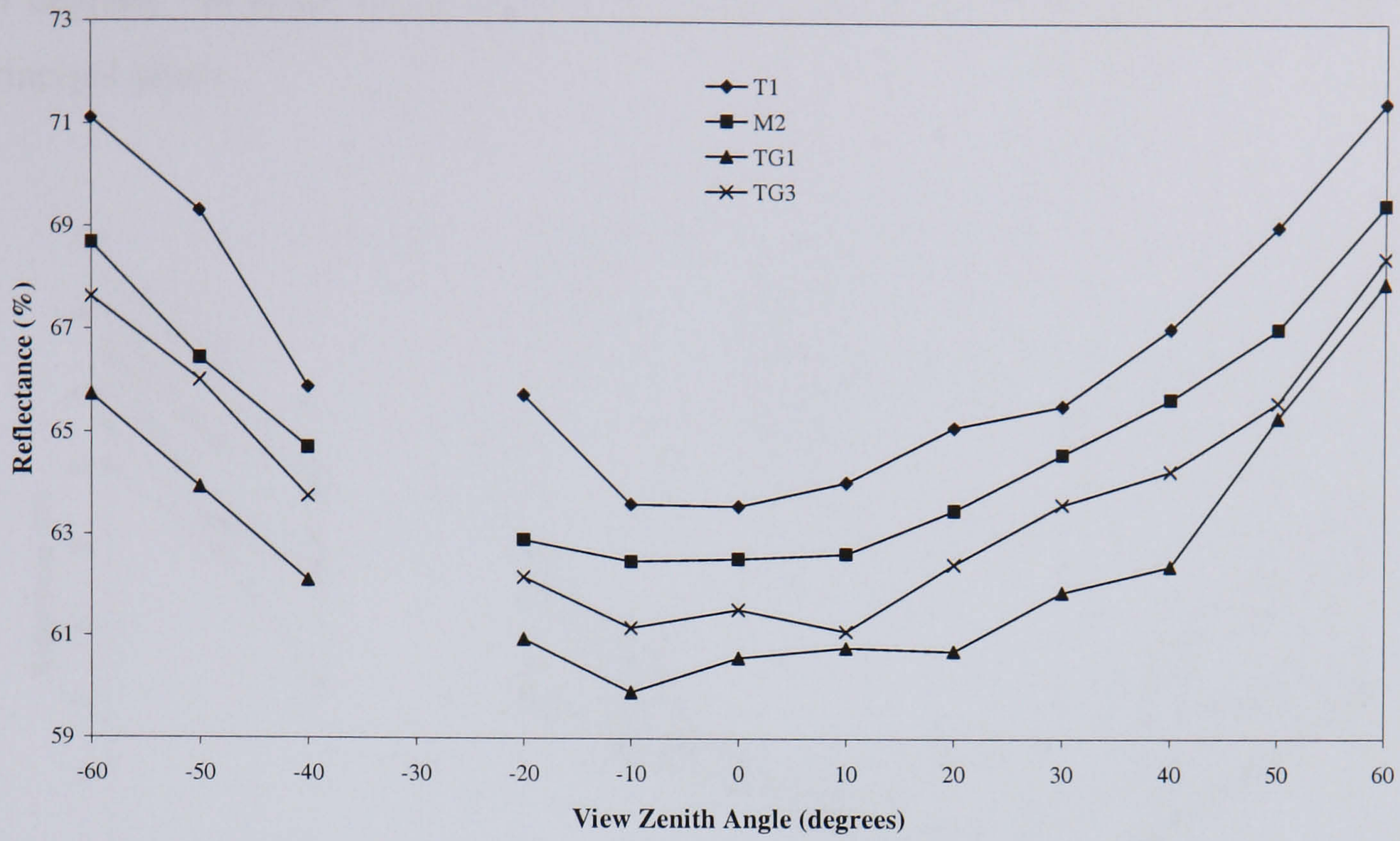

(e)

Figure 5.5 Continued.

5.3.4 Spectral bidirectional reflectance variation as a function of viewing azimuth plane

Spectral bidirectional reflectances are shown as a function of viewing azimuth plane in Figure 5.6-5.9, for the four different soil samples. For brevity, reflectances at the red (660nm) and NIR (860nm) are shown. For all soil samples and at both red and NIR reflectances, there is decreasing reflectance and anisotropy as measurements are made away from the principal plane, i.e. soils become more Lambertian. Nadir reflectances are shown to be relatively independent of the azimuthal plane in which the measurement was made, with less than 1% difference between azimuthal planes. Measurements made at 5 and 10 degrees in azimuth are very similar to the measurements made in the principal plane, and in some cases have higher reflectances in the backscatter direction than those made in the principal plane (cf. Figure 5.6 and 5.8). In the forwardscatter direction these differences are less pronounced. This is most likely a result of errors in the measurements rather than there being any underlying physical explanation. What these results do indicate however, is that in terms of the features they show, and therefore the information they contain, sampling up to 10 degrees away from the principal plane, the distinctive dark spot feature of the BRDF is still strong in evidence. Clearly, the soils remain highly anisotropic over a fairly broad swath in azimuth, before becoming progressively more isotropic beyond

45 degrees. In other words there is no sharp fall off in anisotropy once outside the principal plane.

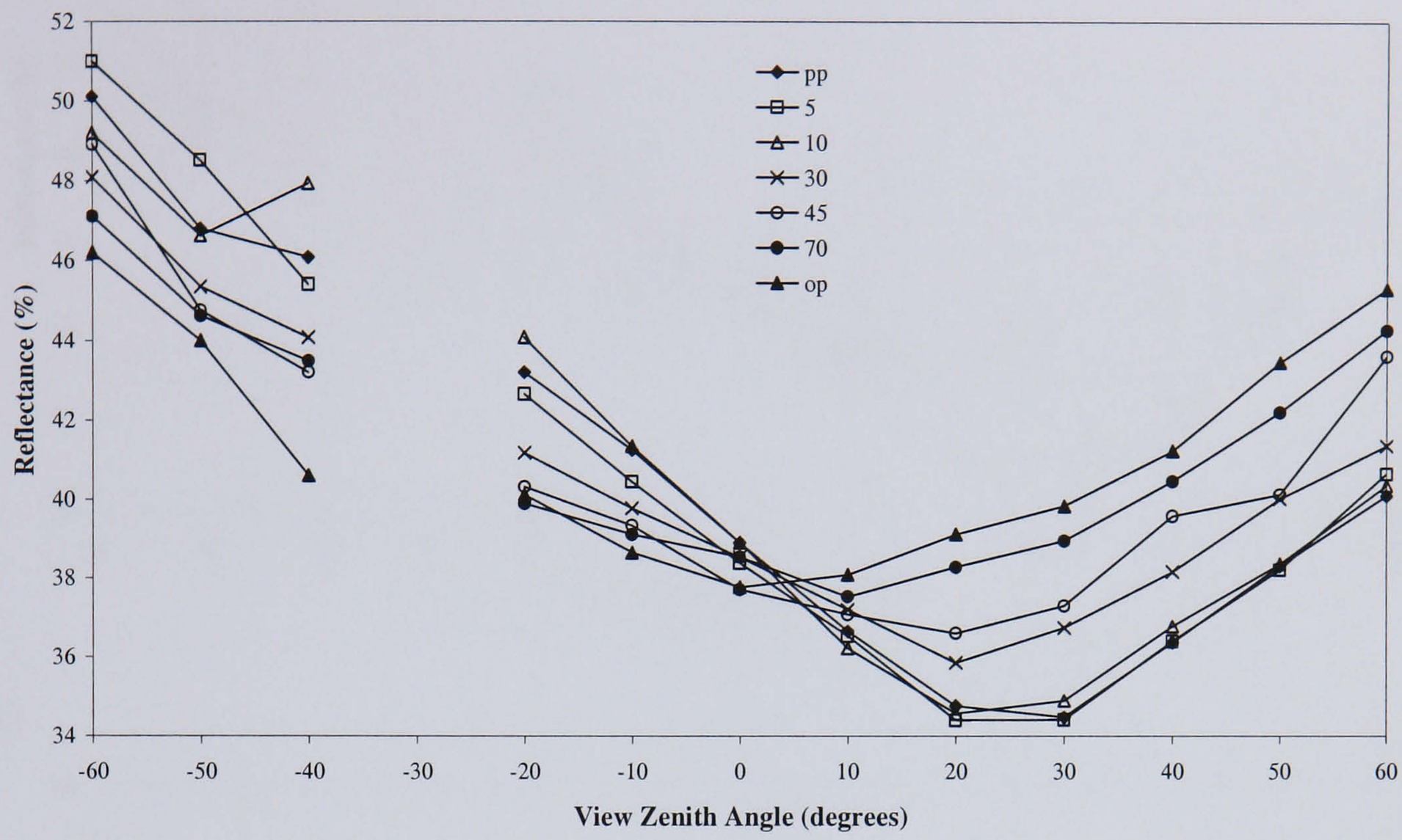

(a)

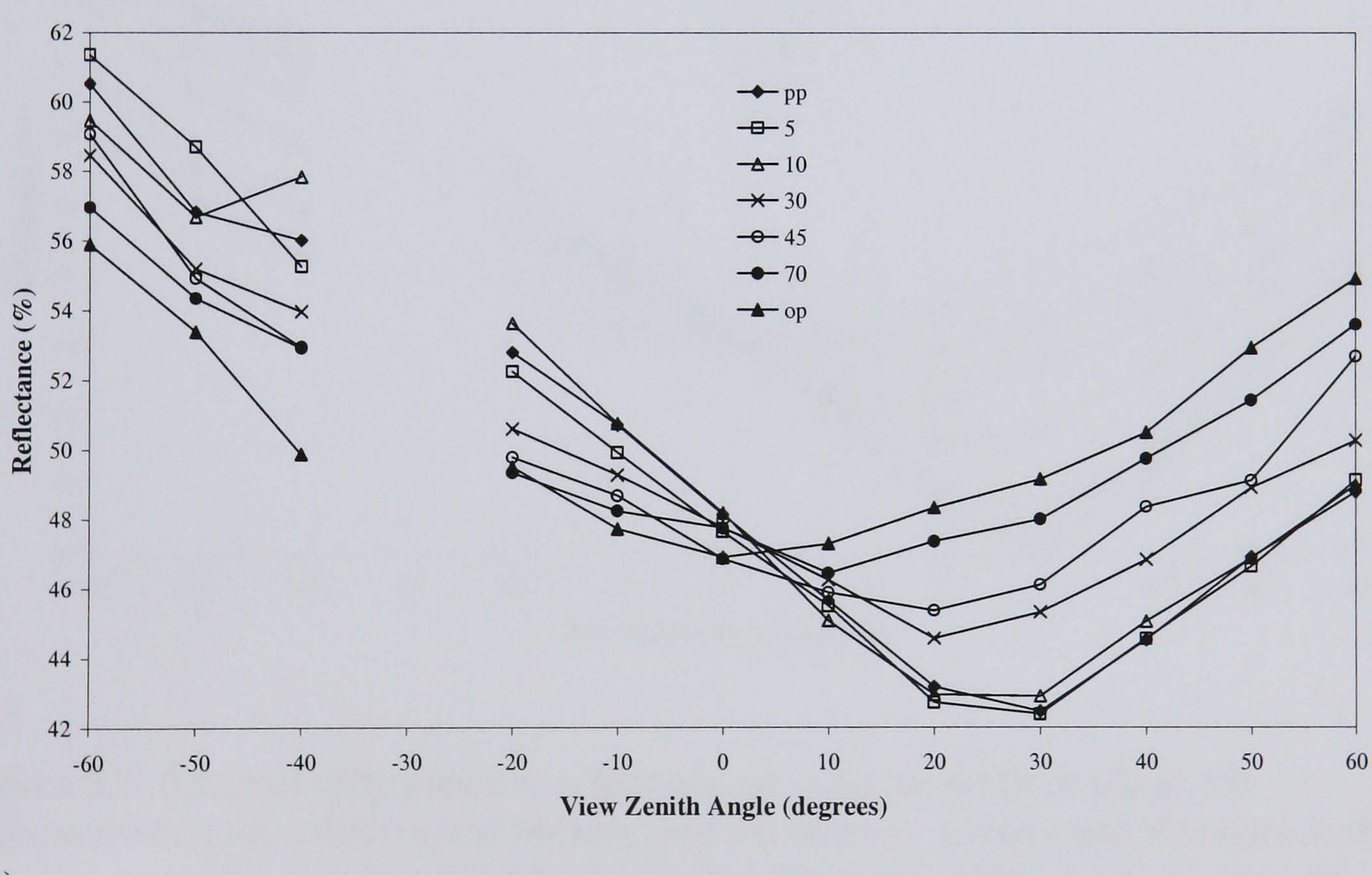

(b)

Figure 5.6 Spectral reflectance as a function of viewing azimuth plane, for Tshane plot 1 (T1) at (a) 660nm, and (b) 860nm. Letters and numbers in the legend refer to the angular plane the measurements were made in, where pp is the principal plane and op is the orthogonal plane. No data are shown in the hot spot for reasons of consistency.

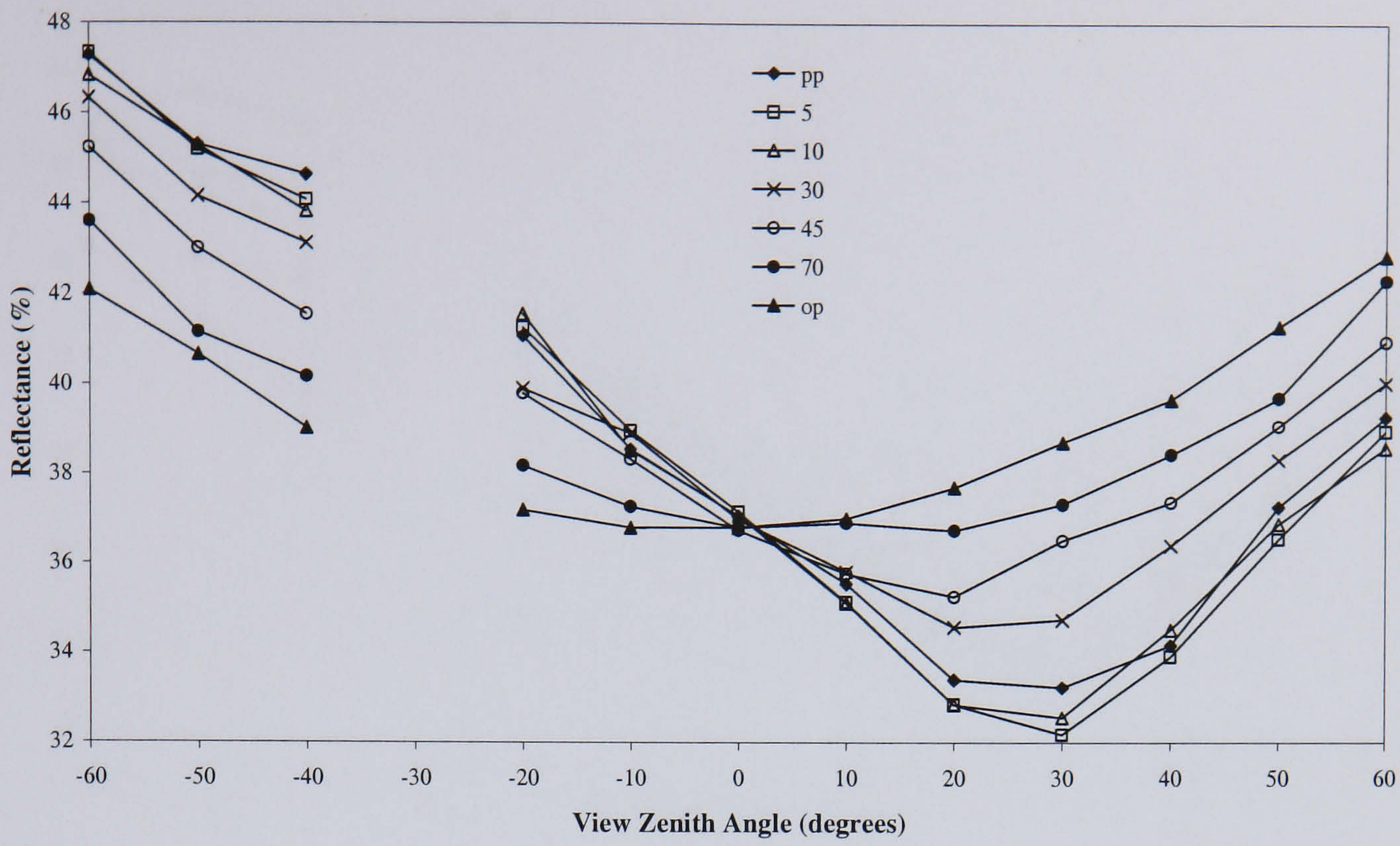

(a)

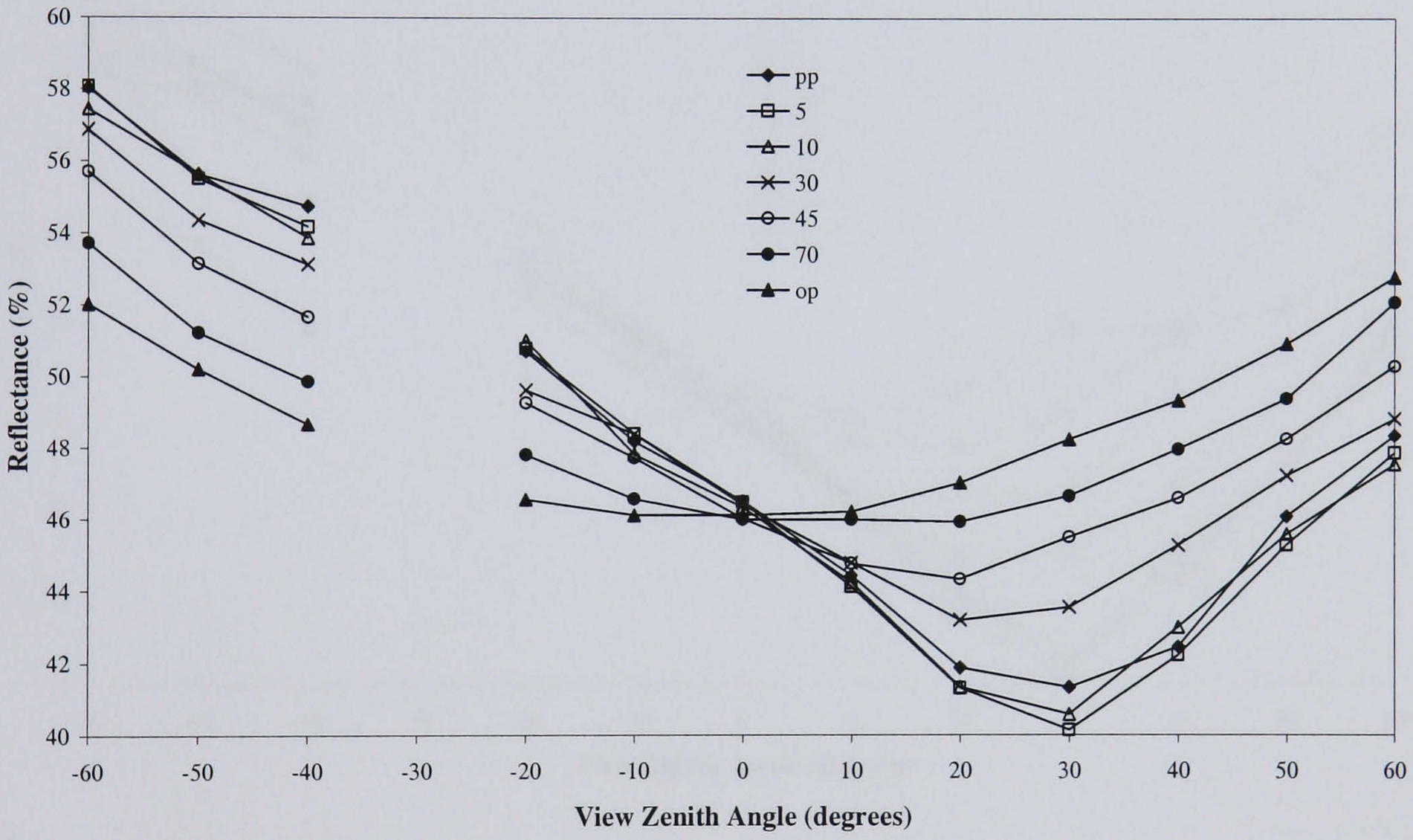

(b)

Figure 5.7 Spectral reflectance as a function of viewing azimuth plane, for Mabuasehube plot 2 (M2) at (a) 660nm, and (b) 860nm. Letters and numbers in the legend refer to the angular plane the measurements were made in, where pp is the principal plane and op is the orthogonal plane. No data are shown in the hot spot for reasons of consistency.

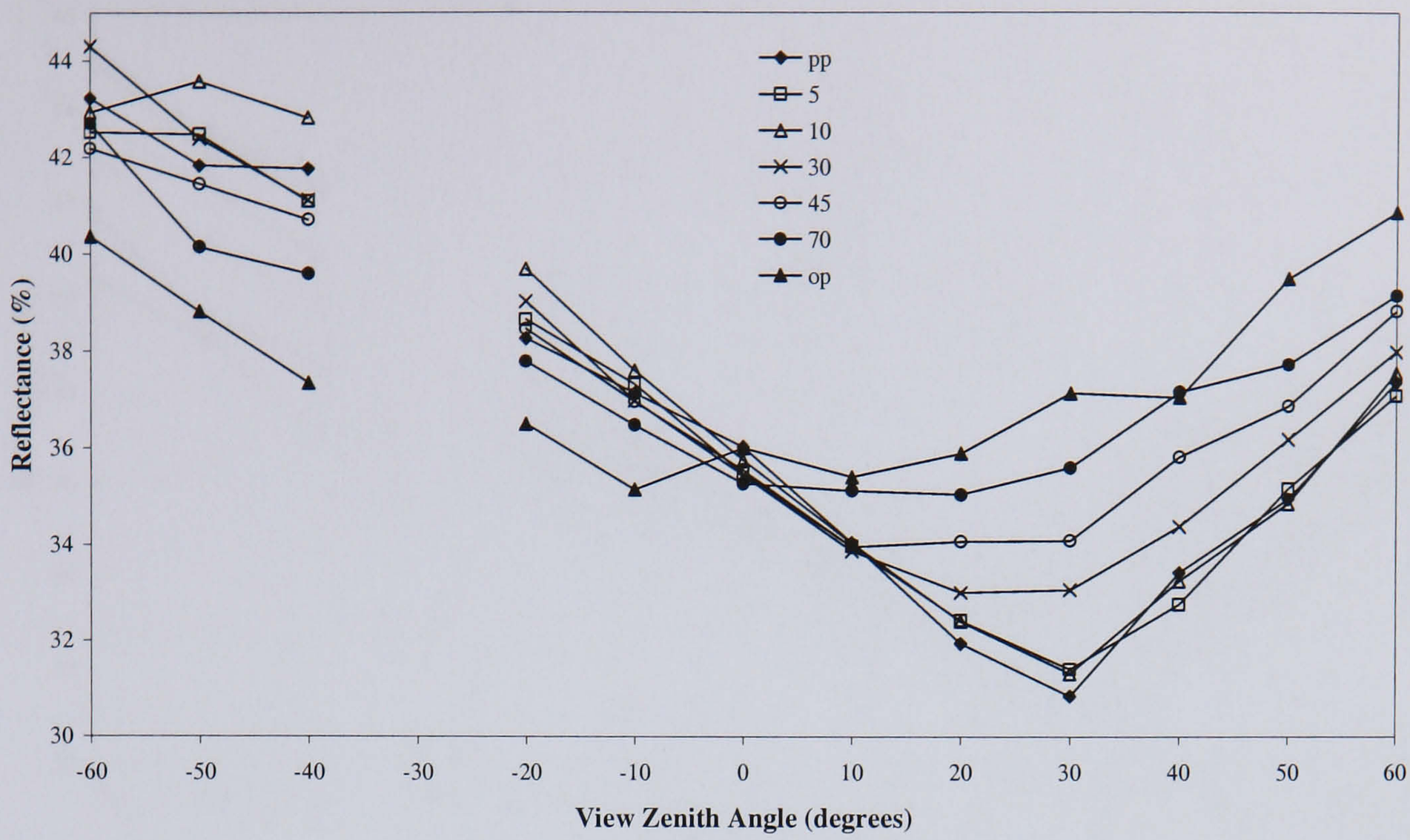

(a)

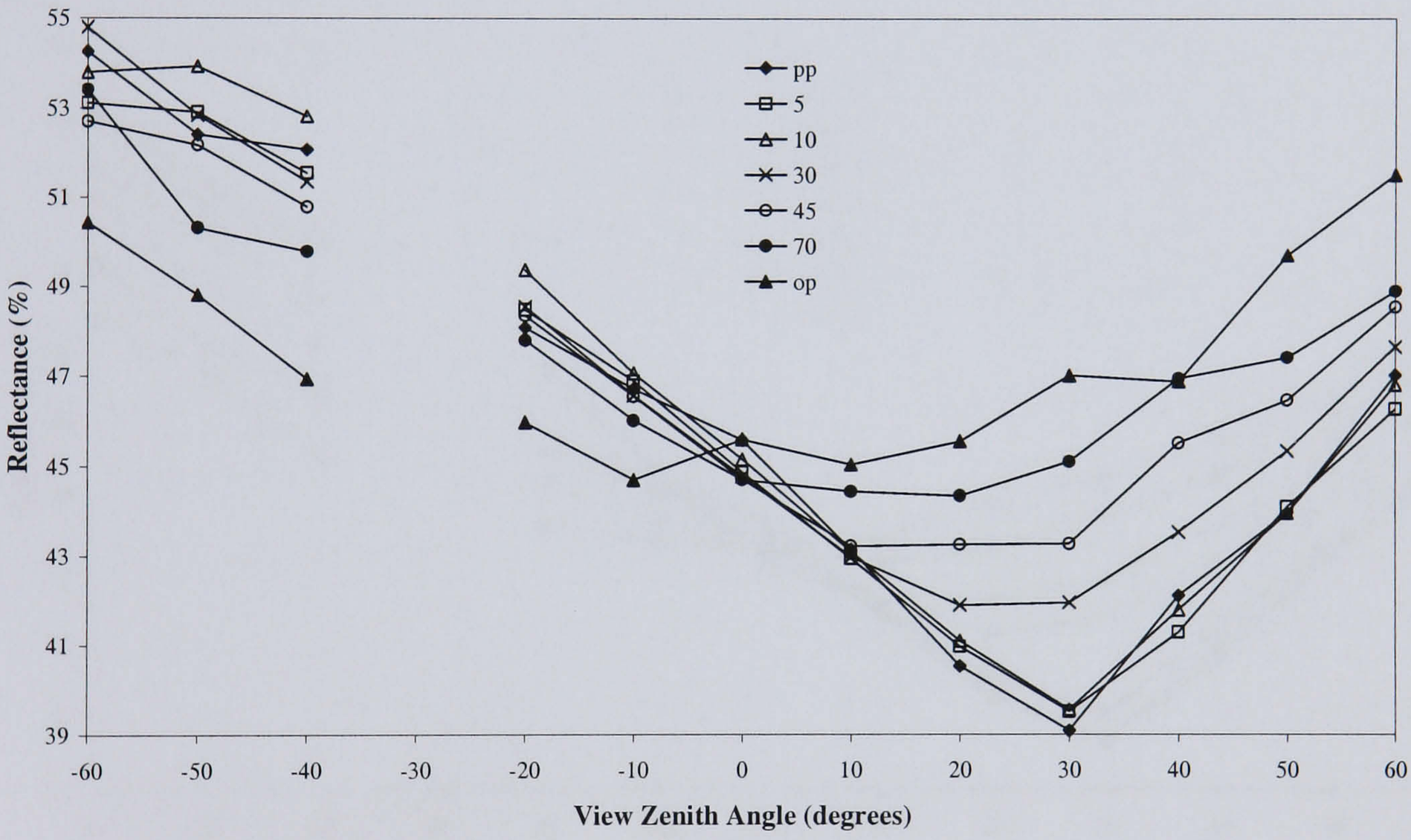

(b)

Figure 5.8 Spectral reflectance as a function of viewing azimuth plane, for Tshabong plot 1 (TG1) at (a) 660nm, and (b) 860nm. Letters and numbers in the legend refer to the angular plane the measurements were made in, where pp is the principal plane and op is the orthogonal plane. No data are shown in the hot spot for reasons of consistency.

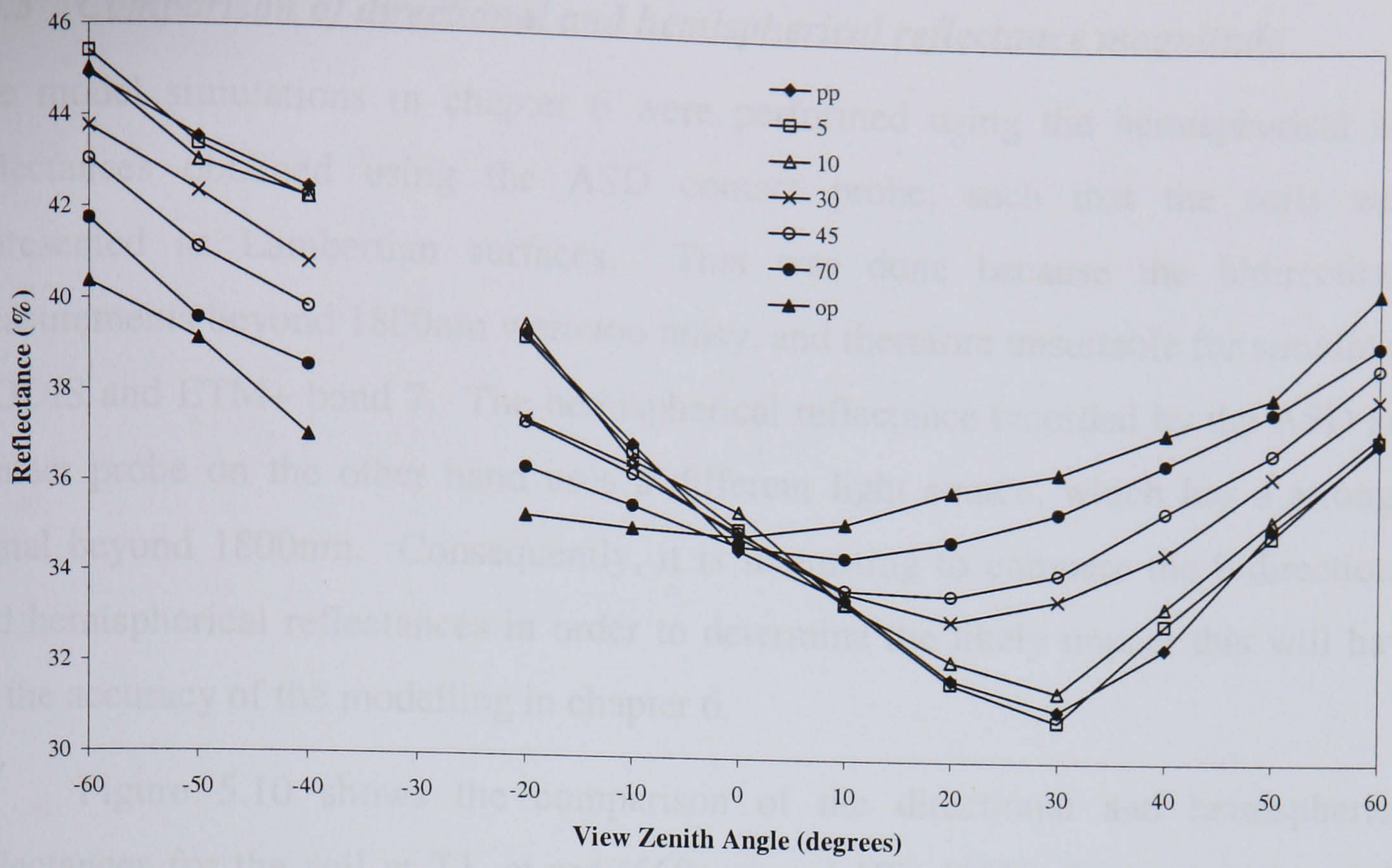

(a)

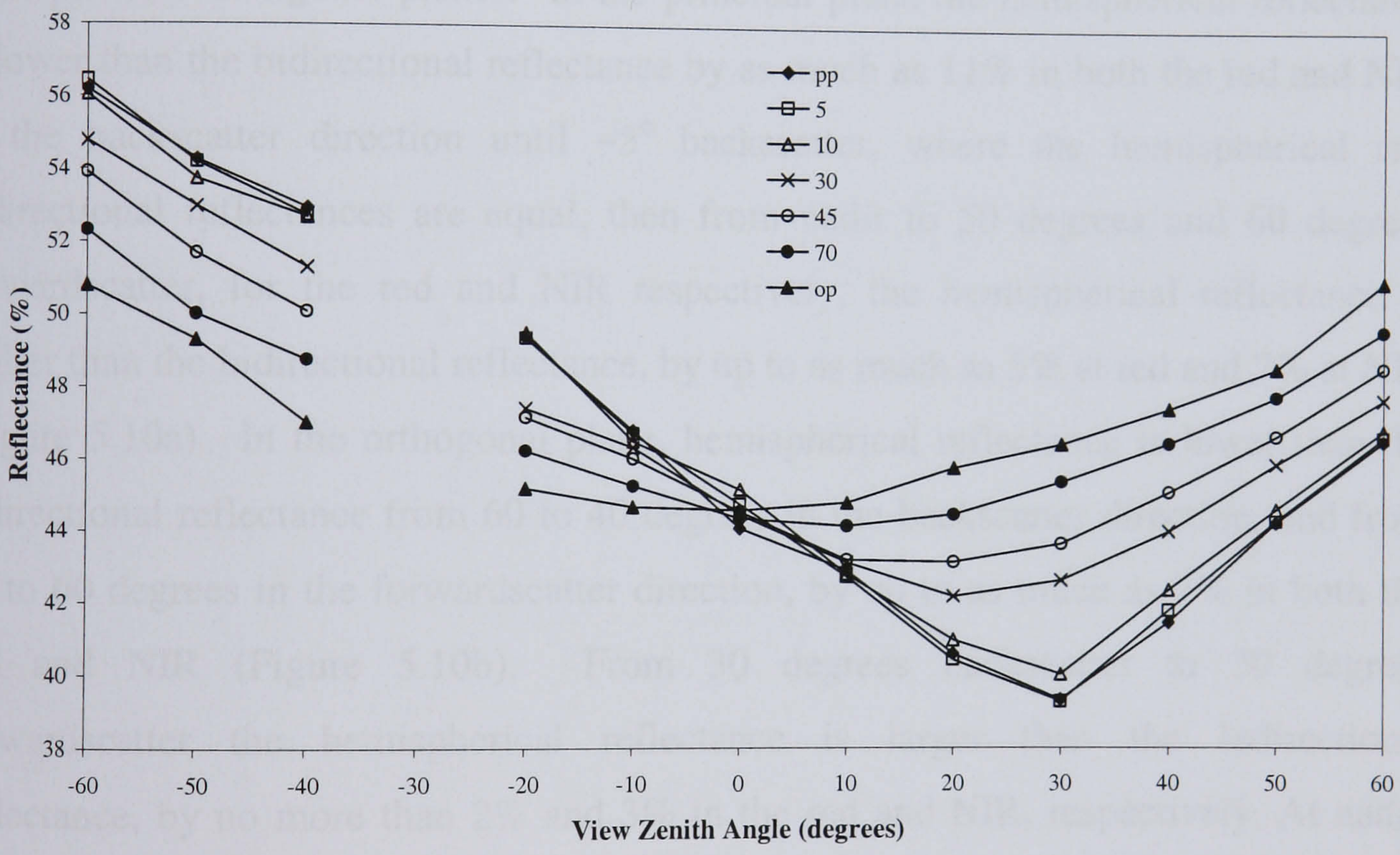

(b)

Figure 5.9 Spectral reflectance as a function of viewing azimuth plane, for Tshabong plot 3 (TG3) at (a) 660nm, and (b) 860nm. Letters and numbers in the legend refer to the angular plane the measurements were made in, where pp is the principal plane and op is the orthogonal plane. No data are shown in the hot spot for reasons of consistency.

5.3.5 Comparison of directional and hemispherical reflectance magnitude

The model simulations in chapter 6 were performed using the hemispherical soil reflectances obtained using the ASD contact probe, such that the soils were represented as Lambertian surfaces. This was done because the bidirectional measurements beyond 1800nm were too noisy, and therefore unsuitable for simulating MODIS and ETM+ band 7. The hemispherical reflectance recorded by the ASD and contact probe on the other hand uses a different light source, which has a stronger signal beyond 1800nm. Consequently, it is interesting to compare the bidirectional and hemispherical reflectances in order to determine the likely impact this will have on the accuracy of the modelling in chapter 6.

Figure 5.10 shows the comparison of the directional and hemispherical reflectances for the soil at T1, at red (660nm) and NIR (860nm) wavelengths in the principal and orthogonal planes. In the principal plane the hemispherical reflectance is lower than the bidirectional reflectance by as much as 11% in both the red and NIR in the backscatter direction until ~5° backscatter, where the hemispherical and bidirectional reflectances are equal, then from nadir to 50 degrees and 60 degrees forwardscatter, for the red and NIR respectively, the hemispherical reflectance is higher than the bidirectional reflectance, by up to as much as 5% at red and 7% at NIR (Figure 5.10a). In the orthogonal plane, hemispherical reflectance is lower than the bidirectional reflectance from 60 to 40 degrees in the backscatter direction, and from 30 to 60 degrees in the forwardscatter direction, by up to as much as 7% in both the red and NIR (Figure 5.10b). From 30 degrees backscatter to 30 degrees forwardscatter the hemispherical reflectance is larger than the bidirectional reflectance, by no more than 2% and 3% in the red and NIR, respectively. At nadir, differences between the hemispherical and bidirectional reflectances are very small (~1%) in the principal plane, at both red and NIR, while in the orthogonal plane the difference are slightly larger at up to 3% in the NIR. In both planes the hemispherical reflectance is higher than the bidirectional reflectance. The same pattern of results is repeated in both the principal and orthogonal planes for all other wavelengths, and for the other three soil samples.

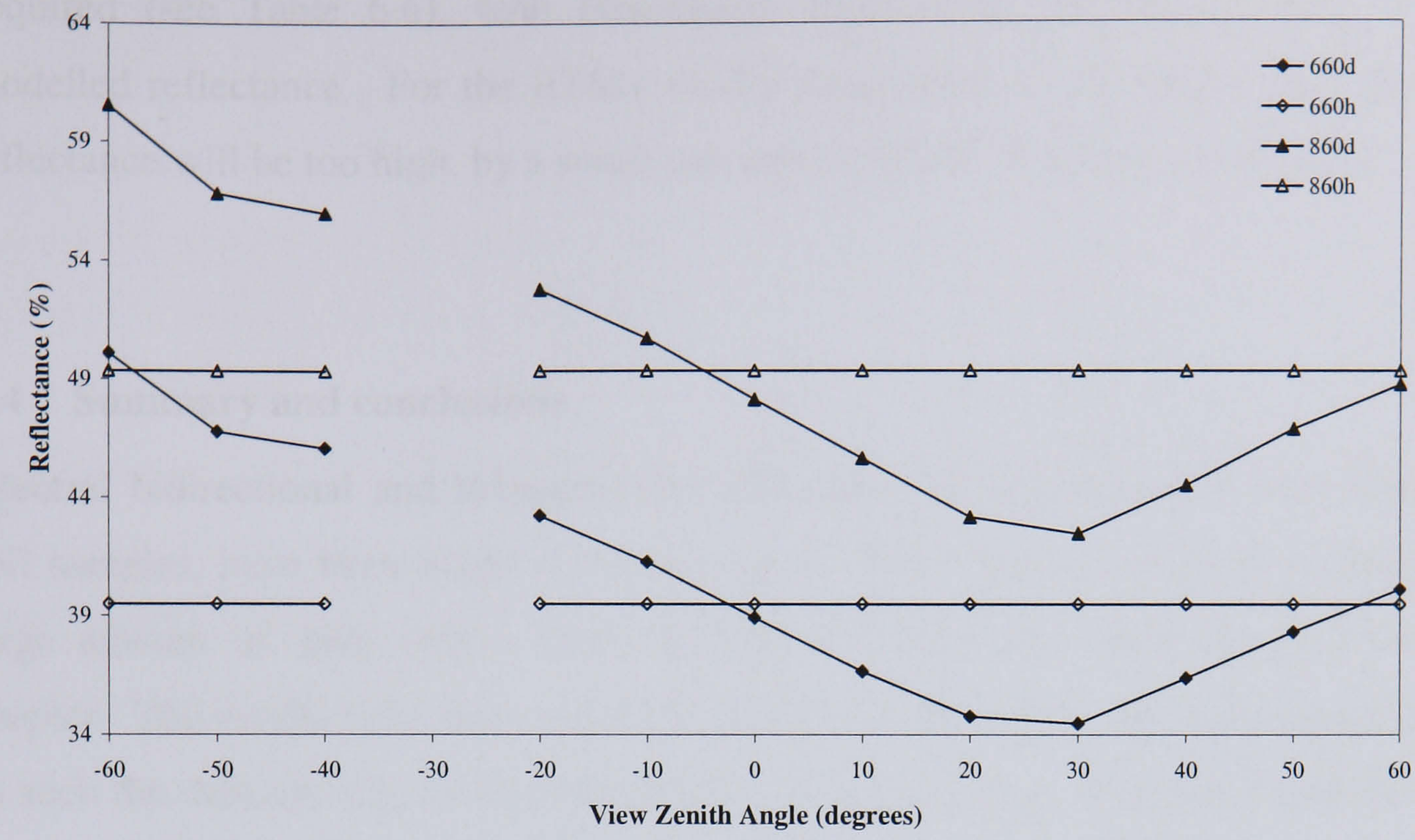

(a)

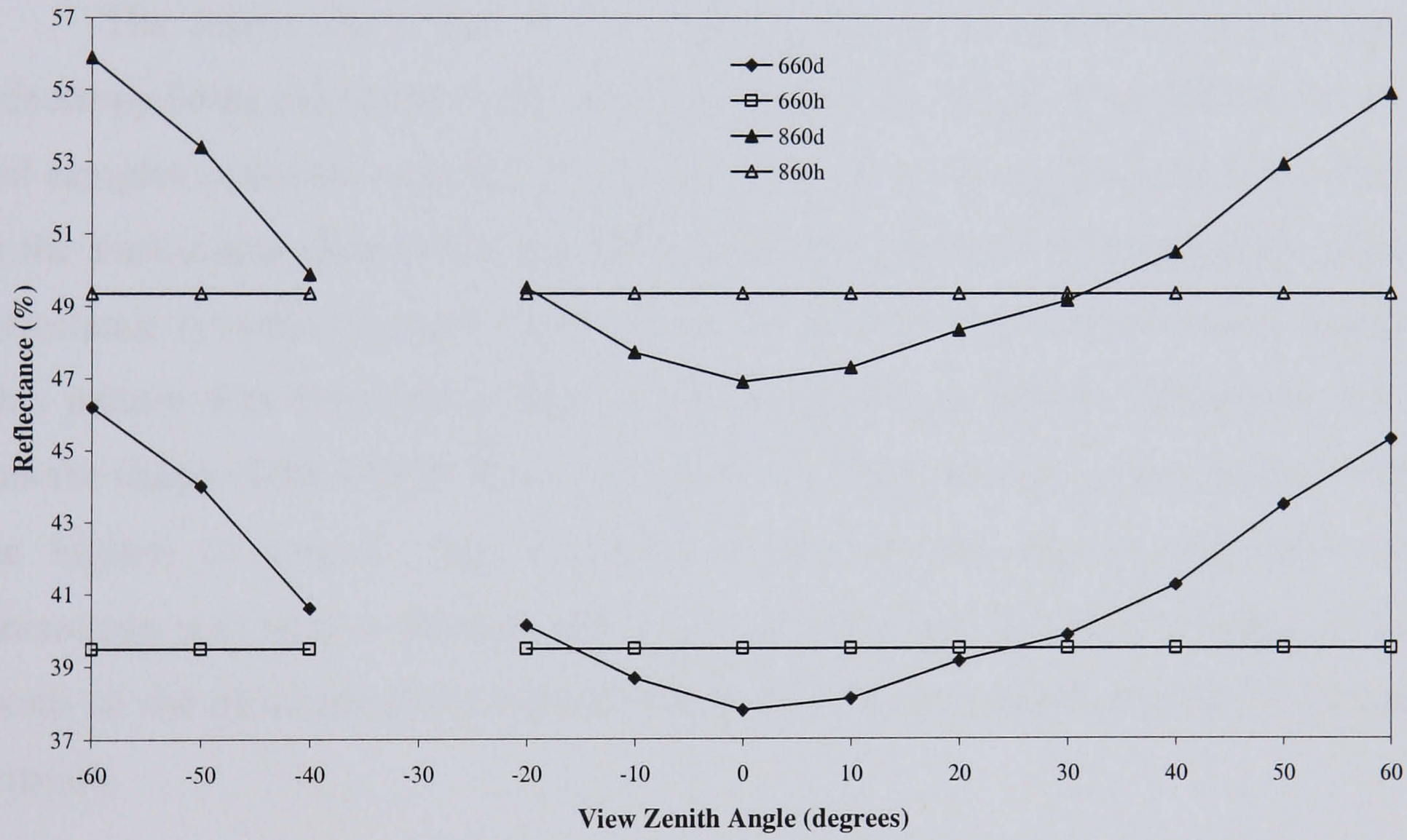

(b)

Figure 5.10 comparison of the directional and hemispherical reflectances at red (660) and NIR (860), for the soils at T1, in (a) the principal plane, and (b) the orthogonal plane. In the legend, the number is the wavelength and d indicates directional reflectance while h indicates hemispherical reflectance. No data are shown in the hot spot for reasons of consistency.

The implication of these results is that, because the MODIS model simulations in chapter 6 have been parameterised with hemispherical soil reflectance rather than bidirectional reflectance, the soil reflectance will either be too high or too low, depending on the viewing angle and relative azimuth at which the MODIS data were

acquired (see Table 6.6), with consequent implications for the accuracy of the modelled reflectance. For the ETM+ model simulations on the other hand, the soil reflectance will be too high, by a small amount (up to 3% absolute), in all cases.

5.4 Summary and conclusions

Spectral bidirectional and hemispherical reflectance measurements of four Kalahari soil samples, have been made in the laboratory. The data set obtained represents a large amount of data, only a small fraction of which has been presented in this chapter. The results have shown that the features of the BRDF are captured well, and as such the data set may be considered to be of high quality. The data could be used as a test data set against which soil BRDF models could be compared.

The results show that all the soils are highly non-Lambertian, with greatest anisotropy being displayed in the principal plane. The shape of the BRDF for all four soil samples is almost identical, being characterised as having predominant reflectance in the backscatter direction in the principal plane, while in the orthogonal plane the reflectance is more symmetric with respect to the back and forwardscatter directions. This pattern was consistent across all wavelengths considered. Moreover, not only was the shape of the BRDF almost identical, but the anisotropy (measured as a ratio of the highest to lowest value for each sample in each plane) was very similar. Anisotropy was seen to decrease slowly as measurements are made within a 10 degree swath of the principal plane before falling away more rapidly beyond 30 degrees in azimuth.

Differences in reflectance magnitude were apparent between the four samples, however, this difference was never greater than 5% absolute reflectance across the wavelengths considered. Clearly, the spectral bidirectional reflectance of the four soils is very similar, and is most likely a reflection of the homogeneity of the soils, they are all Kalahari sands. This lends confidence to the idea that LAI may be estimated with reasonable accuracy, over the field plots, given that there is relatively little variation in the underlying soil substrate which constitutes the largest fractional area of a pixel. Variation in pixel reflectance may well be driven by subtle changes in the vegetation cover therefore. This issue is investigated in chapter 7.

Clearly, representing these soil surfaces as Lambertian scatterers is a crude approximation. Comparing the bidirectional and hemispherical reflectances it was shown that in the principal plane the impact of using the hemispherical reflectance in the model simulations of chapter 6, will be to generally underestimate bidirectional reflectance in the backscatter direction, and overestimate bidirectional reflectance in the forwardscatter directions. In the orthogonal plane the hemispherical reflectance underestimates bidirectional reflectance from around 30^{o} to 60^{o} in both the back and forwardscatter directions, while from 30^{o} backscatter to 30^{o} forwardscatter, the hemispherical reflectance overestimates bidirectional reflectance. These results will be used to aid in the interpretation and understanding of the accuracy of the MODIS and ETM+ model simulations in the next chapter.

6 Simulating Canopy Reflectance

6.1 Introduction

The successful use of canopy reflectance models (CRMs) to estimate biophysical parameters via model inversion depends on a number of factors, among the most critical of which, is the model accuracy (Goel 1989). Unless the model used provides a close fit to the measured reflectance, the likely success of model inversion will be seriously compromised. A related issue is that of model suitability. Model suitability relates to whether or not the assumptions made in the formulation of the model are consistent with the structure of the vegetation canopy being modelled. This issue is particularly relevant to modelling the reflectance of savanna vegetation, where there is a large range of canopy structures, from grassland savannas, to shrubland savannas, and low tree/shrub savannas. In grassland savanna, composed entirely of a herbaceous understorey, the assumptions of turbid medium (TM) models may be satisfied, and a TM model deemed to be the most suitable. In shrubland savanna, where the vegetation is composed entirely of shrubs, then a hybrid model may be considered the most suitable. In low tree/shrub savanna, however, where there is a herbaceous understorey together with an overstorey of trees and shrubs, the question of model suitability is more difficult to assess, since the various CRMs which are available are designed to model one specific vegetation layer. Whilst a turbid medium approach may be suitable for modelling a herbaceous understorey, it may not be suitable for modelling trees and shrubs of the overstorey. Similarly, a hybrid model may be suitable for modelling the trees and shrubs of the overstorey, but unsuitable for modelling herbaceous understoreys.

Given the need to invert one single model, and the fact that no one model is ideally suited to modelling this range of vegetation structures, presents a serious impediment to the faithful representation of savanna vegetation structure in CRMs. Clearly, a TM model could be used to represent all savanna types. Doing so,

however, will result in the structural effects of the overstorey (i.e. shadow) being ignored, and the assumptions of the TM models are clearly inconsistent with the structure of the shrubland and low tree/shrub savanna. In this case, it is important to determine the effect this has on the accuracy with which reflectance is modelled. Table 6.1 provides a summary of the issues involved in modelling savanna vegetation, as they relate to the field plots used in this thesis.

Table 6.1 Summary of the canopy reflectance modelling considerations in savanna vegetation.

Vegetation Type	Low Tree/Shrub Savanna	Shrub Savanna	Grassland Savanna
Canopy morphology	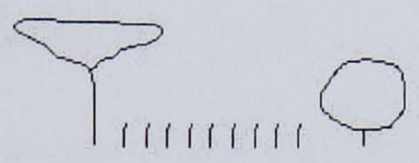	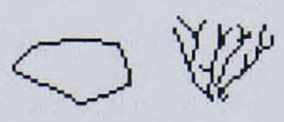	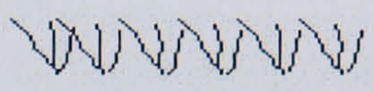
Description	Continuous herbaceous layer, interspersed with trees and shrubs, against a soil background	Discontinuous shrub vegetation, against a soil background	Continuous herbaceous layer, against a soil background
Model Type	Hybrid or Turbid medium? How to represent two distinct canopy layers?	Hybrid	Turbid medium
Field Plots	Tshane plots 1 and 2, and Tshabong plot 2	Tshabong plots 1 and 3	Mabuasehube plots 1 and 2

This chapter presents the results of a series of model simulations designed to investigate the accuracy with which three different canopy reflectance models (selected for study in chapter 2), represent reflected radiation from savanna vegetation. Specifically, TM and hybrid model simulations were compared, together with modelling which explicitly took account of two distinct canopy layers. In so doing, the importance of the overstorey structure in determining canopy reflectance could be investigated. The aim of this chapter was to determine the most accurate model for representing the reflectance of savanna vegetation.

6.2 Experimental methodology

A series of modelling experiments were carried out, where answers to the following questions were sought:

- How accurately do the three different canopy reflectance models simulate the reflected radiation from savanna vegetation?
- What are the relative differences in accuracy between the different models?
- Is the explicit incorporation of a two-layer canopy into model simulations necessary for increased accuracy, or does a TM treatment suffice? In other words, how important is the overstorey in determining canopy reflectance?

6.2.1 Model simulations

Model simulations were performed with the SAIL, GeoSAIL, and FLIGHT canopy reflectance models. Two sets of simulations were performed: 1) for evaluation with Landsat ETM+ data, and 2) for evaluation with MODIS data. GeoSAIL was not used in the MODIS simulations because it can only simulate nadir viewing angles. In the absence of any field or laboratory measured leaf reflectance and transmittance data, the PROSPECT model (Jacquemoud & Baret 1990; Jacquemoud *et al.* 1996) was used to simulate leaf reflectance and transmittance. PROSPECT was coupled to the SAIL and GeoSAIL models directly, and are thus referred to as PROSAIL and PROGeoSAIL respectively. FLIGHT is not renamed as PROFLIGHT because the two models were not directly coupled. Table 6.2 provides a list of the input parameters required for each model.

The models were used in various ways and the model simulations are summarised in Table 6.3. The specific case of modelling vegetation which is composed of two distinct canopy layers is an area of research which has received little attention, with, at the time the simulations were performed, only four models which explicitly incorporate two distinct canopy layers. These are, the SAIL-Cylinder model of Bégué *et al.* (1996), an enhanced version of this SAIL-Cylinder model produced by Hanan (2001), the 4-Scale model of Leblanc *et al.* (1999), and the radiosity-graphics model (RGM) of Qin & Gerstl (2000). None of these models were suitable for use in this work, since the code for the SAIL-Cylinder model was not available, and the enhanced version of this model only simulates reflectance in the PAR and NIR

wavelengths; the two-layer modelling of the understorey in 4-Scale relies on a geometric-optical (G-O) approach (Figure 6.1), which was considered unsuited to the modelling of grass understoreys; while the RGM model is too computationally expensive to be considered. Since the simulations were performed another model which incorporates two canopy layers, and which is based on RGM has been published (Chopping *et al*. 2003).

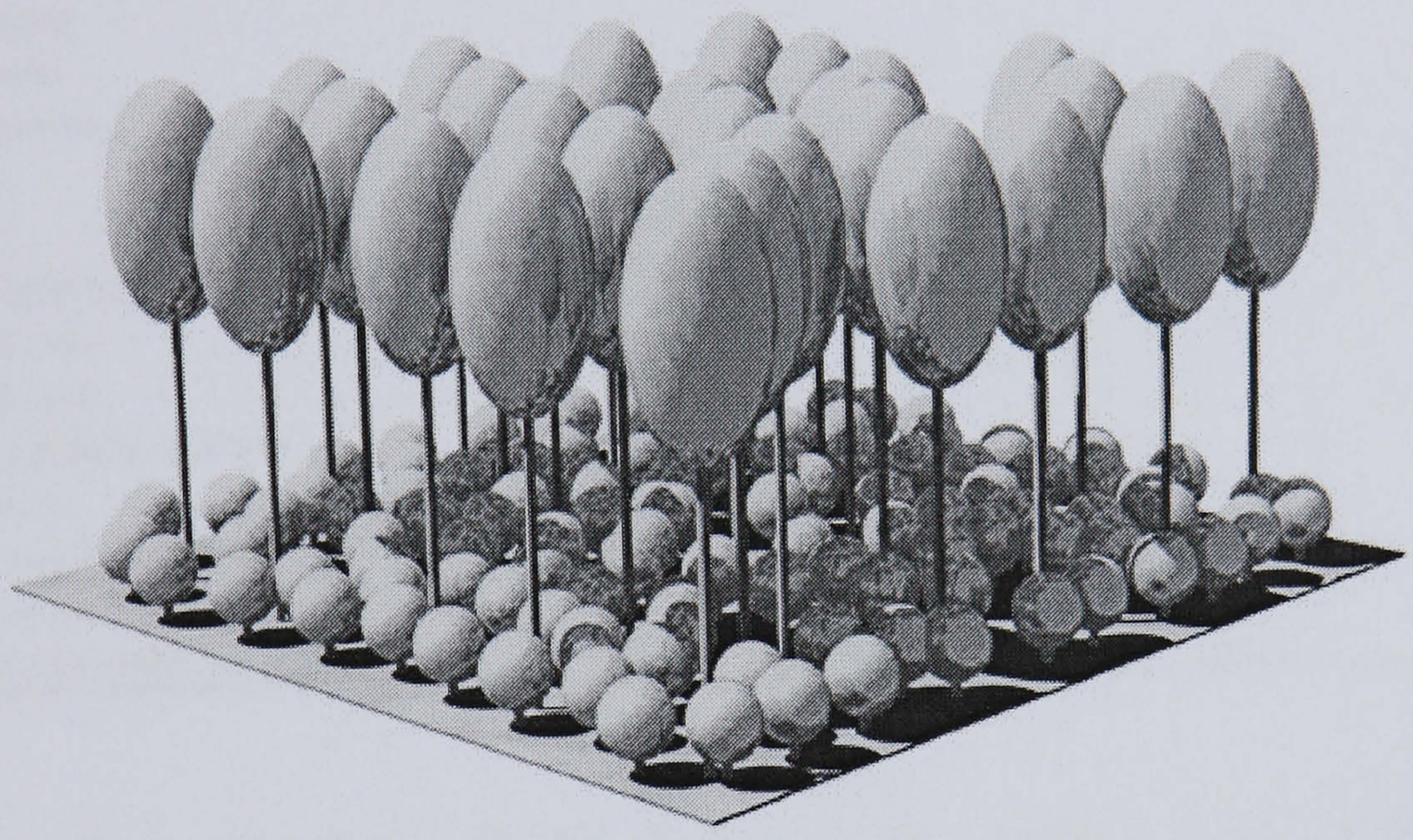

Figure 6.1 Illustration of the modelling of two-layer canopies in the 4-scale model (*Source*: www 6.1)

Table 6.2 Input parameters required for the PROSAIL, PROGeoSAIL and FLIGHT models.

Parameter and Units	PROSAIL	PROGeoSAIL	FLIGHT
Leaf structure parameter (N)	X	X	X
Leaf chlorophyll content (C_{a+b} μg cm^{-2})	X	X	X
Equivalent water thickness (EWT g cm^{-2})	X	X	X
Dry matter content (DMC g cm^{2-})	X	X	X
Soil reflectance	X	X	X
Bark reflectance		X	X
Shoot reflectance		X	X
Soil BRDF			X
Hotspot	X	X	X
LAI (m^{-2} m^{-2})	X	X	X
Leaf angle distribution	X	X	X
Soil roughness			X
Fraction of green		X	X
Fraction of bark		X	X
Fraction senescent		X	X
Leaf size (m)			X
Crown shape		X	X
Min/Max Height to crown (m)			X
Crown height (m)		X	X
Crown radius (m)		X	X
Fraction of vegetation cover		X	X
Number of trees			X
Solar zenith angle (degrees)	X	X	X
View zenith angle (degrees)	X	X	X
Relative azimuth angle (degrees)	X	X	X

Therefore, in order to model the two-layer canopies found at plots T1, T2, and TG2 an approach was adopted whereby the simulations were performed in two steps.

1. A TM model is parameterised to represent the grass understorey, and executed. The output from this simulation is then used as the background reflectance, for the second simulation.

2. A hybrid model is parameterised to represent the overstorey. The output from this run of the model is then treated as the reflectance from a two-layer canopy.

The aim of these two-layer canopy simulations, was to determine the importance of the structural effects (e.g. shadow) of the overstorey, in determining the reflectance of the plots, and whether a TM treatment led to significant error. The PROSAIL and FLIGHT-1D models were also used at these plots in order to permit the comparison (Table 6.3).

Table 6.3 Summary of the model simulations performed in this chapter.

Model ID	Simulation Details	ETM+/MODIS	Field Plots
PROSAIL	Parameterised with the total LAI of the plot, and a spherical LAD.	Both	T1, T2, M1, M2, TG1, TG2, TG3
PROGeoSAIL	Parameterised with the overstorey LAI, LAD and fractional cover.	ETM+	TG1, TG3
PROGeoSAIL 2-LAYER	Understorey simulated with PROSAIL, parameterised with understorey LAI and LAD. Overstorey simulated with PROGeoSAIL parameterised with overstorey LAI and LAD.	ETM+	T1, T2, TG2
FLIGHT 1-D mFC	FLIGHT used in turbid medium mode, parameterised with total LAI of the plot, measured total fractional cover, and a spherical LAD.	Both	T1, T2, M1, M2, TG1, TG2, TG3
FLIGHT 1-D 1FC	FLIGHT used in turbid medium mode, parameterised with total LAI of the plot, and a spherical LAD. Fractional cover is declared to be 1 to provide complementary inputs to the PROSAIL model.	Both	T1, T2, M1, M2, TG1, TG2, TG3
FLIGHT 3-D	Parameterised with overstorey LAI, LAD and fractional cover.	Both	TG1, TG3
FLIGHT 3-D mFC 2-LAYER	Understorey simulated with FLIGHT 1-D, parameterised with understorey LAI, LAD and measured fractional cover. Overstorey simulated with FLIGHT in 3-D mode, parameterised with overstorey LAI, LAD, and fractional cover.	Both	T1, T2, TG2
FLIGHT 3-D 1FC 2-LAYER	Understorey simulated with FLIGHT 1-D, parameterised with understorey LAI and LAD, but fractional cover set to be 1. Overstorey simulated with FLIGHT in 3-D mode, parameterised with overstorey LAI, LAD and fractional cover.	Both	T1, T2, TG2

Note: T1 T2 are Tshane plots 1and 2, M1 M2 are Mabuasehube plots 1 and 2, TG1 TG2 TG3 are Tshabong plots 1, 2, and 3.

Reflectance was simulated across the solar spectrum at 5nm intervals, and convolved to the wavebands of the ETM+ and MODIS sensors, using the sensor specific spectral response functions which are shown in Figure 6.2. Table 6.4 lists the full width half maximum (FWHM) for the ETM+ and MODIS wavebands.

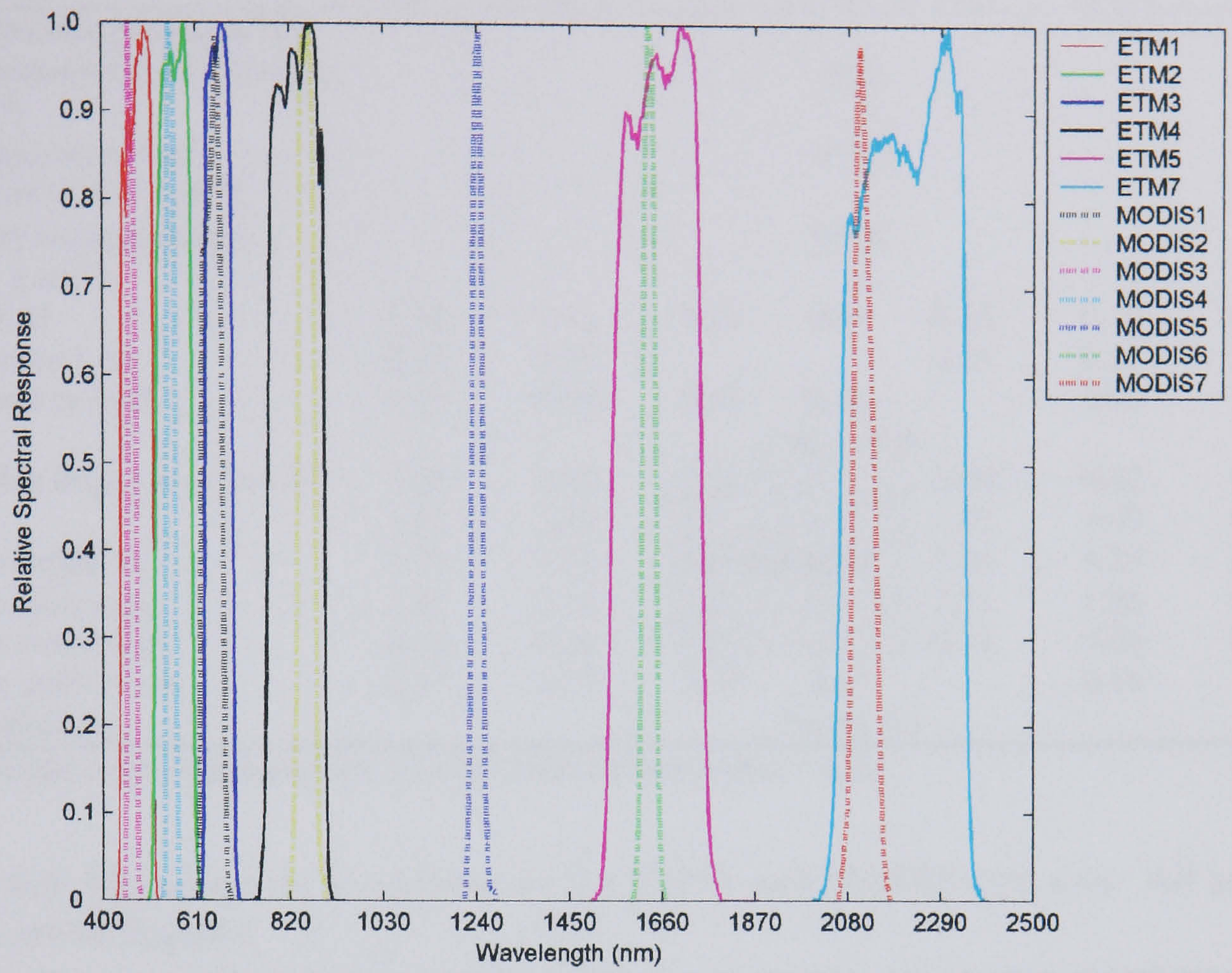

Figure 6.2 Spectral response functions for the Landsat ETM+ and Terra-MODIS wavebands.

Table 6.4 Full width half maximum (nm) for the Landsat ETM+ and Terra-MODIS optical wavebands, simulated in this chapter.

Band	ETM+	MODIS
1	450-515	620-670
2	525-605	841-876
3	630-690	459-479
4	750-900	545-565
5	1550-1750	1230-1250
6		1628-1652
7	2090-2350	2105-2155

6.2.2 Model parameterisation

Simulations were performed with model parameters set to the mean of all field recorded values for each plot, and are given in Table 6.5, while Table 6.6 contains the viewing and illumination geometry for the ETM+ and MODIS simulations.

Table 6.5 Input parameter values for the model simulations.

Parameter	Plot ID						
	T1	T2	M1	M2	TG1	TG2	TG3
Leaf structure parameter (N)	2						
Leaf chlorophyll content (C_{a+b} $\mu g\ cm^{-2}$)	35.0						
Leaf equivalent water thickness (EWT g cm^{-2})	0.012						
Leaf dry matter content (DMC g cm^{2-})	0.006						
Total LAI	0.35	0.45	0.01	0.06	0.25	0.16	0.22
Overstorey LAI	0.28	0.35			0.25	0.10	0.22
Understorey LAI	0.07	0.10	0.01	0.06		0.06	
LAD	Figure 6.4b						
Min/Max height to crown (m)	0.05/ 1.37	0.15/ 3.59			0.00/ 1.02	0.02/ 4.00	0.00/ 0.82
Crown height (m)	1.75	1.51	Not modelled		1.68	1.23	1.27
Crown radius (m)	2.47	2.27			2.31	1.66	2.12
Fcover overstorey	0.16	0.20			0.18	0.06	0.08
Fcover understorey	0.17	0.23	0.18	0.17		0.16	
Soil reflectance	Figure 6.3						

Note: all plots were parameterised with the same leaf parameter values.

Table 6.6 Measurement conditions for the ETM+ and MODIS data sets. All angular values are in degrees.

Sensor	Plot ID						
	T1	T2	M1	M2	TG1	TG2	TG3
ETM+							
View zenith angle	Nadir	Nadir	No ETM+ image available		Nadir	Nadir	Nadir
Solar zenith angle	43.36	43.36			37.42	37.42	37.42
Rel. azimuth angle	55.28	55.28			74.97	74.97	74.97
Day of year image	87	87			48	48	48
Image path/row	175/077	175/077			174/078	174/078	174/078
MODIS							
View zenith angle	19.05f	55.46b	5.69b	21.79f	25.1f	24.64f	12.14f
Solar zenith angle	29.03	37.55	32.11	29.33	29.53	29.50	32.76
Rel. azimuth angle	137.99	33.75	35.74	137.2	136.34	136.74	132.75
Day of year image	62	61	64	62	62	62	71
Day in field	*59*	*60*	*62*	*63*	*65*	*66*	*67*

Note: f in the view zenith angle row indicates the forward scatter direction, and b the backscatter direction. Day of year image and day in field are in Julian days, and refer to the date of the images, and day on which field measurements of canopy structure were made, respectively.

As mentioned previously, leaf reflectance and transmittance data were simulated with the PROSPECT model. Ideally, measured reflectance and transmittance values would be used, however, no such data sets were available. In order to parameterise the PROSPECT model, the leaf chlorophyll content, equivalent water thickness, and dry matter content were assigned the average values contained in

the LOPEX93[1] database (Hosgood *et al.* 1994, Jacquemoud *et al.* 1996). These values were used because a search of the literature failed to provide any guidance on the values of these parameters, for the species under study. Specifying a value for the leaf structure parameter N, presents a problem because it cannot be measured. Therefore, a value of 2.0 was used for the N parameter as this has been shown to represent a range of species accurately (Weiss *et al.* 2000, Combal *et al.* 2002b, Jacquemoud personal communication May 2003).

The values of LAI used were obtained from the field measurements and scaled to plot values using the measurements of fractional vegetation cover and equation 4.4. It is important to state that the values of LAI used are the same for the ETM+ and MODIS simulations. Intuitively, one might expect that there should be differences in the plot level LAI, for simulations which represent pixels of 30 metres and 500 metres, for the ETM+ and MODIS sensors, respectively. This effectively assumes that there is perfect linear spatial scaling between LAI at 30 metres and 500 metres. Liang (2000), has shown that this is possible, depending on the homogeneity of the vegetation over the area considered. For the plots studied here, an indication of the homogeneity of the LAI over the area sampled (see Figure 4.1), is provided by the fact that there was no significant difference between the LAI recorded on the MODIS and ETM+ sampling schemes (MWUT, $P>0.05$). Errors in the estimation of the LAI and fractional cover values will translate into an under- or over-estimation of the plot level LAI with consequent implications for the accuracy of the simulation

Soil reflectance was modelled as a Lambertian surface with soil spectra coming from the laboratory measurements made with the ASD contact probe (Figure 6.3). Despite the observed non-Lambertian properties of these soils, the directional measurements made in chapter 5 were not used because of the instability of the lamp beyond 1820nm, which would have meant that ETM+ band 7 and MODIS band 7 could not have been simulated.

---

[1] LOPEX93 was an experiment carried out at the Joint Research Centre in Italy, where biophysical and spectral measurements were made on ~55 different species of plants.

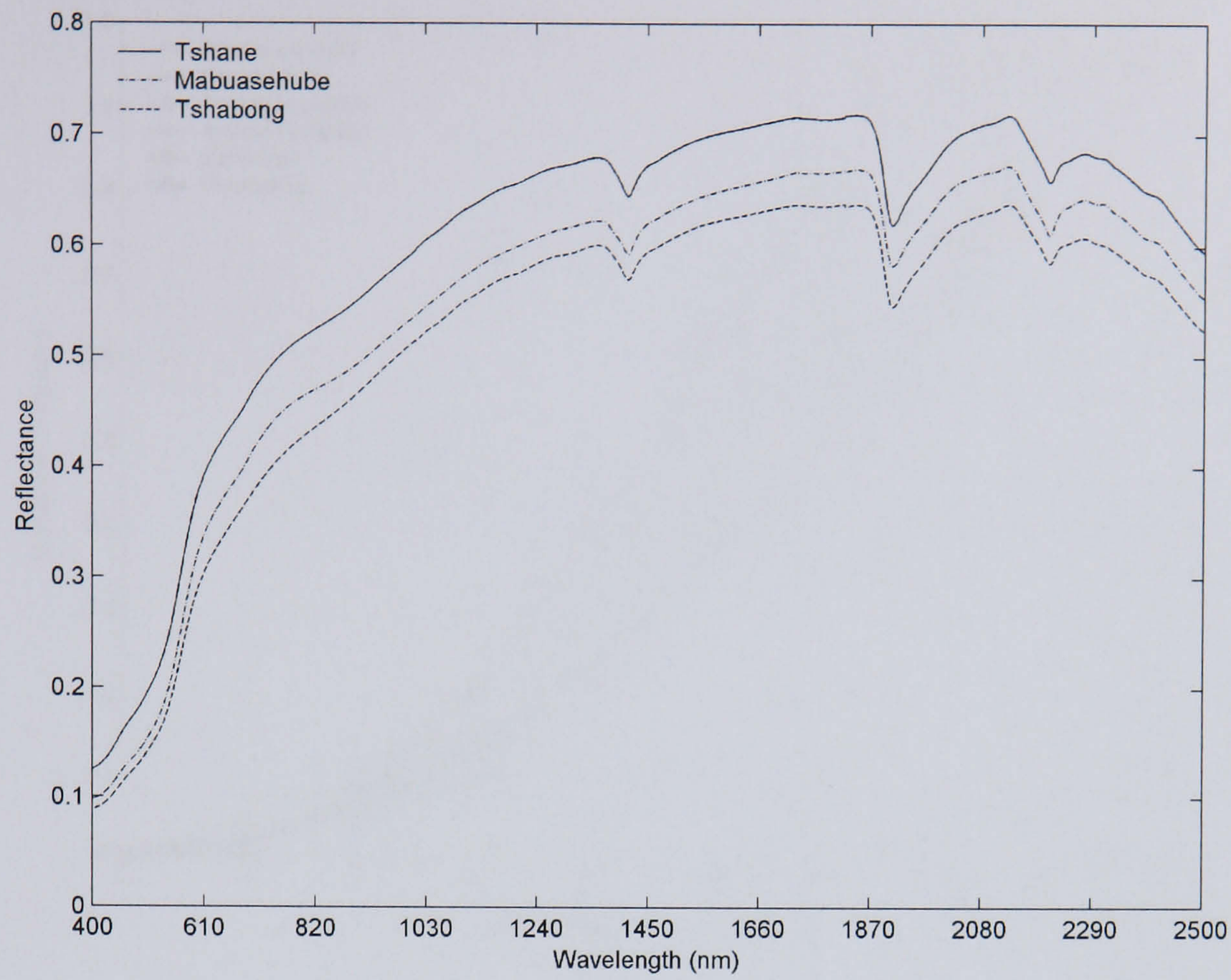

Figure 6.3 Laboratory measured soil reflectance spectra for the three study sites.

The leaf angle distribution (LAD) was determined by comparing the measured leaf angle data to the theoretical leaf angle distributions of Bunnik (1978). Figure 6.4a shows the cumulative frequency distribution of leaf angles for each species measured, as well as the theoretical spherical and plagiophile distributions. It can be seen that two species *Grewia flava* and *Acacia leuderitzii* fit more closely the spherical than the plagiophile distribution, while the other two species *Acacia erioloba*, and *Acacia mellifera* fit more closely the plagiophile than the spherical distribution. This was confirmed by correlation analysis (not shown). Given the requirement for one single LAD in the models, the LAD was determined by linearly combining the LAD of the dominant species at each plot. All grass understorey simulations were assumed to conform to an erectophile LAD. The actual LAD used for each plot is shown in Figure 6.4b.

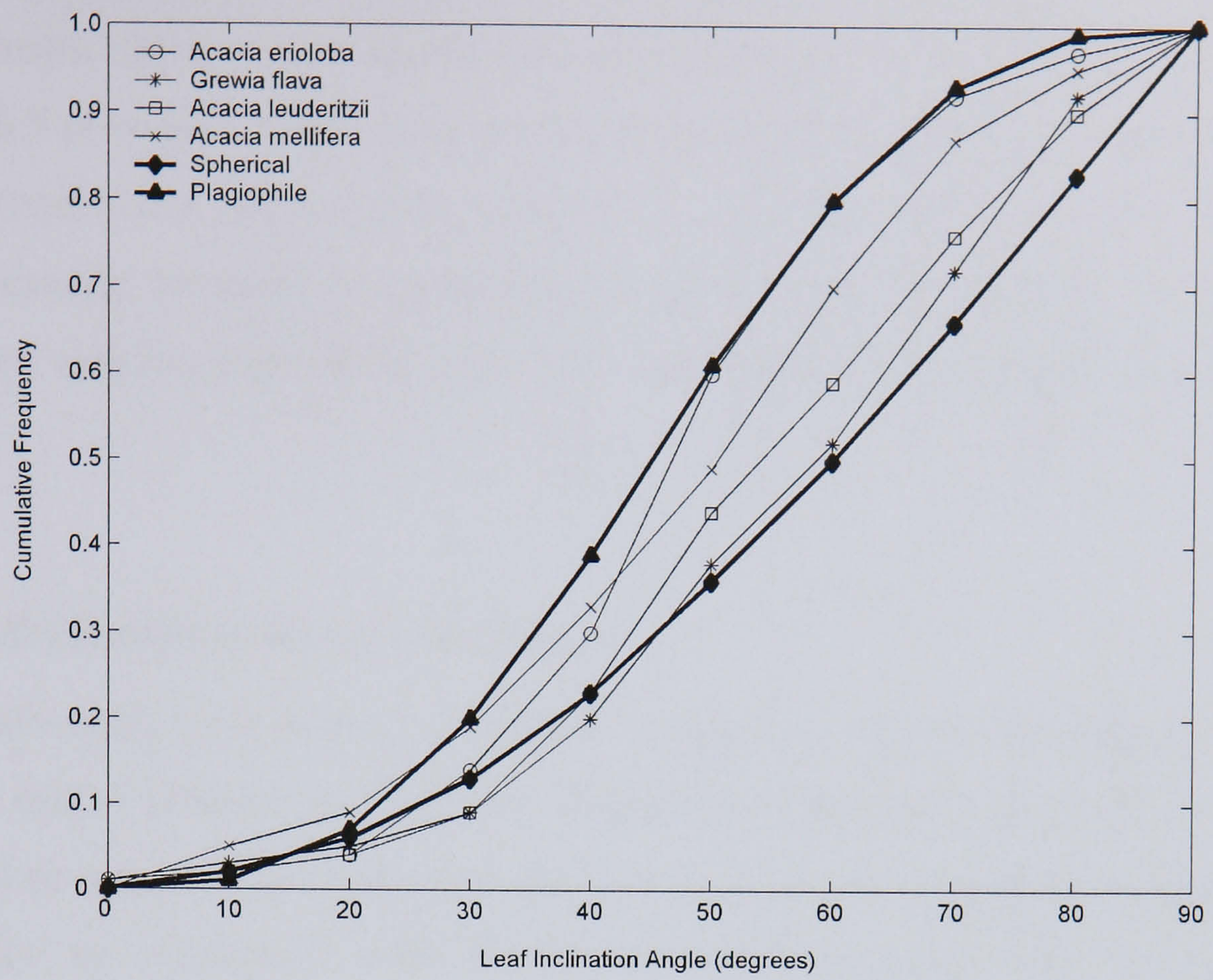

(a)

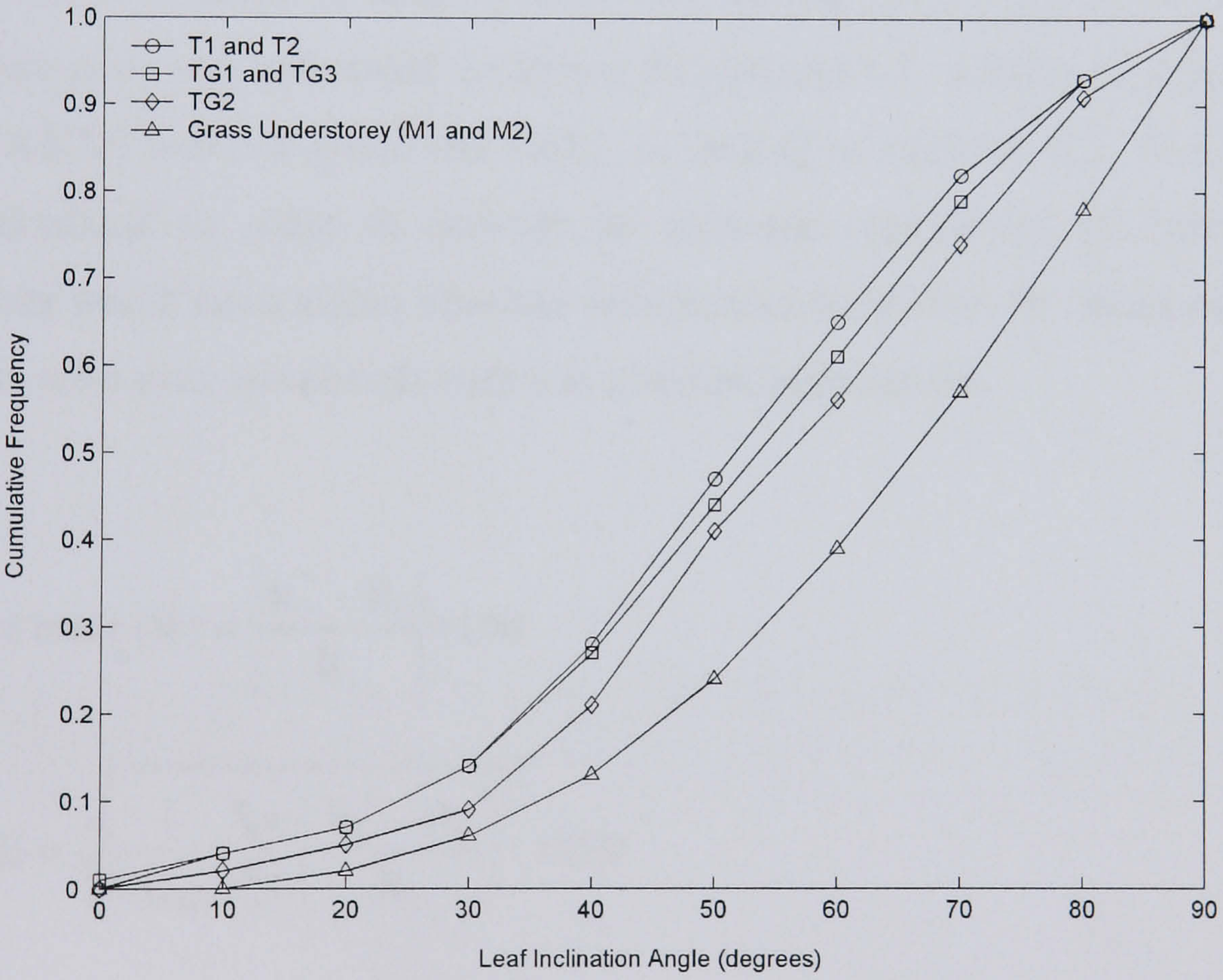

(b)

Figure 6.4 (a) Field measured cumulative LAD by species and theoretical spherical and plagiophile distributions of Bunnik (1978), (b) actual LAD used in model parameterisation for all field plots. The grass understorey LAD is Bunnik's erectophile distribution.

PROGeoSAIL simulations were performed with a spherical crown shape, while crown shape was modelled with an ellipse in the FLIGHT 3-D simulations. Figure 6.5 provides a view of the overstorey scene representation for the FLIGHT 3-D ETM+ (nadir view zenith angle) simulations. The Figure serves to illustrate the effect of the canopy structure in generating shadow within the scenes. Each scene is generated with the solar zenith angle and canopy dimensions as given in tables 6.5 and 6.6.

6.2.3 Evaluation of model performance

The philosophy with respect to model 'validation' adopted throughout this work follows that of Oreskes *et al.* (1994). When modelling open systems it is impossible to establish any absolute truth, such that it is not possible to validate such models, they can only be evaluated with respect to the agreement they show with the measurements. In order to assess the accuracy and relative performance of the model simulations, two values of relative error were calculated. By waveband, the relative percentage error was calculated according to equation 6.1, and for all wavebands the relative RMSE was calculated (RRMSE), according to equation 6.2. Relative values were calculated in order to provide an unbiased assessment of error, whereby wavebands which have higher absolute reflectances would not be interpreted as being in greater error than wavebands with low absolute reflectances.

$$\text{Relative error } (\%) = \left| \frac{R_i^* - R_i}{R_i} \right| * 100 \tag{6.1}$$

$$\text{RRMSE} = \sqrt{\frac{1}{n_{bands}} \sum_{i=1}^{n_{bands}} \left(\frac{R_i^* - R_i}{R_i} \right)^2} * 100 \tag{6.2}$$

where R_i^* is the modelled canopy reflectance in waveband $_i$, and R_i is the measured reflectance in waveband $_i$.

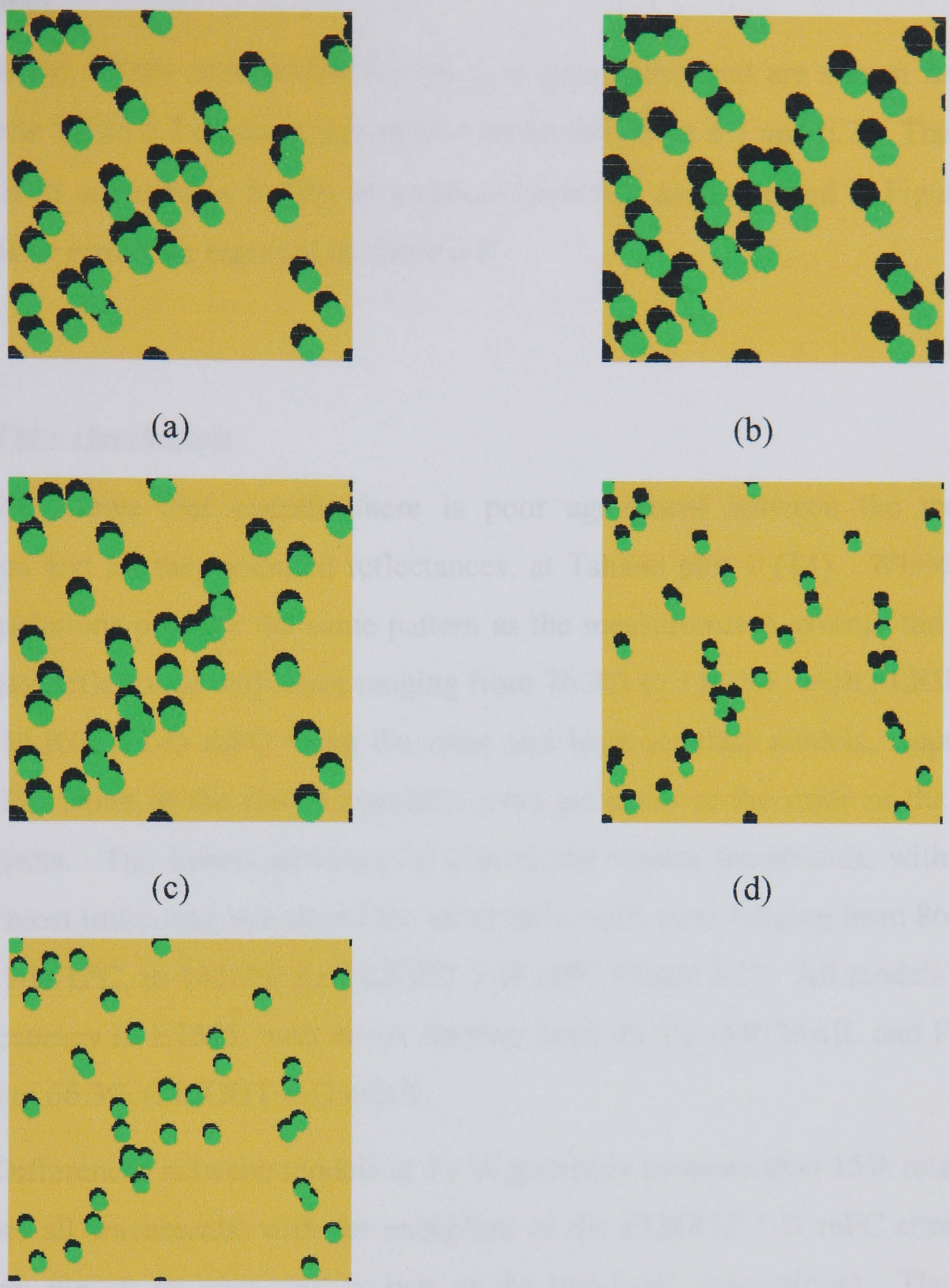

(a)

(b)

(c)

(d)

(e)

Figure 6.5 Scene representations of the overstorey and shadowing effects from FLIGHT for the ETM+ simulations at the five field plots, (a) Tshane plot 1, (b) Tshane plot 2, (c) Tshabong plot 1, (d) Tshabong plot 2, (e) Tshabong plot 3.

6.3 Results

Results for the ETM+ simulations for the five plots simulated are shown in Figure 6.6a-e, while Table 6.7 contains the relative errors (equation 6.1 and 6.2). The results of the MODIS simulations for the seven plots simulated are presented in Figure 6.7a-g, and relative errors are reported in Table 6.8.

6.3.1 ETM+ simulations

Figure 6.6a shows that overall, there is poor agreement between the measured reflectances and all the modelled reflectances, at Tshane plot 1 (T1). While all the model simulations produce the same pattern as the measurements, overall the models overestimate reflectance with error ranging from 76.3% to 114.5%, with FLIGHT 1-D 1FC and FLIGHT 1-D mFC being the most and least accurate models, respectively (Table 6.7). None of the model estimates even get close to the error of the ETM+ measurements. The lowest accuracy is seen in the visible wavebands, with ETM3 being the most inaccurate waveband for all models, with error ranging from 86.8% for FLIGHT 1-D 1FC, to 142.7% for FLIGHT 1-D mFC (Table 6.7). All models display highest accuracy in ETM5, with errors ranging from 48.3% (PROSAIL and FLIGHT 1-D 1FC) to 66.3% (FLIGHT 1-D mFC).

Differences between models at T1 of generally no more than 15% relative are seen across all wavebands, with the exception of the FLIGHT 1-D mFC simulations (both when run on its own, and as part of the two-layer simulations). The largest differences between models are observed in the visible wavebands, and smallest differences are observed in ETM4 and ETM5, which probably reflects the dominance of the soil reflectance in these wavebands (Table 6.7). Overall, the TM models provide the closest fit to the measurements, with only 4% difference between FLIGHT 1-D 1FC and PROSAIL. The two canopy layer modelling (PROGeoSAIL 2-layer and FLIGHT 3-D 1FC) performed with the combination of the TM and hybrid models, produce very similar accuracies compared to each other, but are approximately 10% less accurate than the best performing turbid medium results.

Simulations performed for Tshane plot 2 (T2) are shown in Figure 6.6b, where it can be seen that there is a similar pattern to Tshane plot 1. Clearly, there is generally poor correspondence between the models and measurements. All models

overestimate reflectance by between 43.9% and 78.0% overall, with FLIGHT 1-D 1FC and FLIGHT 1-D mFC, again being the most and least accurate, respectively (Table 6.7). Again, none of the model estimates get close to the error of the ETM+ measurements. Four of the models have lowest accuracy in ETM3, with errors ranging from 68.1% to 101.9%, while two of the models - FLIGHT 1-D 1FC and PROSAIL, have lowest accuracy in ETM4, overestimating reflectance by 58.5% and 60.3% respectively (Table 6.7). All but one of the models (FLIGHT 1-D 1FC) display highest accuracy in ETM5, with errors ranging from 31.0% to 50.1%.

Differences between models at T2 are slightly more pronounced than at T1, but still no more than 20% across all wavebands (excluding FLIGHT 1-D mFC simulations). The pattern of differences between models is the same as at T1 however, with largest divergence between models being seen in the visible wavebands of ETM3 and ETM1, and smallest in ETM4 and ETM5 (Table 6.7). The TM models again provide the highest accuracy overall, with errors of 43.9% and 47.7% for the FLIGHT 1-D 1FC and PROSAIL models, respectively. Similarly, the two canopy layer modelling simulations, again produce comparable results to one another, and are still approximately 10% less accurate than the best performing turbid medium results.

At Tshabong plot 1 (TG1) there is very close agreement between all of the models and the measurements (Figure 6.6c). Models generally underestimate reflectance in the visible wavebands, and overestimate in the NIR and SWIR, with overall errors ranging from 9.3% to 14.3%, with PROGeoSAIL and FLIGHT 1-D mFC being most and least accurate, respectively (Table 6.7). Lowest accuracy is observed in ETM7 for all but one of the models, FLIGHT 1-D 1FC, with errors ranging from 12.6% to 31.9%. Highest accuracy is generally seen in ETM4 and ETM5, with only one model, FLIGHT 3-D, displaying highest accuracy in ETM3, overestimating reflectance by 2.5%.

Table 6.7 Relative error (%) for the ETM+ wavebands, together with the overall relative error (RRMSE) for all wavebands and each model (the All column). Negative sign indicates model underestimation. Model which provides the highest accuracy is emboldened.

Plot/Model ID	ETM 1	ETM 2	ETM 3	ETM 4	ETM 5	ETM 7	All
Tshane plot 1							
PROSAIL	89.4	90.4	90.6	76.7	50.5	76.5	80.3
PROGEOSAIL 2-LAYER	96.9	98.3	105.6	71.9	48.3	84.1	86.4
FLIGHT 1D mFC	134.8	128.7	142.7	76.0	66.3	115.6	114.5
FLIGHT 1D 1FC	**80.3**	**85.2**	**86.8**	**75.0**	**48.3**	**75.4**	**76.3**
FLIGHT 3D mFC 2-LAYER	110.6	107.8	120.1	72.9	56.0	98.6	97.0
FLIGHT 3D 1FC 2-LAYER	96.9	99.1	107.5	72.6	52.5	90.3	88.5
Tshane plot 2							
PROSAIL	37.1	47.0	53.1	60.3	33.9	49.7	47.7
PROGEOSAIL 2-LAYER	49.0	54.4	68.1	55.4	31.8	58.1	53.9
FLIGHT 1D mFC	75.3	80.6	101.9	60.0	50.1	88.8	78.0
FLIGHT 1D 1FC	**28.8**	**41.9**	**48.5**	**58.5**	**31.0**	**47.7**	**43.9**
FLIGHT 3D mFC 2-LAYER	54.3	62.3	81.1	55.2	39.3	72.1	62.2
FLIGHT 3D 1FC 2-LAYER	43.5	53.9	69.3	56.5	36.3	63.9	55.1
Tshabong plot 1							
PROSAIL	-15.3	-8.6	-5.3	3.0	3.0	16.6	10.2
PROGEOSAIL	**-6.8**	**-3.6**	**1.8**	**0.7**	**1.3**	**21.2**	**9.3**
FLIGHT 1D mFC	-2.5	3.0	10.9	1.6	8.1	31.9	14.3
FLIGHT 1D 1FC	-20.3	-11.7	-9.5	2.3	-0.5	12.6	11.6
FLIGHT 3D	-11.0	-3.6	2.5	2.6	4.2	24.0	11.1
Tshabong plot 2							
PROSAIL	1.9	15.4	33.8	27.0	29.1	57.8	32.4
PROGEOSAIL 2-LAYER	4.7	17.2	37.8	25.9	28.7	60.9	34.1
FLIGHT 1D mFC	12.1	24.3	49.1	25.0	34.4	72.7	41.3
FLIGHT 1D 1FC	**-1.9**	**13.0**	**31.1**	**25.9**	**27.8**	**56.9**	**31.1**
FLIGHT 3D mFC 2-LAYER	6.5	20.1	42.8	25.0	31.3	67.2	37.4
FLIGHT 3D 1FC 2-LAYER	0.9	15.4	36.0	24.7	28.9	61.3	33.5
Tshabong plot 3							
PROSAIL	-4.6	1.6	4.5	9.9	9.1	25.4	12.1
PROGEOSAIL	5.5	9.2	16.8	8.2	10.6	35.7	17.6
FLIGHT 1D mFC	8.3	13.0	21.6	7.9	15.4	42.1	21.5
FLIGHT 1D 1FC	**-11.0**	**-2.7**	**-0.4**	**8.7**	**6.3**	**21.5**	**10.9**
FLIGHT 3D	3.7	8.7	16.8	8.9	12.5	37.4	18.3

Note: see Table 6.3 for notes on the model ID.

Differences between models at TG1 are very small indeed, only in ETM1 and ETM7 is there any significant divergence, which is of the order of approximately 15%. Interestingly, in contrast to its performance at plots T1 and T2, the FLIGHT 1-D mFC representation shows very similar accuracy to the other models, though it is still least accurate overall. The hybrid model PROGeoSAIL is the most accurate

overall, but there is only around 2% difference between PROGeoSAIL accuracy and the two TM models (PROSAIL and FLIGHT 1-D 1FC).

Results of the model simulations for Tshabong plot 2 (TG2) are shown in Figure 6.6d, where it can be seen that there is moderate agreement between measurements and modelled estimates for all models. Overall, models overestimate reflectance by between 31.1% and 41.3%, with FLIGHT 1-D 1FC and FLIGHT 1-D mFC, being the most and least accurate, respectively (Table 6.7). All models display lowest accuracy in ETM7, with errors ranging from 56.9% to 72.7%. There is also significant error in ETM3. Highest accuracy is shown in ETM1 for all models, with errors ranging from an underestimate of 0.9% (FLIGHT 3-D 1FC 2-LAYER) to an overestimate of 12.1% (FLIGHT 1-D mFC). All the models are within the error of the measurements in ETM1. There is also good accuracy in ETM2 with errors not getting above 25%.

Differences between models are again small, generally of the order of 10% across all wavebands. The TM models are most accurate overall with less than 2% difference between FLIGHT 1-D 1FC and PROSAIL, the two-layer modelling approaches are a further 2% more inaccurate than the turbid mediums. Again, the FLIGHT 1-D mFC is the least accurate model though the difference is less than 10%.

The results from Tshabong plot 3 (TG3) are shown in Figure 6.6e, where it can be seen that the models are in close agreement with the measurements. Generally, the models overestimate reflectance, with overall errors ranging from 10.9% to 21.5%, FLIGHT 1-D 1FC and FLIGHT 1-D mFC being the most and least accurate, respectively (Table 6.7). Accuracy across wavebands is generally high, apart from in ETM7 where there is significantly more error than in other wavebands, ranging from 21.5% (FLIGHT 1-D 1FC) to 42.1% (FLIGHT 1-D mFC). Highest accuracy is achieved in the visible wavebands for all but one model, and most of the model estimates are within the errors of the measurements in these wavebands. PROGeoSAIL and FLIGHT 3-D show highest accuracy in ETM1, PROSAIL in ETM2, and FLIGHT 1-D 1FC in ETM3, while FLIGHT 1-D mFC shows highest accuracy in the NIR band of ETM4.

There are only small differences between models in the visible to NIR wavebands. Differences in the SWIR (ETM5 and ETM7) are greatest, but the maximum difference between any two models is not greater than 20%. In contrast to

TG1 where a hybrid model provided the most accurate results, at this shrubland plot, the TM models (excluding FLIGHT 1-D mFC) showed closer correspondence to the measurements than the hybrid models by between approximately 5% and 8%.

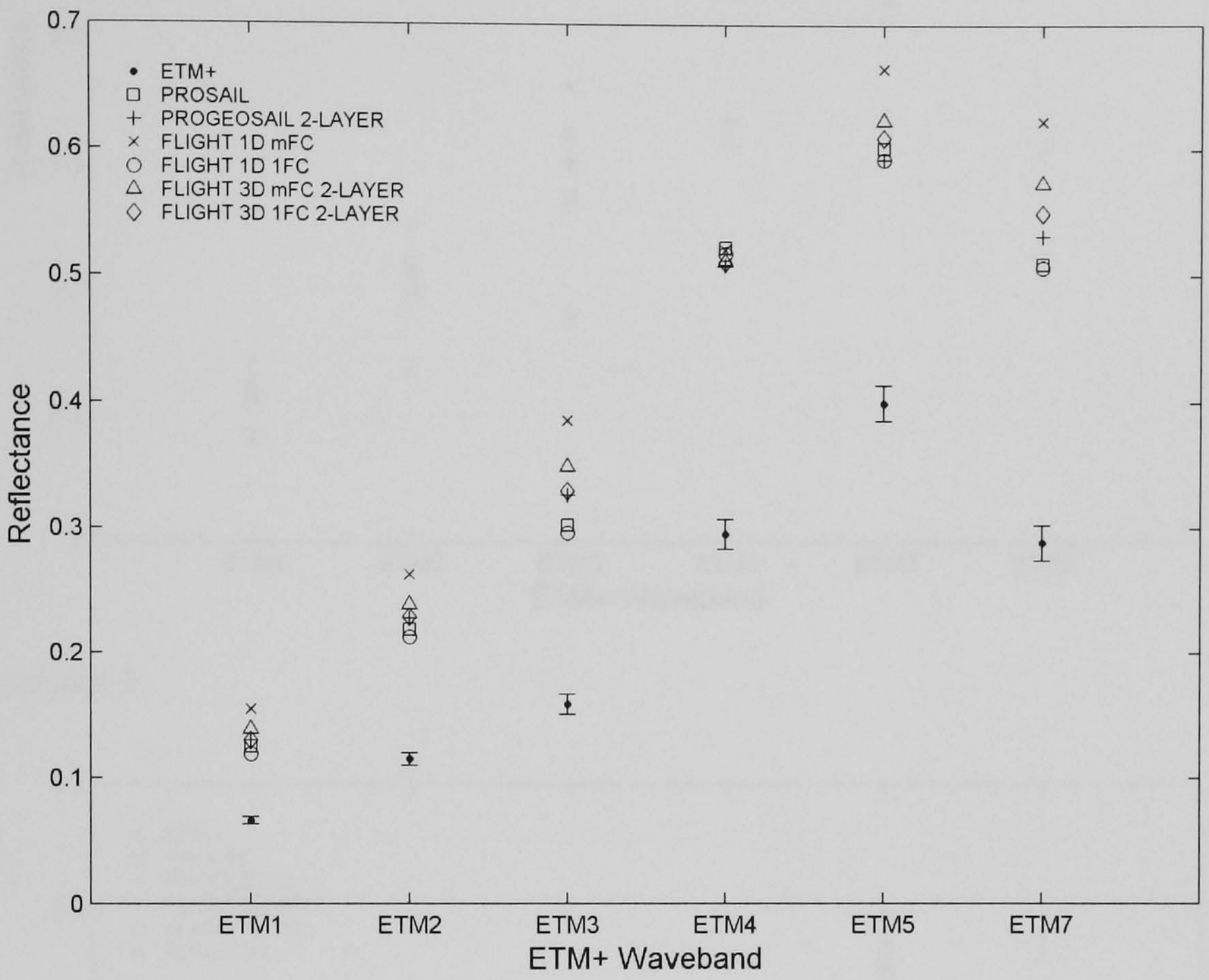

(a) Tshane plot 1

Figure 6.6 Relative performance of ETM+ model simulations for all models. Error bars on the ETM+ measurements represent the upper and lower 95% confidence limits.

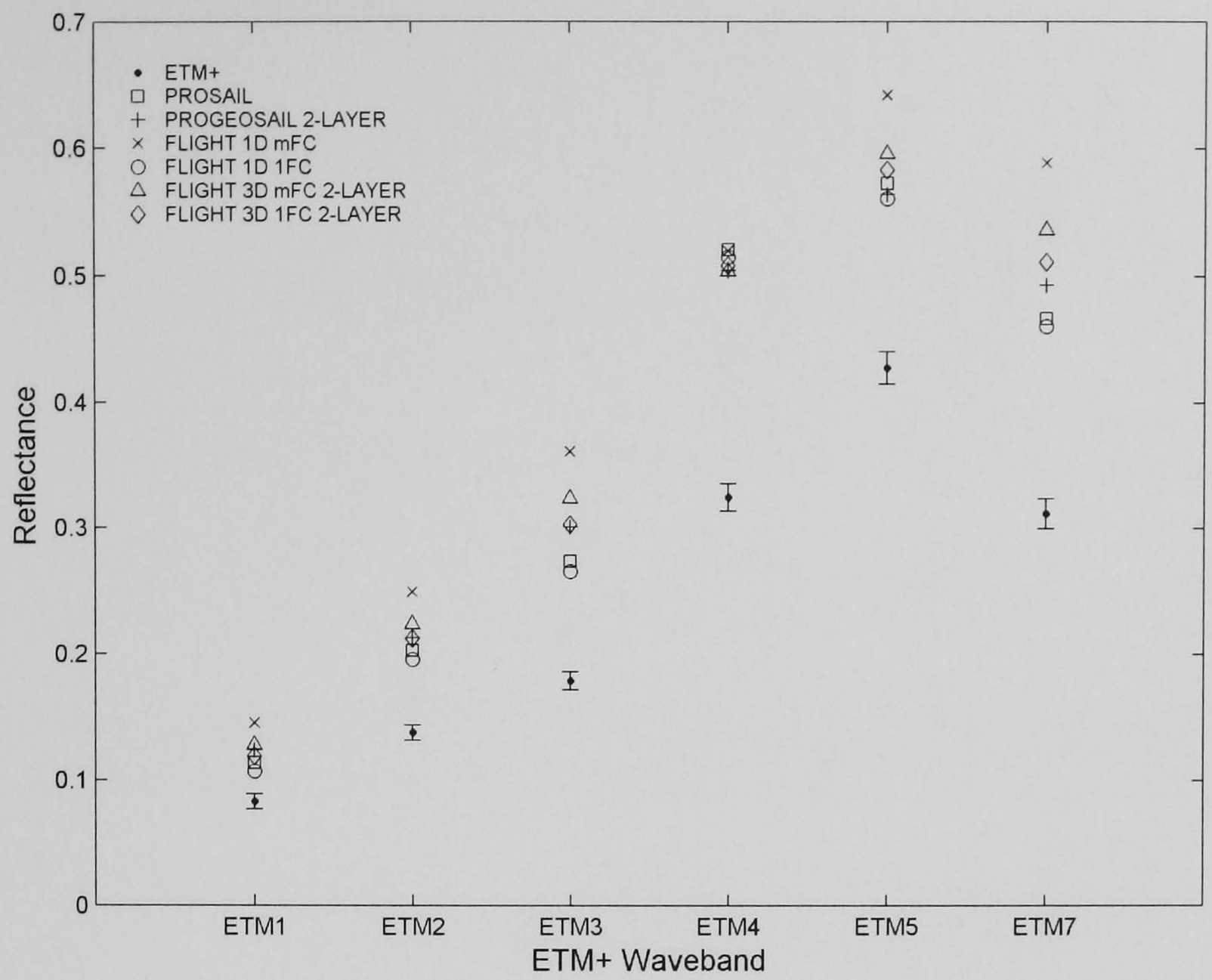

(b) Tshane plot 2

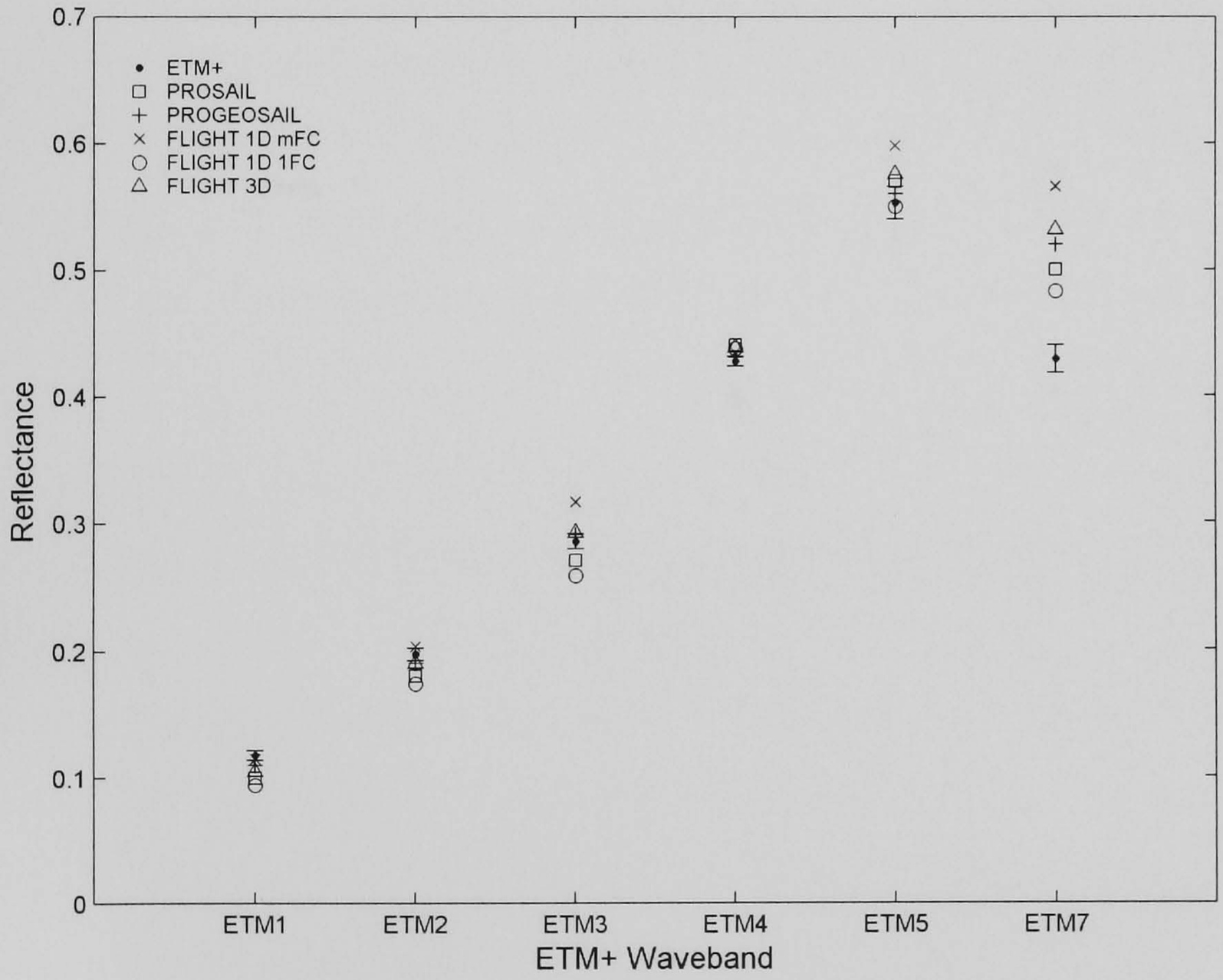

(c) Tshabong plot 1

Figure 6.6 Continued.

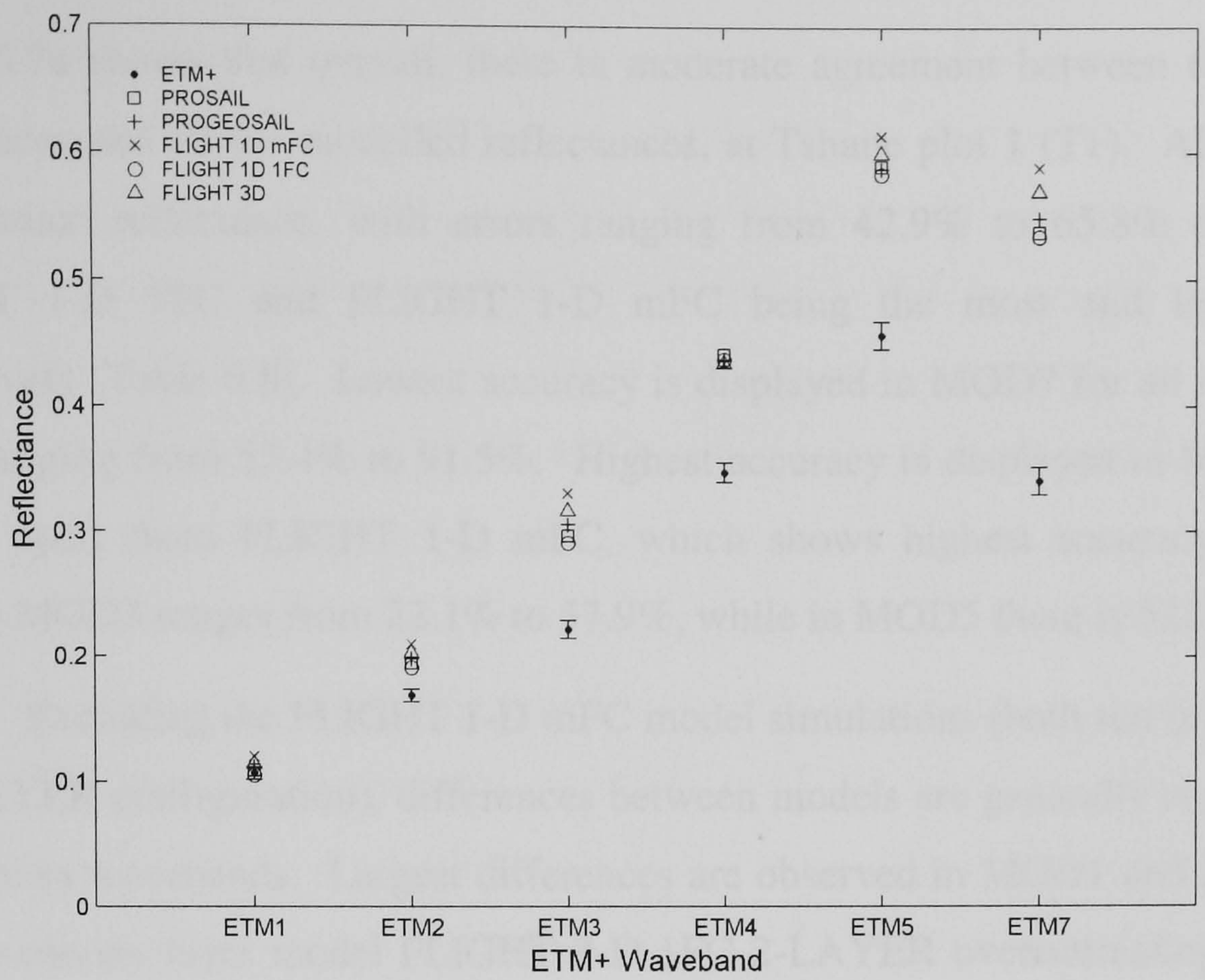

(d) Tshabong plot 2

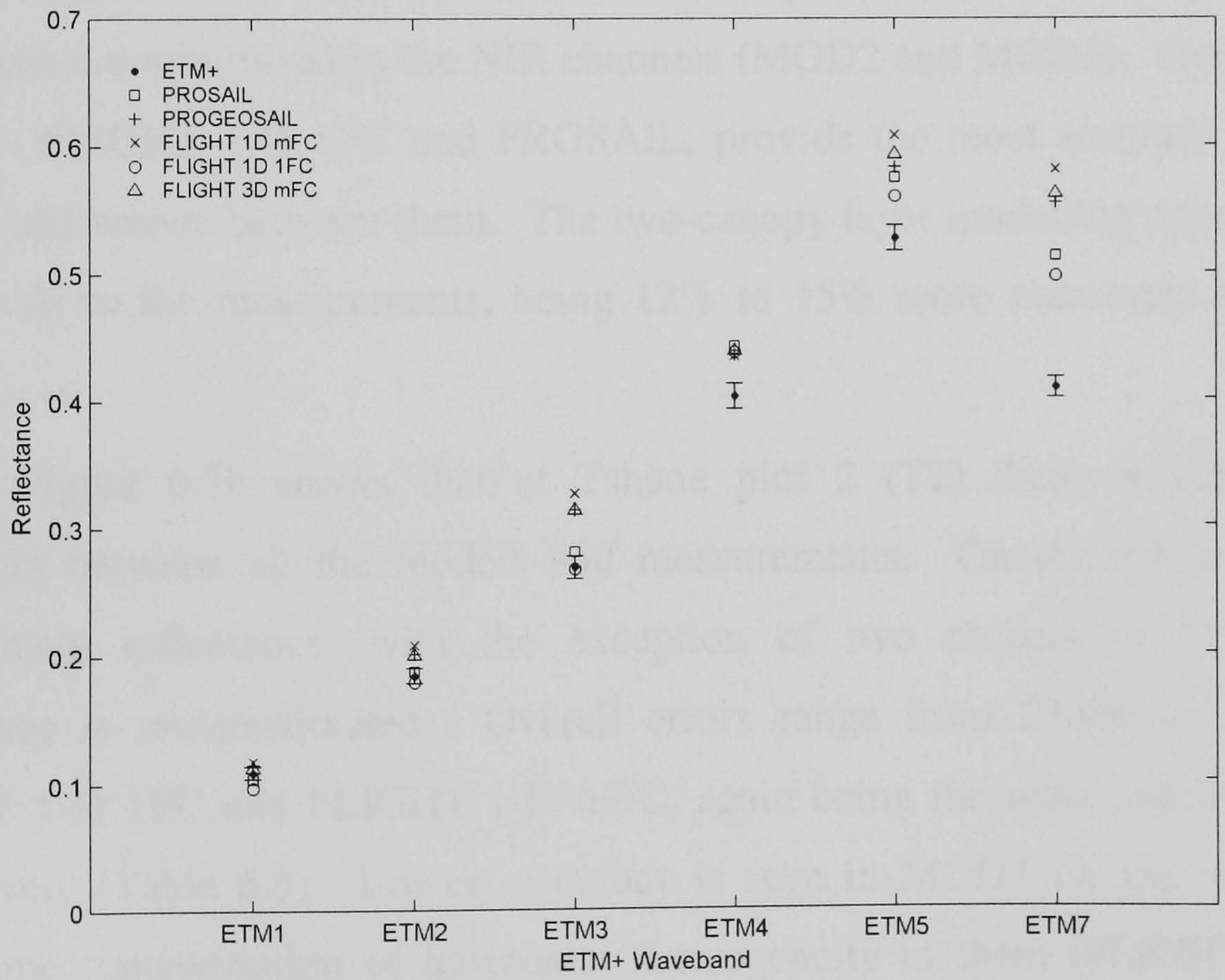

(e) Tshabong plot 3

Figure 6.6 Continued.

6.3.2 MODIS simulations

Figure 6.7a shows that overall, there is moderate agreement between the measured reflectances and all the modelled reflectances, at Tshane plot 1 (T1). All the models overestimate reflectance, with errors ranging from 42.9% to 65.8% overall, with FLIGHT 1-D 1FC and FLIGHT 1-D mFC being the most and least accurate respectively (Table 6.8). Lowest accuracy is displayed in MOD7 for all models, with errors ranging from 55.4% to 91.5%. Highest accuracy is displayed in MOD3 for all models apart from FLIGHT 1-D mFC, which shows highest accuracy in MOD5. Error in MOD3 ranges from 22.1% to 57.9%, while in MOD5 there is 52.2% error.

Excluding the FLIGHT 1-D mFC model simulations (both run on its own and in 2-LAYER configuration), differences between models are generally no greater than 20% across wavebands. Largest differences are observed in MOD1 and MOD7, with the two-canopy layer model FLIGHT 3-D 1FC 2-LAYER overestimating reflectance by 21% more than the TM models, in both cases. The FLIGHT 1-D mFC model produces much more inaccurate results than any of the other models, though the differences are minimised in the NIR channels (MOD2 and MOD5). Overall, the TM models - FLIGHT 1-D 1FC and PROSAIL, provide the most accurate results, with only 1% difference between them. The two-canopy layer modelling does not provide a closer fit to the measurements, being 12% to 15% more inaccurate than the TM models.

Figure 6.7b shows that at Tshane plot 2 (T2) there is generally close agreement between all the models and measurements. On the whole the models overestimate reflectance, with the exception of two models in MOD3, where reflectance is underestimated. Overall errors range from 23.6% to 53.8%, with FLIGHT 1-D 1FC and FLIGHT 1-D mFC, again being the most and least accurate, respectively (Table 6.8). Lowest accuracy is seen in MOD7 for the models which have some representation of horizontal heterogeneity in them (FLIGHT 1-D mFC, FLIGHT 3-D mFC 2-LAYER, and FLIGHT 3-D 1FC 2-LAYER), with errors ranging from 46.1% to 74.1%. PROSAIL and FLIGHT 1-D 1FC, on the other hand, display lowest accuracy in MOD2. Highest accuracy is again achieved in MOD 3 for all models, with errors ranging from an underestimate of 4.1% to an overestimate of 40.2%.

Differences between models show a similar pattern to that at Tshane plot 1, with error generally being no greater than 20% across wavebands, with the exception of the FLIGHT 1-D mFC simulations (both run on its own and in 2-LAYER configuration), and in MOD1 and MOD7. Differences in MOD1 are as great as 26% between FLIGHT 1-D 1FC and FLIGHT 3-D 1FC 2-LAYER. Again, the TM models FLIGHT 1-D 1FC and PROSAIL, provide the most accurate results overall, being approximately 9% to 14% more accurate than the two-canopy layer modelling.

Simulations performed at Mabuasehube plot 1 are compared to measurements in Figure 6.7c. It can be seen that there is moderate correspondence between all models and measurements, models overestimate reflectance in all wavebands. Overall errors range from 33.8% to 44.5%, with PROSAIL and FLIGHT 1-D mFC being the most and least accurate, respectively (Table 6.8). All models display lowest and highest accuracy in MOD7 and MOD6 respectively, with errors ranging from 44.3% to 59.4% in MOD7, and 24.2% to 32.8% in MOD6.

Differences between models are not particularly marked, with a maximum overall error of approximately 10%, though it should be pointed out that only TM models have been tested for this grassland site. What is interesting is the relative performance of FLIGHT 1-D mFC at this plot, in that it compares favourably with the other two models, in contrast to its performance at plots T1 and T2. However, this model does not reproduce the same pattern as the measurements with modelled reflectance increasing from MOD6 to MOD7, whereas the other two models show a reduction in reflectance consistent with the measurements (Figure 6.7c).

Table 6.8 Relative error (%) for the MODIS simulations, together with the overall relative error (RRMSE) for all wavebands and each model (the All column). Negative sign indicates model underestimation. Model which provides the highest accuracy is emboldened.

Plot/Model ID	MOD 1	MOD 2	MOD 3	MOD 4	MOD 5	MOD 6	MOD 7	All
Tshane plot 1								
PROSAIL	42.1	52.4	26.3	34.4	47.6	41.0	56.6	43.9
FLIGHT 1D mFC	79.4	54.5	57.9	59.2	52.2	55.5	91.5	65.8
FLIGHT 1D 1FC	**39.7**	**53.6**	**22.1**	**33.1**	**47.3**	**39.9**	**55.4**	**42.9**
FLIGHT 3D mFC 2-LAYER	66.8	54.5	44.2	49.0	50.6	49.8	81.0	57.8
FLIGHT 3D 1FC 2-LAYER	60.7	56.8	37.9	45.9	52.2	49.5	76.7	55.4
Tshane plot 2								
PROSAIL	17.5	39.5	-4.1	12.6	33.7	18.6	24.2	24.2
FLIGHT 1D mFC	74.0	44.4	40.2	46.5	43.5	40.6	74.1	53.8
FLIGHT 1D 1FC	**15.0**	**40.1**	**-8.2**	**10.7**	**32.6**	**16.8**	**23.3**	**23.6**
FLIGHT 3D mFC 2-LAYER	50.5	38.4	18.6	27.7	35.0	27.5	53.3	37.7
FLIGHT 3D 1FC 2-LAYER	41.0	39.5	10.3	22.6	35.0	25.1	46.1	33.5
Mabuasehube plot 1								
PROSAIL	**38.1**	**35.9**	**27.9**	**32.1**	**29.9**	**24.2**	**44.3**	**33.8**
FLIGHT 1D mFC	53.3	41.1	39.8	42.9	35.9	32.8	59.4	44.5
FLIGHT 1D 1FC	42.2	39.7	30.1	35.3	33.4	27.9	49.7	37.5
Mabuasehube plot 2								
PROSAIL	**101.8**	**88.9**	**60.3**	**78.1**	**69.9**	**54.4**	**83.8**	**78.3**
FLIGHT 1D mFC	123.0	93.3	75.3	92.1	75.4	63.5	101.8	91.1
FLIGHT 1D 1FC	108.5	94.5	63.0	83.3	75.1	59.9	91.6	83.8
Tshabong plot 1								
PROSAIL	**19.2**	**14.8**	**3.4**	**10.7**	**20.1**	**19.3**	**31.8**	**18.9**
FLIGHT 1D mFC	48.1	18.7	27.3	29.3	26.3	33.0	59.6	37.0
FLIGHT 1D 1FC	22.9	21.5	5.7	15.3	25.5	24.0	36.7	23.4
FLIGHT 3D	36.9	20.5	15.9	22.0	25.9	28.5	49.9	30.5
Tshabong plot 2								
PROSAIL	**55.9**	**35.9**	**20.0**	**30.7**	**41.6**	**42.8**	**69.5**	**44.9**
FLIGHT 1D mFC	78.3	38.7	35.3	43.8	46.3	52.8	91.2	58.6
FLIGHT 1D 1FC	60.3	42.4	22.4	35.8	47.5	48.7	76.2	50.2
FLIGHT 3D mFC 2-LAYER	72.3	40.2	30.6	40.9	46.5	51.1	86.3	55.6
FLIGHT 3D 1FC 2-LAYER	64.7	40.2	24.7	36.5	45.8	48.4	79.9	51.5
Tshabong plot 3								
PROSAIL	**35.9**	**21.7**	**20.3**	**24.8**	**27.9**	**30.5**	**51.8**	**32.0**
FLIGHT 1D mFC	63.6	20.9	43.0	40.9	29.7	40.4	77.8	48.6
FLIGHT 1D 1FC	36.9	25.2	18.9	26.3	30.8	33.0	54.9	34.0
FLIGHT 3D	62.6	26.6	40.5	40.1	33.9	42.2	78.7	49.3

Note: see Table 6.3 for notes on the model ID.

The results from Mabuasehube plot 2 (M2) are shown in Figure 6.7d, where it can be seen that the models are in poor agreement with the measurements. Results at this plot are the worst of all the MODIS simulations. All models overestimate reflectance in all wavebands and overall errors range from 78.3% to 91.1%, with

PROSAIL and FLIGHT 1-D mFC again being the most and least accurate, respectively (Table 6.8). Lowest accuracy is displayed in MOD1 for all models, with all errors greater than 100%. Highest accuracy is achieved in MOD6 for all models, though error is still significant ranging from 54.4% to 63.5%.

The pattern of differences between models is almost identical to that seen at M1, with the magnitude of differences being slightly higher overall. These differences are expressed most strongly in MOD1, where there is a maximum difference of approximately 22% between PROSAIL and FLIGHT 1-D mFC (Table 6.8).

Figure 6.7e shows the results of the model simulations from Tshabong plot 1 (TG1), where it can be seen that there is generally close agreement between all models and measurements. Results at this plot provide the closest fit to measurements of all the simulations. Models overestimate reflectance in all wavebands, with overall errors ranging from 18.9% to 37.0%, with PROSAIL again being the most accurate and FLIGHT 1-D mFC the least accurate (Table 6.8). Lowest accuracy is observed in MOD7 for all models, with errors ranging from 31.8% to 59.6%. Highest accuracy is shown in MOD3 by all but one of the models, with FLIGHT 1-D mFC achieving highest accuracy in MOD2, with an error of 18.7%.

Differences between models are generally no greater than 20% across wavebands, if the FLIGHT 1-D mFC simulations are excluded. If FLIGHT 1-D mFC simulations are included then differences increase significantly, to as much as 29% in MOD1. Overall, the largest differences between models are seen in bands MOD1 and MOD7. The TM models PROSAIL and FLIGHT 1-D 1FC have lowest overall errors, with the hybrid model having between approximately 7% to 12% more error.

Results from the Tshabong plot 2 (TG2) simulations are compared to measurements in Figure 6.7f. It can be seen that all the models overestimate reflectance in all wavebands, and that generally the models are in moderate agreement with the measurements, with overall errors of between 44.9% and 58.6% for the best (PROSAIL) and worst (FLIGHT 1-D mFC) performing models, respectively (Table 6.8). Lowest accuracies are again displayed in MOD7 for all models, differences ranging from 69.5% to 91.2%. Highest accuracy is displayed in MOD3 for all models, differences ranging from 20.0% to 35.3%.

Differences between models are generally no greater than 20% across wavebands, for all models. Overall, differences are not greater than approximately 14% between the best and worst performing models. In contrast to results obtained at T1, T2 and TG1, but consistent with the results obtained at M1 and M2, the FLIGHT 1-D mFC simulations are not significantly outperformed by the other models. The TM models PROSAIL and FLIGHT 1-D 1FC again provide the closest fit to the measurements, with the two-layer canopy modelling being between 5% and 10% more inaccurate.

Figure 6.7g shows the results of the simulations for Tshabong plot 3 (TG3). It can be seen that there is moderate correspondence between all the models and the measurements, with the models overestimating reflectance in all wavebands. Overall errors range from 32.0% to 49.3% for the best and worst models, PROSAIL and FLIGHT 3D, respectively (Table 6.8). Results here are consistent with those obtained at T1, T2, M1, TG1, and TG2, in that lowest accuracy is obtained in band MOD7, with errors ranging from 51.8% to 78.7%. Highest accuracy is observed in band MOD2, with errors ranging from 20.9% to 26.6%.

There are some interesting differences between models. For the first time, the FLIGHT 1-D mFC model simulations are not the most inaccurate, FLIGHT 3-D simulations are. However, the differences between models are generally not greater than 20%, with the exception of bands MOD1 and MOD7, and overall the maximum difference between models is approximately 17%. The TM models PROSAIL and FLIGHT 1-D 1FC, again provide the closest fit to the measurements, with only 2% difference between them.

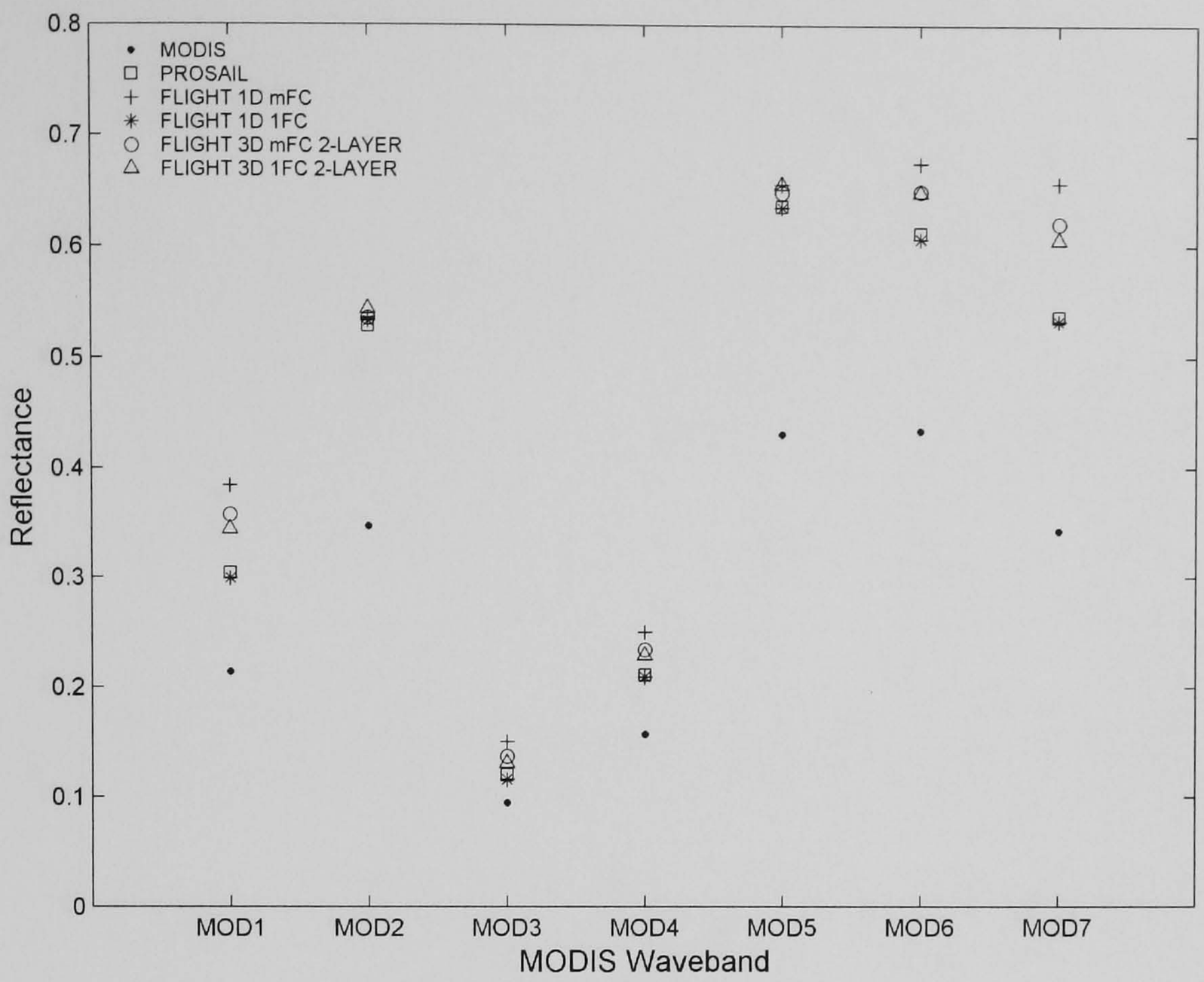

(a) Tshane plot 1

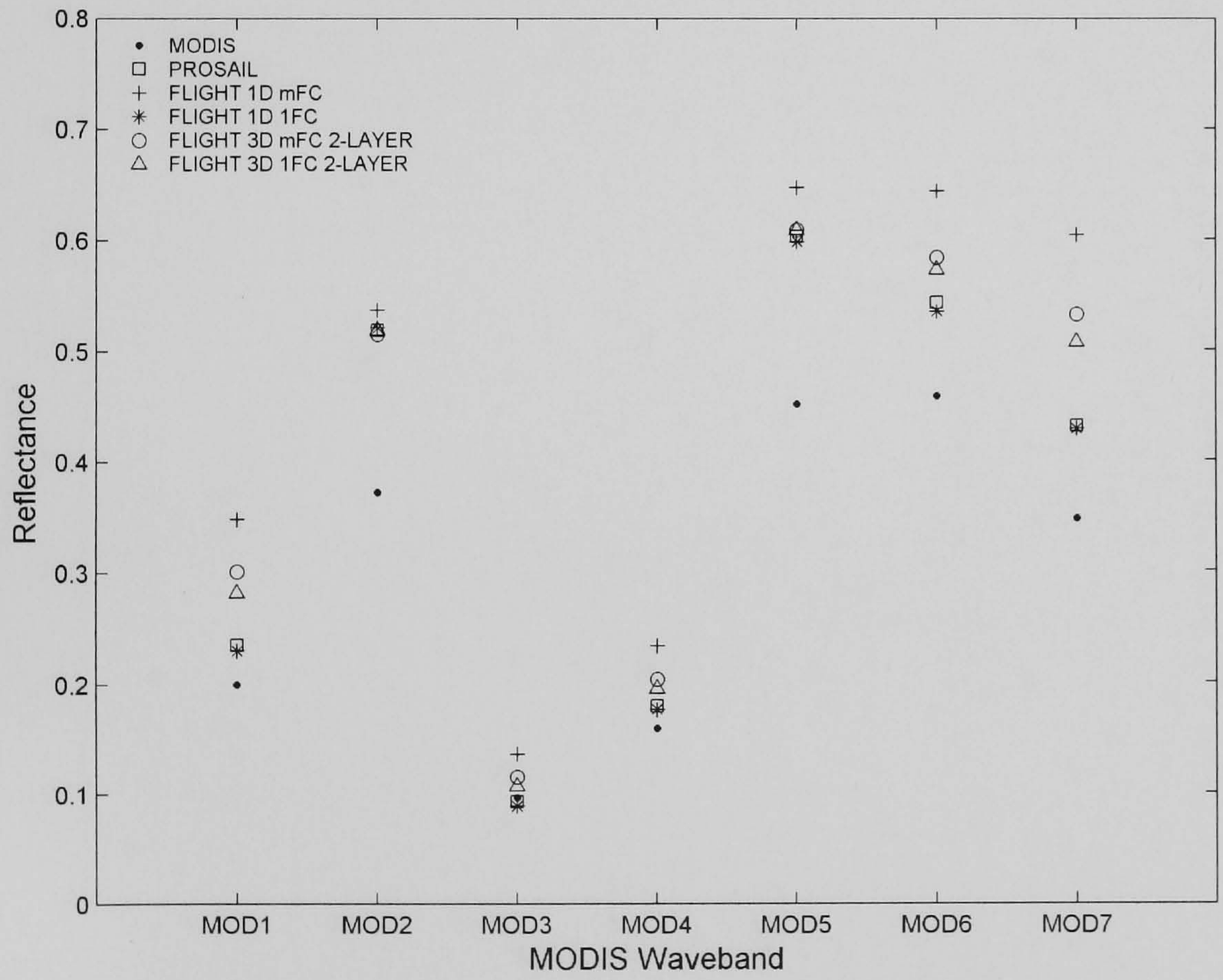

(b) Tshane plot 2

Figure 6.7 Relative performance of the MODIS simulations, for all models.

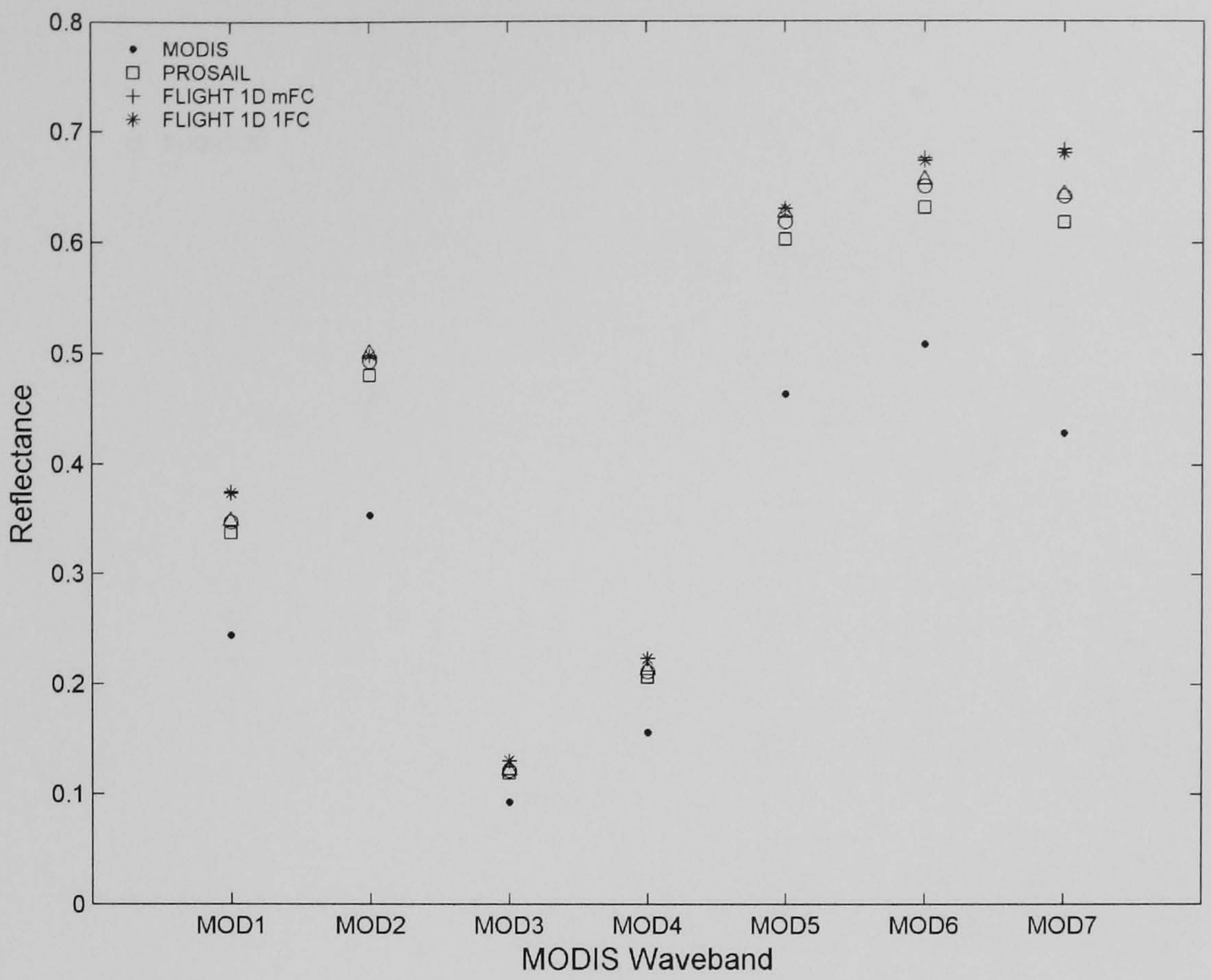

(c) Mabuasehube plot 1

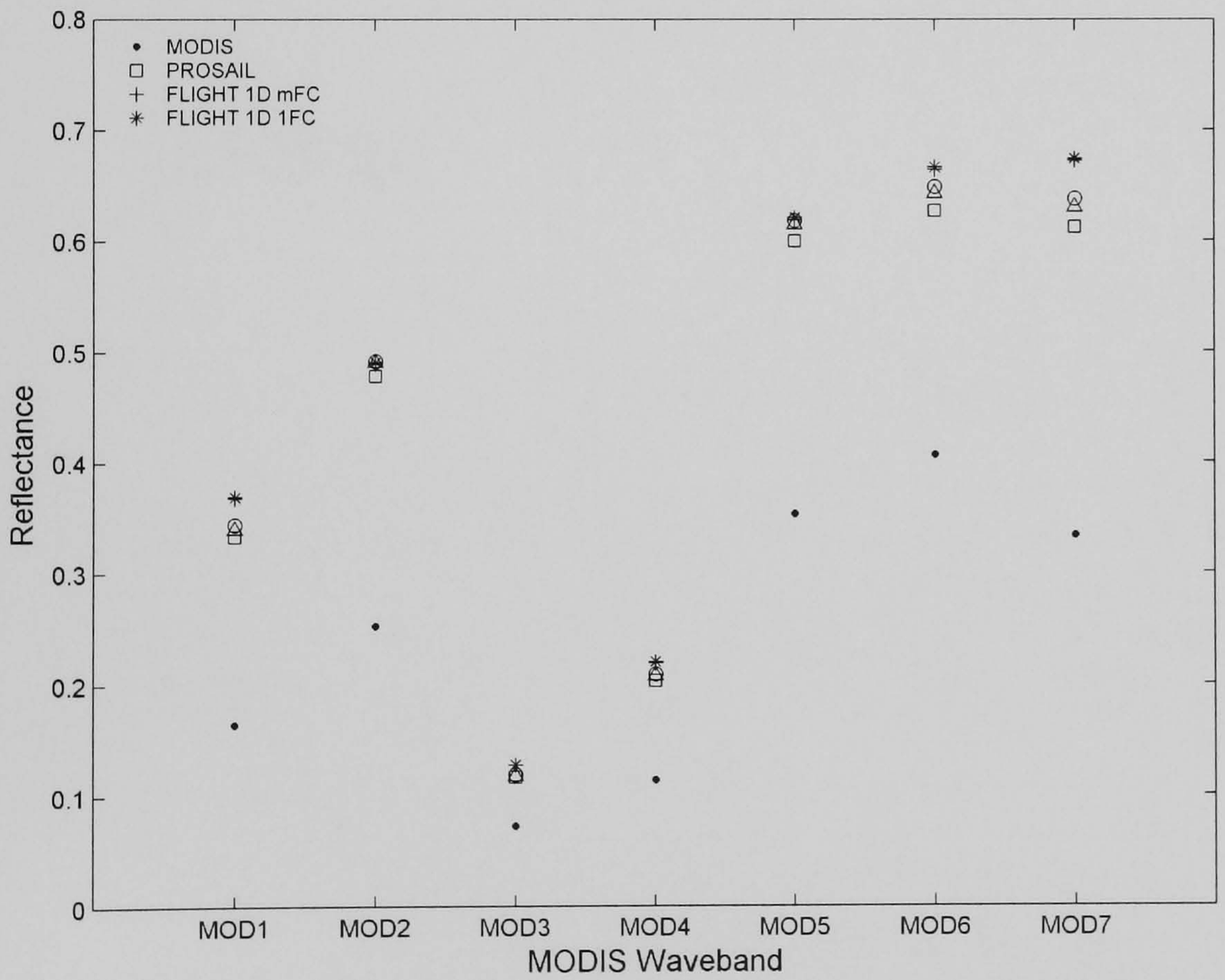

(d) Mabuasehube plot 2

Figure 6.7 Continued.

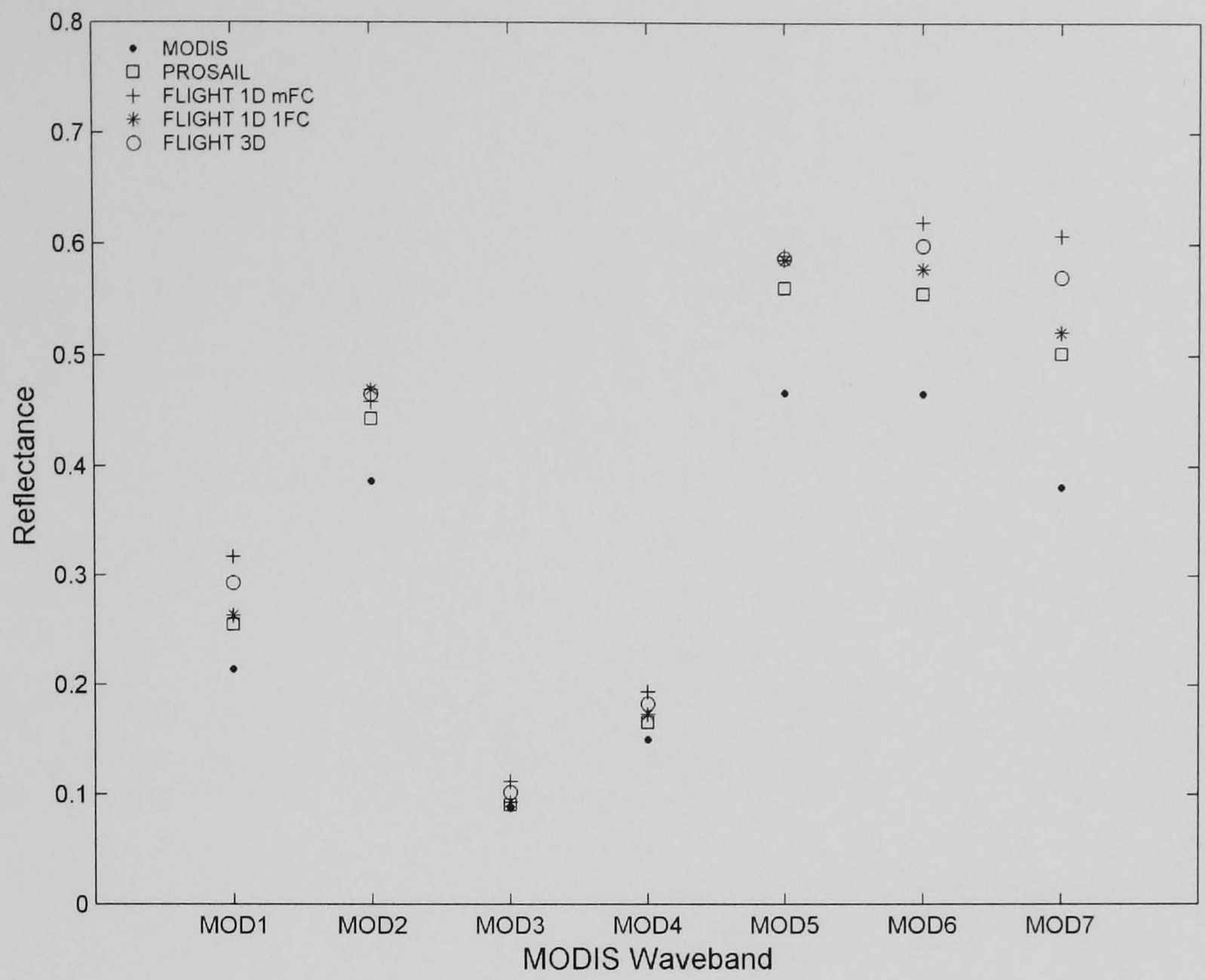

(e) Tshabong plot 1

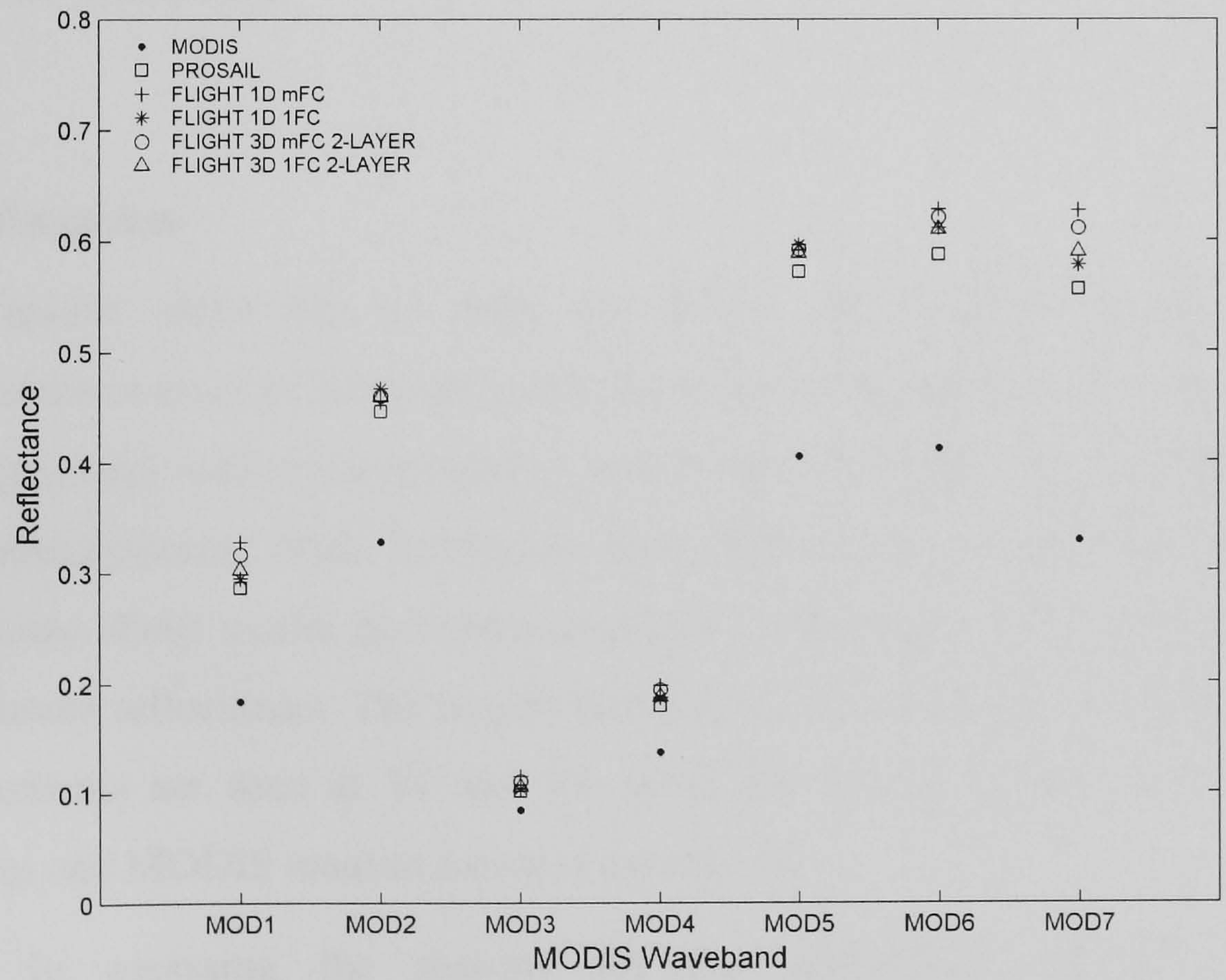

(f) Tshabong plot 2

Figure 6.7 Continued.

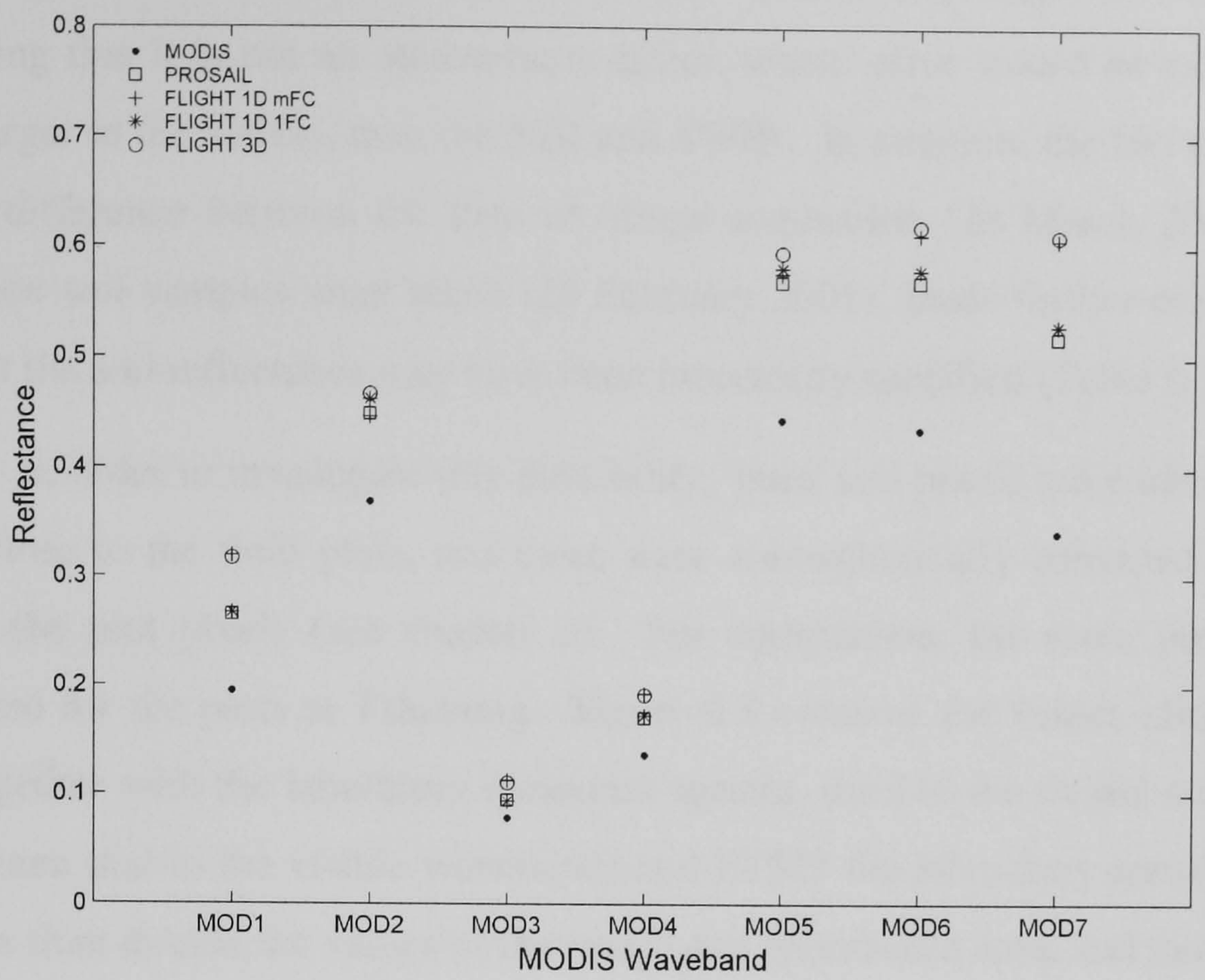

(g) Tshabong plot 3

Figure 6.7 Continued.

6.4 Discussion

These results show that in both the ETM+ and MODIS simulations, model performance is more or less evenly split between those which show very close to very poor agreement with measurements, and those which display moderate agreement with measurements. With having so few field plots it is difficult to draw firm conclusions about model performance overall. Generally, all the model simulations overestimate reflectance. The largest differences between model estimates and ETM+ measurements are seen at T1 and T2, while the largest difference between model estimates and MODIS measurements is seen at M2.

In assessing the reasons for the differences between models and measurements, it is clearly very difficult to separate the model uncertainties from the uncertainties associated with the measurements, i.e. are the measurements correct or are the models correct? Notwithstanding the measurement uncertainties which emanate from, among others, imperfect geometric correction, and atmospheric correction, it seems reasonable to suggest that the large differences observed at T1 and T2 for the ETM+ simulations, are a result of incorrect model input values for the soil

reflectance. This is because the errors are consistently high in all wavebands, suggesting that it is not an atmospheric effect, where error would be expected to be much larger in the visible, than the NIR and SWIR. In addition, the fact that there is a 28 day difference between the date of image acquisition (28 March 2001), and the date when soil samples were taken (28 February 2001), lends further credence to the idea that the soil reflectance may have been incorrectly specified (Table 6.5).

In order to investigate this possibility, 'pure' soil pixels were identified in the image close to the field plots, and these were atmospherically corrected in the same way as the plot pixels (see chapter 3). For comparison, the same procedure was performed for the plots at Tshabong. Figure 6.8 contains the values obtained in this way, together with the laboratory measured spectra, used in the model simulations. It can be seen that in the visible wavebands and ETM7 the laboratory measured spectra are more than double the values of the image soil reflectance data, and more than 50% higher in ETM4 and ETM5. In contrast, the image and laboratory measurements made at Tshabong are broadly in agreement. It seems likely therefore, that the uncertainty associated with the soil reflectance values, would, in large part, account for the divergence between models and measurements at T1 and T2. This idea would appear to be supported by the fact that the largest soil differences are observed in the visible wavebands and ETM7, and smallest in ETM4 and ETM5, which concurs with the error pattern seen in the model and measurement comparisons (Table 6.7).

It also seems likely that the large differences between the models and MODIS measurements at M2, is a result of incorrect values of soil reflectance, though this is more difficult to test or establish because of the difficulty in identifying a 'pure' soil pixel at 500m spatial resolution. It is not clear why the models perform considerably better for the MODIS than the ETM+ simulations at plots T1 and T2. However, it might be related to the coincidence of the image acquisition with field data such that the soil reflectance values are more accurate, or alternatively, as a result of different viewing and illumination geometries (Table 6.5), where soil effects play a less important role in determining canopy reflectance. This will be investigated through model sensitivity analyses in chapter 7. More generally, the results of the MODIS simulations may be in error as a result of the soil being modelled as a Lambertian surface, when it clearly is not. From the results of chapter 5, the following observations may be made with respect to this issue. If the soils were

modelled as non-Lambertian, then results at plots T1, M2, TG1, TG2, and TG3 would be more accurate (soil reflectance is overestimated by using a Lambertian soil), while at plot T2 accuracy would decrease (soil reflectance is underestimated by using a Lambertian soil), while at plot M1 there would be little change, owing to the fact that the VZA here (5.69 degrees backscatter, Table 6.6) is very close to nadir where the difference between Lambertian and non-Lambertian soils is minimal (see chapter 5).

Although the relative performance of the various models is comparable, there is one striking difference. That is, the performance of FLIGHT 1-D mFC with respect to all other models at plots T1 and T2, in the ETM+ simulations. This observation is most probably accounted for by the already noted soil effects. The FLIGHT 1-D mFC simulations provide a TM representation, together with information on the fractional cover which introduces horizontal heterogeneity into the simulations. This in effect, leads to a larger proportion of the soil background being 'seen', compared to the other TM models, leading to an increase in reflectance (in wavebands where the soil has higher reflectance than the vegetation); while the TM treatment means that there are minimal shadowing effects, which serve to reduce reflectance in the hybrid and two-layer canopy modelling. Consequently, the FLIGHT 1-D mFC reflectances are a lot higher than the other models. The fact that FLIGHT 1-D mFC generally provides similar performance to the other models at all other plots, reinforces the idea that there is an error in the soil reflectance values used for the ETM+ simulations at plots T1 and T2.

The lowest accuracy for all models is generally displayed in the SWIR2 for both the ETM+ and MODIS simulations (ETM7 and MOD7). It is not entirely clear why this should be so. However, it may be a result of running simulations with too little water in the leaves, which would result in the overestimation of reflectance observed. This is a possible limitation caused by parameterising PROSPECT with the average leaf water content contained in the LOPEX93 database. Not only is the SWIR2 the waveband region where errors are generally largest, but it is also where, together with the red wavebands (ETM3 and MOD1), the differences between models is largest at each plot. This is possibly due to the influence of the LAI in these waveband regions. Conversely, highest accuracy for the MODIS simulations is generally observed in the blue wavebands (MOD3). There is a less clear pattern for the ETM+ simulations, with the NIR (ETM4) and SWIR1 (ETM5) sometimes being

most accurate, while other times the visible wavebands provide the highest accuracy. With only five plots for the ETM+ comparisons, it is difficult to generalise. What is clear however, is that differences between models are generally minimised in the NIR channels for both ETM+ and MODIS simulations (ETM4 and MOD2 and MOD5), which probably reflects the dominance of the soil reflectance in these wavebands.

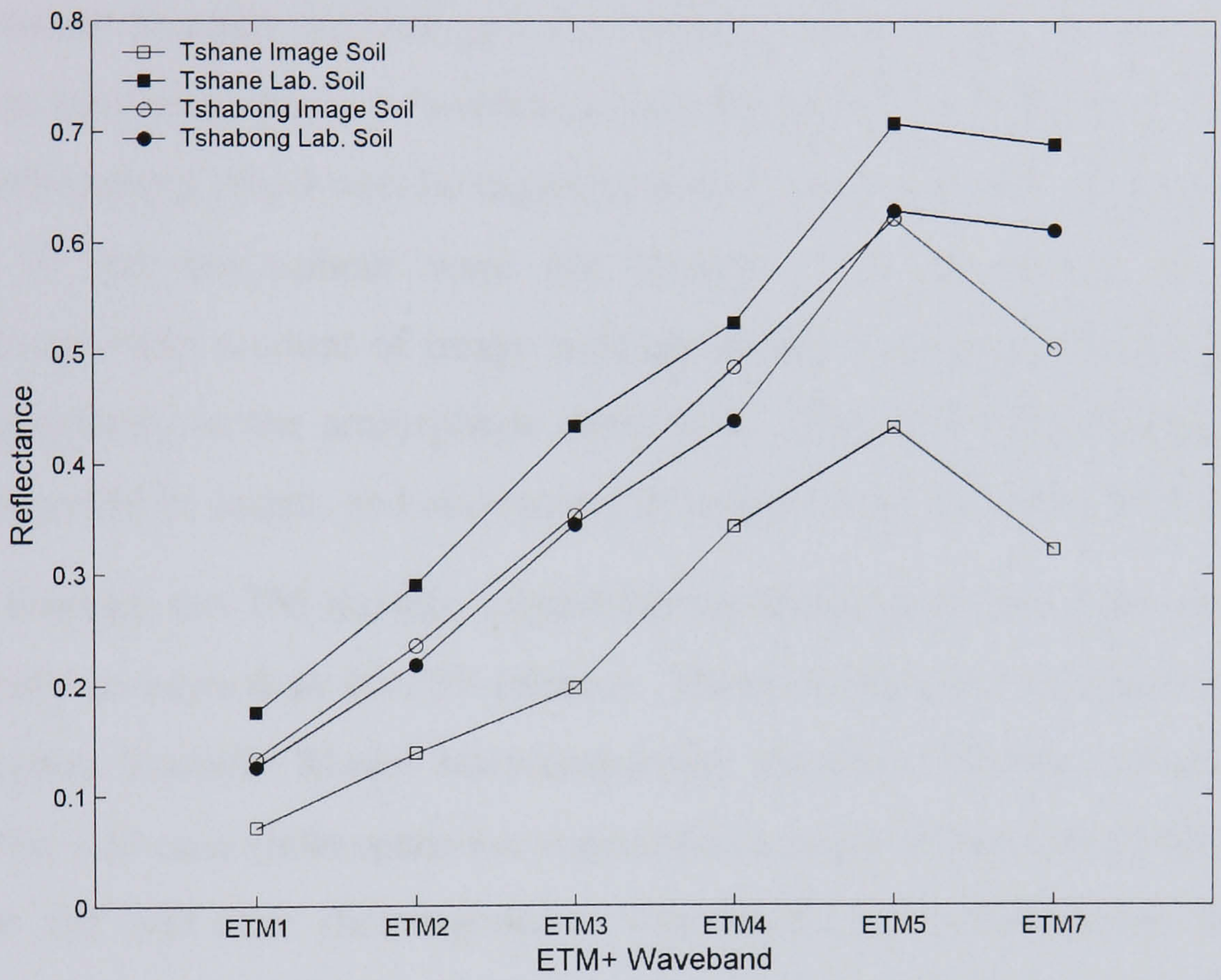

Figure 6.8 Comparison of laboratory and image obtained soil reflectance.

For both the ETM+ and MODIS simulations the TM models are seen to provide a closer fit to the measurements in all but one case, with a hybrid model providing a closer fit to the ETM+ measurements at TG1, a shrubland savanna plot, although the difference is less than 1%. The two-canopy layer modelling simulations performed at plots T1, T2, and TG2, do not provide a closer fit to the measurements. It would appear that in these low LAI canopies where the tree/shrub overstorey occupies around 10-20% of the ground cover then the effect of the canopy structure in introducing shadow into the scene is insufficient to demand explicit incorporation of two distinct canopy layers into the modelling, or indeed the use of a hybrid model, since a turbid medium can provide higher accuracy. The fact that there is little difference between the PROGeoSAIL and FLIGHT hybrid modelling would seem to

underline this view. Clearly, this conclusion applies to these results only. Under different conditions, for example a larger SZA, larger range of VZA, different time of year, greater fractional cover or LAI, a two-layer modelling approach may be required (Fuller *et al.* 1997). These conditions could be modelled relatively easily, and would serve as a useful addition to the question of which type of model is needed in order to represent canopy reflectance with sufficient accuracy (Pinty *et al.* 2004).

In the particular case of assessing model accuracy in the ETM+ simulations, it is important to point out that given a different atmospheric correction, the hybrid models or two-layer canopy modelling may be the most accurate. The measured ETM+ reflectances could well be higher or lower, since the exact gaseous and aerosol loadings of the atmosphere were not known. The error bars on the ETM+ measurements take account of image misregistration only. They do not take account of the uncertainty in the atmospheric correction. Had this been considered then the error bars would be larger, and assessment of model accuracy might well be different.

Overall, the TM models outperform the hybrid and two-layer representations by generally no more than 10-15% relative. These results provide a further addition to the Radiation Transfer Model Intercomparison exercise (RAMI), which has shown that for the 1-D case (homogeneous vegetation) a range of models perform similarly, while for the 3-D case (heterogeneous vegetation), large differences are observed between models, depending on the complexity of the scene (Pinty *et al.* 2001, 2004). The TM models generally estimate reflectance to be lower in all wavebands (apart from the NIR), than both the hybrid models or the two-canopy layer modelling. This would seem to indicate that the differences observed might be attributed to incorrect specification of fractional vegetation cover in the hybrid and two-layer simulations. Although, the TM models provide the closest fit to the measurements, the PROSAIL and FLIGHT 1-D 1FC deviate by an average of 2% and 3% in the ETM+ and MODIS simulations, respectively. FLIGHT 1-D 1FC provides a closer fit than PROSAIL in the ETM+ simulations, and vice versa in the MODIS simulations. Taking the ETM+ and MODIS simulations together, PROSAIL performs with 38% error, and FLIGHT 1-D 1FC with 39% error. Whether or not this is sufficient accuracy in order to provide accurate estimates of LAI on inversion, remains to be seen. North (2002), suggests that for model inversion to be successful, a model must approximate the measured signal to within 15%. Clearly, some of the plots here meet this criterion,

while others do not. The effect this has will be determined in the inversion work of chapter 8.

6.5 Summary and Conclusion

Canopy reflectance was simulated with three different models used in various formulations, designed to provide a robust test of the accuracy with which the models represent radiation emergent from savanna vegetation. Model simulations were parameterised with the mean values of the field recorded data, and evaluated against Landsat ETM+ and Terra-MODIS satellite data.

Results showed that overall, all the models were generally able to simulate reflectance with moderate accuracy at most sites, for both the ETM+ and MODIS measurements. Relative differences between the models were generally no greater than 10-15% overall. However, the TM models were consistently the most accurate in all but one case. The hybrid models and the two-layer canopy representations achieved no higher accuracy. Therefore, in terms of model realism or suitability, it would appear that in these optically thin canopies where overstorey canopy cover is 10-20%, the errors introduced by using a model which does not match the physical realism of the canopy as closely as another, would have little consequence on the accuracy with which reflectance is simulated.

The fact that differences between models are relatively small, and are minimised in the NIR, is most likely a reflection of the dominance of the soil, in determining canopy reflectance. The plots with the largest errors, T1 and T2 in the ETM+ simulations, is where there is the largest time difference between image acquisition and field data collection, such that there is most likely an error in the soil reflectance values used in model parameterisation. This also serves to highlight the difficulty in using satellite data to evaluate model performance when there is a considerable time difference between samples being taken and image acquisition. The simulations performed here and evaluated as they are with ETM+ and MODIS data, represents one of the few attempts to assess CRM performance with satellite sensor data.

In view of the results of this chapter, future model simulations and inversions will be performed with the PROSAIL model. PROSAIL was selected over the

FLIGHT 1-D because it performed to within 2% of the FLIGHT 1-D simulations for the ETM+ simulations, while it was the most accurate model overall in the MODIS simulations. Additionally, PROSAIL is more suited to inversion studies than FLIGHT 1-D because the solution to the radiative transfer equation is solved analytically rather than by Monte-Carlo methods, and as such is more computationally efficient.

This chapter has dealt with one area of model uncertainty, the pertinence of the model assumptions to the canopy which is being modelled, and consequent implications for accuracy. The next chapter of this thesis will quantify the sources of variability in reflectance, such that information on the effect of uncertainty in model parameterisation will be obtained. Thus, it will provide information which will help explain and account for some of the observations and assertions made in this chapter, as well as inform the design of the inversion work in chapter 8.

7 Quantifying Reflectance Sensitivity

7.1 Introduction

In order to estimate LAI through the inversion of a physically-based CR model, it is necessary to have confidence in the model, and to know which of the biophysical parameters the model responds to, and by how much. Results from chapter 6 have shown that the PROSAIL model is able to estimate canopy reflectance with moderate accuracy at most of the field plots, such that one may have confidence in the model. This chapter presents the results of a series of model sensitivity analyses (SAs), designed to quantify the sources of variability in reflectance. Three different SAs were performed, two of which addressed theoretical questions, while the final experiment was designed to aid and inform the design of inversion schemes to estimate LAI over the field plots in this thesis.

7.2 Sensitivity analysis background and objectives

Estimating biophysical parameters via CR model inversion will be most successful for those parameters to which the model is most sensitive (Goel and Strebel 1983, Verstraete *et al.* 1996). If a given parameter does not influence reflectance variability significantly, then the search for the minimum distance between modelled and measured reflectance (in the case of numerical or LUT inversions), or the underlying, but unknown empirical relationship between reflectance and the biophysical parameter (in the case of ANN inversion), will be a considerable challenge.

To determine which parameters a model is most sensitive to, sensitivity analysis may be performed. Saltelli (2000), defines sensitivity analysis as:

"*...the study of how the variation in the output of a model (numerical or otherwise) can be apportioned, qualitatively or quantitatively, to different sources of variation* [in the model input parameters], *and of how the given model depends upon the information fed into it.*"

A SA therefore provides information on how a model output changes in response to changes in the input parameters. The results of a sensitivity analysis can be used in many ways, for example:

(i) To identify which of the input parameters drive most of the variation in the model output, and conversely, those that account for least variation in the model output, which may allow them to be fixed or ignored in the inversion (e.g. Braswell *et al.* 1996)

(ii) To identify a subset of the most influential model parameters. Doing so may permit the use of a simpler model (Oreskes *et al.* 1994)

(iii) To understand how the model parameters interact with one another

(iv) To determine if there is a region in the parameter space of the input parameters where model output variation is maximal

(v) To identify wavelength regions or viewing configurations which contain the greatest information content for a particular model parameter (e.g. Privette *et al.* 1996, Bacour *et al.* 2002).

Clearly, model SA provides a means of obtaining information about the physical system under study, such that the complexity of the inversion process can be considerably reduced. The method used to test and measure the sensitivity of the model output will affect the outcome of the sensitivity analysis in terms of understanding what drives model output variation, and by how much.

Two different approaches to SA have been implemented in the terrestrial remote sensing literature, local and global SA. Traditionally, the local SA has been the method of choice. Local SA concentrates on the local impact of the factors on the model. The model parameters are allowed to vary within a small range about a mean value, and the range of the variation is usually the same for each of the model parameters, typically ± 10% (Privette *et al.* 1994, Asner *et al.* 2000). A basecase is defined where a simulation is run with all parameters set to their mean value, then each parameter in turn is perturbed by ±10% of its range, keeping all other model parameters fixed at their mean value. The sum of squared difference between the basecase and each perturbation is then calculated for each parameter. The sum of the squared difference is then used as a measure of the relative importance of each parameter in driving variation in reflectance (e.g. Bicheron and Leroy 1999).

Alternatively, the sum of squared difference may be submitted to a principal components analysis (PCA), where the scores on the first component are used as a measure of each parameter's influence in driving variation in reflectance (Schluessel *et al.* 1994, Privette *et al.* 1994, Asner 1998a, Asner *et al.* 2000). A local SA provides information on how variation in each parameter produces variation in the model output, known here as the first-order effects.

More recently, global SA methods have been used to conduct sensitivity analyses in remote sensing (Ceccato *et al.* 2001, 2002, Bacour *et al.* 2002, Bowyer & Danson 2004). A global SA differs significantly from the local SA method. First, in a global SA the full range of a parameter's variability is exhaustively searched, rather than just a local area around a mean value. Second, a probability density function (PDF) is specified for each of the model parameters, such that information is supplied on the shape of the variation. Third, the model parameters are varied simultaneously in model runs, rather than varying one parameter at a time. In doing so, the results of a global SA provide information on the interactions of the model parameters in driving model output variance. This is the key difference between the global and local approaches.

Clearly, a local SA will provide information on factors i, ii, iv and v listed above, whereas a global SA will provide information on all of the factors. The global SA may therefore be seen as an information rich approach, from which more information is obtained about the system under study. A global SA provides

information on how variation in the model output is produced by variations in the model input parameters individually - the 'first-order effects', and, collectively, through their interactions with the other model parameters, known as the 'total-order effects'.

Whichever SA method is used - local or global, the aim is to obtain a hierarchy of the most important parameters in explaining model output variance. There were three different sensitivity analysis experiments carried out in this chapter:

(i) **Local and global SA comparison**.

Objective: to determine and quantify the importance of interaction effects between canopy reflectance model parameters, and how the two approaches estimate the relative importance of the model parameters.

Rationale: a local SA varies model parameters sequentially such that no information is obtained on the likely interaction effects between them. This has serious implications for designing model inversion schemes. Although a parameter may not influence reflectance variability on its own (first-order effect), when varied in unison with another may explain a lot of the variance in reflectance (total-order effect). A local SA does not provide this information, a global SA does.

(ii) **Leaf level SA to investigate the effect of the PDF specified for model input parameters**.

Objective: to determine the likely impact of mis-specifiying the PDF for a given parameter in a canopy reflectance model.

Rationale: to perform a global SA a PDF must be specified for the model parameters. Where there is no measured data and therefore no information on the PDF, what is the effect of mis-specifiying the PDF?

(iii) Field plot specific SA for the ETM+ and MODIS data

Objective: to determine the sensitivity of reflectance to variation in LAI at each of the field plots, in order to identify the prospects for estimating LAI through CR model inversion.

Rationale: it is well known that the sensitivity of canopy reflectance model parameters will depend on the viewing and illumination geometries (Privette *et al.* 1996a, Bacour *et al.* 2001). Given that both ETM+ and MODIS data are used, and that the field plots are not located on the same ETM+ image, there is a large range of viewing and illumination geometries. Therefore, SAs were performed for each set of viewing and illumination geometries, and one where the full range of variability in all model parameters at all plots was considered.

7.3 Experimental method

7.3.1 Local sensitivity analysis

The local sensitivity analyses were performed as follows. For a given model SA, 1000 random draws were made for each parameter according to its specified range and distribution. These were used to simulate the basecase canopy reflectance. For each basecase simulation, each parameter in turn was perturbed by ± 10% of its range, and a new simulation was generated. A database was thus created with 1000 basecase simulations plus 1000*7*2 perturbed parameters producing a database with 15,000 simulations (for all the local SA there were seven perturbed parameters, see section 7.3.3.1). The sum of squared difference between each basecase simulation and each perturbed simulation was used as a measure of the relative importance of each parameter at each wavelength, in explaining reflectance variability (equation 7.1).

$$\text{Relative Impact } \lambda_i = \frac{\sum_{j=1}^{2000}(R_{base} - R_{pert})^2}{\sum_{j...k}^{14000}(R_{base} - R_{pert})^2} * 100 \qquad (7.1)$$

Where R_{base} and R_{pert} are the basecase reflectance and perturbed reflectance spectra, respectively.

7.3.2 Global EFAST sensitivity analysis

The global SA were performed with the extended Fourier amplitude sensitivity test (EFAST) (Saltelli *et al.* 1999), an extension of the classical Fourier Amplitude Sensitivity Test (FAST) (Cukier *et al.* 1973, 1978) and first applied to remotely sensed data by Ceccato *et al.* (2001, 2002).

EFAST uses Fourier analysis to decompose the model output variance into partial variances of increasing dimensionality. Because the total number of terms in a variance decomposition is 2^n -1, where n is the number of model parameters, EFAST does not provide a complete breakdown of the system. To do so is currently too computationally demanding, even with moderate values of n. EFAST is however, currently the most computationally efficient of the variance based methods (Chan *et al.* 2000).

EFAST therefore allows calculation of the effect of each model parameter in accounting for model output variance (here, reflectance variability), termed the 'first-order sensitivity index'; and the overall effect of a parameter in accounting for output variance, termed the 'total-order sensitivity index'. The first-order index represents the percentage of the output variance which is accounted for by variation in one model parameter X_i, whereas the total-order index represents the percentage of the output variance which is accounted for by variation in X_i together with the interaction of parameter X_i with all the other model parameters.

The EFAST method proceeds by defining a search curve which scans the entire parameter space of the model inputs converting a multi-dimensional integral to a one-dimensional integral. In generating samples of the model parameters EFAST searches each axis of the parameter space at a different frequency. These samples are then submitted to the model, where each parameter varies between simulations. Fourier decomposition is then used to obtain the fractional contribution of the model parameters to the model output variance. Figure 7.1 provides a schematic overview of the procedure followed for performing a SA with EFAST.

The first- and total-order indices are derived by exploring different frequencies from the Fourier analysis. If a parameter X_i has a strong influence on the output, the oscillations of the output at a given frequency ω_i will be of high magnitude. This is the basis for computing the sensitivity. The portion of the output variance arising from uncertainty in X_i is obtained by calculating the sum of squares of the Fourier coefficients at the fundamental and all harmonics of ω_i. Frequencies which are not used in the first-order sensitivity calculation are used to calculate the total-order sensitivity.

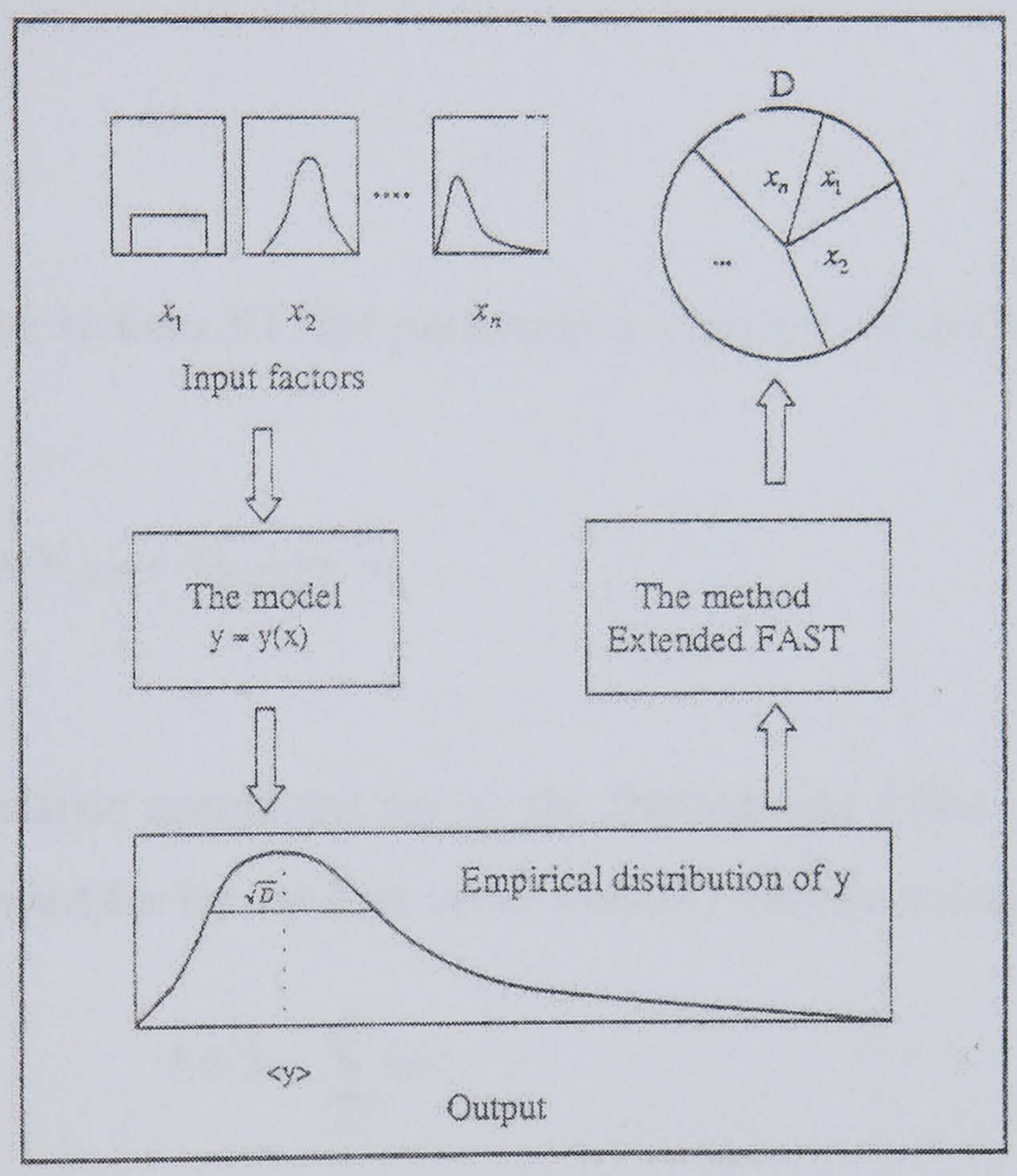

Figure 7.1 Schematic overview of the EFAST sensitivity process (*Source*: Saltelli *et al*. 1999).

A worked example of how EFAST calculates the first- and total-order indices follows. Considering a model with three input parameters, the total variance V of the model output is calculated via:

$$V = V_{x1} + V_{x2} + V_{x3} + V_{x12} + V_{x13} + V_{x23} + V_{x123} \quad (7.2)$$

where V_{x1}, V_{x2}, and V_{x3} are the variances of model parameters 1, 2, and 3 respectively, V_{x12} is the variance of interactions between model parameters 1 and 2, V_{x13} is the variance of interactions between model parameters 1 and 3, V_{x23} is the variance of interactions between model parameters 2 and 3, and V_{x123} is the variance of interactions between parameters 1, 2, and 3. The first-order sensitivity index S_{x1}, for parameter x_1 is then obtained from:

$$S_{x1} = V_{x1} / V \quad (7.3)$$

While the total-order indices ST, for parameter x_1 may be calculated as:

$$ST = (V_{x1} + V_{x12} + V_{x13} + V_{x123}) / V \quad (7.4)$$

The percentage variance accounted for by the interactions I (the percentage of output variance not accounted for by the first-order indices) may be calculated from:

$$I = 1 - \sum_{i=1}^{3} Sxi \quad (7.5)$$

In this research 5000 model simulations were performed with the EFAST SA, in order to provide robust estimation of the first- and total-order indices (Saltelli *et al.* 1999).

7.3.3 Model sensitivity analyses

7.3.3.1 Local versus global EFAST sensitivity analyses

To assess the importance of interaction effects between model parameters, two different experiments were defined. First, in order to provide a robust test of the

comparative performance of the local and global EFAST SA, model parameter ranges were set to encompass a large range of variability, as would be expected to be found in different vegetation types throughout the world, and are given in Table 7.1, together with information on the PDF. This experiment is referred to as the 'LG entire world' model SA. The second experiment was designed to determine the importance of interaction effects in some of the field plots used in this thesis, and the model parameter ranges and PDF are given in Table 7.2. The ranges represent the measurements made at the shrubland plots at Tshabong plot 1 and Tshabong plot 3. Soil reflectance is the hemispherical reflectance measured in chapter 5, for these two plots, and the range is shown in Figure 7.2. This experiment is referred to as the 'LG Botswana' model SA.

All model simulations were performed with the PROGeoSAIL model rather than PROSAIL, to provide a more robust test of the differences between the local and global approaches, since the interaction effects are likely to be more significant as model complexity increases.

Table 7.1 Range of variation and PDF for the LG entire world model SA.

Parameter	Range	Probability density function
Leaf structure parameter (N)	1 - 6.65	Uniform
Leaf chlorophyll content (C_{a+b})	1 - 75	Uniform
Leaf water content (EWT)	0.0001 - 0.085	Uniform
Leaf dry matter content (DMC)	0.0014 - 0.05	Uniform
Leaf area index (LAI)	0.001 - 6.0	Uniform
Vegetation cover (Fcov)	1 - 100	Uniform
Solar zenith angle (SZA)	17 - 70	Uniform

Table 7.2 Range of variation and PDF for the LG Botswana model SA.

Parameter	Range	Probability density function
Leaf structure parameter (N)	1.5 - 3.0	Uniform
Leaf chlorophyll content (C_{a+b})	20 - 60	Uniform
Leaf water content (EWT)	0.0001 - 0.015	Uniform
Leaf dry matter content (DMC)	0.005 - 0.01	Uniform
Leaf area index (LAI)	0.03 - 0.90	Gaussian
Vegetation cover (Fcov)	0.1 - 0.35	Gaussian
Soil reflectance (ρ_{soil})	Figure 7.2	Uniform

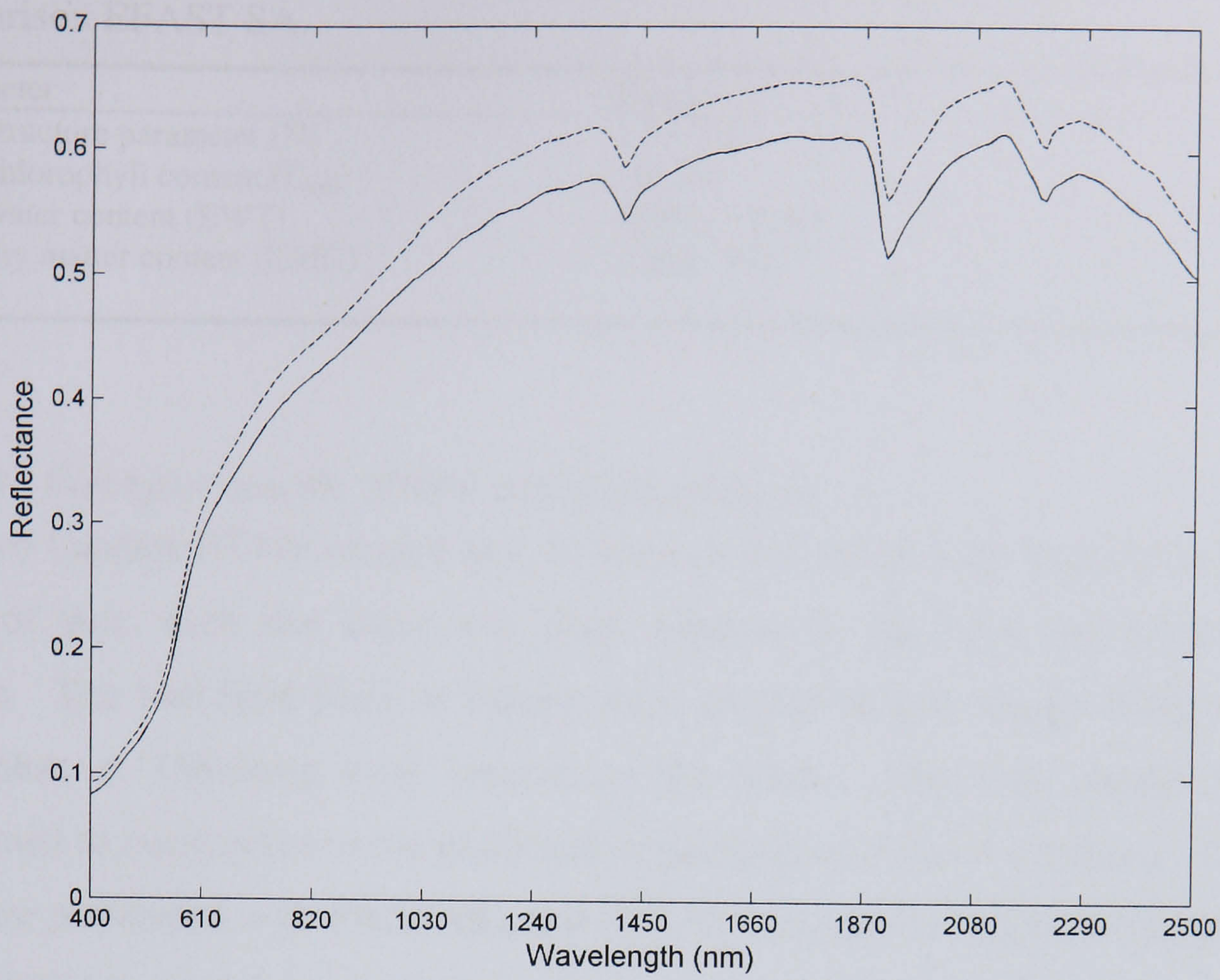

Figure 7.2 Minimum and maximum soil reflectance used in the 'LG Botswana' model SA.

7.3.3.2 Gaussian versus uniform PDF sensitivity analyses

In order to investigate the effect that the PDF specified for a given model parameter has on reflectance sensitivity, a model SA was carried out at the leaf level, with the PROSPECT model. The investigation was performed at the leaf level since there was no measured leaf reflectance and transmittance data available for use in this thesis.

A leaf model had to be used to generate leaf reflectance and transmittance data. Consequently, it was important to determine what effect mis-specification of the PDF might have on reflectance sensitivity, and the implication this would have for selection of a PDF for subsequent work in this chapter (the field plot specific SA), and also in chapter 8, where modelled reflectance will be used to generate training and testing data for the ANN.

Model ranges used in these simulations are presented in Table 7.3 and were determined based on the literature. EFAST was used to calculate the sensitivity.

Table 7.3 Range of variation for the PROSPECT model parameters for the PDF comparison EFAST SA.

Parameter	Range
Leaf structure parameter (N)	1.5 - 3.0
Leaf chlorophyll content (C_{a+b})	20 - 60
Leaf water content (EWT)	0.0001 - 0.015
Leaf dry matter content (DMC)	0.005 - 0.01

7.3.3.3 Field plot specific ETM+ sensitivity analyses

The two Landsat ETM+ images that are used in this thesis were acquired at different times of year, such that there was large variation in the SZA and SAA between images. The two field plots at Tshane were located on one image, while the three field plots at Tshabong were located on the other. Therefore, model SA were performed to correspond to the illumination geometries of the two images. All model SA were performed with PROSAIL, and EFAST was used to calculate the sensitivity. The PROSAIL model was used since this model provided the highest accuracy results in chapter 6, and is the most suitable for inversion work.

As was noted in chapter 6, part of the explanation for the large differences between modelled and measured reflectances at the two Tshane plots, might lie in inaccurate soil reflectance values. Consequently, two different SA were performed for the Tshane field plots. First, the range of the soil reflectance was set to that measured in the laboratory (as was used in the forward simulations of chapter 6). Second, the range of the soil reflectance was defined to be much greater. The minimum being that obtained from the image soil reflectance (in chapter 6), and the maximum from the laboratory measured soil. This SA would test how sensitive LAI was when there was a more variable background. The two experiments are referred to as 'Tshane LAB SOIL', and 'Tshane IMAGE SOIL', respectively. The range and PDF for the PROSAIL parameters submitted to the SA are given in Table 7.4, while Table 7.5 gives the minimum and maximum soil reflectance values used in both experiments.

The model parameters for the SA for the Tshabong plots are given in Table 7.6, and soil reflectance values used are given in Table 7.7. This experiment is referred to as Tshabong ETM+.

In all the SA the ranges for the model parameters were determined by using the minimum and maximum of all field recorded data for the plots located on the same image.

Table 7.4 Range of variation and PDF for the two PROSAIL Tshane ETM+ EFAST SA.

Parameter	Range	Probability density function
Leaf structure parameter (N)	1.5 - 3.0	Uniform
Leaf chlorophyll content (C_{a+b})	20 - 60	Uniform
Leaf water content (EWT)	0.0001 - 0.015	Uniform
Leaf dry matter content (DMC)	0.005 - 0.01	Uniform
Leaf area index (LAI)	0.12 -1.37	Gaussian
Soil reflectance (ρ_{soil})	Table 7.5	Uniform

Table 7.5 Minimum and maximum soil reflectance values used in the two Tshane ETM+ EFAST SA.

Waveband	Tshane LAB SOIL	Tshane IMAGE SOIL
ETM 1	0.155 -0.188	0.061 - 0.188
ETM 2	0.256-0.309	0.114 - 0.309
ETM 3	0.380-0.464	0.185 - 0.464
ETM 4	0.465-0.561	0.314 - 0.561
ETM 5	0.659-0.739	0.405 - 0.739
ETM 7	0.642-0.716	0.320 - 0.716

Table 7.6 Range of variation and PDF for the Tshabong ETM+ EFAST SA.

Parameter	Range	Probability density function
Leaf structure parameter (N)	1.5 - 3.0	Uniform
Leaf chlorophyll content (C_{a+b})	20 - 60	Uniform
Leaf water content (EWT)	0.0001 - 0.015	Uniform
Leaf dry matter content (DMC)	0.005 - 0.01	Uniform
Leaf area index (LAI)	0.03 -0.90	Gaussian
Soil reflectance (ρ_{soil})	Table 7.7	Uniform

Table 7.7 Minimum and maximum soil reflectance values for the Tshabong ETM+ EFAST SA.

Waveband	Tshabong ETM+
ETM 1	0.119 -0.130
ETM 2	0.208 - 0.226
ETM 3	0.330 - 0.359
ETM 4	0.422 - 0.455
ETM 5	0.599 - 0.653
ETM 7	0.583 - 0.636

7.3.3.4 Field plot specific MODIS sensitivity analyses

The MODIS data coincident with the seven field plots all have different viewing and illumination geometries (see Table 6.5). Consequently, seven different SA were performed with PROSAIL, and EFAST was used to calculate the sensitivity. Model parameter ranges and PDFs are given in Table 7.8, while Table 7.9 contains the minimum and maximum soil reflectance values used. The SA which considered the full range of the biophysical model parameters at each site took the minimum and maximum observed values for the range, given in Table 7.8. The minimum and maximum for the range in viewing and illumination conditions, was taken from Table 6.6.

Table 7.8 Range of variation and PDF for the PROSAIL parameters used in the field plot specific MODIS EFAST SA.

Parameter	T1	T2	M1	M2	TG1	TG2	TG3
Leaf structure parameter (N)				1.5 - 3.0 (U)			
Leaf chlorophyll content (C_{a+b})				20 - 60 (U)			
Leaf water content (EWT)				0.0001 - 0.015 (U)			
Leaf dry matter content (DMC)				0.005 - 0.01 (U)			
Leaf area index (LAI)	0.12 - 0.88 (G)	0.17 - 1.37 (G)	0.001 - 0.03 (G)	0.01 - 0.13 (G)	0.03 - 0.90 (G)	0.04 - 0.48 (G)	0.07 - 0.47 (G)
Soil reflectance (ρ_{soil})				Table 7.9 (U)			

Note: Letter in brackets indicates the PDF, G being Gaussian, and U being Uniform. T1 and T2 is Tshane plots 1 and 2, M1 and M2 are Mabuasehube plots 1 and 2, TG1, TG2, and TG3 are Tshabong plots 1, 2, and 3.

Table 7.9 Minimum and maximum soil reflectance values for the field plot specific MODIS EFAST SA.

Waveband	Tshane Plots	Mabuasehube Plots	Tshabong Plots
MOD1	0.370 - 0.452	0.351 - 0.392	0.319 - 0.347
MOD2	0.473 - 0.568	0.462 - 0.502	0.430 - 0.464
MOD3	0.146 - 0.178	0.116 - 0.143	0.112 - 0.122
MOD4	0.237 - 0.285	0.200 - 0.233	0.190 - 0.206
MOD5	0.608 - 0.698	0.590 - 0.631	0.557 - 0.608
MOD6	0.657 - 0.737	0.638 - 0.677	0.597 - 0.651
MOD7	0.664 - 0.742	0.647 - 0.688	0.606 - 0.660

7.4 Results and discussion

The results of the SA experiments are presented in sequential order, in Figures 7.3 through 7.12. The figures represent the contribution that each model parameter makes to reflectance variability. Figures 7.4, 7.6, and 7.8 represent the relative difference between two methods: the LG entire world range of variation SA, the LG Botswana range of variation, and the uniform and Gaussian PDF comparison, respectively. These figures are obtained by subtracting one method or PDF from the other.

7.4.1 Local versus global SA comparison

Analysis of the results will focus on the differences between the two approaches for both the LG entire world and LG BOTSWANA experiments, rather than trying to provide a biophysical interpretation. Specifically, focus is targeted at the importance of the interaction effects in the global SA, and the relative importance of the model parameters in explaining reflectance variance, estimated by both approaches. The global SA results are treated as the truth when comparing the two approaches.

The results of the LG entire world SA are shown in Figure 7.3. The importance of model interactions in driving reflectance variability are shown to be significant, accounting for 15.2% of the variance across the solar spectrum (Figure 7.3b). Interactions are most important in the NIR region where they account for 21.4% of the variance. Clearly, the local SA has failed to capture the total variance of the system, and this will have implications for the estimation of the relative importance of model parameters in driving reflectance variability.

Comparing Figure 7.3(a) and 7.3(b), there are clear differences in the relative importance of all the model parameters obtained from both methods, and these are most pronounced for the C_{a+b} content, LAI, and Fcov. Figure 7.4 shows that the local SA overestimates the importance of C_{a+b} in explaining reflectance variability by up to 47% more than the global EFAST SA, with an average of 33.6% across the PAR wavelengths. Not only are there differences in the magnitude of the importance of C_{a+b}, but also the rank importance. For example, at 440nm in the local SA, C_{a+b} is the most important parameter explaining 58% of the variance in reflectance, yet in the global EFAST SA, it is the fourth most important parameter explaining only 13% of the variance in reflectance.

The importance of LAI is overestimated in the local SA (compared to the global SA), by an average of 14.4% across the solar spectrum, with maximum overestimation occurring in the SWIR region (21%) (Figure 7.4). The rank importance of LAI across wavelengths, does not, however, differ greatly between the two approaches. Largest differences between the two methods for Fcov are observed in the blue and red wavelength regions, with the local SA overestimating the importance of Fcov by 18.0% and 14.1%, respectively. Fcov is overestimated in the local SA at NIR wavelengths by an average of 14.2%, and underestimated in the SWIR region by 6.0% (Figure 7.4).

Results of the LG BOTSWANA experiment are shown in Figure 7.5. Clearly, the importance of interactions between model parameters in explaining reflectance variability is much reduced compared to the LG entire world experiment (cf. Figure 7.3a and 7.5a). Interactions account for just 6% of the variance across the solar spectrum, and are greatest in the visible regions with a maximum of 11.3% at 420nm (Figure 7.5a). Figure 7.6 shows the difference in relative contribution that each parameter makes to reflectance variability. It can be seen that the largest differences between the two methods are in the estimation of the importance of LAI and soil reflectance (ρ_{soil}), all other parameters generally displaying differences of roughly a few per cent. The symmetry in the difference between LAI and soil reflectance is striking, across the solar spectrum. The local SA method overestimates and underestimates the importance of LAI and ρ_{soil} by 21.6% and 16.3% respectively, across the solar spectrum.

This shows that while the interaction effects may not be significant, there are still large differences between the two methods in terms of the relative contribution that parameters make to reflectance variability. In other words, even if the interaction effects in a given SA are not large, this does not mean that the local and global SA approaches will provide equivalent outcomes. For example, at 820nm the local SA shows LAI to be the second most important parameter, explaining 22% of the variance in reflectance, whereas the EFAST first-order effects show LAI to be the third most important parameter, but only weakly so, explaining 6% of the variance in reflectance (Figure 7.5). Similarly, at 1240nm, the local SA shows LAI to be the most important parameter explaining 51% of the variance in reflectance, whereas the EFAST first-order effects show LAI to explain only 24% of the variance in reflectance, LAI being

the second most important parameter. In the visible wavelengths both methods report LAI as the most important parameter, but the local SA overestimates the importance of LAI by 13% - 17% (Figure 7.6).

Taken together, these two experiments have illustrated the clear benefit of performing global SA compared to a local SA. In a global SA the full variance of the system is quantified and accounted for. Depending on the range of variation considered in a SA the interaction effects may be more or less important in driving reflectance variability. Regardless, even when the interaction effects are small, the global EFAST SA and the local SA cannot be considered equivalent. The results from both experiments show that there are marked differences in the relative importance of parameters, obtained from the two different methods. When the purpose of the model SA is to inform the design of model inversion schemes to estimate biophysical or biochemical parameters, very different strategies would be adopted depending on which method of SA had been used.

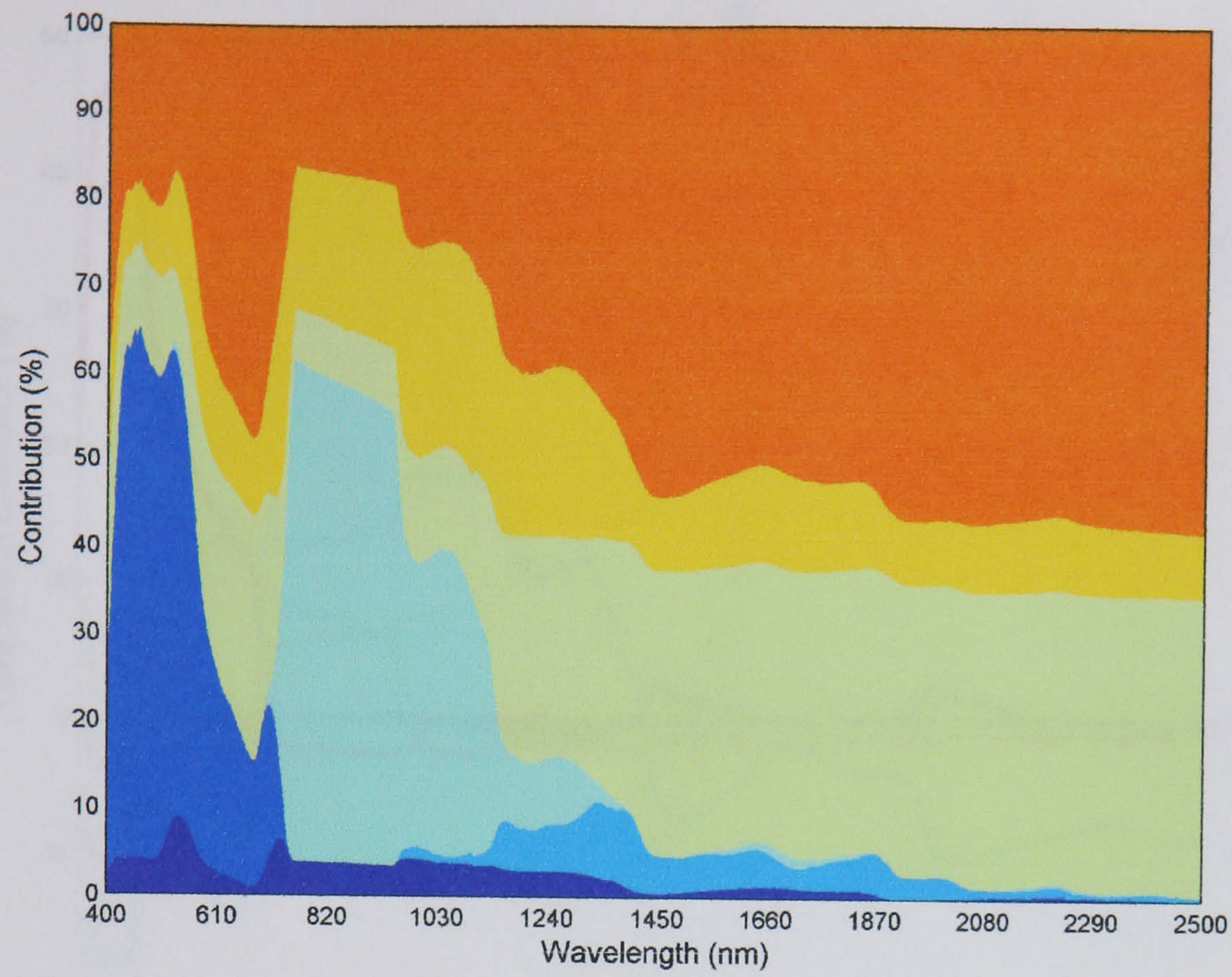

(a) Local SA

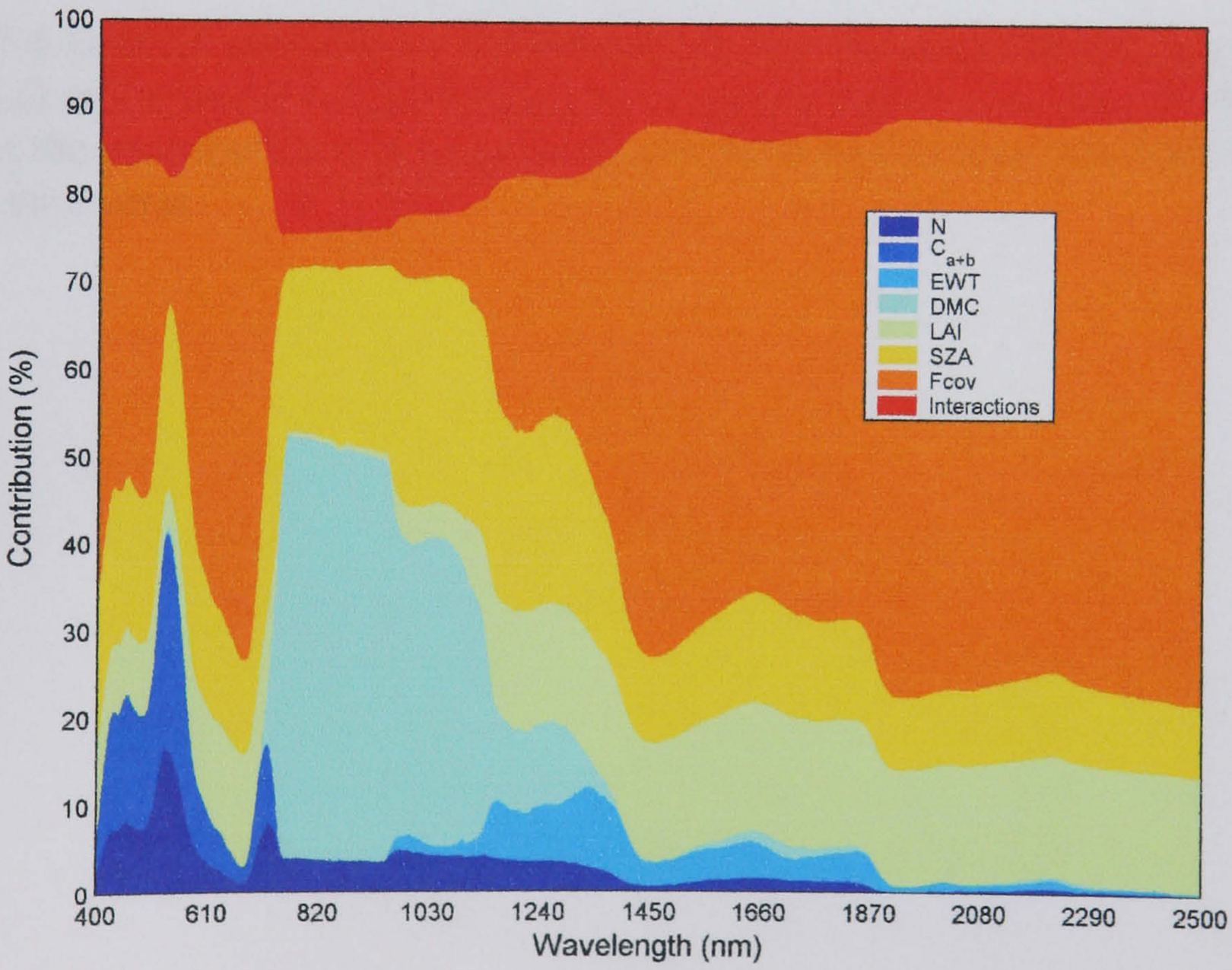

(b) Global EFAST SA

Figure 7.3 First-order effects for the (a) local versus (b) global EFAST SA comparison, considering the 'LG entire world' range of variability. The EFAST SA contains the model interaction effects also. The legend is given in Figure 7.3(b).

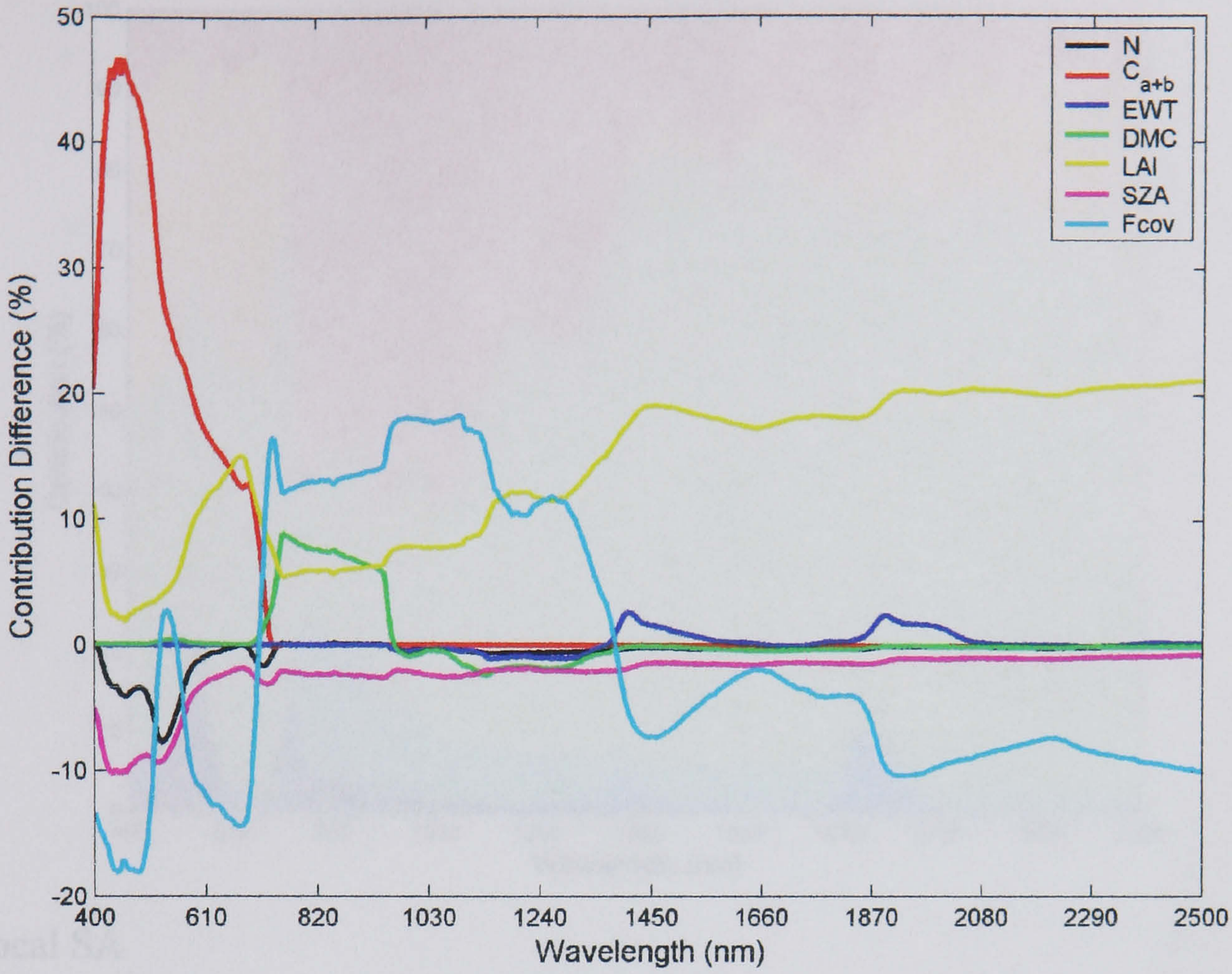

Figure 7.4 Relative contribution differences between the local and global EFAST SA, for the 'LG entire world' range of variation. Negative differences indicate that EFAST estimates the contribution of a given parameter to be greater than that from the local SA, and vice versa.

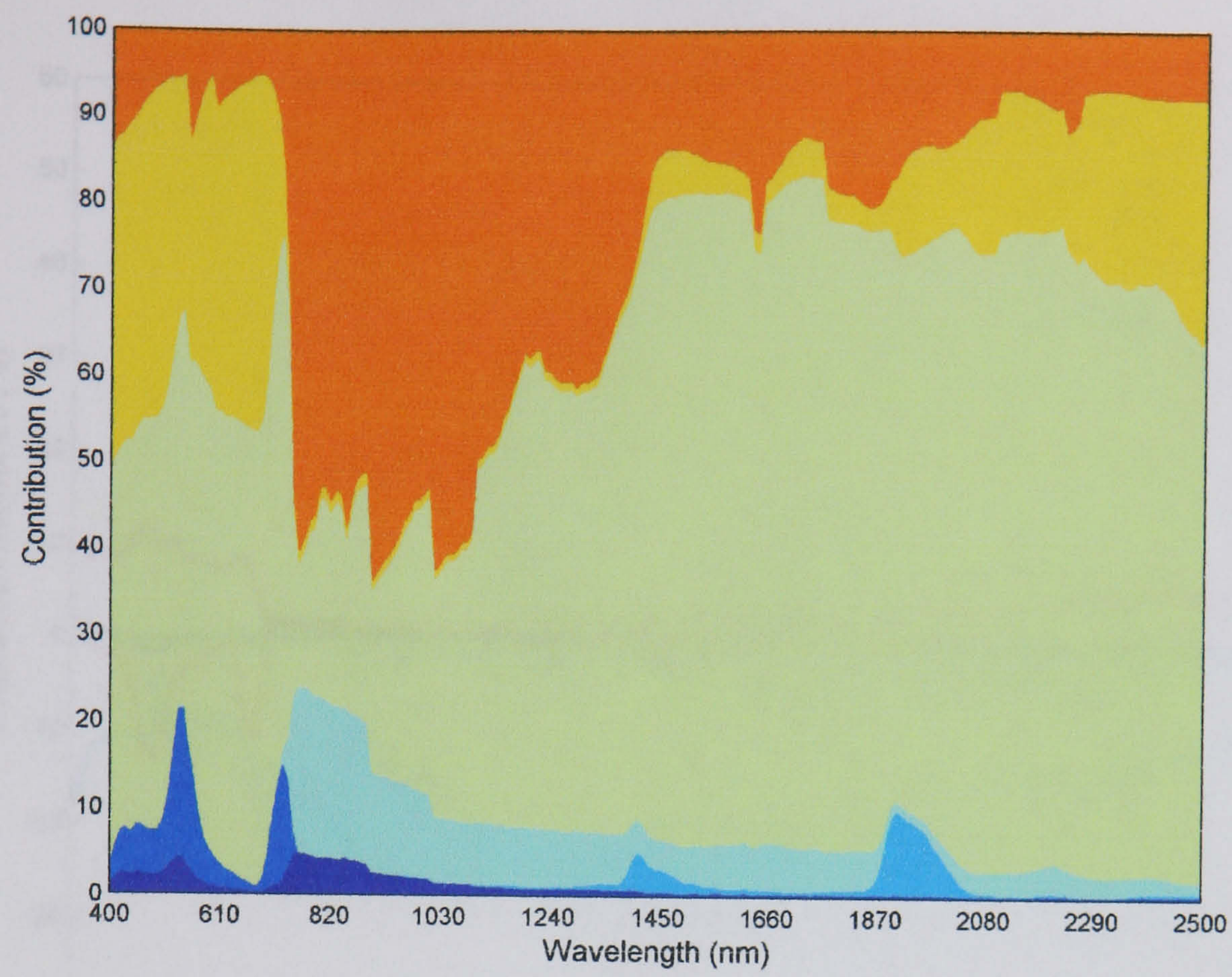

(a) Local SA

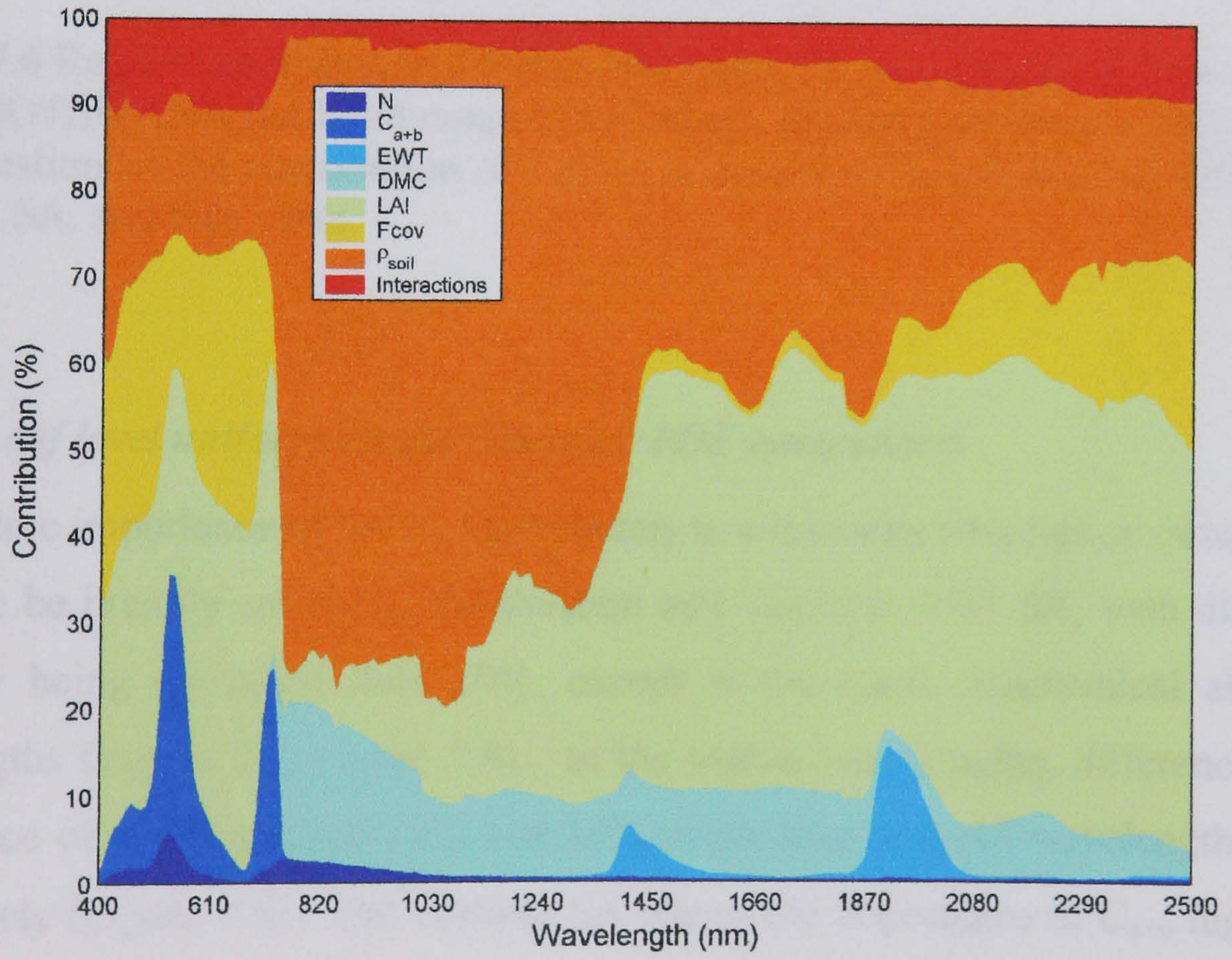

(b) Global EFAST SA

Figure 7.5 First-order effects from the (a) local versus (b) global EFAST SA comparison, with field measured LG BOTSWANA range of variability. The EFAST SA contains the model interaction effects also. The legend is given in Figure 7.4(b).

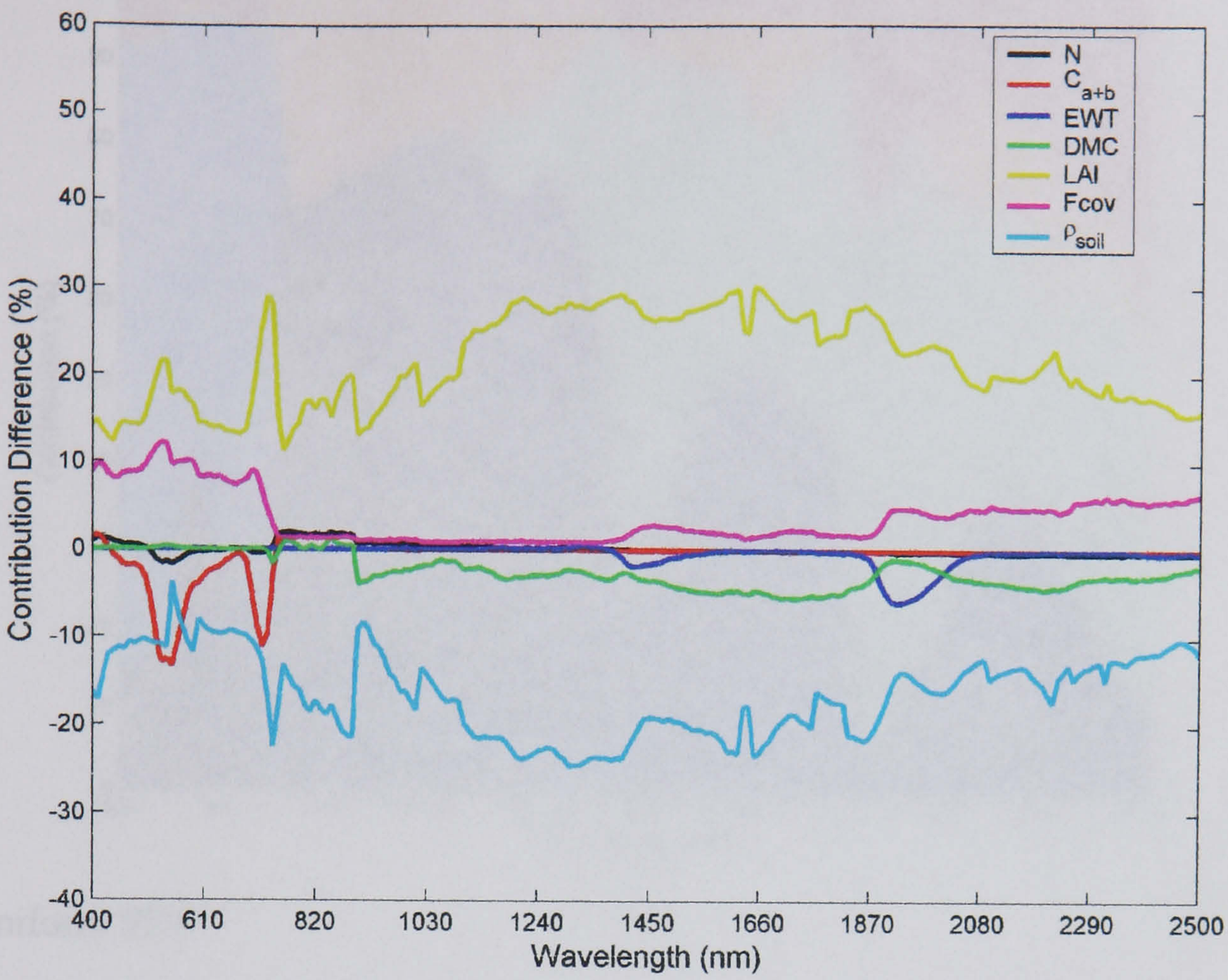

Figure 7.6 Relative contribution difference between the local and global EFAST SA for the BOTSWANA field plot range of variation. Negative differences indicate that EFAST estimates the contribution of a given parameter to be greater than that from the local SA, and vice versa.

7.4.2 Leaf level uniform versus Gaussian PDF comparison

The relative importance of the leaf parameters in explaining reflectance variability are shown to be broadly similar in the uniform and Gaussian PDF SA, with differences generally being no larger than 10%, except at the major biochemical absorption wavelengths (Figure 7.7, Figure 7.8). In the visible wavelengths, differences in the importance of C_{a+b} approach 18% and 14% in the blue and red wavelength regions, respectively (Figure 7.8). The uniform SA places the importance of C_{a+b} higher than the Gaussian PDF SA. The most pronounced difference however, is seen at around 1900nm, where simultaneously, the uniform SA places the importance of EWT at roughly 37% higher, and the importance of parameter interactions roughly 39% lower, than the Gaussian PDF SA (Figure 7.8).

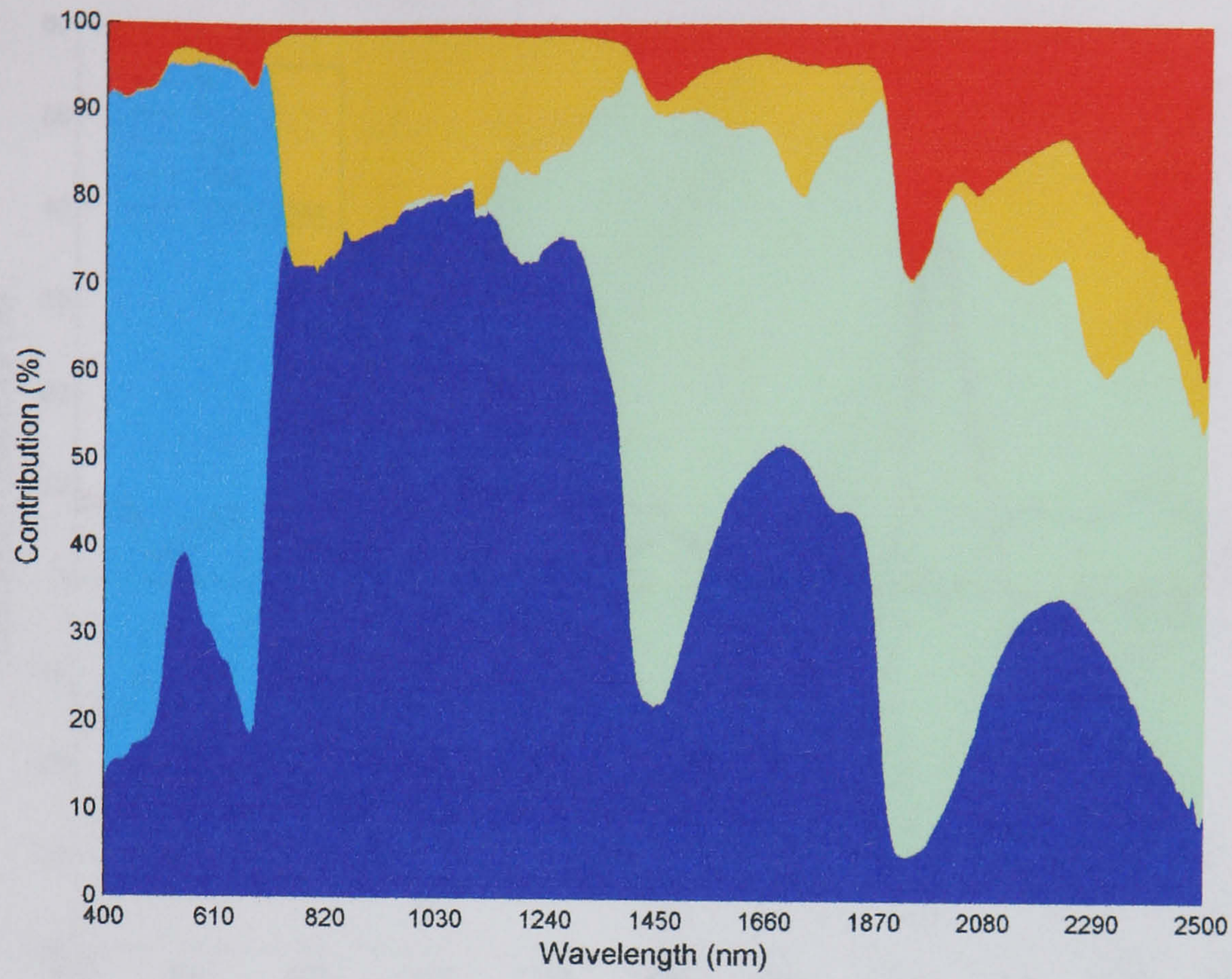

(a) Uniform PDF

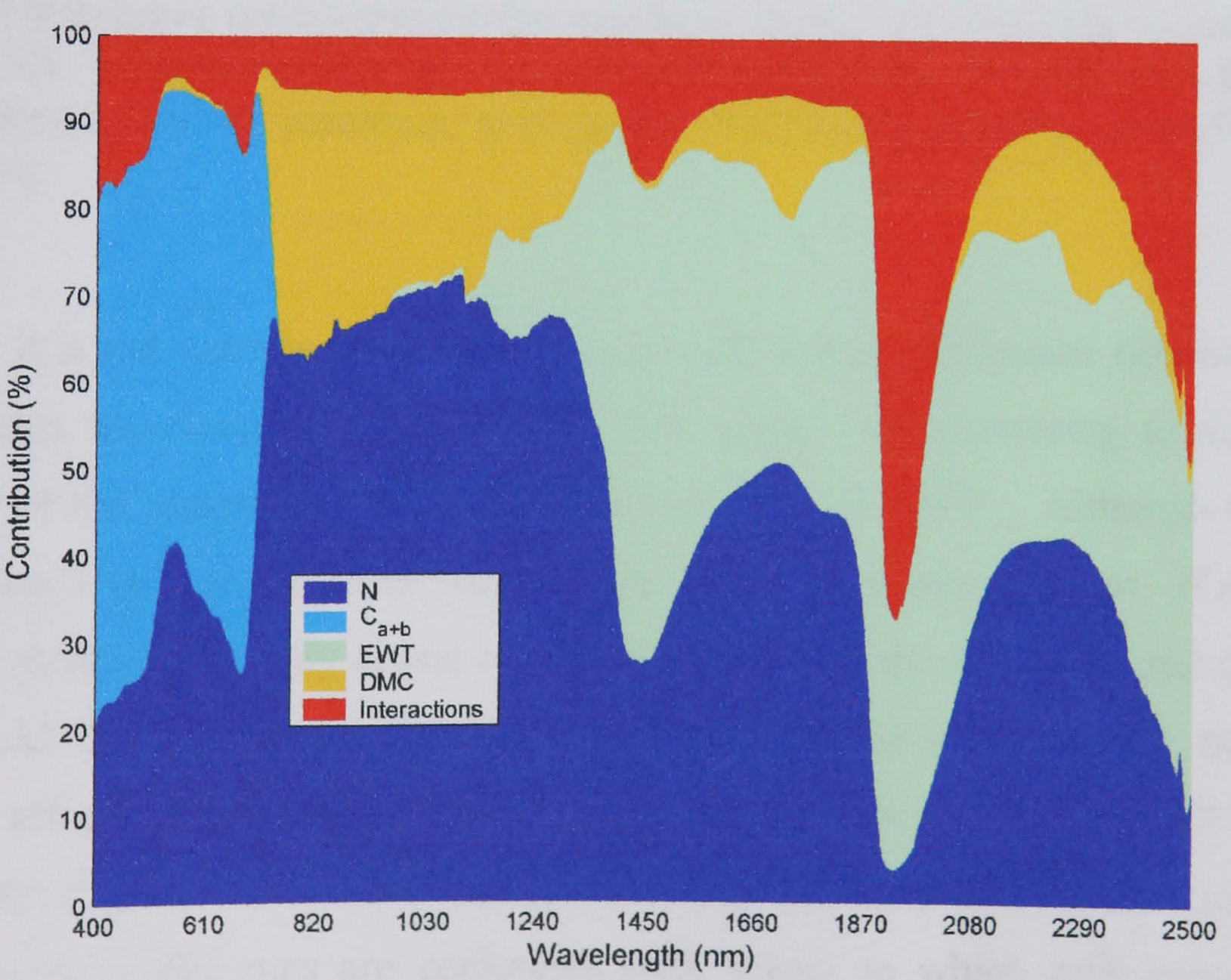

(b) Gaussian PDF

Figure 7.7 First-order and interaction effects from the (a) uniform and (b) Gaussian PDF comparison EFAST SA. The legend is given in Figure 7.7(b)

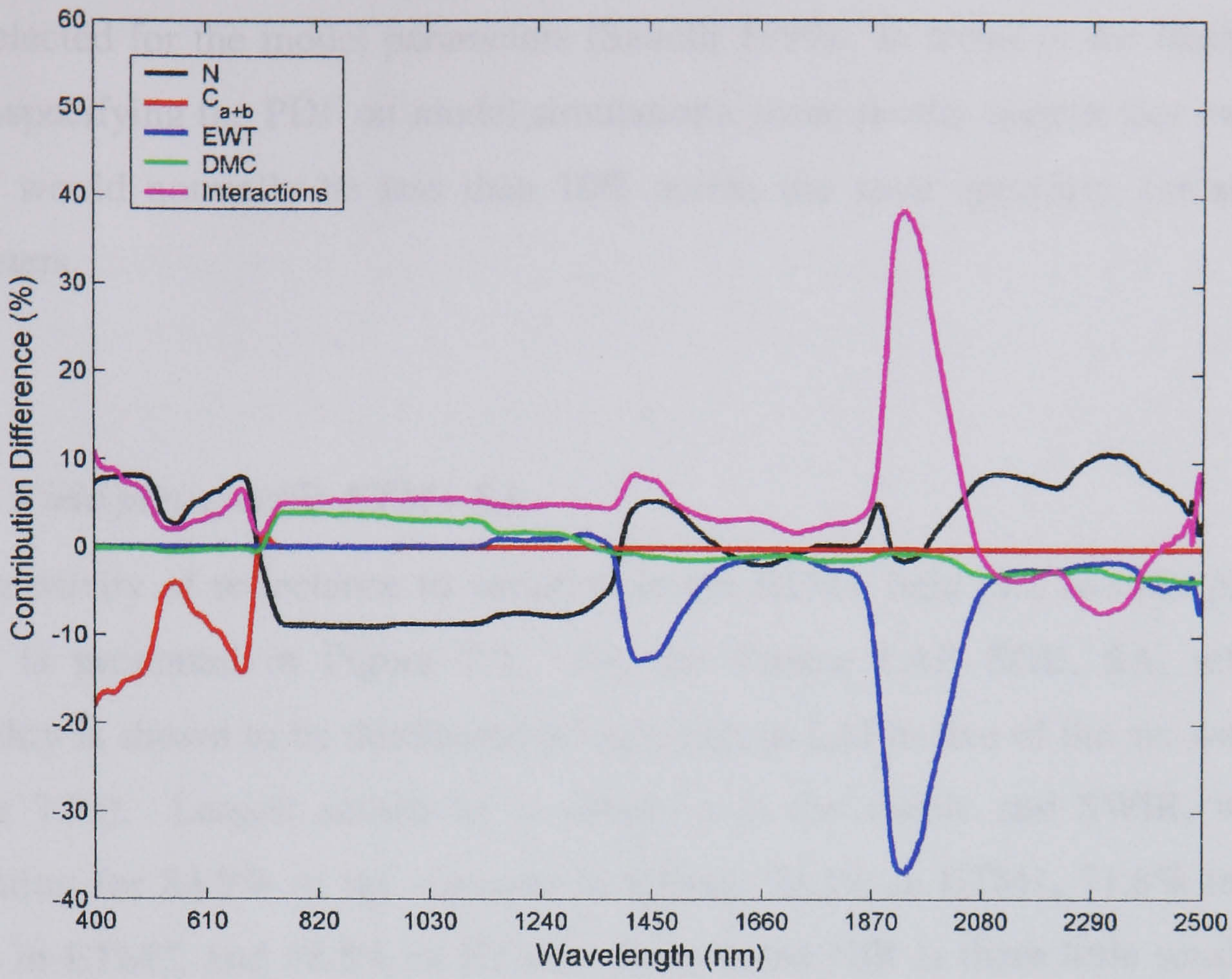

Figure 7.8 Relative contribution difference between the Uniform and Gaussian PDF EFAST SA. Negative differences indicate that the Uniform PDF estimates the contribution of a given parameter to be greater than that from the Gaussian PDF, and vice versa.

It is not entirely clear why there is such a large difference between the two SAs in this wavelength region. The reason might have something to do with the linearity of the sensitivity of reflectance to variation in EWT. Although the ranges for the two SAs were the same, the sampling of the range was different. If reflectance displays greater sensitivity at one end of the range than the other (e.g. red reflectance and 2>LAI>3) , and there is a greater density of samples in this region, then clearly this will affect the calculation of the sensitivity. Given the fact that EFAST calculates the sensitivity as a linear sum of the squares of the Fourier coefficients for each model run, if more model runs are performed with values to which reflectance is more sensitive, then the sum of squares of the coefficients will be larger. Various studies have shown that the sensitivity of reflectance to variation in EWT is greatest at low values of EWT (Peñuelas *et al.* 1997, Ceccato *et al.* 2001), supporting this interpretation.

The implication of this is that the EFAST method is not independent of the PDF selected for the model parameters (Saltelli 1999). In terms of the likely impact of mis-specifying the PDF on model simulations, these results suggest that overall the impact would normally be less than 10% across the solar spectrum, for all model parameters.

7.4.3 Field plot specific ETM+ SA

The sensitivity of reflectance to variation in the ETM+ field plot specific parameter ranges is presented in Figure 7.9. For the Tshane LAB SOIL SA, reflectance variability is shown to be dominated by variation in LAI in five of the six wavebands (Figure 7.9a). Largest sensitivity is observed in the visible and SWIR, with LAI accounting for 84.9% of the variance in ETM3, 79.3% in ETM1, 71.8% in ETM7, 66.8% in ETM2, and 48.6% in ETM5. Only in the NIR is there little sensitivity to LAI. In this waveband variation in soil reflectance dominates, accounting for 85.8% of the variance. Interestingly, this is the only waveband where the soil has a significant effect, in all other wavebands the importance of soil reflectance does not get above 10%. In the visible wavebands this result can be explained by the fact that there is little variation in soil reflectance in these wavelength regions (see Table 7.5). This has been observed in field studies by Huete (1988), and van Leeuwen *et al.* (1996). In the NIR on the other hand, there is greater variance in the soil reflectance values, while the influence of vegetation is reduced due to low absorption at these wavelengths (Merzlyak *et al.* 2002), and scattering effects are not significant in these optically thin canopies. For this reason, empirical efforts which have combined red and NIR reflectances in VI, to estimate vegetation biomass in semi-arid environments, will be hampered by errors in the NIR soil values (Asner *et al.* 2000). Interaction effects are insignificant across wavebands, indicating that variance in reflectance is driven by first-order effects only. The influence of EWT is strong in ETM5, accounting for 35.6% of the variance.

When the range of the soil reflectance is increased in the Tshane IMAGE SOIL SA, the sensitivity of reflectance to variation in LAI is reduced considerably (Figure 7.9b). Variation in soil reflectance is now the dominant control on reflectance variability, in all wavebands. Nevertheless, LAI is still an important parameter in four

of the six wavebands, explaining greater than 25% of the variance in ETM3 (40.8%), ETM1 (29.2%), ETM7 (27.8%), and ETM2 (27.0%). The importance of LAI in the NIR is negligible, where soil reflectance totally dominates reflectance variability. These results serve to highlight the effect of inaccurate soil reflectance parameterisation in the simulations performed in chapter 6, and further support the idea that the differences between modelled and measured reflectances are attributable to mis-specification of soil reflectance values. Interaction effects are negligible across all wavebands.

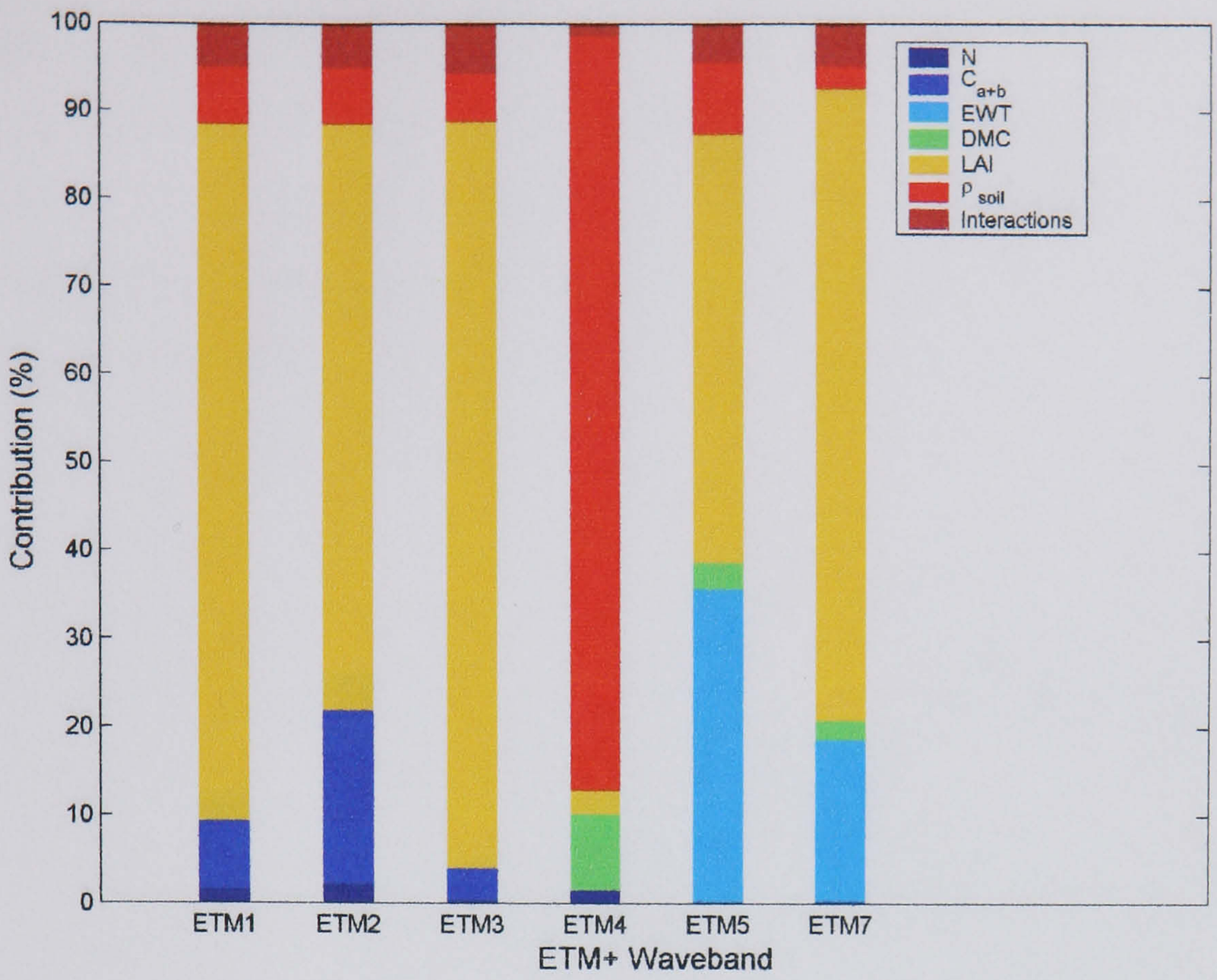

(a) Tshane LAB soil

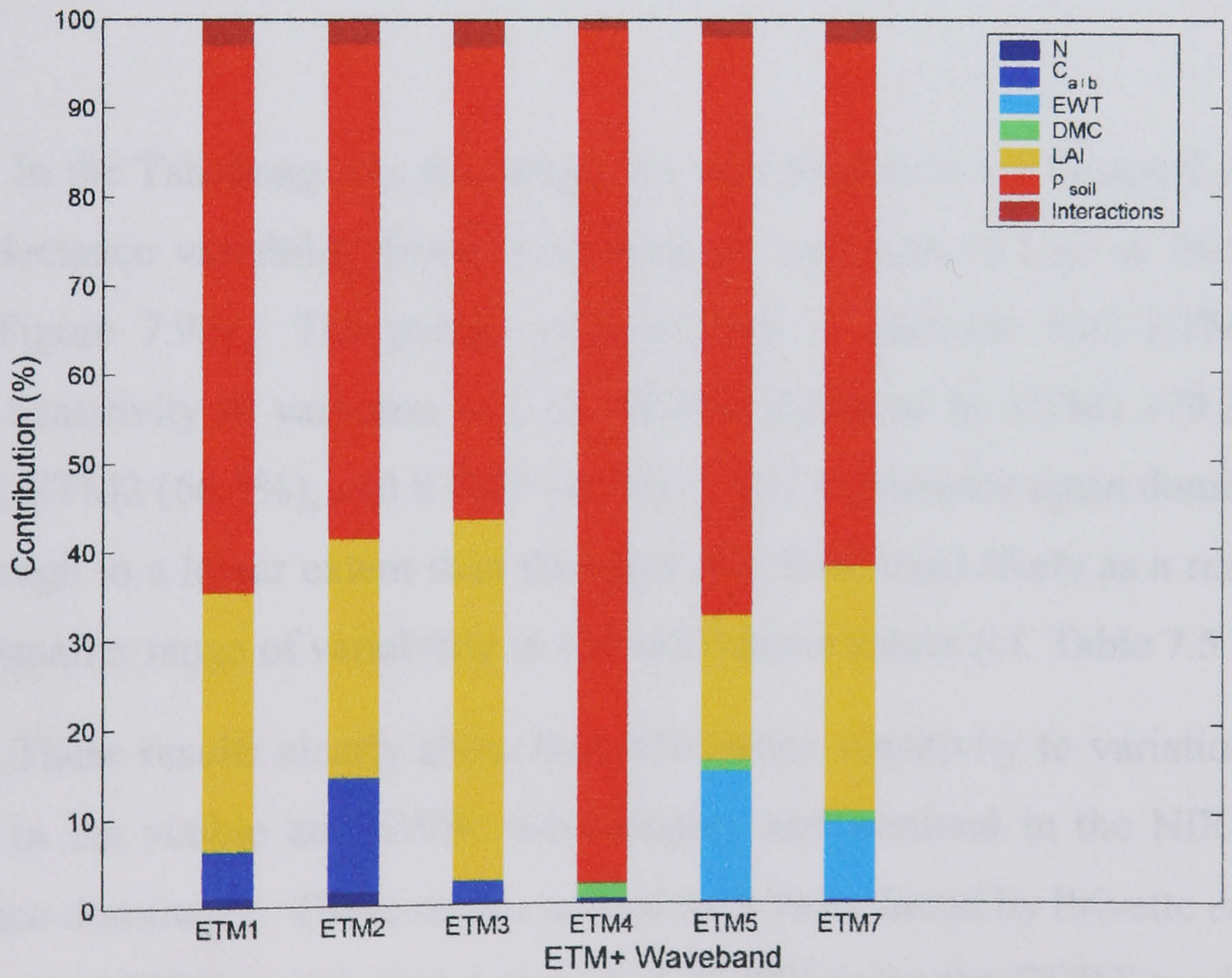

(b) Tshane IMAGE soil

Figure 7.9 First-order effects and interactions from the EFAST field plot specific ETM+ SA.

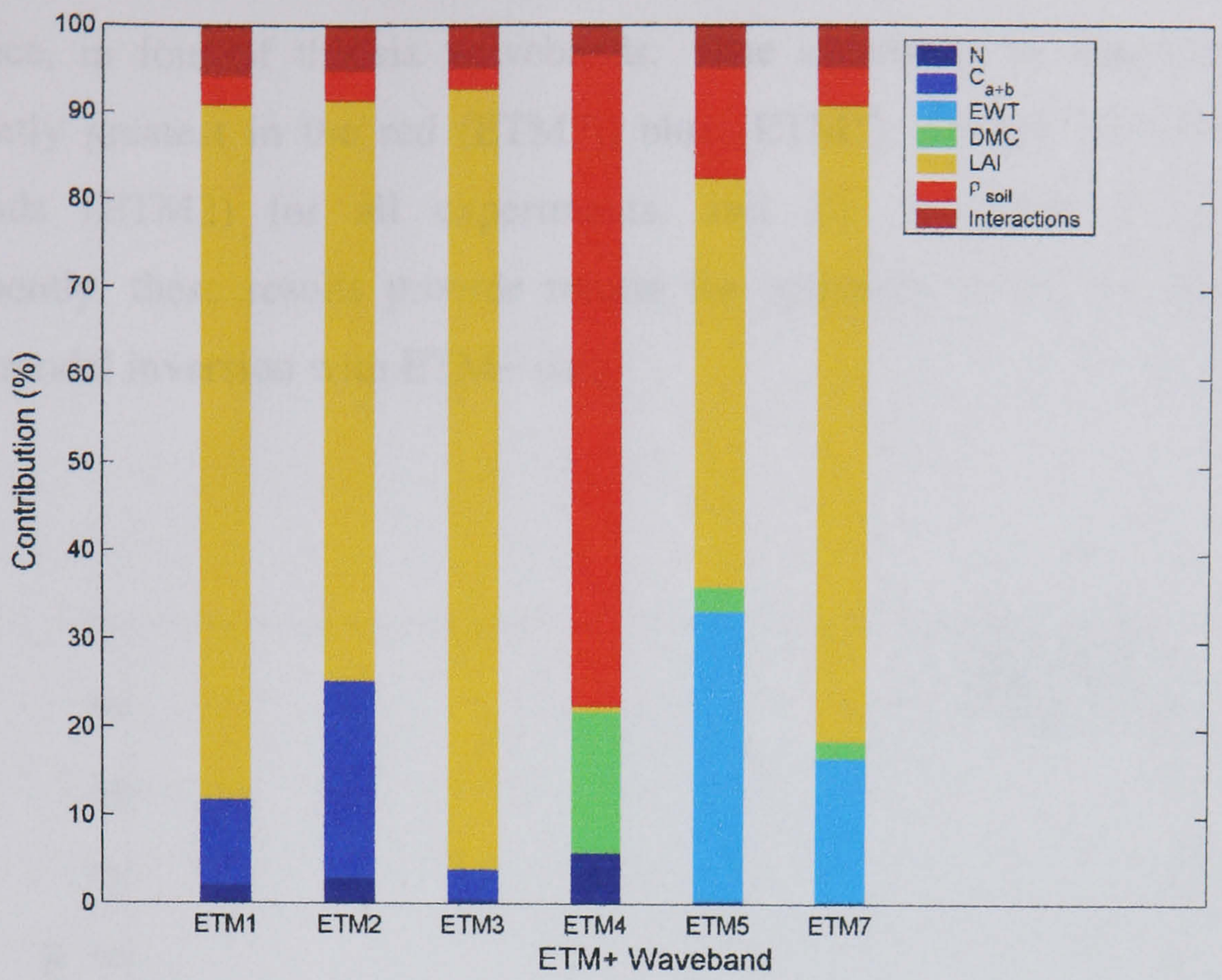

(c) Tshabong

Figure 7.9 Continued.

In the Tshabong SA, the results are very similar to the Tshane LAB soil SA, with reflectance variability being dominated by variation in LAI in five of the six bands (Figure 7.9c). The pattern of sensitivity is identical with ETM3 showing greatest sensitivity to variation in LAI (88.8%) followed by ETM1 (79.2%), ETM7 (72.2%), ETM2 (66.1%), and ETM5 (46.4%). Soil reflectance again dominates in the NIR, though to a lesser extent than the other two SAs, most likely as a result of there being a smaller range of variability in soil reflectance values (cf. Table 7.5 Table 7.7).

These results clearly show that reflectance sensitivity to variation in LAI is greatest in the visible and SWIR wavelengths, and minimal in the NIR where soil reflectance dominates. These results accord with those found by Privette *et al.* (1994), using the CANTEQ model, and Asner *et al.* (2000) using the GORT model, working in similarly optically thin canopies in the USA. The fact that soil reflectance only dominates reflectance variability in the NIR in all three experiments is attributable to the small range of variation in soil reflectance observed at these plots, particularly in the visible wavelengths. This is a reflection of the relative homogeneity of the soil background, the Kalahari sands (see chapter 5). Even when tested over a relatively

large range of soil values, LAI still accounts for a large amount of the variance in reflectance, in four of the six wavebands. The sensitivity to variation in LAI is consistently greatest in the red (ETM3), blue (ETM1), SWIR2 (ETM7) and green wavebands (ETM2) for all experiments, and this is shown in Figure 7.10. Consequently, these results provide reason for optimism in the estimation of LAI through model inversion with ETM+ data.

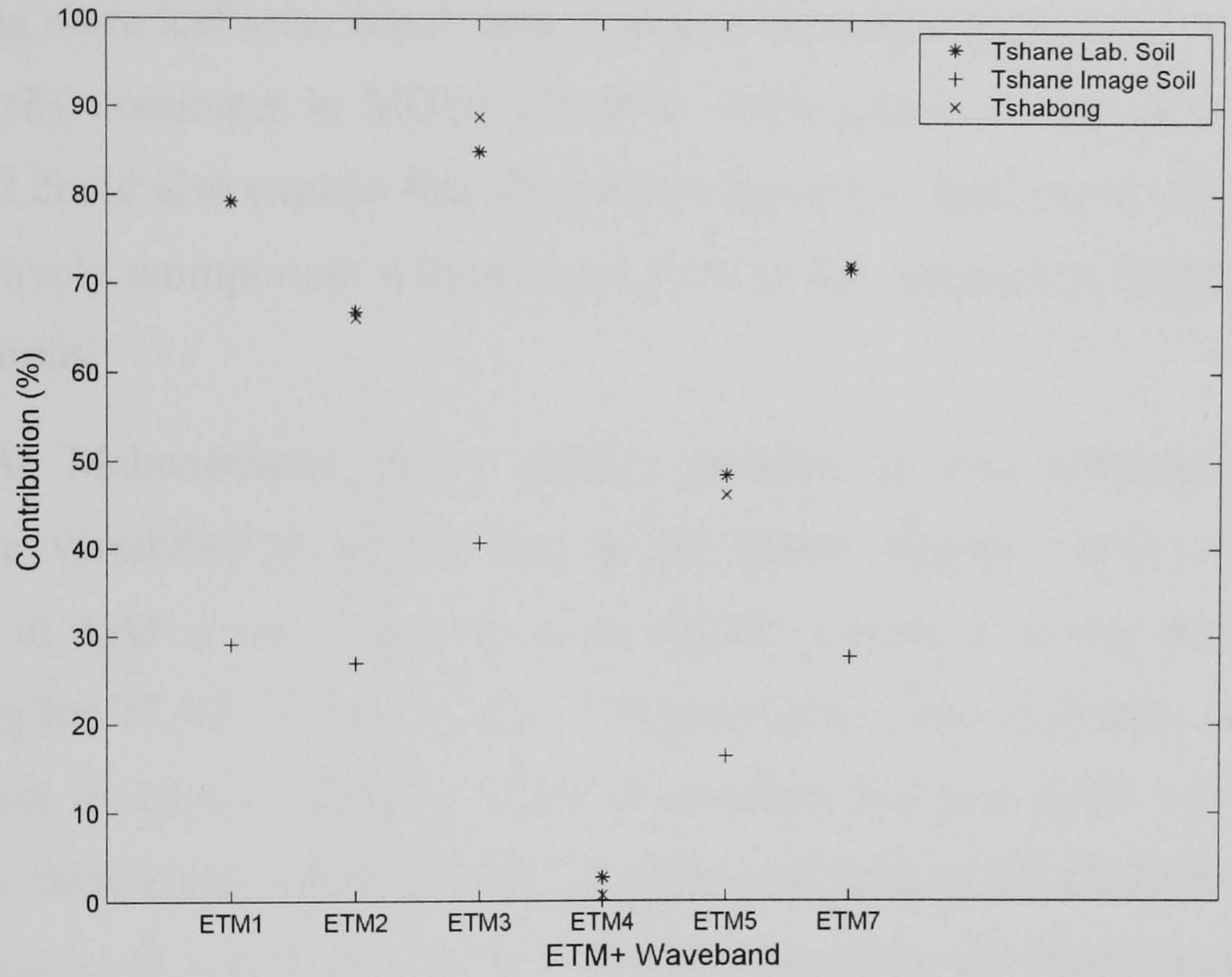

Figure 7.10 Summary of LAI sensitivity in the three ETM+ EFAST SA.

7.4.4 Field plot specific MODIS SA

The sensitivity of reflectance to variation in the MODIS field plot specific parameter ranges is presented in Figure 7.11. At Tshane plot 1 (T1) sensitivity of reflectance to variation in LAI is shown to be strong in five of the seven wavebands (Figure 7.11a). Greatest sensitivity is displayed in the visible and SWIR wavebands with LAI accounting for 73.7% of the variance in MOD1, 71.2% in MOD3, 60.9% in MOD7, and 51.4% in MOD4. Lowest sensitivity to LAI is observed in the two NIR wavebands MOD2 and MOD5, where LAI accounts for 1.0% and 10.8% of the variance respectively. Soil reflectance drives reflectance variability in these two wavebands, accounting for 95.0% and 76.8% of the variance respectively. Variation

in soil reflectance is shown to be important in SWIR1 (MOD6) and the visible wavebands also (MOD1, MOD3, MOD4), where it accounts for approximately 20% of the variance.

At Tshane plot 2 (T2), there is a very similar pattern to T1 with variation in LAI being the main driver of reflectance variability in five of the seven wavebands, and co-dominant in one other (MOD5) (Figure 7.11b). The pattern of sensitivity is the same as T1 with greatest sensitivity to LAI being shown in the visible and SWIR wavebands. The co-dominance of LAI in MOD5 at this plot is most likely due to there being more leaf area, which acts to reduce the importance of the soil reflectance, which totally dominates in MOD2 (76.5%). Differences in viewing angles between T1 and T2 could also explain this observation however. Interaction effects are shown to be relatively unimportant with at most 5.2% of the variance in MOD1 attributable to interactions.

At Mabuasehube plot 1 (M1), variation in soil reflectance dominates reflectance variability in all but one of the bands (Figure 7.11c). Sensitivity to variation in LAI is only significant in MOD1 where it is the dominant factor accounting for 72.8% of the variance. The only other band to express any sensitivity to variation in LAI is MOD7, where it accounts for just 2.6% of the variance. Doubtless, these results are due to the very low LAI value at M1 (Table 7.8), however, the importance of LAI in the red waveband compared to all others is startling. The interaction effects are negligible across all wavebands.

At Mabuasehube plot 2 (M2), the soil reflectance again dominates in all wavebands, though to a lesser extent than at M1 (Figure 7.11d). Greatest sensitivity to variation in LAI is displayed in MOD7 (29.8%), followed by MOD1 (24.7%). The difference in importance of LAI in MOD1 between plots M2 and M1, of ~48% is remarkable. While the difference in the range of LAI at both plots is relatively large (Table 7.8), and, there is also a large difference in viewing angle, 5.69 degrees backscatter and 21.79 degrees forwardscatter at M1 and M2, respectively, it is not possible to say which factor might account for these results. In order to investigate this, new SA were performed where the viewing configuration for M1 was swapped for that of M2 and vice versa, keeping the range of LAI the same as previously. The results showed that the importance of LAI increased by 1.4% at M1, and decreased by 1.4% at M2. Clearly, the large differences are a result of the LAI range, rather than

the viewing configuration. The implication is clearly that LAI is more important at very low levels than at low levels, in the red region. The blue and green wavebands also show some sensitivity to LAI but only weakly so, accounting for approximately 8% of the variance in both MOD3 and MOD4.

Reflectance sensitivity is dominated by variation in LAI and soil reflectance across all wavebands, at Tshabong plot 1 (TG1). Greatest sensitivity to variation in LAI is again displayed in the visible and SWIR wavebands, with LAI explaining 88.7% of the variance in MOD1, 88.3% in MOD3, 71.3% in MOD7, 59.1% in MOD4, and 45.6% in MOD6 (Figure 7.11e). Variation in EWT is significant in MOD6, accounting for 33.9% of the variance. Soil reflectance only dominates in the NIR, accounting for 79.8% of the variance in MOD2, and 54.9% in MOD5. Interaction effects are again relatively unimportant, with the largest impact observed in MOD4 (4.9%).

At Tshabong plot 2 (TG2), variation in LAI drives reflectance variability in four of the seven wavebands (Figure 7.11f). Greatest sensitivity is again observed in the visible and SWIR wavebands. LAI accounts for 81.5% of the variance in MOD1, 75.9% in MOD3, 59.4% in MOD7, and 51.8% in MOD4. Variation in soil reflectance is dominant in the NIR and also SWIR1, accounting for 93.5% of the variance in MOD2, 83.3% in MOD5, and 37.2% in MOD6. The increase in importance of soil reflectance in the SWIR1 compared with TG1 is most likely a result of differences in the LAI between the two plots, especially given the fact that there are minimal differences in viewing conditions (cf. Table 7.8 Table 6.5).

A very similar pattern is observed at Tshabong plot 3, where LAI dominates reflectance variability in four of the seven wavebands, and soil reflectance dominates in the other three (Figure 7.11g). Greatest sensitivity to LAI is displayed in MOD1 (77.5%), MOD3 (70.1%), MOD7 (52.4%), and MOD4 (42.7%). Overall, the importance of LAI is reduced by between 4% and 10% compared to TG2. Variation in soil reflectance dominates in MOD2 (92.8%), MOD5 (85.8%), and MOD6 (40.0%). Interaction effects are again relatively unimportant, with at most 4.0% of reflectance variability being attributable to interactions in MOD4, where variation in C_{a+b} is also significant (33.8%).

The all plots all parameters SA (Figure 7.11h), displays the same general pattern as the field plot specific SA. LAI and soil reflectance dominate reflectance

variability in the visible/SWIR, and NIR respectively. Of the viewing and illumination variables, only the view zenith angle, has any real impact on reflectance variability, though it is still relatively insignificant at approximately 5% across the wavebands. Interaction effects are slightly more important than the field plot specific SA, though this is to be expected since there are more model parameters (Saltelli 1999).

Clearly, these results mirror those of the ETM+ SA, where reflectance sensitivity to variation in LAI is greatest in the visible and SWIR wavelengths, and minimal in the NIR, where soil reflectance dominates. These results therefore also accord with the previous research findings cited above (Privette *et al.* 1994, Asner *et al.* 2000). Consistent with the results from the ETM+ SA, greatest sensitivity to variation in LAI is shown in the red waveband (MOD1) for all plots, except M2, followed by the blue (MOD3), and SWIR2 (MOD7). Figure 7.12 shows that in all wavebands there are considerable differences in the importance of LAI at the different plots, which reflects the different level of LAI at each plot. Generally, as the plot LAI increases, the sensitivity of reflectance to variation in LAI increases across all wavebands. These results would seem to indicate that the prospects for the accurate estimation of LAI through model inversion against MODIS data, are high.

It should be pointed out however, that these results were obtained with leaf parameter ranges based on the literature. If the values used were not representative, then clearly the results of these SAs would be different. Given the large range of variation covered (Table 7.8), it might be that if measurements were available, these ranges would be reduced, such that the importance of LAI and soil reflectance would likely increase.

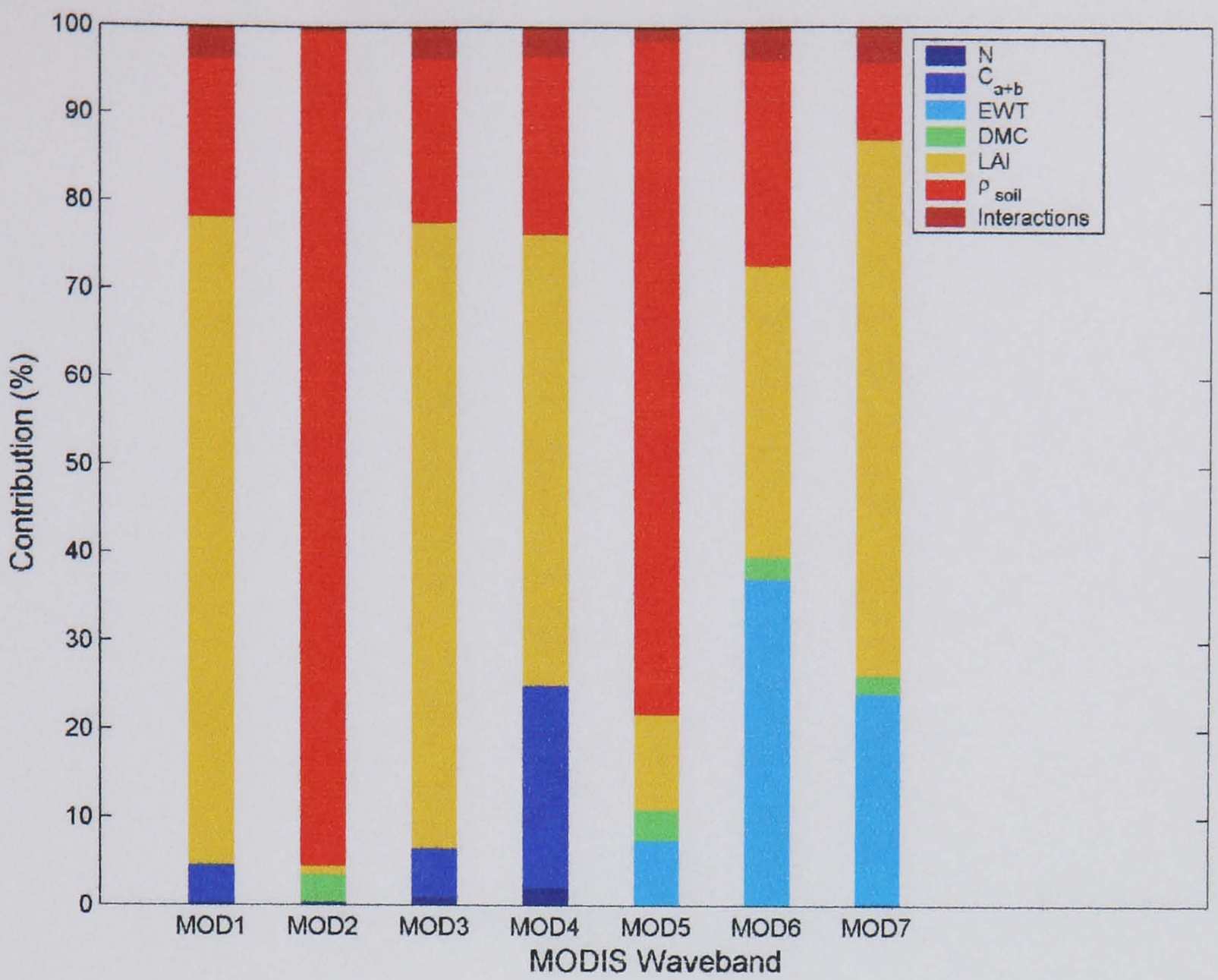

(a) Tshane plot 1

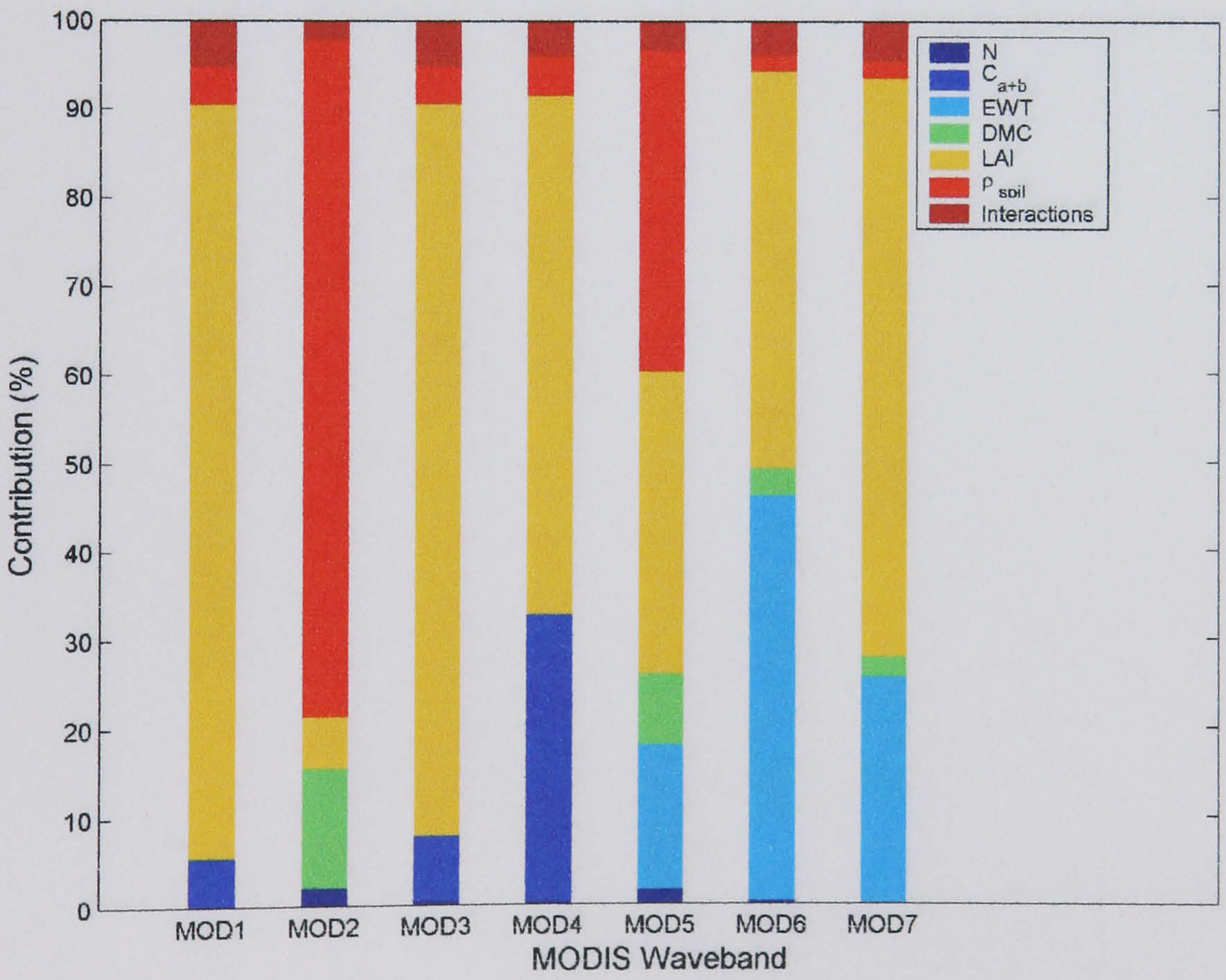

(b) Tshane plot 2

Figure 7.11 First-order effects and interactions from the EFAST field plot specific MODIS SA.

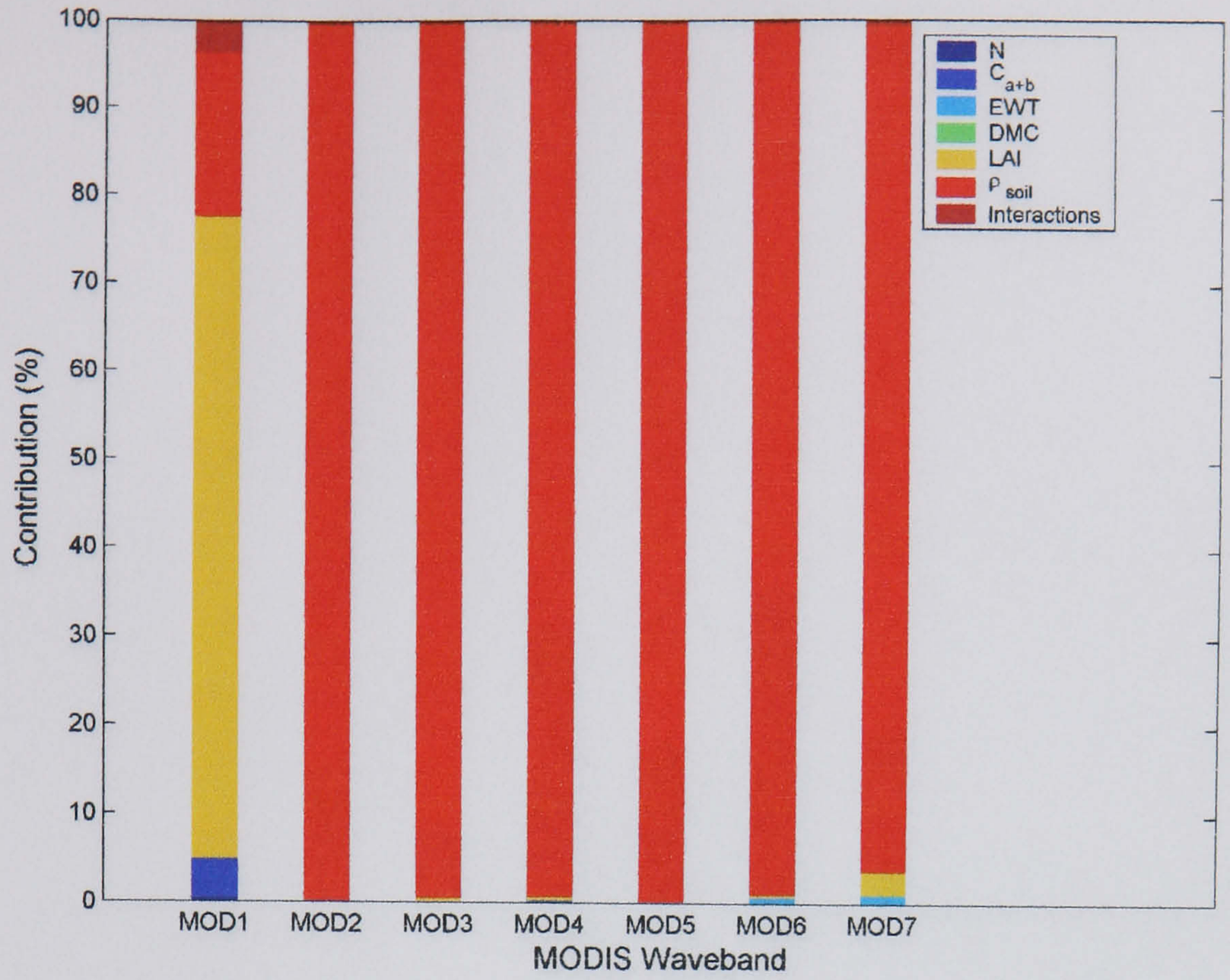

(c) Mabuasehube plot 1

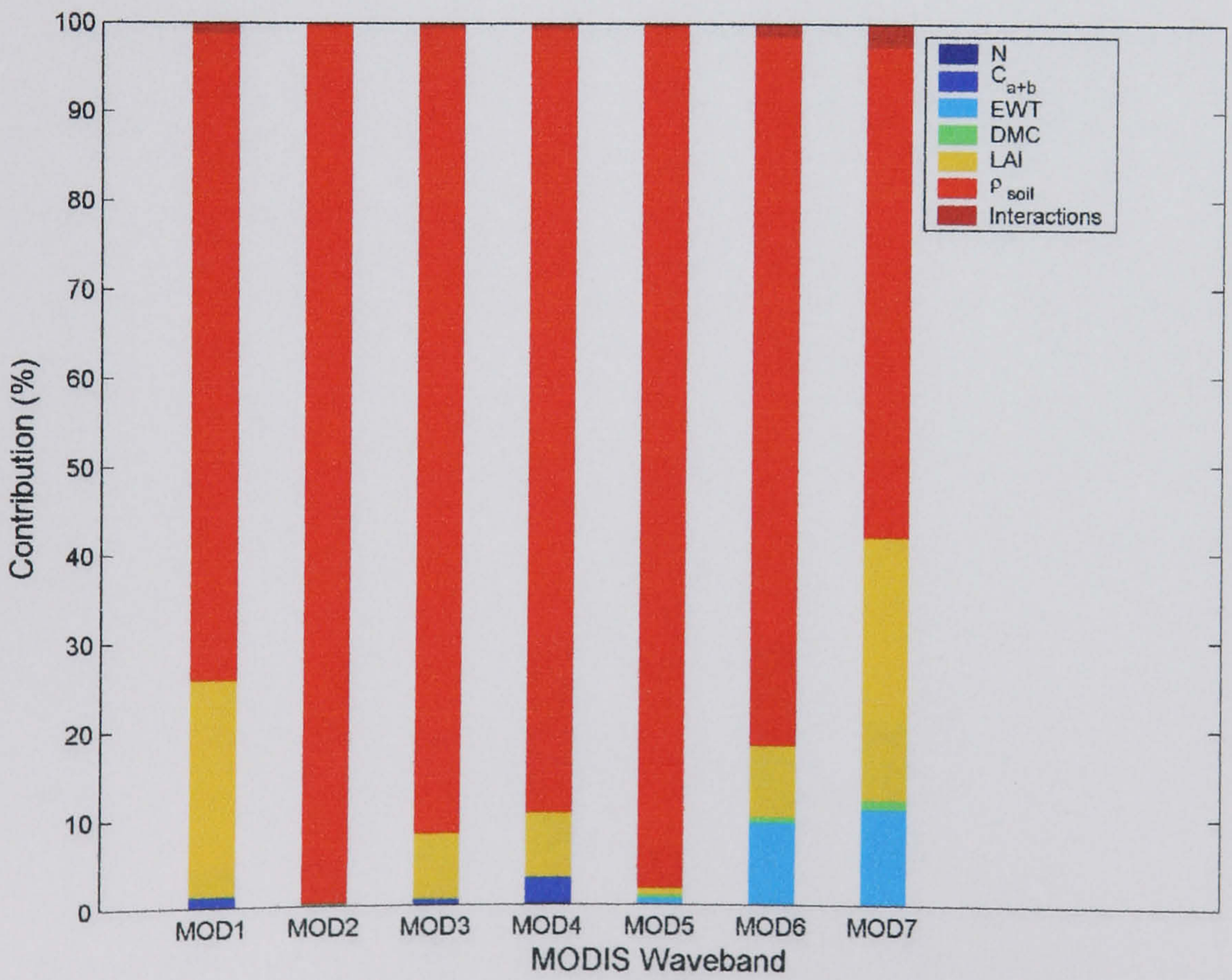

(d) Mabuasehube plot 2

Figure 7.11 Continued.

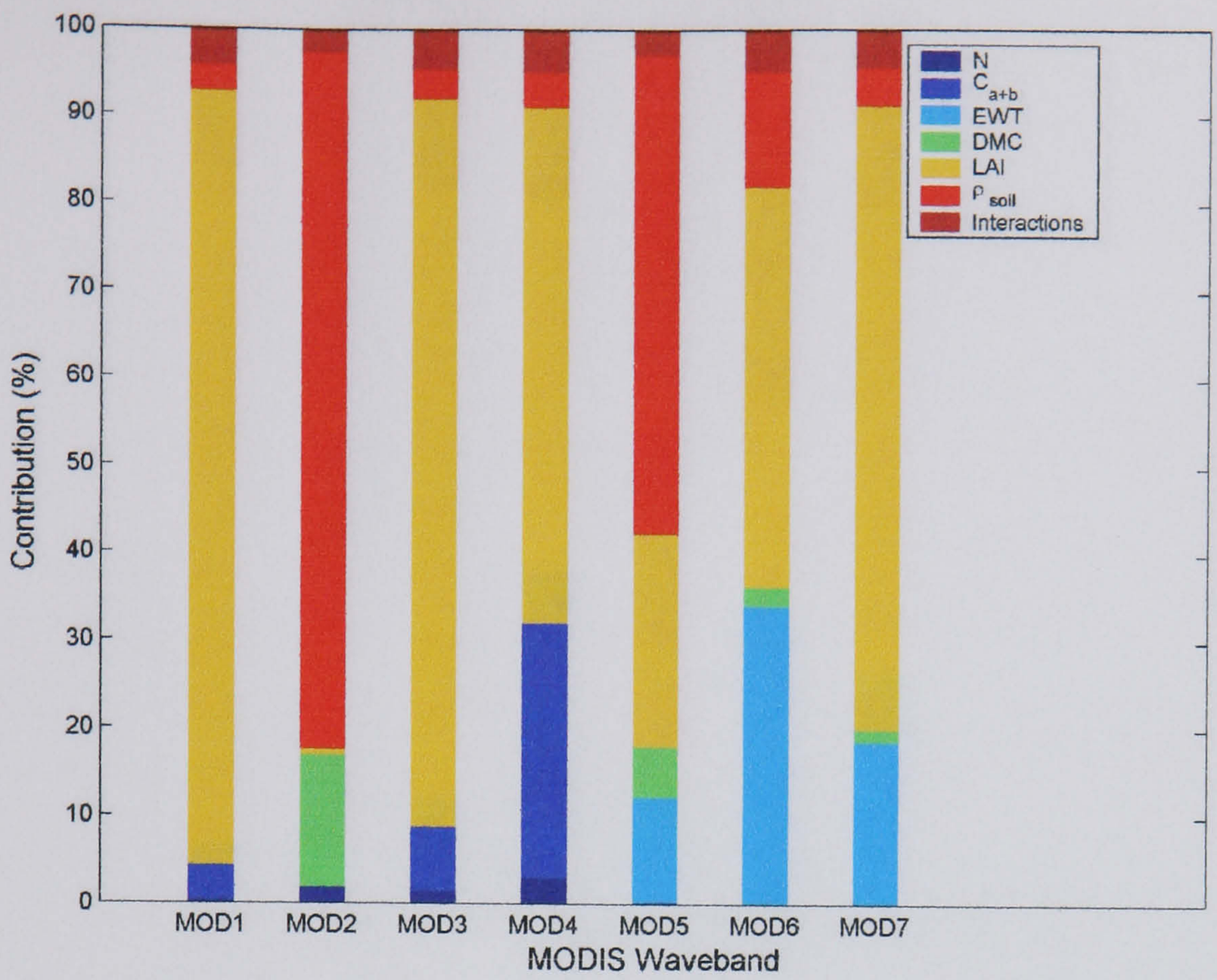

(e) Tshabong plot 1

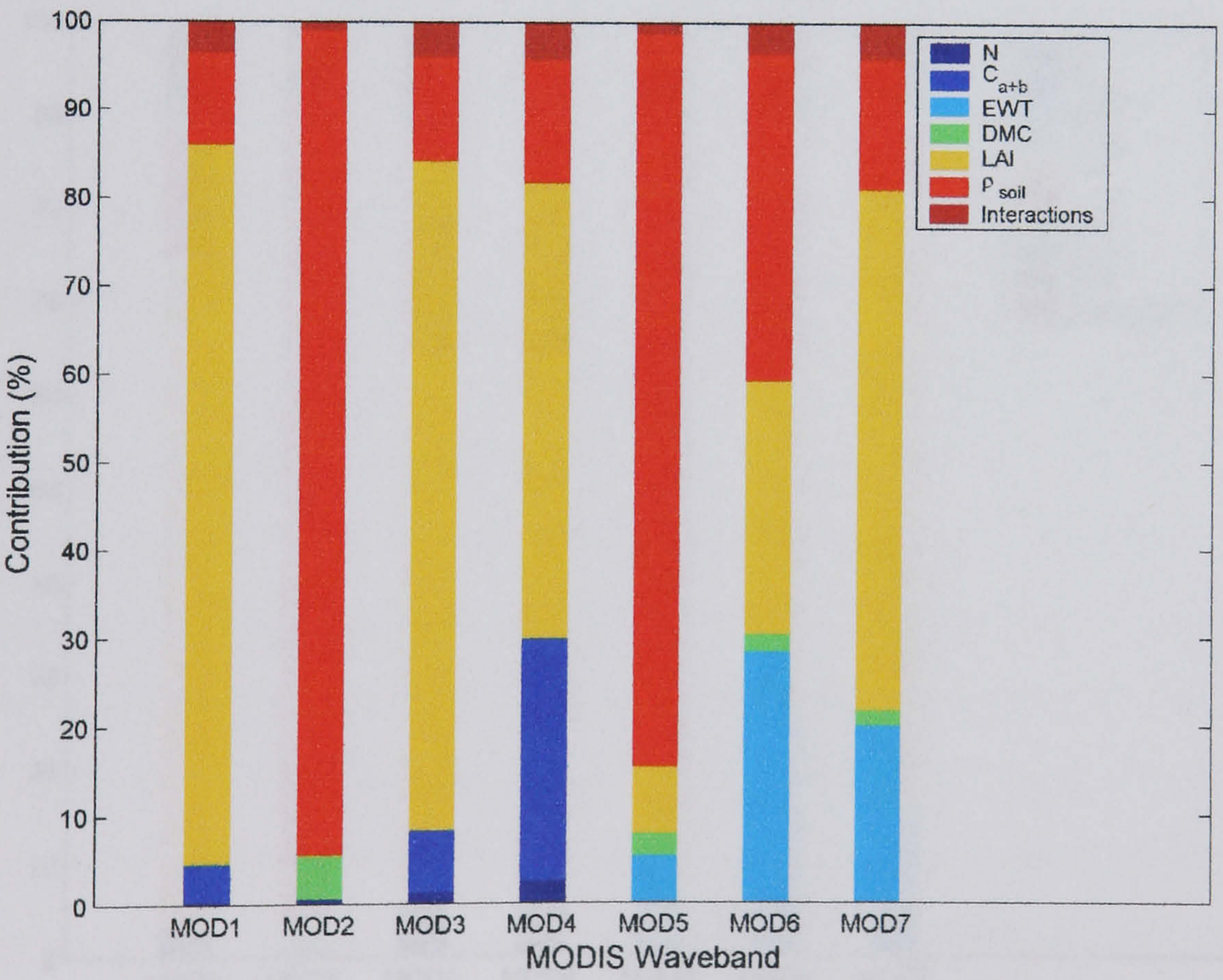

(f) Tshabong plot 2

Figure 7.11 Continued.

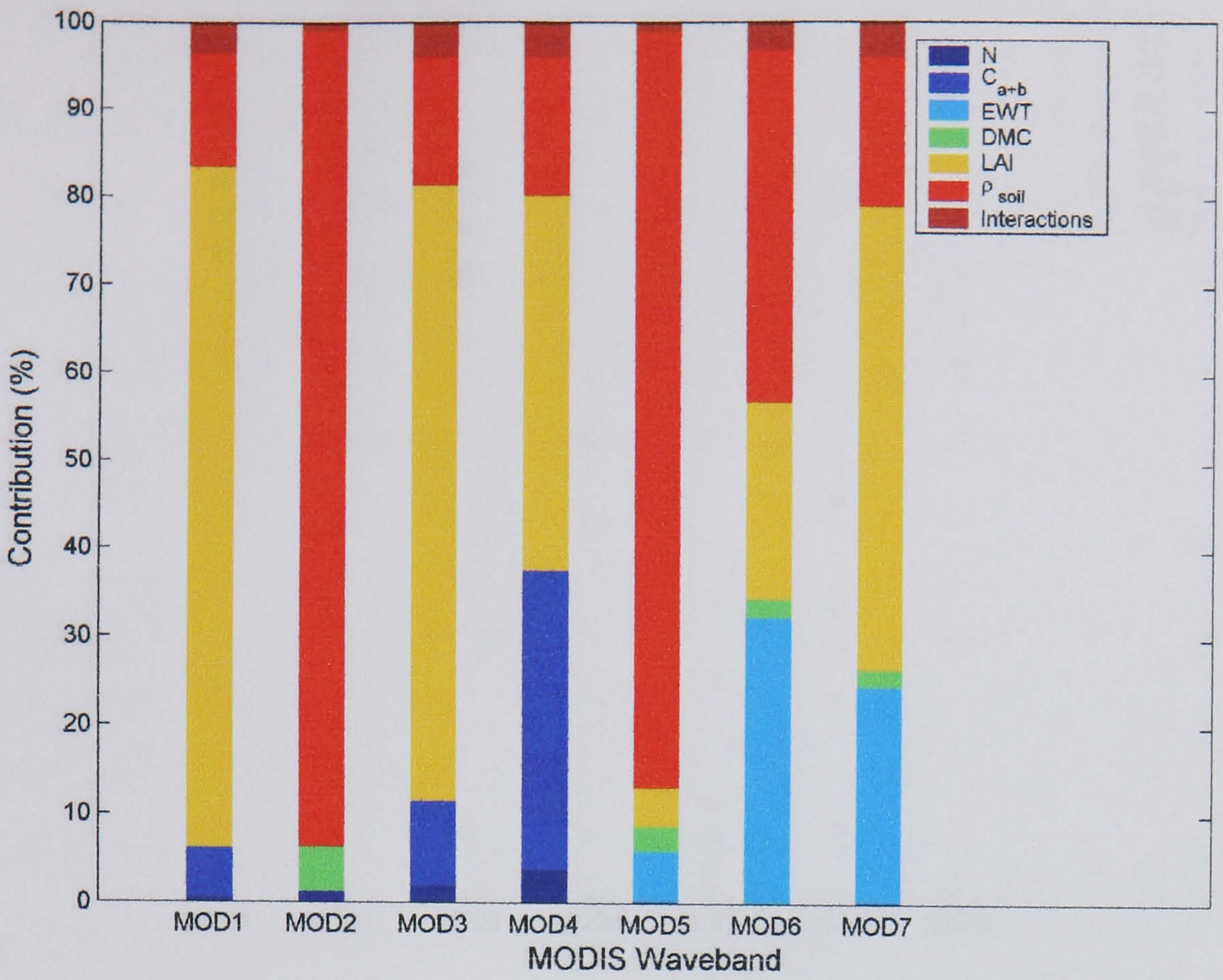

(g) Tshabong plot 3

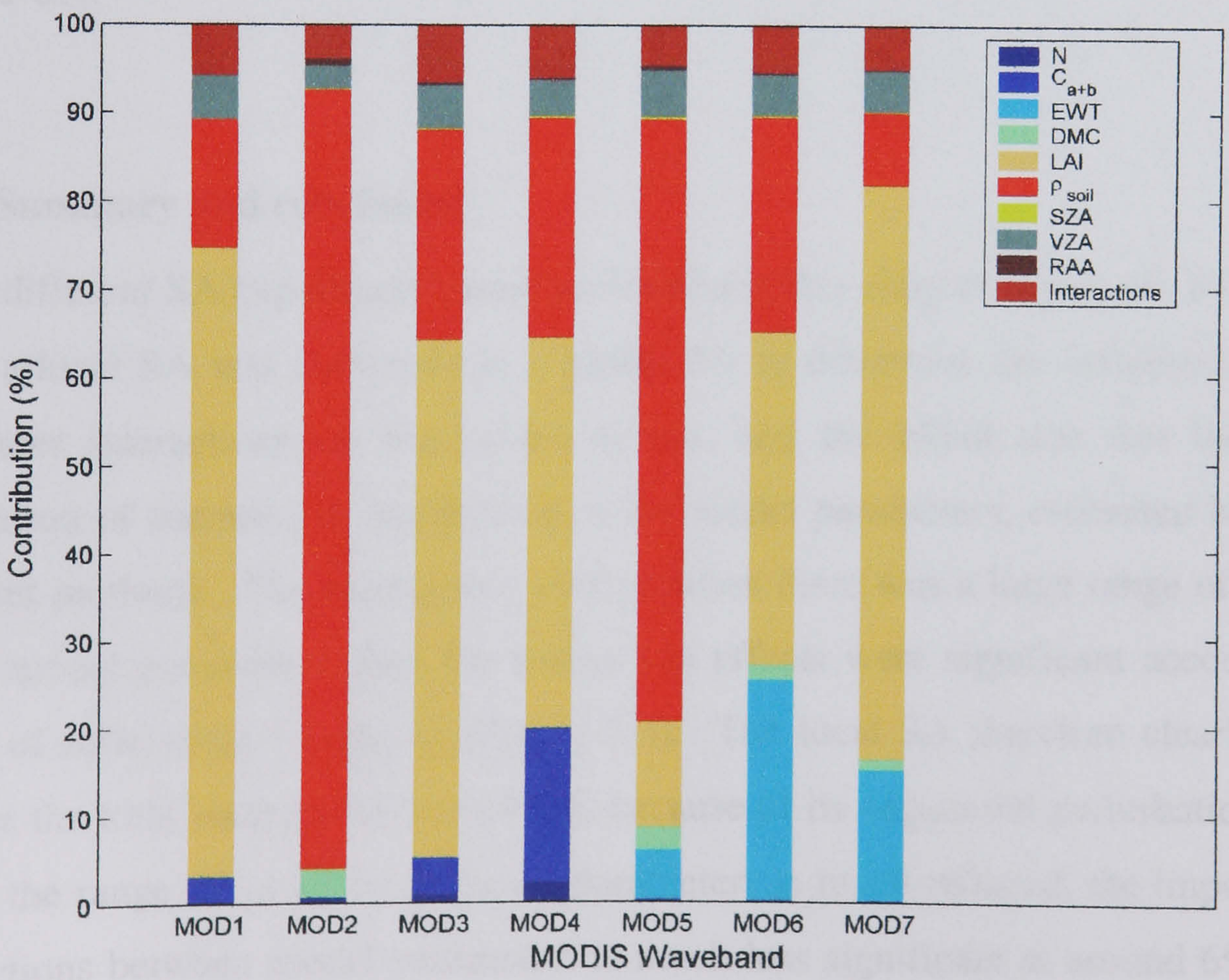

(h) All Plots all model parameters

Figure 7.11 Continued.

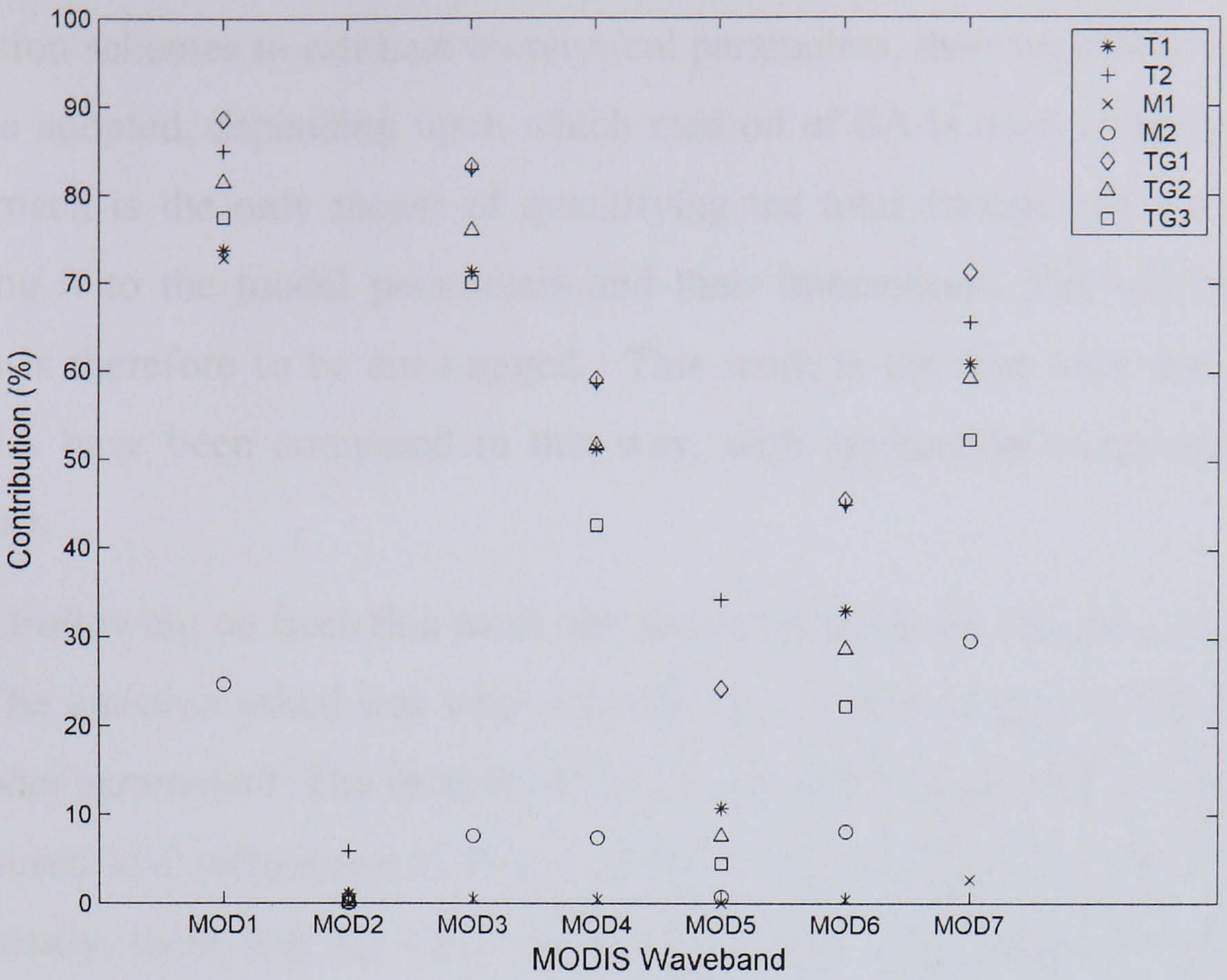

Figure 7.12 Summary of LAI sensitivity in the seven field plot specific MODIS EFAST SA.

7.5 Summary and conclusion

Three different SA experiments were performed in this chapter. First, on a theoretical level, a local SA was compared to a global SA to determine the influence of model parameter interactions on the model output, and the effect that this had on the calculation of the relative importance of the model parameters, estimated by the two different methods. The results showed that when there was a large range of variation in the model parameters, then the interaction effects were significant accounting for ~15% of reflectance variability (Figure 7.3). The local SA therefore clearly fails to capture the total variance of the system, because of its sequential perturbation design. When the range of variation in model parameters is much reduced, the importance of interactions between model parameters is much less significant at around 6% (Figure 7.5). However, there are still marked differences between the two methods in terms of the relative importance of the model parameters. This is also true when there is a large range of variation, and the relative importance of parameters can vary by as much as 47%. In addition there are some large differences in terms of the rank importance of the model parameters.

The implication is that if the results of the SA are used to inform the design of inversion schemes to estimate biophysical parameters, then very different strategies would be adopted, depending upon which method of SA is used. Clearly, the global SA approach is the only means of quantifying the total variance of the system, and attributing it to the model parameters and their interactions. The use of global SA methods is therefore to be encouraged. This work is the first time that a local and global SA have been compared in this way, with application to remote sensing of vegetation.

Following on from this work, the second experiment was also on a theoretical level. The question asked was what was the likely effect of mis-specifiying the PDF for a model parameter? The motivation for this experiment was the fact that there was no measured leaf reflectance and transmittance data available for use in this thesis. Consequently, there was no information on the PDF. SA were performed with the PROSPECT model and two different PDFs were specified for the model parameters, a uniform and Gaussian. Results showed that although differences were as large as 39% in the major water absorption bands, overall, differences in the relative importance of model parameters were generally no greater than 10% across the solar spectrum (Figure 7.8). Consequently, it would seem that the effect of mis-specification of a PDF, would generally not have a significant effect on the overall sensitivity of the model to variation in its parameters.

The final experiment was more practical, where the objective was to quantify the sensitivity of reflectance to variation in LAI at the field plots used in this thesis. Simulations were performed for both the ETM+ and MODIS sensor configurations, using the PROSAIL model and EFAST. Results from both showed that LAI generally dominated reflectance variability in the visible and SWIR regions (cf. Figure 7.9 Figure 7.11). This depended, however, on the range of variation in soil reflectance for the ETM+, and plot level LAI variation in the MODIS simulations. Generally, sensitivity of reflectance to variation in LAI increased as the LAI value increased. Reflectance variability in the NIR was driven by variation in soil reflectance, and LAI had a negligible effect. Interaction effects between parameters were shown to be relatively unimportant in all the simulations, such that variation in reflectance was driven by variation in individual parameters. This will enable parameters which do not account for significant proportions of variance to be fixed in model inversion

work. Given the dominance of LAI in generally more than three wavebands, the prospects for estimating LAI through model inversion would seem to be high with both ETM+ and MODIS data. In the MODIS SA, when the viewing and illumination parameters were included, it was shown that only the view zenith angle has any effect on reflectance variability. This confirms previous work which has shown that most information lies in the spectral domain (Barnsley *et al.* 1997).

The use of canopy reflectance models together with global SA methods represents a powerful tool in the remote sensing toolbox with which to obtain information about the system under study. The information obtained from such work can be used to provide better designed inversion schemes, where data which exhibits greater sensitivity to the parameter of interest can be used, whereas data which exhibits little sensitivity can be omitted from the analysis. In so doing the likely accuracy of model inversions will be increased (Privette *et al.* 1996a). The next chapter of this thesis will use the results obtained in this chapter to inform the design of inversion schemes to estimate LAI.

8 Estimating Leaf Area Index Via Neural Network Inversion

8.1 Introduction and objectives

This chapter uses the results from chapter 7 to aid the design and implementation of a number of experiments to estimate leaf area index (LAI) from artificial neural networks (ANN), using both ETM+ and MODIS data. Clearly, a neural network can be trained with various inputs, however, it is desirable to use inputs which contain the most information about the parameter to be estimated. In chapter 7 it was shown that different wavebands of the ETM+ and MODIS sensors, display differing sensitivity to variation in LAI, with sensitivity generally being greater in the visible (VIS) and short-wave infrared (SWIR), than the near infra-red (NIR), which displayed very little sensitivity to variation in LAI. A neural network inversion involves training a network to try to learn the underlying relationship between the inputs, and the output, and thereby establish a mapping function between them. It is known that networks can be confused, and perform sub-optimally, when data which contains little or no information about the parameter of interest are used in the training process (Crooks 1992). A problem arises however, since it is not known *a priori* which data inputs will provide the highest accuracy, nor what the underlying relationship between inputs and outputs are. Consequently, a number of experiments were carried out in this chapter, with the aim of estimating LAI with as a high an accuracy as possible. Specifically, there were four objectives:

(i) To determine the optimal network architecture and the effect that network architecture has on the resistance of neural networks to noise. ***Rationale***: the underlying relationship between the network inputs and outputs is unknown *a priori*, and needs to be discovered. In addition, all networks will be trained with modelled data, which are essentially error free, yet tested with satellite measurements which contain noise.

(ii) To determine the optimal set of spectral data inputs to the neural networks. ***Rationale***: different wavebands display different sensitivity to

leaf area index, and different accuracy when compared to modelled reflectances. Therefore it was desired to use the optimal band combination to estimate LAI.

(iii) To investigate the effect of adding viewing geometry as an input to the training stage, in addition to the spectral data. ***Rationale***: viewing geometry contains information about the canopy structure which may lead to more accurate inversions.

(iv) To compare the performance of the MODIS LAI product with respect to field measurements, and scaled ETM+ LAI from the neural network inversions. ***Rationale***: field measurements provide an assessment of how well the MODIS LAI product is performing. Because of the difficulty in assessing a product with a few field points, and given that in low LAI value areas the relative estimation error is likely to be high, the spatial variation in LAI is a useful source of information.

8.2 Experimental methods

8.2.1 Artificial neural networks

Multi-layer feed-forward neural networks with back-propagation learning were used in all the experiments carried out in this chapter. Network training was performed with the Levenberg-Marquardt training algorithm (Levenberg 1944; Marquardt 1963). This training algorithm was selected as it is known to provide faster training since it only involves computation of the inverse Hessian matrix when updating the network weights (Bishop 1995), and has been shown to provide accurate results in experimental studies (e.g. Baret *et al.* 1995). Prior to network training the inputs were normalised to lie in the range -1 to 1, so that there was no difference in the input ranges between the different wavebands, which may bias the training. Network training was performed in batch mode where the weights and biases are updated only after the complete training set has been presented and propagated through the network. For all the experiments, networks were trained for 250 epochs, the error goal was set to 0.001, and the learning rate was also set to 0.001. For each network architecture, network training was repeated twenty times in order to experiment with

different initial weights and biases, and also to overcome the potential for local minima to be found. In addition, the activation function from the input layer to the hidden layer was a hyperbolic tangent function, while the activation function from the hidden layer to the output layer was a linear function (Haykin 1999). The performance of the various networks trained was evaluated by calculating the root mean squared error (RMSE) and the coefficient of determination, with both modelled and measured test data sets. The specific details of the various network architectures experimented with are given in the inversions section.

8.2.2 Generating reflectance data

To train a neural network to estimate LAI from reflectance data requires a training data set. Ideally, this training set would consist of measurements of spectral reflectance and corresponding leaf area index values. Unfortunately, this was not, and rarely is, the case in remote sensing where ground measurements of the biophysical parameter of interest and companion reflectances are in short supply (Walthall *et al.* 1993; Cohen & Justice 1999; Privette *et al.* 2000). In the absence of sufficient measurements with which to train and test the networks, the PROSAIL model was used to generate reflectance data.

The training data for the ETM+ inversions were generated according to the ranges and distributions given in Table 8.1. In the light of the results from chapter 6, where it was suggested that the most likely explanation for the discrepancy between the modelled reflectances and measurements is due to inaccurate specification of the soil reflectance, the range of the soil reflectance was set to the minimum value obtained from the 175/077 (Tshane) image, and the maximum was set to that measured in the laboratory, the ranges are given in Table 8.2. 5000 random draws of each of the model parameters were made and PROSAIL was then run for each combination. Because LAI would be estimated from two different ETM+ images (which covered the five ETM+ field plots), there were two different solar zenith angles (SZA) to consider. Consequently, reflectances were simulated for each SZA (43.36 and 37.42 degrees), and then combined to form the training set. The reflectance database thus consisted of 10000 sets of reflectance and corresponding

LAI. The training set was finally created by drawing 5000 samples at random from this database.

A similar approach was adopted for the creation of the MODIS training reflectances. Apart from the soil reflectance, the model parameter ranges were the same as those given in Table 8.1, the range of the soil reflectance is given in Table 8.3. Because the measured reflectances which PROSAIL would be inverted against were all obtained under different illumination and viewing geometries at the seven MODIS field plots, it was required that the training data were consistent with this. Therefore, the seven different SZA, view zenith angles (VZA), and relative azimuth angles (RAA), were included in the PROSAIL simulations (Table 8.4). This may be considered analogous to the way in which a neural network might be trained to estimate biophysical properties from sensors with a fixed viewing geometry (e.g. MISR, CHRIS-PROBA). For each of the seven sets of viewing and illumination geometries, PROSAIL was run for 1000 combinations of the model parameter ranges. The reflectance database thus consisted of 7000 sets of reflectance and corresponding LAI. The training set was finally created by drawing 5000 samples at random from this database. A spherical leaf angle distribution (LAD) was specified for both the ETM+ and MODIS simulations.

Table 8.1 Minimum and maximum parameter values and probability density function for generating the training data.

Parameter	Minimum/Maximum	Probability density function
Leaf structure parameter (N)	1.5 - 3.0	Uniform
Leaf chlorophyll content (C_{a+b})	20 - 60	Uniform
Leaf water content (EWT)	0.0001 - 0.015	Uniform
Leaf dry matter content (DMC)	0.005 - 0.01	Uniform
Leaf area index (LAI)	0.001 -1.37	Gaussian

Table 8.2 Minimum and maximum soil reflectance for generating the ETM+ training data.

Waveband	ETM 1	ETM 2	ETM 3	ETM 4	ETM 5	ETM 7
Minimum	0.061	0.114	0.185	0.314	0.405	0.320
Maximum	0.188	0.309	0.464	0.561	0.739	0.716

Table 8.3 Minimum and maximum soil reflectance values for the field plot specific MODIS EFAST SA.

Waveband	Tshane Plots	Mabuasehube Plots	Tshabong Plots
MOD1	0.370 - 0.452	0.351 - 0.392	0.319 - 0.347
MOD2	0.473 - 0.568	0.462 - 0.502	0.430 - 0.464
MOD3	0.146 - 0.178	0.116 - 0.143	0.112 - 0.122
MOD4	0.237 - 0.285	0.200 - 0.233	0.190 - 0.206
MOD5	0.608 - 0.698	0.590 - 0.631	0.557 - 0.608
MOD6	0.657 - 0.737	0.638 - 0.677	0.597 - 0.651
MOD7	0.664 - 0.742	0.647 - 0.688	0.606 - 0.660

Table 8.4 Viewing and illumination geometries for the seven MODIS field plots, for creating the MODIS training data.

	Field plot						
Parameter	T1	T2	M1	M2	TG1	TG2	TG3
View zenith angle	19.05f	55.46b	5.69b	21.79f	25.1f	24.64f	12.14f
Solar zenith angle	29.03	37.55	32.11	29.33	29.53	29.50	32.76
Relative azimuth angle	137.99	33.75	35.74	137.2	136.34	136.74	132.75

Note: f indicates forward scatter, and b the backscatter direction.

8.3 ETM+ inversions

8.3.1 Objective 1: Determining optimal network architecture

A priori, the complexity of the relationship between the network inputs (reflectance) and the network output (LAI) is not known. Using a neural network to invert a canopy reflectance model (or any other model), therefore, almost inevitably involves some experimentation with the number of layers and nodes in each layer, in order to determine the optimal network architecture to perform the task. Here, a series of experiments were conducted where networks consisting of one and two hidden layers, with various numbers of nodes in each layer, were tested. The single hidden layer networks were composed of 5 to 20 nodes, whilst the two hidden layer networks consisted of 5 to 20 nodes in the first hidden layer, and 1 to 6 nodes in the second hidden layer. In total, 16 one hidden layer and 96 two hidden layer networks were tested.

The networks were trained and tested with independent modelled datasets, using simulated ETM+ wavebands 1, 2, 3, 5 and 7. Since the ultimate objective is to estimate LAI from satellite measurements of reflected radiance, and given the fact that no measurement is ever noise free, it is important to examine the effect of noise on the relationship between network architecture and performance (prediction accuracy). Therefore the test data sets were contaminated with white proportional noise, according to equation 8.1:

$$R_\lambda' = R_\lambda + \Delta R_\lambda \qquad (8.1)$$

Where R_λ' is the noisy data set, R_λ is the simulated reflectance, and ΔR_λ is the noise added to each simulated reflectance value. ΔR_λ is obtained by multiplying the simulated reflectance R_λ by the error level E, which varied from 0-5%, 10%, 20% and 30%, such that there were nine test data sets.

8.3.1.1 Results and discussion

The performance of the single hidden layer networks is displayed in Figure 8.1. It can be seen that with respect to the RMSE of the predictions there is no relationship between network architecture (hereafter size) and network accuracy of estimation, for noise levels up to 10% (Figure 8.1a). For noise levels of 20% and 30% however, there is a negative relationship between network size and network accuracy of estimation, accuracy decreases as the network size increases (Figure 8.1a). With respect to the coefficient of determination there is a clear positive relationship between network size and accuracy of estimation for noise levels up to 10%, accuracy increases as network size increases, and a clear negative relationship for noise levels of 20% and 30%, accuracy decreases as network size increases (Figure 8.1b). To avoid any confusion, it is important to make clear that the sign of the relationship between network size and the RMSE/coefficient of determination is assessed with respect to what an increase/decrease in the particular statistic means with respect to accuracy, where an increase in the RMSE indicates a decrease in accuracy, while an increase in the coefficient of determination indicates an increase in accuracy. This is done so that the assessment is effectively independent of the direction (up/down) in which the two statistics move.

Figures 8.2a,b show the results for the two hidden layer networks, where it is clear that there is a positive relationship between network size and accuracy of estimation with respect to both the RMSE and coefficient of determination, for noise levels up to 5% (Figure 8.2a,b). At noise levels of 10% there is a less clear relationship between network size and accuracy, while beyond 20% noise the relationship reverses and becomes negative - as network size increases accuracy decreases. This is the same pattern as observed with the single hidden layer networks, and indicates that as the test data set departs from the data the network was trained with, the increase in network size leads to the network learning the training set too well, and thus loses generalisation power.

For both the one and two hidden layer networks the accuracy of estimation is generally independent of network size for noise levels of up to 5%, beyond which there is a fairly rapid degradation in network performance overall. This relationship is shown in Figure 8.3, where the best performing one and two hidden layer network at each noise level, is plotted against RMSE. Figure 8.3 also shows that the difference in performance between the one and two hidden layer networks only becomes marked at noise levels of 30%. Up to 10% noise in the test data sets there is no difference between the one and two hidden layer networks; at 20% noise the two hidden layer network outperforms the one hidden layer network by 0.022 RMSE (0.233 one hidden layer, 0.211 two hidden layers), a difference which is likely to be well below the accuracy achievable with measured data sets; while at 30% noise there is a difference of 0.081 (0.307 one hidden layer, 0.226 two hidden layers), again a difference which is likely to be well beyond the accuracy achievable with measured data sets. The architecture of the best performing one hidden layer network at 20% and 30% noise contained 9 nodes in the hidden layer in both cases, while the architecture of the best performing two hidden layer networks contained 6 and 1, and 15 and 1 nodes in the first and second hidden layers, respectively. The smaller two hidden layer networks provide higher accuracy than the larger two hidden layer networks.

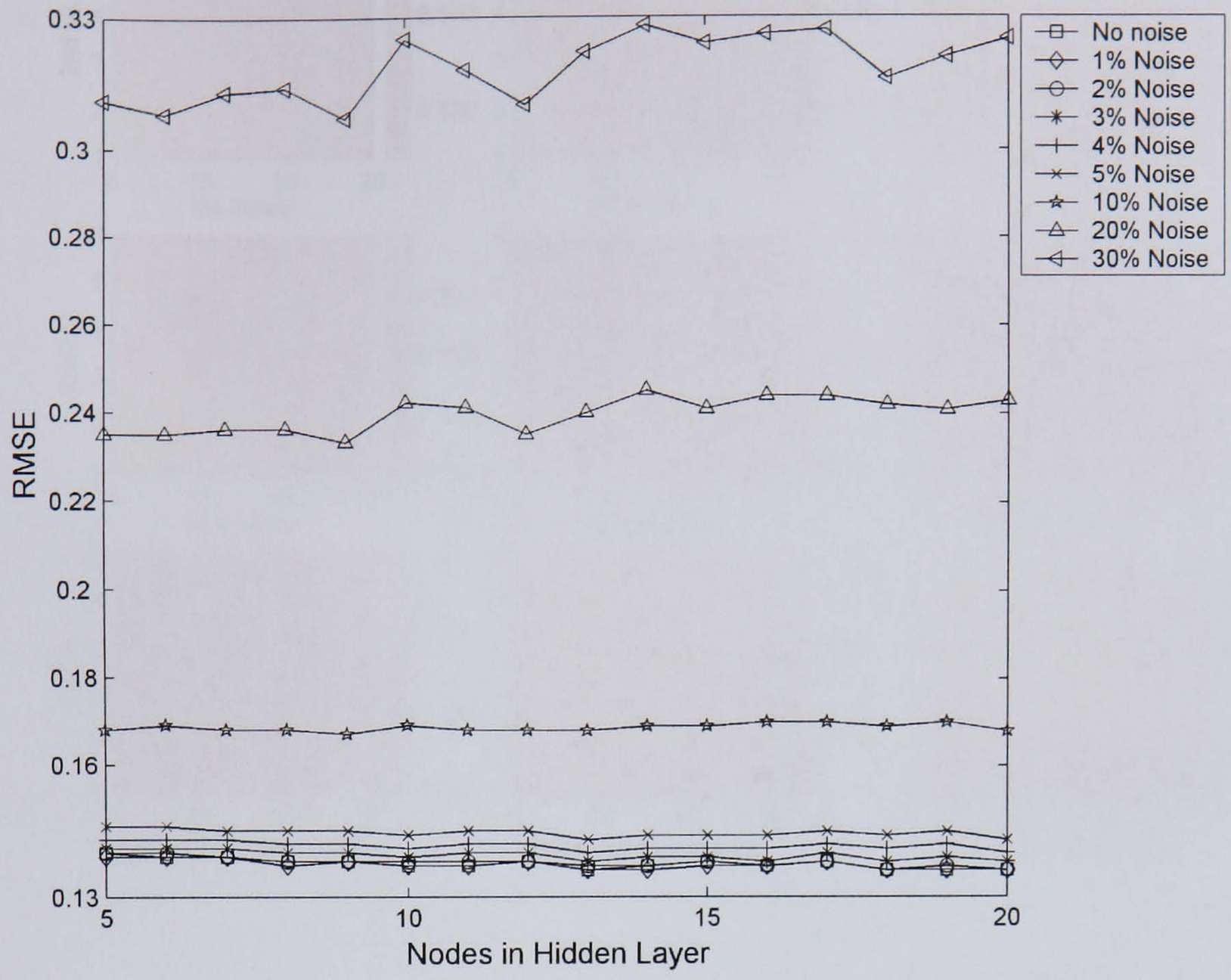

(a)

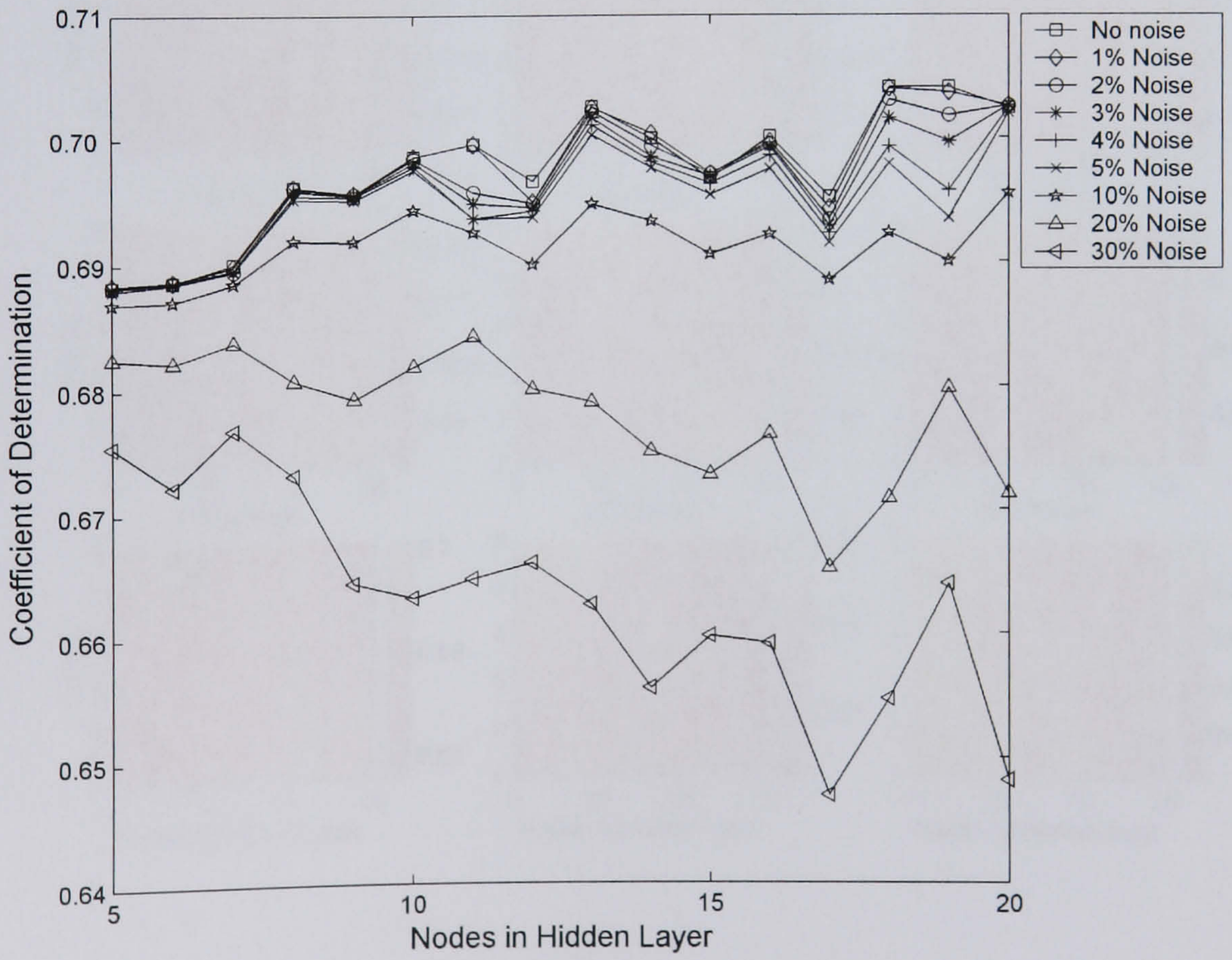

(b)

Figure 8.1 Summary results of training different networks with one hidden layer, when tested with nine different levels of noise in the testing data, (a) root mean squared error, (b) coefficient of determination.

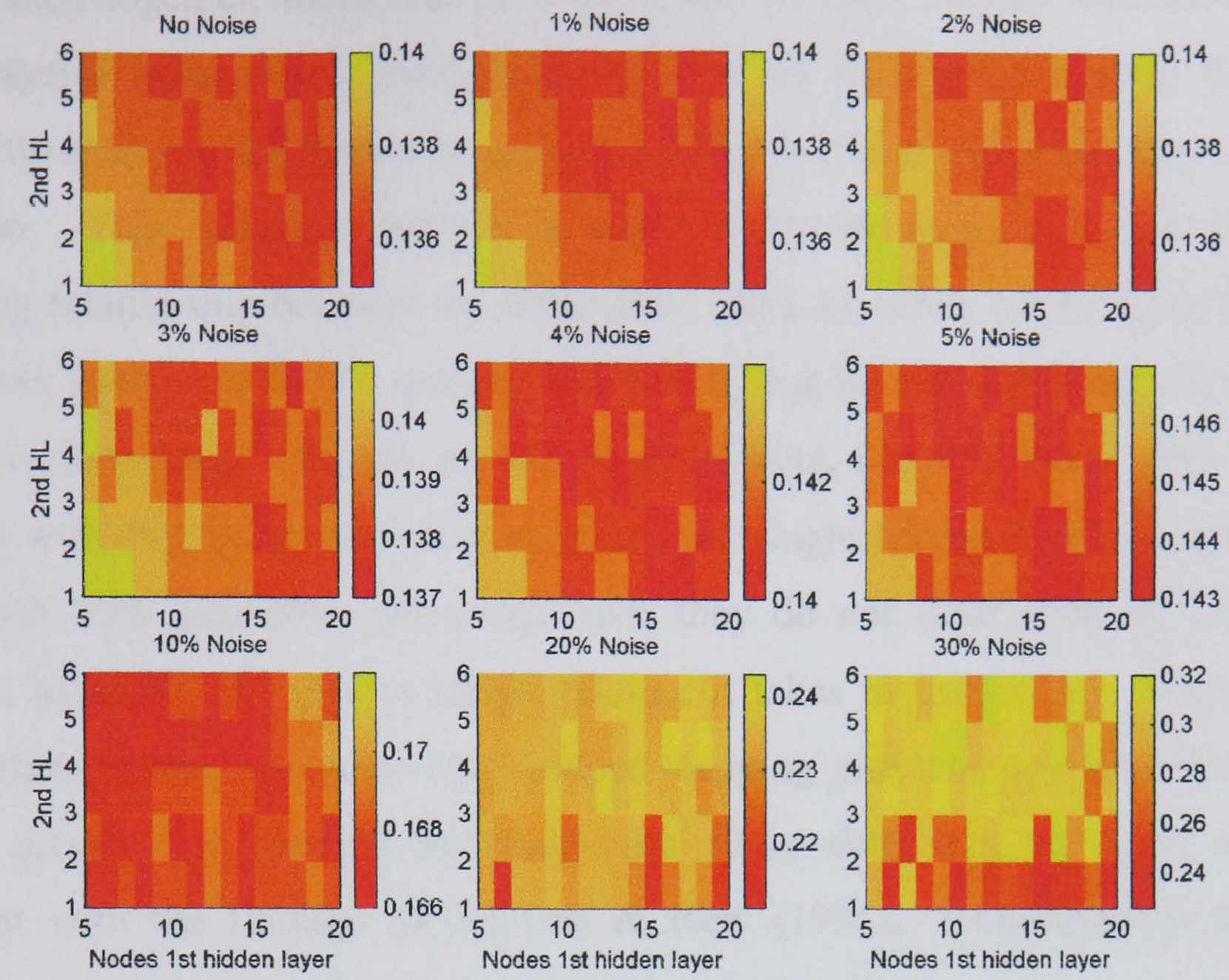

(a)

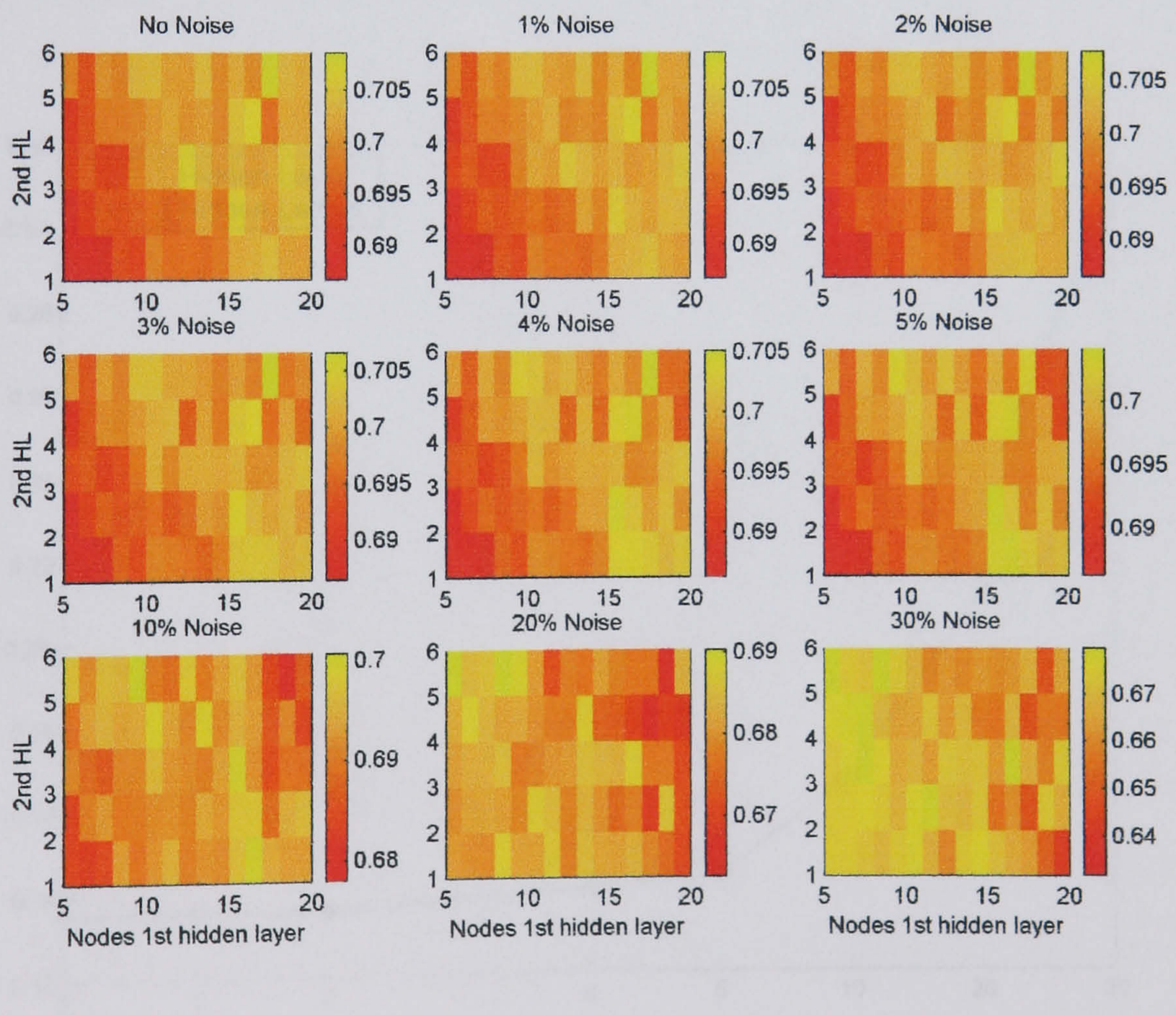

(b)

Figure 8.2 Summary results of training networks with two hidden layers, tested with nine different levels of noise in the testing data, (a) root mean squared error, (b) coefficient of determination.

Taken together, these results suggest that as network size increases (to two hidden layers) there is less sensitivity to noise up to a point beyond which the relationship reverses and further increases in network size produce poorer accuracy of estimation. This confirms that the network has to be large enough to learn the underlying relationship between the reflectance and LAI, while not being so large that the network starts to learn the training set so well, that the generalisation ability of the network is diminished. For the results presented here, it would appear that although networks with two hidden layers outperform the single hidden layer networks when tested with 20% and 30% noise data sets, they do not offer such an increase in accuracy, to justify the greater length of time it takes to train them. These results suggest that for this particular input-output mapping problem, smaller networks are able to produce comparable accuracy with noisy data sets as larger networks, consistent with the findings of Sietsma & Row (1991). Consequently, all future inversions were carried out with one hidden layer networks.

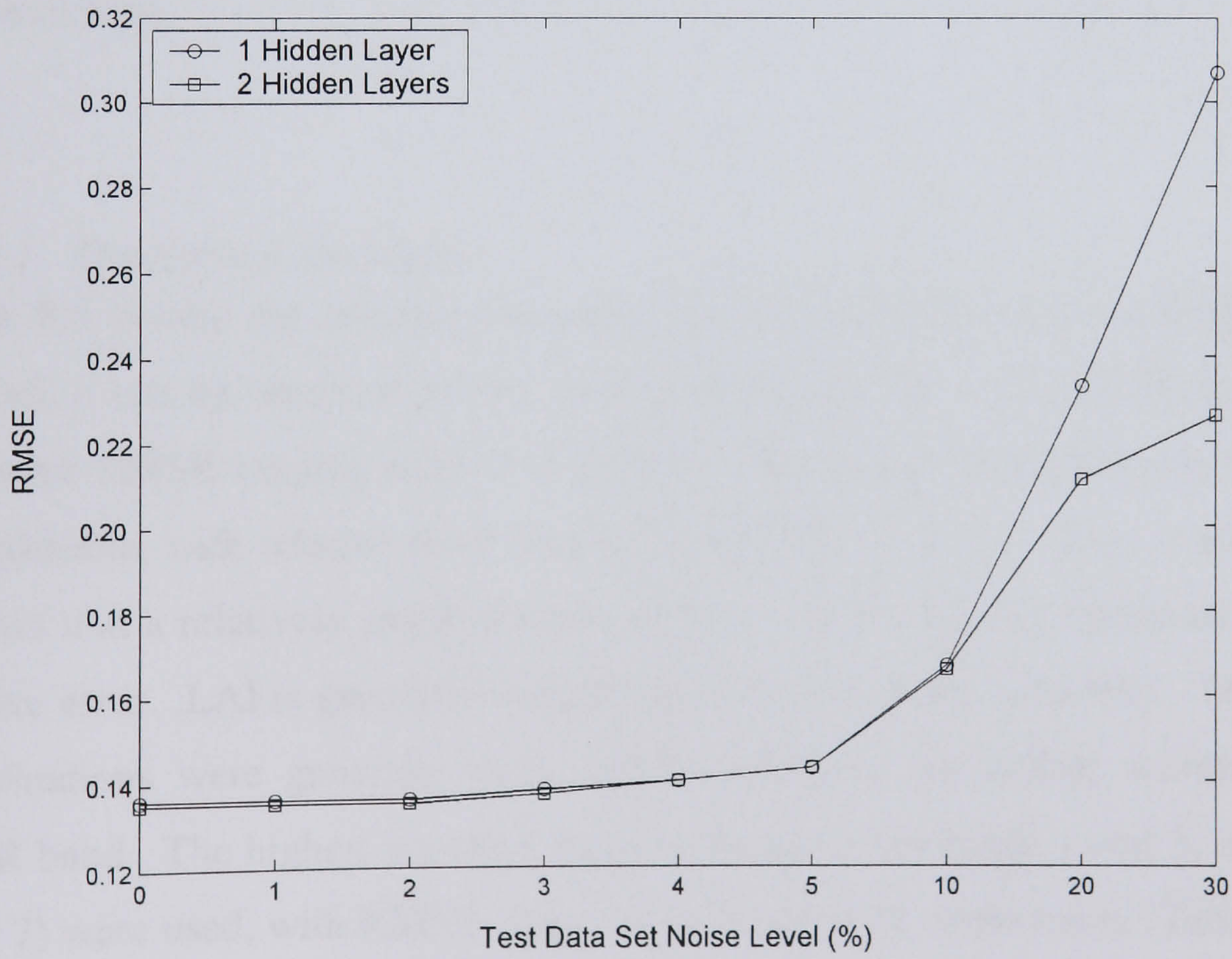

Figure 8.3 Comparative performance of the best one and two hidden layer networks, against the nine different test data sets.

8.3.2 Objective 2: Determining optimal band combinations

The results of chapter 7 showed that different wavebands display different sensitivity to variation in LAI. It is likely therefore, that use of different waveband combinations will result in different accuracy of estimated LAI. In order to test this, eleven different band combinations were used as input to the neural network. It was expected *a priori*, that using the near-infrared band (ETM4) would provide sub-optimal input, since the results of the model sensitivity analyses showed that the NIR exhibits very little sensitivity to variation in LAI. For this reason the NIR was only used as an input to the networks on two occasions, once to provide a test of the network performance when all ETM+ wavebands were used, and second, in combination with the red waveband (ETM 3), to provide a test of the commonly used red and NIR waveband combination. The results of these band combinations would therefore provide a test of the sensitivity analysis results. For each band combination, 16 different single hidden layer networks were trained with 5 to 20 nodes in the hidden layer. The best network was selected based on its performance with respect to the measurements, where a low value of RMSE was required along with a high value for the coefficient of determination.

8.3.2.1 Results and discussion

Table 8.5 details the summary accuracy for the different band combinations used. Overall, it can be seen that for all band combinations the error of estimation is fairly low with RMSE ranging from 0.31 to 0.41. In relative terms however, the error is considerable, with relative error ranging from 132% to 221%. This is attributable to the fact that a relatively small absolute error at a low LAI plot, translates into a large relative error. LAI is generally overestimated by the neural networks. The best band combinations were generally those which combined the visible wavebands and a SWIR band. The highest accuracy being achieved when bands 1 and 3, and 1, 3, and 5 (or 7) were used, with RMSE values of 0.31 and 0.32 respectively (Table 8.5). The results for bands 1 and 3 and 1, 3, and 5 are shown in Figure 8.4a,b. The fact that the best results were obtained with the VIS and SWIR wavebands reflects the sensitivity of these wavebands to variation in LAI. This suggestion is supported by the results obtained when the NIR waveband (insensitive to variation in LAI), is submitted as an input. When the NIR (band 4) is used in combination with all other bands there is an

RMSE of 0.41 - the second lowest accuracy overall, whilst when used in combination with the red waveband, produced the lowest accuracy, with an RMSE of 0.43 (Table 8.5). Interestingly, the coefficient of determination for the band 3 and 4 combination is the highest recorded.

Comparing across field plots, Figures 8.4a,b show that for the best two band combinations (bands 13 and 135), the results obtained at plot TG1 consistently achieve the highest accuracy, with mean estimated LAI being 0.38 and 0.40 respectively, against a field measured LAI of 0.25 (Table 8.6). Results at the other plots are poor, with RMSE ranging from 0.25-0.46 for both band combinations. A possible explanation for the results at TG1 is that there exists a stronger relationship between the spectral data recorded over this site and LAI, as learned by the neural network. This suggestion is supported by the results of the modelling in chapter 6, which show that the PROSAIL model is most accurate at TG1, while significantly poorer for the other plots, especially T1 and T2.

Table 8.5 ETM+ neural network LAI inversion results for all band combinations.

Band combination	Network	RMSE	R^2	Relative error (%)
123457	6:14:1	0.41	0.177	200
12357	5:5:1	0.34	0.438	141
1237	4:7:1	0.34	0.486	146
1235	4:6:1	0.35	0.470	143
123	3:7:1	0.34	0.461	141
137	3:5:1	0.32	0.382	139
357	3:5:1	0.39	0.090	187
135	3:9:1	0.32	0.494	134
13	2:10:1	0.31	0.494	132
37	2:6:1	0.39	0.092	188
34	2:18:1	0.43	0.499	221

Note: network architecture notation is: input nodes:hidden layer nodes:output nodes

Table 8.6 ETM+ neural network inversion LAI estimation summary statistics for the best two (13 and 135) and the commonly used red/NIR (34) band combinations, by field plot.

Bands/Plot	Min P	Max P	S.D. P	Mean P	Mean O
13					
T1	0.75	0.84	0.03	0.81	0.35
T2	0.65	0.79	0.04	0.71	0.45
TG1	0.34	0.43	0.03	0.38	0.25
TG2	0.42	0.57	0.04	0.51	0.16
TG3	0.39	0.57	0.06	0.49	0.22
135					
T1	0.74	0.85	0.03	0.81	0.35
T2	0.65	0.78	0.04	0.71	0.45
TG1	0.35	0.45	0.04	0.40	0.25
TG2	0.41	0.58	0.04	0.51	0.16
TG3	0.39	0.60	0.07	0.50	0.22
34					
T1	0.22	0.55	0.09	0.37	0.35
T2	0.41	0.76	0.10	0.55	0.45
TG1	0.73	0.74	0.01	0.74	0.25
TG2	0.71	0.83	0.05	0.78	0.16
TG3	0.72	0.75	0.01	0.74	0.22

Note: P indicates predicted, and O observed LAI. S.D. is the standard deviation.

In contrast, there is a striking difference with respect to estimation accuracy and precision at the field plots, when using bands 3 and 4. Highest accuracy is achieved over plots T1 and T2 (Figure 8.4c), with mean estimated LAI lying very close to the 1:1 line at 0.37 and 0.55, against field measured LAI of 0.35 and 0.45, respectively (Table 8.6). The estimates at these two plots however are not very precise, with a range of 0.33 and 0.35, respectively (Table 8.6). Conversely, the accuracy at plots TG1 and TG3 is considerably lower than with the two best band combinations of 13, and 135, with mean estimated LAI at 0.74 for both plots, compared to a field estimate of 0.25 and 0.22 respectively. The precision is considerably higher however, with a range of 0.01 and 0.03 for TG1 and TG2, respectively. It is difficult to say why plots T1 and T2 outperform the other plots with this band combination, given that these two plots displayed the lowest accuracy with respect to the spectral measurements in chapter 6.

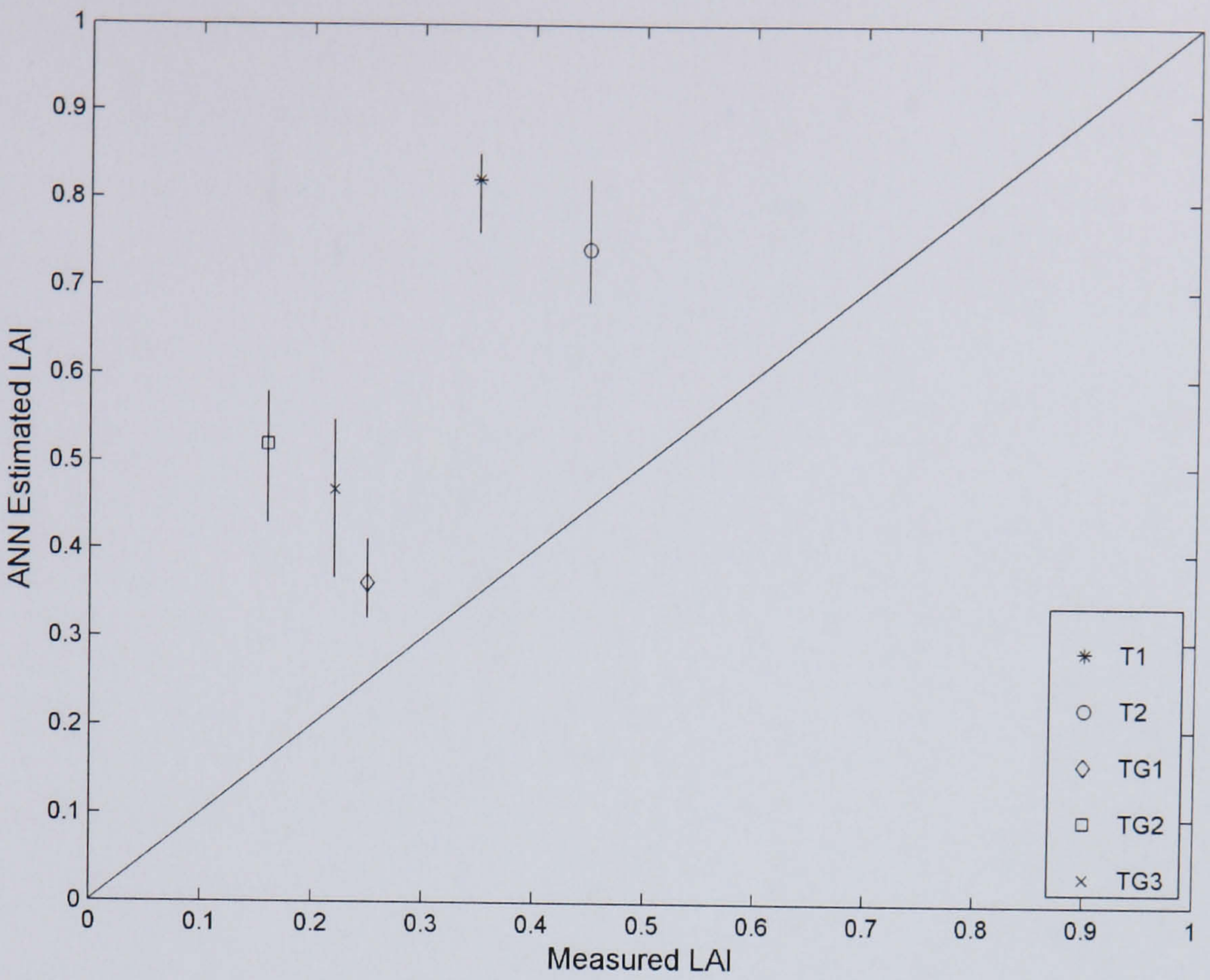

(a)

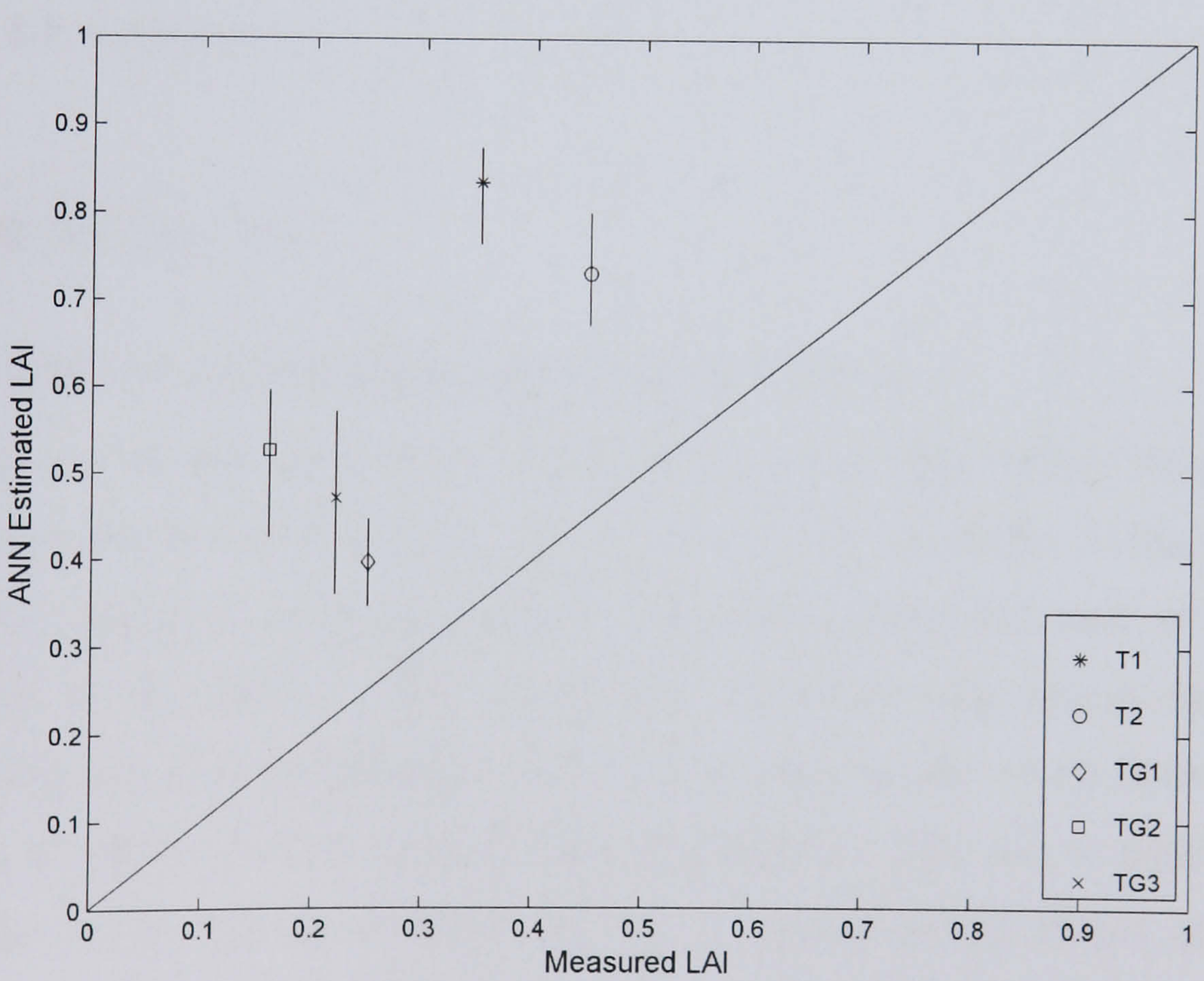

(b)

Figure 8.4 Neural network estimated LAI from ETM+ data against field measured LAI, using (a) bands 1 and 3, and (b) bands 1, 3, and 5, and (c) bands 3 and 4. Error bars represent the minimum and maximum estimated values. Measured LAI is that obtained from ground measurements with the SunScan plant canopy analyser.

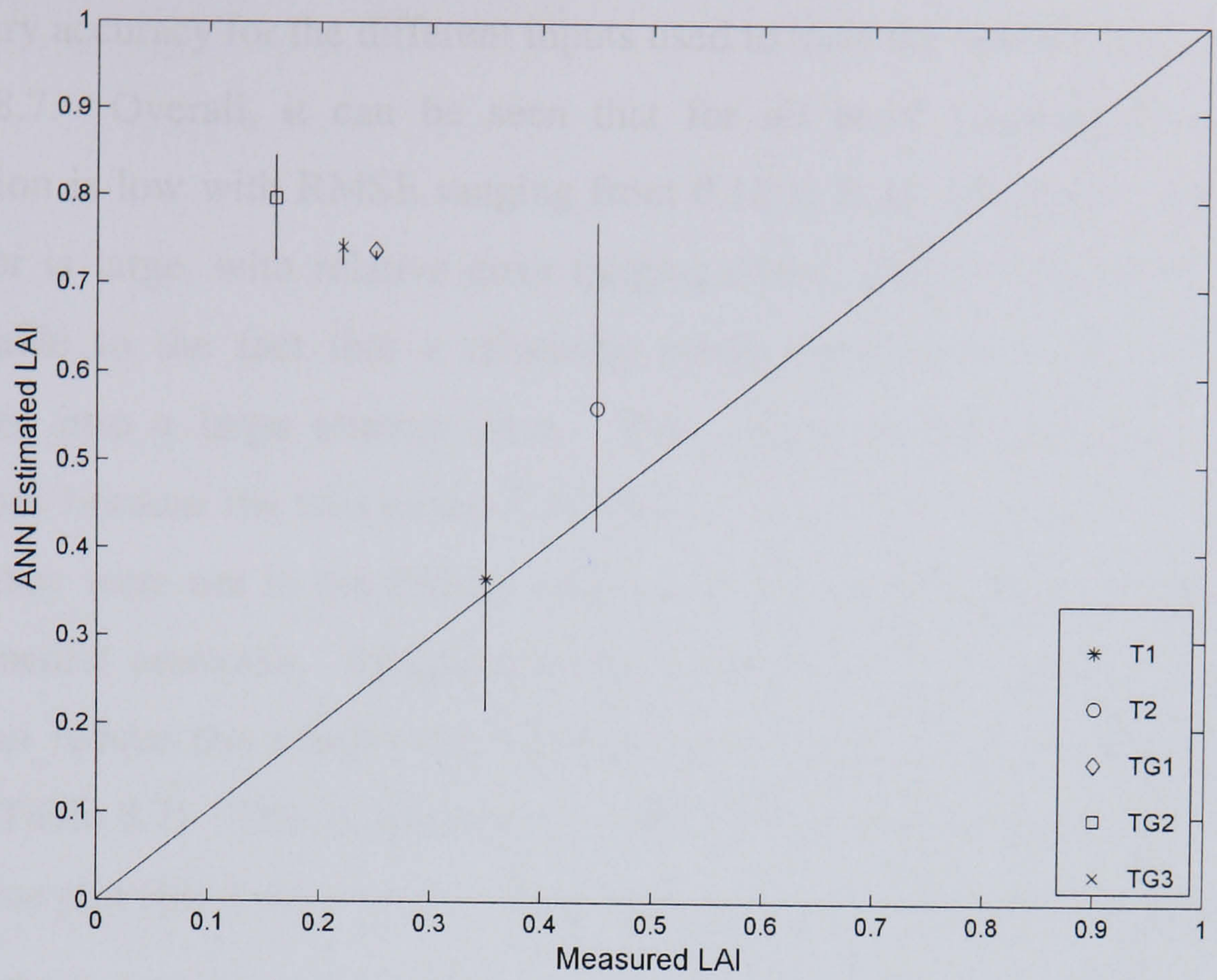

(c)

Figure 8.4 Continued.

8.4 MODIS inversions

8.4.1 Objective 1: Determining optimal network inputs

Not only do different wavebands contain different information about the parameter to be inverted, but it is well known, and has been shown in chapter 7, that the angle at which the image is acquired contains information about the state of the surface (Barnsley *et al.* 1997). This experiment therefore investigated the effect of introducing the view zenith angle (VZA) as an input to the neural network training process, in addition to the various band combinations. The way in which VZA was introduced as an input is described in §8.2.2. Based on the results of the ETM+ inversions, and the results of chapter 7, the two MODIS NIR wavebands (2 and 5) were not used as input to the networks. Again, for each different set of network inputs, 16 different networks were trained with 5 to 20 nodes in the hidden layer, and the best network was selected based on its performance with respect to the measurements, where a low value of RMSE was required along with a high value for the coefficient of determination.

8.4.1.1 Results and discussion

Summary accuracy for the different inputs used to train the neural networks is given in Table 8.7. Overall, it can be seen that for all band combinations the error of estimation is low with RMSE ranging from 0.18 to 0.35. In relative terms however, the error is large, with relative error ranging from 1298% to 291%. Again, this is attributable to the fact that a relatively small absolute error at a low LAI plot, translates into a large relative error. This fact is exacerbated for these MODIS inversions because the two lowest LAI plots - M1 and M2, are part of the estimates, which they were not in the ETM+ inversions. LAI is again generally overestimated by the neural networks. Intriguingly, inclusion of the VZA in the network training serves to reduce the relative error substantially in all cases, to between 291% and 455% (Table 8.7). This is primarily a result of increasing the accuracy at the lowest LAI value plot (M1 LAI = 0.01). This increase is shown in Figures 8.5a,b.

Table 8.7 shows that the highest accuracy is achieved when MODIS bands 1, 3, 4 and 6 are used together with the VZA, an RMSE of 0.18. Estimated LAI for plots T1, T2, TG3 and M1 sit very close to the 1:1 line, while the estimated LAI at the other three plots are overestimated significantly (Figure 8.5a). The next highest accuracy is achieved when the same band combination is used without the VZA, an RMSE of 0.21 (Figure 8.5b). Clearly, use of the VZA in addition to the spectral data, has helped to increase the accuracy in this case. However, this is not true in all cases. When each of the different band combinations are compared against the same band combination with the VZA, there is no clear relationship observed with respect to the RMSE, with the spectral data alone sometimes providing the highest accuracy, while in others introduction of the VZA serves to increase the accuracy (Table 8.7). Interestingly, when the VZA was used as an input the network training actually met the error goal in all cases, and training of the network proceeded much quicker, indicating that the network was better able to learn the relationship between the inputs and outputs, and this is shown graphically in Figure 8.6. The fact that there is no consistent relationship with respect to the RMSE of the estimations when the VZA is used as an input, indicates that meeting the error goal does not automatically transfer into higher accuracy of estimation.

It is worthwhile to consider the difference in performance with respect to the RMSE for the best two combinations, there is a difference of 0.03. The fact that

spectral data alone are able to produce comparable accuracy to use of the VZA, indicates that use of viewing conditions may not add that much extra information to the inversion, since much of the information will already be contained in the spectral data acquired under given viewing conditions. A similar observation, though with respect to the SZA, was reported by Kimes *et al.* (2002), where the SZA was not selected as input to a neural network by a variable selection algorithm, because it did not improve the network accuracy. These results therefore confirm the SA work in chapter 7.

These results would seem to indicate that use of known ancillary data in the network training process does not lead to appreciable improvements in network performance. This implies that the oft quoted limitation of neural networks - that they have not been generalised to handle any arbitrary viewing/illumination angles, may not be as insurmountable as had been thought. The results presented here provide only a limited test of this issue however. It is important to point out also that, had the soil reflectance been modelled as non-Lambertian, different results might be expected, given the influence of soil reflectance in these low LAI ecosystems. Nevertheless, the issue is deserving of further investigation, where, if a network trained with spectral data generated over a large range of viewing and illumination conditions, can be shown to produce acceptable accuracy, then the generalisation of neural networks to arbitrary viewing/illumination angles may be established.

Table 8.7 MODIS inversion results for all band/input combinations.

Band combination	Network	RMSE	R^2	Relative error (%)
1,3,4,6,7	5:16:1	0.23	0.66	1253
1,3,4,6,7,VZA	6:8:1	0.30	0.41	323
1,3,4,6	4:20:1	0.21	0.18	1298
1,3,4,6,VZA	5:12:1	0.18	0.36	291
1,3,4	3:20:1	0.24	0.03	1218
1,3,4,VZA	4:8:1	0.24	0.18	400
1,3,6	3:5:1	0.35	0.14	1281
1,3,6,VZA	4:10:1	0.27	0.23	455
1,3	2:17:1	0.31	0.13	1204
1,3,VZA	3:12:1	0.23	0.52	320

Note: network architecture notation is: input nodes:hidden layer nodes:output nodes

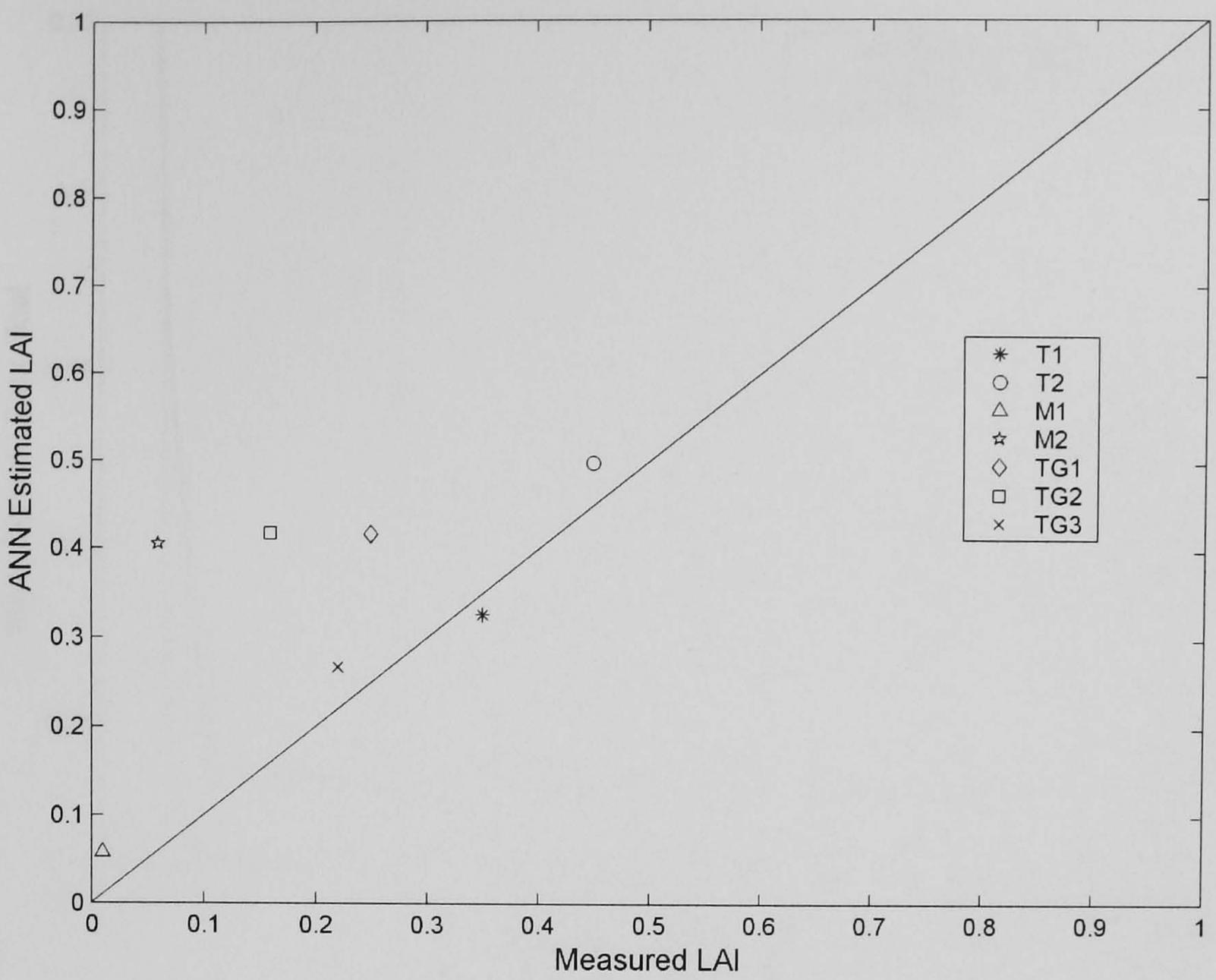

(a)

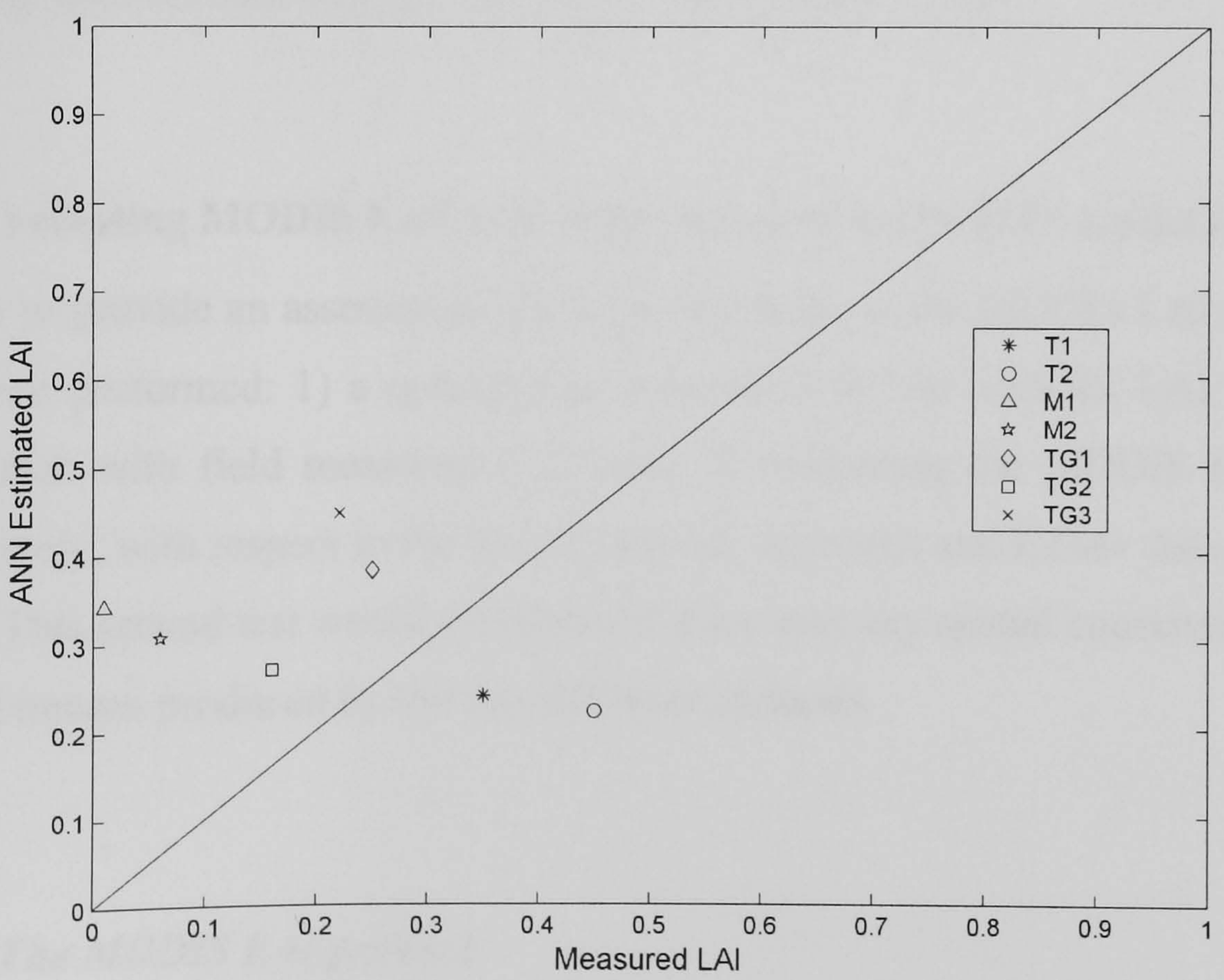

(b)

Figure 8.5 Neural network estimated LAI from MODIS data against field measured LAI, using (a) bands 1, 3, 4, 6 and VZA and (b) bands 1, 3, 4, and 6.

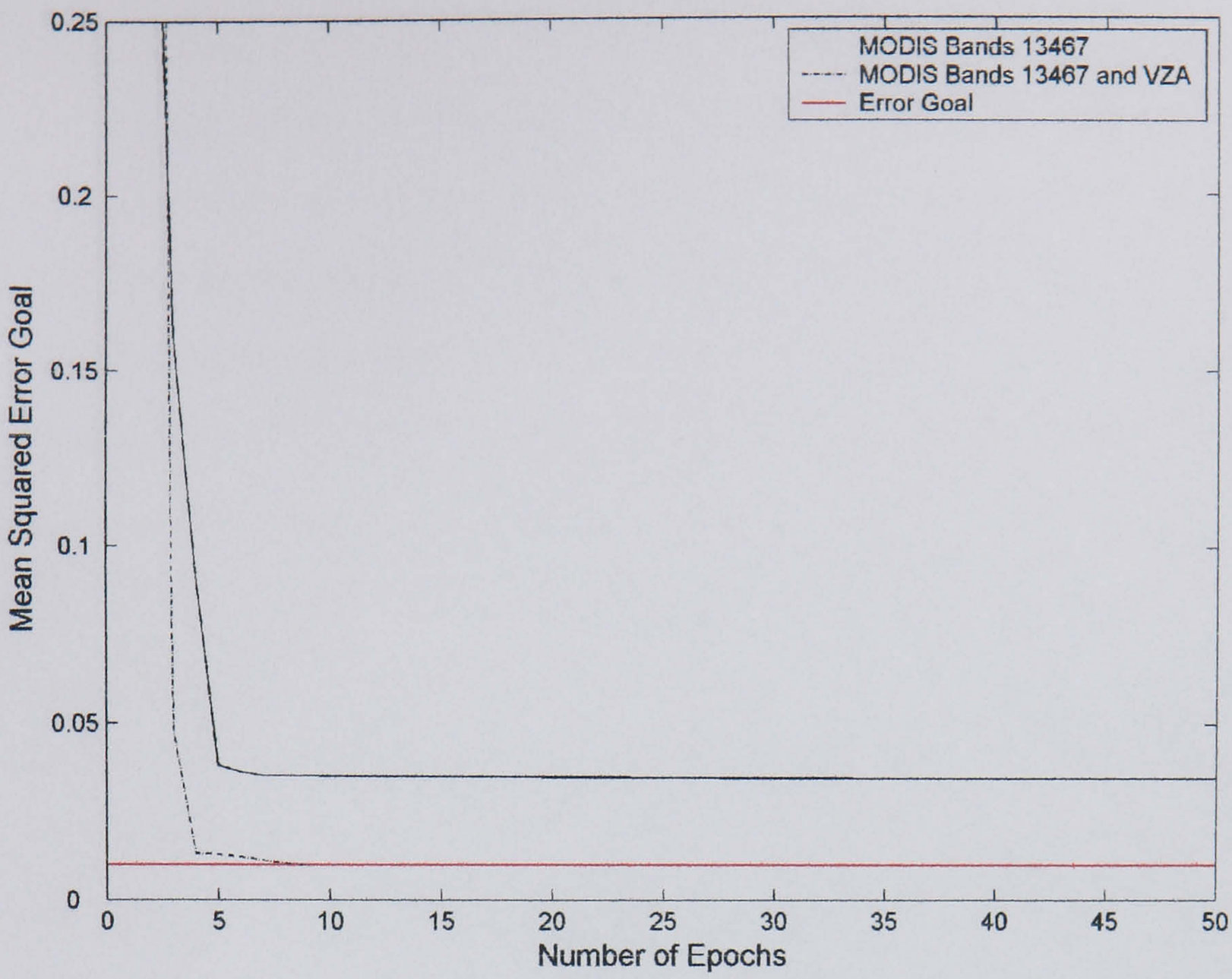

Figure 8.6 Comparison of the training record when the network has spectral data alone and spectral data together with view zenith angle as input.

8.5 Evaluating MODIS LAI with field measured and ETM+ scaled LAI

In order to provide an assessment of the performance of the MODIS LAI product two tests were performed: 1) a quantitative assessment of the MODIS LAI retrieval by comparison with field measured LAI, and, 2) evaluating the MODIS LAI product qualitatively, with respect to the neural network approach and ETM+ data used in this thesis. This second test would determine if there was any spatial consistency between the LAI images produced by the two different methods.

8.5.1 The MODIS LAI product

The MODIS LAI/FPAR product is produced every eight days at a spatial resolution of 1km (product ID: MOD15A2), and is available for free download from the Earth observing data gateway (www 8.1). This product is just one of a suite of products produced routinely by the MODIS sensor (Justice *et al.* 2002). The MODIS LAI product is generated from a radiative transfer (RT) based model look-up table (LUT) inversion. A full description of the MODIS LAI algorithm is provided in Knyazikhin

et al. (1998a,b, 1999). Here, only the fundamental approach is described. The basis for the MODIS LAI algorithm is a global landcover map for six major biomes: 1) grasses and cereal crops, 2) shrubs, 3) broadleaf crops, 4) savannas, 5) broadleaf forests, and 6) needle forests (Myneni *et al.* 1997). For each of these biomes there is a LUT of modelled reflectances which contains biome specific ranges for canopy cover, LAI, soil reflectance, clumping, and viewing and illumination geometries, among others. In this way, the LUT for each biome contains a number of constraints which helps to reduce the number of possible solutions. The algorithm proceeds by finding the correct LUT to search, with reference to the landcover map, then compares the MODIS reflectances in the red and NIR (band 1 and 2) against those stored in the LUT. Those modelled reflectances which are within a given percentage of the MODIS reflectances are considered an acceptable solution (Wang *et al.* 2001). Given the fact that the inverse problem is ill-posed, there are often many solutions to the problem, in such cases the LAI is estimated as a weighted average of all possible solutions. At high levels of LAI, reflectance in the red can become saturated where there is no sensitivity to variation in LAI. In such cases the retrieval is said to belong to the saturation domain. If this LUT method fails to provide a solution, there is a back up algorithm which is based on biome specific NDVI/LAI relationships (Myneni *et al.* 1995, 2002).

Accompanying the LAI/FPAR product are two additional data layers, containing quality control (QC) information about the LAI product, at the pixel level. These QC files provide information, *inter alia*, on the quality of the data used, presence of cloud cover and the retrieval method used, which is one of five possibilities (Myneni *et al.* www 8.2):

(i) Main RT method used with the best possible results

(ii) Main RT method used with saturation

(iii) Main RT method failed due to geometry problems, back up NDVI method used

(iv) Main RT method failed due to problems other than geometry, back up NDVI method used

(v) No retrieval

The retrieval method used at each pixel is used as a measure of the overall quality of the retrieval. The MODIS LAI product used for the comparison with field measured LAI and ETM+ scaled LAI were all collection 4 products.

8.5.2 Objective 3: Comparison of MODIS LAI with field measured LAI

To compare the MODIS LAI produced at a resolution of 1km with the field measurements made within a 200m by 150m grid, clearly presents a scale mismatch. To perform the comparison essentially assumes that there is no difference between LAI measured at the two different resolutions. Tian *et al.* (2002), present results which suggest this may be the case for one of the Tshane plots used in this thesis (T1). They compared LAI measured at 750m scale and 250m scale using the Students t-test, and found that there was no significant difference between the two data sets, thus indicating that there may be spatial uniformity over the field plot. If these results are applicable to the other sites then the scale mismatch problem may be circumvented, to some extent. While this is an obvious limitation, the comparison is made nevertheless, since it at least offers an indication of the performance of the MODIS LAI product, in these semi-arid savanna plots.

The MODIS LAI retrievals at each plot were obtained using the main RT method with 'the best possible results'. Figure 8.7 shows the relationship between the MODIS LAI and field measured LAI, where it can be seen that plots T1, T2, and TG3 almost sit on the 1:1 line, with MODIS LAI slightly overestimating the field value. The other plots, are all overestimated by the MODIS LAI, and overall there is an RMSE of 0.28, while the coefficient of determination is 0.04. This RMSE value is well within the expected accuracy of the MODIS LAI product of 0.5 LAI (Wang *et al.* 2004). Owing to the fact that the sample size is so small, and the obvious scale mismatch, it is difficult to generalise from these results. Clearly, the MODIS LAI appears to be working well for some plots while not as well for others. What can be said is that overall - scale differences notwithstanding - the accuracy achieved by MODIS LAI is lower than that achieved by the neural network inversion with MODIS reflectances in §8.4.1.1.

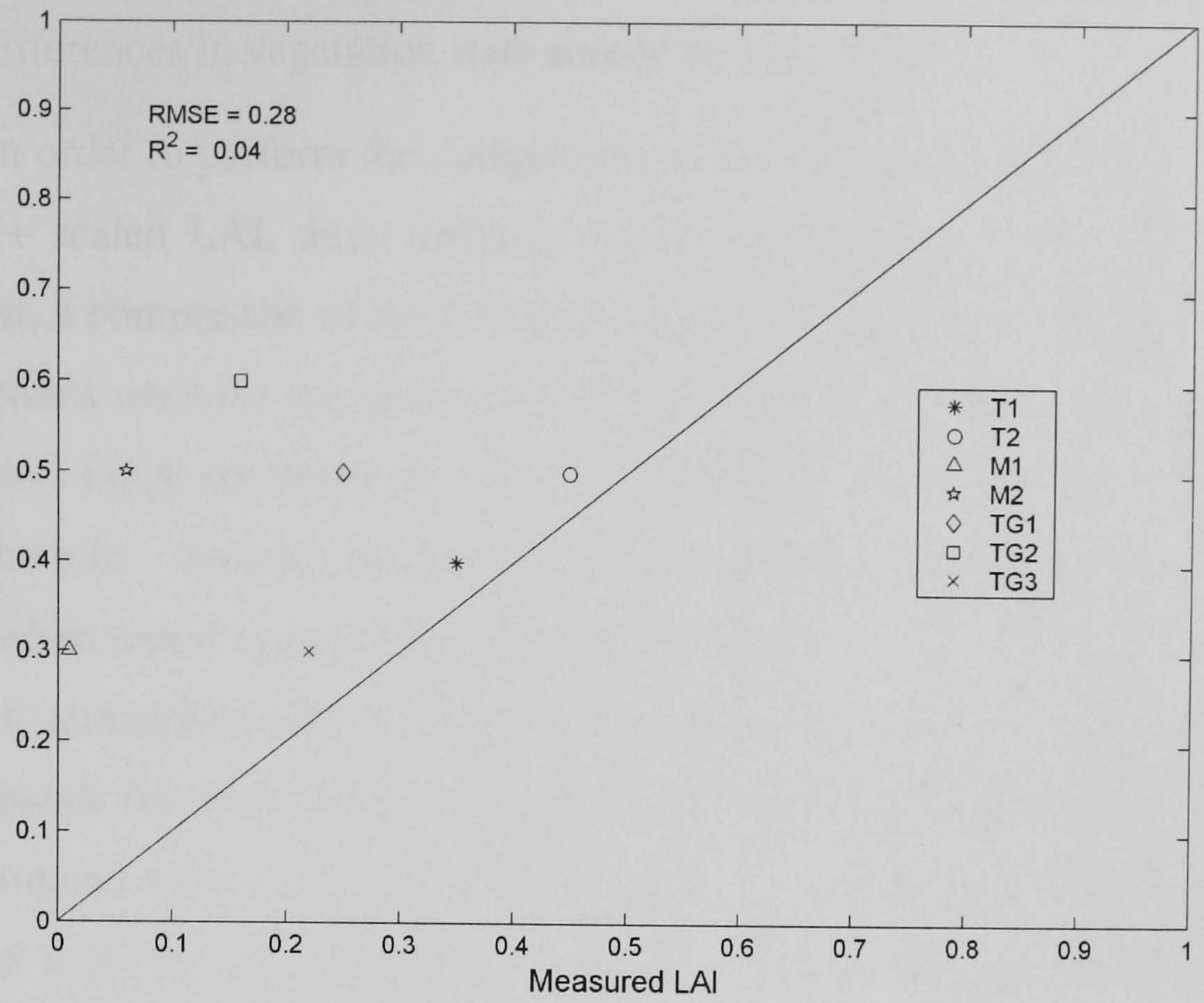

Figure 8.7 Comparison of field measured LAI with the MODIS LAI product. Date of the MODIS LAI is 6 March 2001 for all plots, while field measurements were made on 28 February, 1 March, 3 March, 4 March, 6 March, 7 March, and 8 March for plots T1, T2, M1, M2, TG1, TG2, and TG3 respectively.

8.5.3 Objective 4: Comparison of MODIS LAI and ETM+ scaled ANN LAI

To compare the MODIS LAI with LAI estimated from ETM+ data and a neural network, a subset of the 174/078 ETM+ image was atmospherically corrected using the simplified method of atmospheric correction (SMAC) (Rahman & Dedieu 1994). SMAC was used in preference to 6S since the subset contained ~1.3 million pixels, which would have been too time consuming to correct with 6S. SMAC is based on a set of semi-empirical equations to estimate transmission and scattering with spectral band and sensor specific coefficients, which have been derived using a best-fit technique to predictions from the 5S atmospheric correction routine (Tanre *et al.* 1990). Simulations have shown that SMAC performs with comparable accuracy to 6S, for a range of vegetation and viewing illumination conditions (Quaife & Barnsley 1999). SMAC requires inputs of the aerosol optical thickness at 550nm, ozone concentration and water vapour content. All values used were taken from the tropical atmosphere in 6S, apart from aerosol optical thickness which was obtained from the SAFARI 2000 database (see chapter 3). Given that the date of the image was 17

February 2001, the MODIS LAI product was obtained for the 18 February 2001, such that any differences in vegetation state should be minimised.

In order to perform the comparison of the spatial distribution of MODIS LAI and ETM+ scaled LAI, three different band combinations of the ETM+ data were used. First, a comparison of the LAI estimated from band 3 and 4 to correspond with the wavebands used for the generation of MODIS LAI. Despite, the ETM+ red and NIR dynamic range not being the same as the MODIS red and NIR, the comparison is still worthwhile. Second, the two band combinations which produced the highest accuracy when tested against field measurements, band 1 and 3, and band 1, 3, and 5. The SMAC atmospherically corrected reflectances were input to the respective trained neural network for each band combination (see Table 8.5), and LAI was estimated. These estimated values were then resampled to a resolution of 990m, by taking the average of a 33 by 33 pixel window. The resultant images together with image histograms are displayed in Figure 8.8.

Examination of the quality control data for the MODIS LAI image, revealed that 96% of the pixels were produced using the main radiative transfer method with 'the best possible results', while 4% were produced using the back up NDVI algorithm - the main algorithm failing for 'reasons other than geometry'. The very high percentage of best possible retrievals and no retrievals from the saturation domain, is perhaps not surprising in these low LAI ecosystems.

Comparing the MODIS LAI image with the LAI image generated with band 3 and 4 of the ETM+ and neural network inversion (Figures 8.8 a and b), it is clear that they do not appear to be in close spatial agreement. While the LAI scale on the images is slightly different, LAI increases in value from shades of orange to dark green, in both images. The MODIS LAI surface generally shows highest LAI in the NW, SW and NE of the image, with a zone of lower LAI stretching north to south through the centre of the image, the ETM+ LAI surface conversely, displays the opposite pattern, with highest LAI values stretching through the centre of the image, and lower LAI either side. While there is a clear spatial discrepancy between the two images, the summary statistics mainly differ in the range observed, with a minimum of 0.10 and 0.25, and maximum of 1.0 and 3.23 for the MODIS LAI and ETM+ band 34 LAI respectively (Figure 8.8a,b). Examination of the histogram for the ETM+ LAI reveals that there are no more than 9 pixels which have an LAI greater than 1. The

fact that the value distributions are similar but spatially incongruous suggests that the neural network has not been able to learn or establish a sound mapping function between the red and NIR reflectances and LAI. This result is in keeping with the results of the inversions evaluated with field LAI in §8.3.2.1, where the combination of red and NIR provided the second lowest accuracy. Clearly, the red and NIR combination are sub-optimal for training a neural network to estimate LAI in these semi-arid savannas.

The LAI image produced using band 1 and 3 of ETM+ is displayed in Figure 8.8c, while the LAI image produced with bands 1, 3, and 5 of ETM+ is shown in Figure 8.8d, along with the image histogram of estimated values. Comparing both of these images with the MODIS LAI image (Figure 8.8a) shows that there is a much closer spatial correlation between the two ETM+ LAI images and the MODIS LAI, than was observed with ETM+ band 3 and 4. High and low LAI areas broadly correspond, there is only a section in the far NE corner of the image where there is any significant spatial discrepancy, with the MODIS LAI having high LAI values, while the ETM+ has low LAI values. Inspection of the image histograms shows that the summary statistics are very similar with both ETM+ waveband combinations producing a slighter higher mean than MODIS LAI, means of 0.54, 0.53, and 0.46, for ETM+ band 1 and 3, 1, 3, and 5, and MODIS LAI, respectively. The range of estimated values and standard deviations are virtually identical. Fang & Liang (2005) report a similar overestimation with ETM+ data compared to the MODIS LAI over grasslands in Canada.

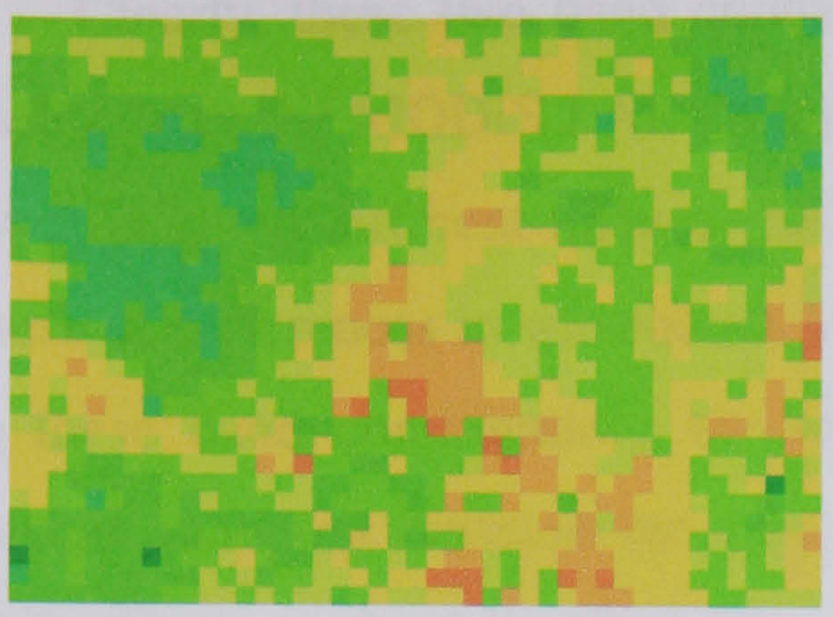

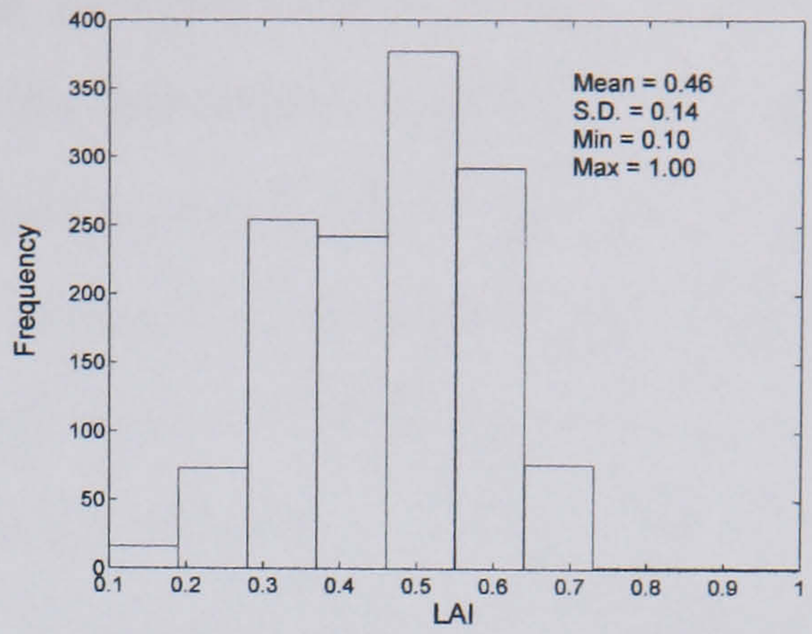

(a)

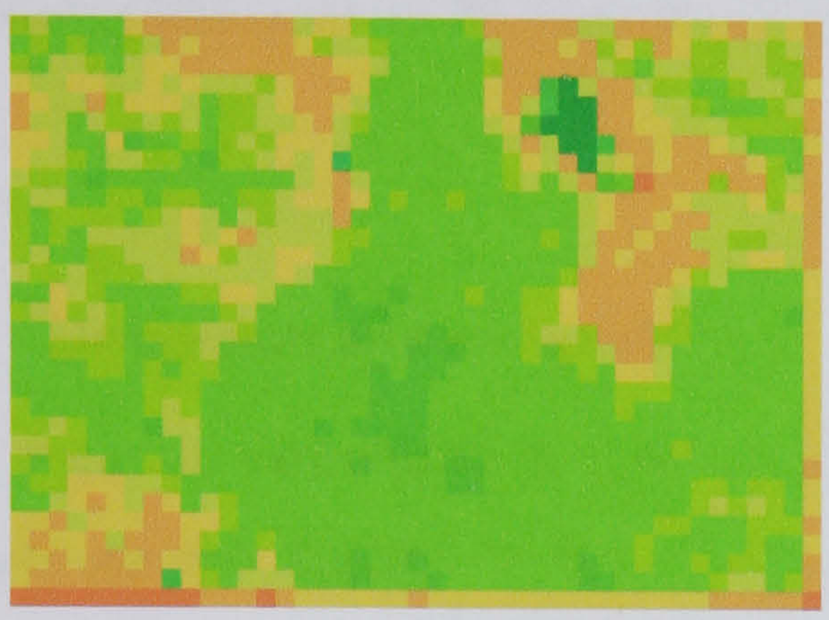

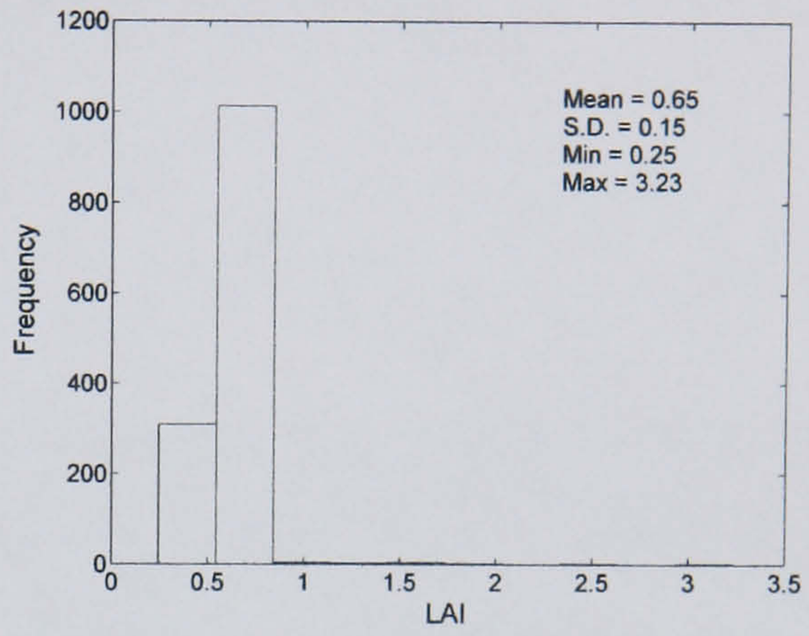

(b)

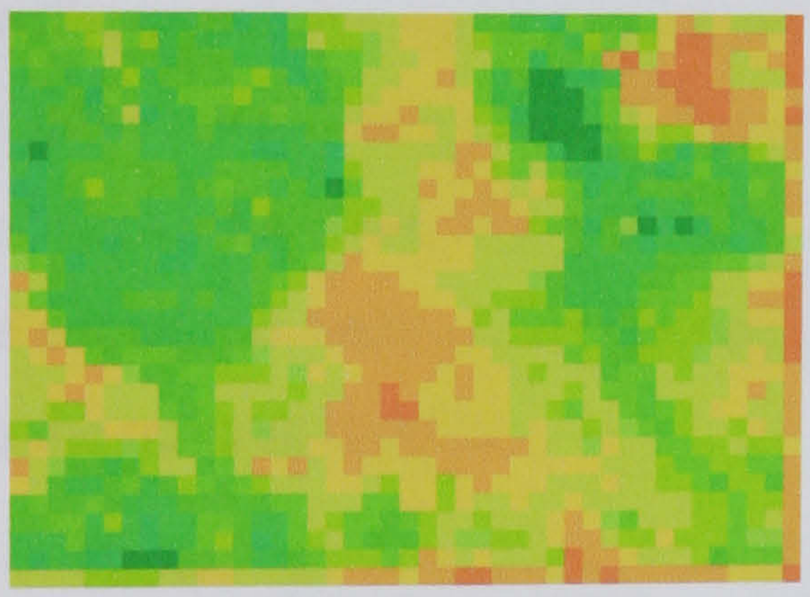

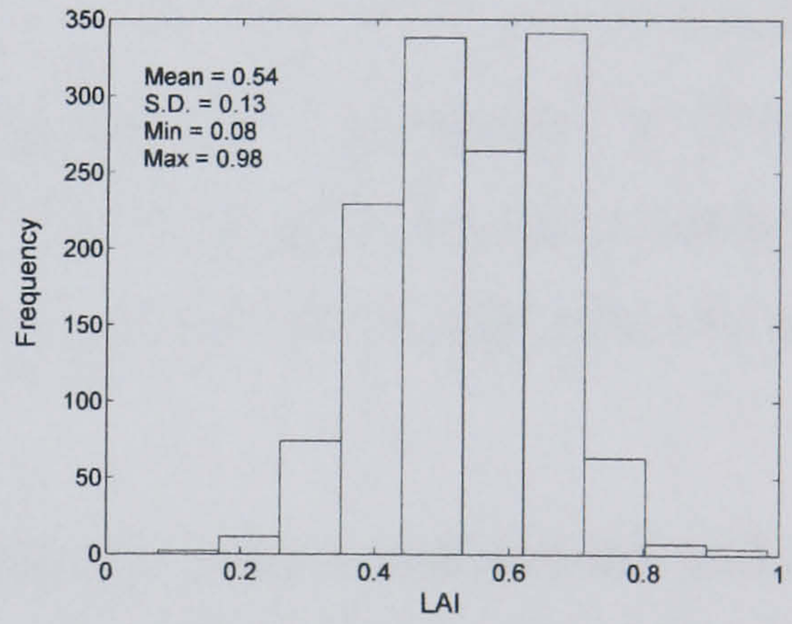

(c)

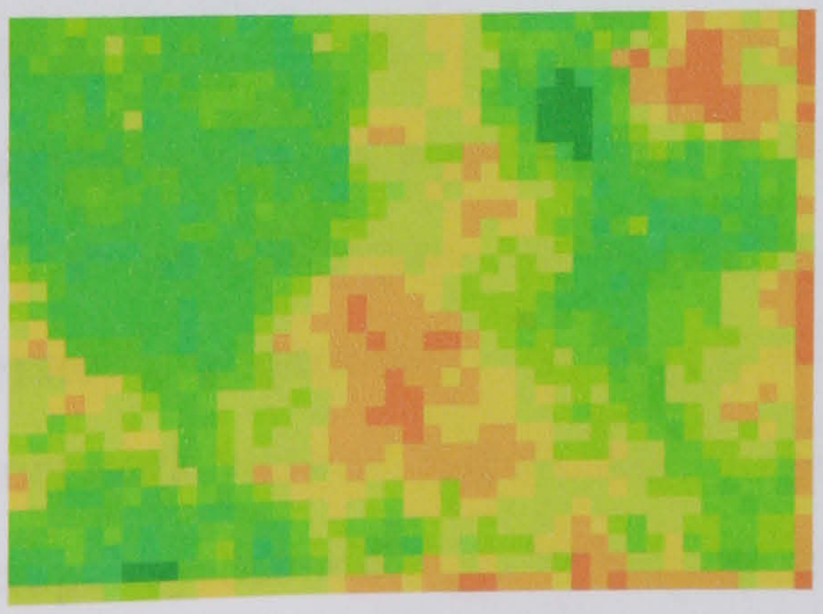

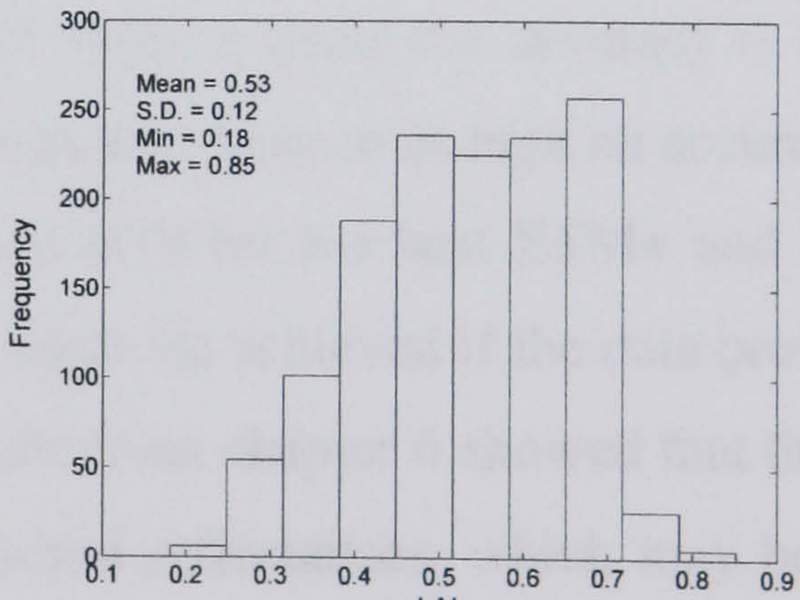

(d)

Figure 8.8 Comparison of (a) the MODIS LAI image of 18 February 2001, with LAI images estimated via neural network inversion of ETM+ data of 17 February 2001, rescaled to 990 metres, using (b) band 3 and 4, (c) band 1, 3, and 5, and (d) band 1 and 3. The colour scale is orange to dark green for low to high LAI.

Clearly, these two band combinations produce results which are comparable spatially, with the MODIS LAI. While it is not possible to make a strict comparison between the two different images (MODIS LAI versus ETM+ LAI band 13 and 135) because of differences in wavebands and the inversion method used, it does show that with these band combinations the neural network is clearly finding a strong and consistent mapping function between reflectance and LAI, which produces a similar spatial pattern to the MODIS LAI image. This underscores the notion that higher accuracy results are to be expected when the NIR band is not used.

8.6 Discussion and conclusions

The accurate estimation of a biophysical parameter from a model inversion depends largely on the quality of the model and reflectance data used to invert the model. Quality of the reflectance data relates to its accuracy, and the information it contains about the parameter to be estimated. Using a neural network to estimate LAI, it has been shown that smaller networks (one hidden layer) offer comparable performance to larger networks when tested with various levels of noise in data sets, since they are large enough to learn the underlying relationships, but not so large that the networks learn the training data too well.

Results presented here show that different band combinations and network inputs provide different accuracy of estimation (Wang *et al.* 2001). Overall, the absolute accuracy is fairly high. However, in relative terms the accuracy is low. In these low LAI ecosystems, however, this is probably close to as high an accuracy as is likely to be achievable, an RMSE of 0.31 and 0.18 for the best ETM+ and MODIS inversions, respectively. Increased accuracy might be achieved if the data provided to the network were of higher quality. The results from chapter 6 showed that there was discrepancy between the modelled and measured reflectances, which may be due to inadequate atmospheric correction, or mis-specification of the soil reflectance. Given the way in which the soil reflectance ranges were set to generate the training data, the network should be able to account for this. An improved atmospheric correction leading to higher quality data would therefore be more likely to increase the accuracy.

The highest accuracy for the ETM+ and MODIS inversions was produced using combinations of data from the VIS and SWIR1 (ETM+ band 5 MODIS band 6).

Using the NIR waveband as input to the ETM+ inversions resulted in the lowest accuracy. This is a result of the low contrast between the soil and leaf material in these semi-arid ecosystems. This result therefore confirms the findings of Price & Bausch (1995) and Gobron *et al.* (1997). It also confirms the results of the sensitivity analyses, where it was shown that there was little sensitivity to variation in LAI. In addition, it provides further evidence that the MODIS LAI product might be improved by using data from the SWIR, which contains more information about the LAI. This finding for these savanna ecosystems supports the observations which have been made over grasslands, agricultural, and forest ecosystems of North America (Cohen *et al.* 2003), and coniferous forests in Finland (Wang *et al.* 2004).

For the MODIS inversions, inclusion of the VZA in network training resulted in marginal improvements in accuracy for some band combinations, while lowering accuracy in others. This indicates that generally, the information contained in the VZA is not sufficient to lead to higher accuracy. In terms of creating networks which can generalise to any arbitrary set of viewing and illumination conditions, the limited test which has been made here suggests that the issue may not be as intractable as widely considered. This deserves further investigation, where one will either need a very large network capable of learning global relationships between reflectance, viewing and illumination conditions, and the biophysical parameter of interest; or else a number of networks trained over specific viewing and illumination conditions, which can be invoked for estimation, similar to the way in which LUT inversions are performed (Gastellu-Etchegorry *et al.* 2003).

In these savanna ecosystems both the ETM+ and MODIS ANN inversions overestimate LAI with respect to the field measurements. In addition, the MODIS LAI product also overestimates with respect to the field measurements. Fensholt *et al.* (2004) report the same observation for semi-arid shrubs and savanna in Senegal. Both the ETM+ and MODIS ANN LAI inversions produce higher accuracy with respect to field measurements, than the MODIS LAI product. This is most probably attributable to the fact that the ANN inversions can use different wavebands (i.e. not the NIR), rather than as a result of the differences in the inversion method. Evidence for this assertion is provided by Fang & Liang (2005), who have demonstrated consistency between the MODIS LAI and ANN estimated LAI from ETM+ data when estimating LAI over needleleaf forests, using the same red/NIR combination to perform the

inversion. When the red/NIR combination is used to estimate LAI from ETM+ data here however, and then scaled to correspond with the MODIS LAI product, there is little spatial correlation between the two. This is because the combination of red/NIR does not contain sufficient information about variation in LAI for the network to learn a strong relationship. While this may seem contradictory to the foregoing discussion, it is not, since the red/NIR combination over forests is likely to contain sufficient information for the neural network to produce comparable results to the MODIS LAI. There is much stronger spatial correlation between ETM+ LAI and MODIS LAI when band 1 and 3 and 1,3, and 5 are used, confirming the results of the field plots.

9 Discussion and conclusions

9.1 Introduction

This chapter provides a discussion of the work which has been presented in this thesis, and the various issues which have been raised. The chapter begins with a summary of the research and the key findings at each stage. Possible directions for further research are then identified, before finishing with the conclusions made from this research.

9.2 Thesis summary

The overall aim of this thesis was to establish a methodology for the estimation of leaf area index via a physically based canopy reflectance model (CRM) inversion, in semi-arid savanna vegetation. In order to achieve this the following objectives were defined:

(i) To investigate and characterise the scattering properties of Kalahari soils.

(ii) To compare the performance of different canopy reflectance models in simulating reflected radiance from savanna vegetation, in order to determine the most suitable model type.

(iii) To quantify the sources of variability in reflectance data, to determine the sensitivity of reflectance data to variation in LAI.

(iv) To investigate the potential of artificial neural networks to accurately estimate LAI.

These four objectives were investigated over a study area containing seven field plots in the Kgalagadi district of the Republic of Botswana (see Figure 3.1). These field plots were all located in the Kalahari desert, where all the soils are

Kalahari sands. The plots span a distance of approximately 200km, over which there exists a north to south moisture gradient from approximately 400mm of rainfall per annum in the north, to approximately 300mm of rainfall per annum in the south. The seven field plots represented a range of savanna types from low tree/shrub savanna, to grassland savanna, and shrub savanna, and were subject to different land use types and pressures. Field measurements of canopy structure and vegetation surveys were made during the 2001 wet season. These measurements were used to parameterise the canopy reflectance models and provided data sets against which the accuracy of the inverted model estimates could be assessed.

In chapter 5 field collected soil samples were measured in the laboratory in order to characterise their scattering properties. So that directional measurements could be made a goniometer was constructed. Spectral directional measurements were then made using an ASD spectrometer, at 10 degree intervals in zenith, and in a range of azimuthal planes. The results showed that all the soil samples were highly non-Lambertian and that this anisotropy was greatest in the solar principal plane for a range of wavelengths. In the principal plane and at up to 30 degrees in azimuth the analysis showed that reflectance was dominated by backscattering. There was less dynamism in the orthogonal plane where reflectance was more equally distributed between the back and forwardscatter directions. The results showed that the shape of the BRDF for all soils was almost identical, and that the differences of reflectance magnitude were generally no greater than 5% absolute in all wavebands, and at all viewing angles, and azimuthal planes. These results were interpreted as an indication of the relatively homogeneous soil substrate across the study area.

These spectral directional measurements were not used to parameterise the soil reflectance in the CRM however, as the measurements were too noisy in the wavelength region 1800-2500nm, preventing simulation of the ETM+ and MODIS SWIR band 7. As a result, hemispherical measurements of soil reflectance were made with an ASD contact probe, which had its own light source. These measurements were used to parameterise soil reflectance in the modelling work of chapter 6. This meant that despite the soils clearly being non-Lambertian, they were modelled as Lambertian surfaces. Comparing the spectral directional and hemispherical measurements therefore provided a check on the likely implications of this for the accuracy of the modelling in chapter 6. The analysis showed that using the

hemispherical reflectances would lead to either an over- or underestimation of the soil reflectance, depending on the viewing angle and azimuthal plane in which the satellite measurements were made.

In chapter 6 three different CRM were compared in a range of different forward modelling experiments. Simulations were performed using turbid medium (TM), hybrid and two-layer canopy modelling. The purpose of the two-canopy layer simulations was to determine the importance of the overstorey in generating shadow in the images, and thereby what effect modelling the canopy as a homogeneous turbid medium would have on accuracy. The results showed that in both the ETM+ and MODIS model comparisons, the TM models, PROSAIL and FLIGHT 1-D provided the closest fit to the measurements, than either the hybrid models or modelling which explicitly took account of two distinct canopy layers. The accuracy of both the ETM+ and MODIS simulations varied, with some plots displaying very close correspondence with the measurements, while at others there was poor correspondence. In the ETM+ simulations, it was suggested that the main reason for discrepancy between the modelled estimates and the measurements, was a consequence of mis-specifying the soil reflectance. This mis-specification was most likely a result of soil reflectance being lower than specified, not because of the use of hemispherical reflectance, but because of a presumed rainfall event which lowered soil reflectances. The same can be said for the MODIS simulations, only here soil mis-specification is most likely related to the effect of a Lambertian soil, rather than a rainfall event lowering reflectance. The effect of the Lambertian soil surface has a greater impact on the accuracy of these simulations, because of the non-nadir viewing angles.

The fact that the two-canopy layer modelling did not provide a closer fit to the measurements than the TM models, indicated that the influence of the overstorey in the remote sensing signal is not significant enough to demand the explicit incorporation of this 3-D structure in the modelling. Consequently, it was concluded that a 1-D model - which clearly does not match the structure of the canopy, could be used with little effect on the accuracy of simulation. This issue directly raises the question of how complex a model is needed to represent the radiation emergent from vegetation canopies. Clearly, the results presented here suggest that it is dependent on the type and nature of the vegetation which is being modelled. The PROSAIL model was chosen for the inversion work since this model was shown to provide comparable

performance to the FLIGHT 1-D modelling, and because it is an analytical model, was better suited to the generation of training data for neural network inversions.

In order to quantify the importance of LAI in driving reflectance variability, and therefore to identify the potential for its estimation from satellite measurements, a series of sensitivity analyses (SAs) were carried out in chapter 7. In total three different experiments were carried out, which addressed various issues associated with SA. The first of these compared the relative performance of local and global SA approaches. The local SA fails to report the effect of interactions between the model parameters, while a global SA does. The results showed that the importance of the interaction effects were significant when there was a large range in the model parameters, while less important when the range was more limited. However, even when the interaction effects were seen to be relatively unimportant, there were still striking differences between the two methods with respect to the importance of the individual parameters. The local SA tended to overestimate the importance of LAI compared to the global SA. All subsequent SAs were performed using the global SA method.

Owing to the fact that there were no leaf reflectance and transmittance data suitable for use with the CRM, these data were simulated with the PROSPECT model. Given that there were also no measurements of the range and distribution of the PROSPECT model parameters, the second experiment investigated the effect of the PDF specified for each of the model parameters. The results showed that there was generally less than 10% difference between a Gaussian and uniform PDF, except at the major water absorption band at 1900nm. In the absence of any prior information, a uniform PDF was used for the plot/site specific SA in experiment three.

The plot level SA showed that in both the ETM+ and MODIS simulations, greatest sensitivity to variation in LAI was displayed in the visible and SWIR bands, with relatively little sensitivity in the NIR. Interaction effects were shown to be relatively unimportant across wavelengths, such that reflectance variability was driven by first-order effects. The results also showed that as the range in the soil reflectance increased the sensitivity of reflectance data to variation in LAI decreased. In the MODIS SA, when the viewing and illumination conditions were input to the SA it was shown that only the VZA had any significant impact on reflectance variability, thus providing further evidence that the main source of variation in reflectance data

lies in the spectral domain. Taken together, these results suggested that LAI may be expected to be estimated with high accuracy, but that this would likely depend on the wavebands selected to perform the inversion.

In chapter 8, the PROSAIL model was used to train multi-layer perceptron neural networks to estimate LAI from ETM+ and MODIS data. The first stage of the chapter investigated the optimal network architecture, by training networks with one and two hidden layers with different numbers of neurons in each layer. To investigate the relationship between network size and resistance of the networks to noise, the networks were tested with nine noisy data sets. The results showed that the accuracy of inversion was independent of network size for data sets which contained up to 5% noise for networks with one hidden layer, while there was a positive relationship for networks with two hidden layers. Once the noise increased to 20% it was shown that a negative relationship existed between network size and accuracy of estimation, for both the one and two hidden layer networks. Clearly, as the test data set departs further from the data the network was trained with, the larger networks learn the training data too well, and generalisation ability suffers. The results also showed that there is little to choose in terms of accuracy between the one and two hidden layer networks. Two hidden layer networks provide higher accuracy with the noisier data sets, however, the difference was shown to be relatively small. Given the longer training time for the two hidden layer networks for only marginal improvement in accuracy, all future work concentrated on the use of single hidden layer networks.

Various band combinations were used as input to the network training for the ETM+ estimates. The results showed that highest accuracy was achieved when the red and blue wavebands (ETM 3 and 1), were used together, an RMSE of 0.31, and in combination with the SWIR bands (ETM 5 and 7), both producing estimates with an RMSE of 0.32. When the NIR waveband was used as input to the network training process, both in combination with all other bands, and in the commonly used red/NIR combination, the results obtained gave the lowest accuracy of all, with an RMSE of 0.41 and 0.43, respectively. These results were therefore consistent with expectation given the results of chapter 7. In the light of the ETM+ results, the NIR waveband was not considered in the MODIS inversions. Focus was still centred on the optimal band combinations, however, attention was also given to the inclusion of the viewing zenith angle (VZA) in the network training process, to determine if this led to

improved estimation accuracy. The results showed that the highest accuracy was achieved when MODIS bands 1, 3, 4 and 6 were used together with the VZA, an RMSE of 0.18. Although the highest accuracy overall was achieved when the VZA was included, on closer inspection however, this was shown not to be true in all cases, and even when it did, the improvement in accuracy was shown to be fairly unimpressive.

Given that the work presented in this thesis is estimating LAI from a CRM inversion, and that the MODIS LAI product is available at a 1km resolution, it was decided to compare the performance of both methods. This comparison proceeded in two phases. First, the MODIS LAI was directly compared with the field measurements made at each field plot. The results showed that the MODIS LAI overestimated LAI at all plots, with an RMSE of 0.28. While this error is within the reported expected error of the MODIS LAI product, it is not as accurate as the results obtained using MODIS reflectances and the neural network approach of this work. It was suggested that this may be a result of the different band combinations used in the estimation, MODIS LAI relying on the red/NIR combination, while the MODIS neural network LAI, used data from 4 wavebands.

Second, given the difficulty in making conclusions about the relative performance of the two different products, when only a small number of point comparisons are available, it was decided to investigate the spatial correlation between the LAI produced by the two different methods (neural network and MODIS LAI LUT). To achieve this, an ETM+ subset was atmospherically corrected and LAI was estimated from three different networks. Estimated LAI was then spatially averaged from 30m to 990m, to match as closely as possible the 1km spatial resolution of the MODIS LAI product. The results showed that when LAI was estimated using a neural network and ETM+ bands 3 and 4 as input, there was weak spatial correlation with the MODIS LAI. However, when LAI was estimated using ETM+ bands 1 and 3 and 1, 3, and 5 there was strong spatial correlation between the two products. It was suggested that the poor correspondence between MODIS LAI and the ETM+ band 3 and 4 neural network LAI, was because the network had insufficient information to establish a strong relationship between the spectral data and LAI.

9.3 Future research directions

The work presented in this thesis represents one of the first attempts to use canopy reflectance models to estimate leaf area index in a semi-arid environment. The issues raised in this thesis and which are likely to receive further research investigation in the future relate to model development, improved fieldwork and modelling data sets, and enhancements to inversions using neural networks. Each of these issues is discussed below.

9.3.1 Model development

There are various ways in which the modelling work presented in this thesis could be extended, with likely improvements in the accuracy with which reflectance is simulated and also the kind of information that might be extracted from remotely sensed data. First, model simulations would do well to model the soil surface as a non-Lambertian scatterer. The work presented in chapter 5 demonstrated that the soils were highly non-Lambertian, yet this was not represented in the model simulations, owing to the incomplete nature of the soil reflectance data set. Clear improvements could be made by coupling a CRM to a soil BRDF model such as SOILSPECT (Jacquemoud *et al.* 1992), as has been demonstrated by Privette *et al.* (1995) and Ni & Li (2000). Using a soil BRDF model would be more flexible an approach than making measurements and would permit a wider range of soil surface conditions to be simulated. This would inevitably involve further issues with respect to model parameterisation, yet is a more feasible approach than making directional measurements in the laboratory with a different light source, or in the field using the PARABOLA instrument.

Second, the incorporation of two distinct canopy layers into one model would be a welcome development. Although the results presented in this thesis indicated that the overstorey 3-D structure was not significant in determining top of canopy reflectance, this was only applicable to the limited simulations performed, and is deserving of further attention. Under different conditions the overstorey may be very influential in the recorded signal, in which case a 3-D representation would be necessary. Recently, Chopping *et al.* (2003, 2004) developed a simplified geometric model (SGM) based on linear kernel modelling, which can model two canopy layers. This model was developed and has been validated over arid/semi-arid

grassland/shrubland transition ecosystems in the USA, and would be ideally suited to the study plots used in this thesis. Whilst modelling two canopy layers may offer new possibilities for information extraction, such as the ratio of woody (overstorey) to grass (understorey) cover, with obvious benefit to studies of savanna community ecology (Scholes & Archer 1997), this needs to be established. The work presented in this thesis has estimated the total LAI of the plot, where woody and grass LAI are simply combined. This may be all that is possible for LAI estimation in these semi-arid vegetation types where LAI is <1. Simulations need to be performed to determine the importance of the overstorey, understorey, and relevant model parameters in driving reflectance variability, over a large range of solar and view angles. Doing so would provide a major addition to the understanding of the radiation emergent from semi-arid vegetation types, with consequent implications for what information can and cannot be extracted from remote sensing data. Additionally, results from such work would provide information on the optimal sampling configuration for estimating vegetation properties in these semi-arid ecosystems.

Finally, the modelling could be extended to include the senescent vegetation which is known to have a significant impact on radiation emergent from these savanna ecosystems (van Leeuwen & Huete 1996). Given the highly variable nature of, and dynamic response of vegetation to rainfall in these ecosystems, senescent vegetation constitutes a large component of the vegetation, and is also a required variable in many biogeochemical models (Sellers *et al.* 1997, Asner *et al.* 1998d), such that its estimation from remotely sensed data could fruitfully be pursued.

9.3.2 Additional fieldwork and modelling data sets

The field data collected and described in chapter 4 was inevitably limited given the short period of time in which measurements could be made, and the fact that time in the field was shared with colleagues working on different projects. Field measurements were required for model parameterisation and to provide a test of the accuracy of the inversion estimates in chapter 8. The results of the inversion work were compared with LAI values which were derived from the measurements of plant area index (PAI). These PAI estimates were corrected for the woody and litter (or senescent) area index by using published values in the literature and visual estimation,

respectively. This correction would likely be more accurate had measurements of WAI been made in the field, however time did not permit this. Future field work would therefore be spent obtaining such data. Measurements of fractional vegetation cover were made visually for reasons of speed. It would be instructive to experiment with different methods of estimating fractional cover in these ecosystems, such as line intercept methods. This is important since an error (under- or overestimate) in the fractional cover would translate into an error in the plot level LAI.

The model simulations in chapters 6, 7 and 8 were made using modelled leaf reflectance and transmittance data. While this is clearly an acceptable approach, little was known about the ranges and PDFs for each of the model parameters, such that either too much or too little variability will have been introduced into the simulations. Future work might involve collecting full range spectral measurements of the species present in the field, or alternatively by taking leaf samples for analysis in a laboratory. Neither of these would be straightforward however, because of the logistical difficulties of working in this region of the Kalahari.

An additional problem which might be improved in future work, was the mis-specification of the soil reflectance for the ETM+ plots at Tshane plots 1 and 2. This issue arose because the laboratory measurements of soil reflectance were made on dry samples, under the assumption that the soils in the field would most likely be dry also. On closer inspection, extracting soil pixels from the image and atmospherically correcting them to reflectance, it was shown that the laboratory measurements were considerably higher than the image values. One approach to account for this difference would be to ignore the laboratory measurements and instead systematically use the image to obtain soil reflectance values, so that they are consistent with the prevailing conditions of the image acquisition. Fang & Liang (2003, 2005) have recently developed a method for doing this. This would require an accurate atmospheric correction however.

The accuracy of the inversion estimates is determined to a large extent by the quality of the input data to the network. This means that the quality of the atmospheric correction is of crucial importance (Rahman 2001). The ETM+ images were corrected using the 6S algorithm, with values for the aerosol optical thickness, and water vapour content being obtained from measurements made a year earlier, and a standard atmosphere respectively. Clearly, these input values are unlikely to be

accurate. Ideally, future work would involve estimation of these gases in the atmosphere using a sun photometer at the time of image acquisition. This would also require the scene to be cloud free on the day of image acquisition, which cannot be guaranteed.

9.3.3 Enhanced neural network inversions

Using CRM to generate reflectance data sets with which to train neural networks is unrealistic for the following reason: the modelled data sets are essentially error free, whereas the measurements from which estimates of LAI are to be obtained, contain some error or noise. While the simulations in chapter 8 showed that the various networks trained were resistant to noise levels up to 20%, it is not known how much error is contained in the measurements, though Vermote (2000) suggests relative values of 50-80%, 5-12%, 10-33%, and 3-6% are to be expected for the MODIS bands 3 (blue), 4 (green), 1 (red), and 2 (NIR), respectively. Clearly, the effect of noise in the measurements is wavelength dependent and so the effect of noise will depend on the wavelengths used to estimate the LAI. It seems worthwhile therefore to investigate the effect of training a neural network with noisy data sets, to determine if this improves the estimation accuracy. Fang & Liang (2005) have recently approached this issue by actually including some real data in the training process, which is another alternative that might be pursued. Another alternative would be to investigate the use of Bayesian neural networks which may be able to explicitly handle some of the error or uncertainty on the network inputs, which, upon inversion would also yield some information on the uncertainty of the estimated LAI values.

A further way in which the neural network inversions may be improved would be to reduce the dimensionality of the training data. This could be based on the results of the sensitivity analyses where the parameters which are shown to be relatively unimportant in explaining reflectance variability could be fixed at a given value, while the most important parameters are allowed to vary. In this way the variability in the training data would be more constrained to the LAI such that the neural network may be better able to learn the relationship between the spectral data and LAI.

9.3.4 Monitoring, classification and management of savanna ecosystems

Given the large range of structural types encountered in savanna ecosystems (savanna grasslands, shrub savanna, low tree-shrub savanna), and the importance of accurate land cover classification, in (1) calculating carbon fluxes (e.g. Ahl *et al.* 2004, 2005), and (2) monitoring landcover changes which result from cattle grazing and global environmental and climatic change (Foley 2005), the approach adopted in this research could be extended to the development of more elegant landcover classification methods, which would have wider implications for the monitoring and management of savanna ecosystems.

Currently, the vast majority of landcover classification schemes generally attempt to exploit the spectral differences between different landcover classes, using statistical classification schemes typically, maximum likelihood, or ANNs (Mather 1999). These classification methods may provide sufficient accuracy when distinguishing between broad biome level classes, however, when more subtle landcover classes are defined, such as those within a biome (savanna grasslands, shrub savanna, low tree-shrub savanna), such methods do not contain sufficient information to produce high accuracy landcover maps (Chopping *et al.* 2002). The different vegetation types have spectral responses which are too similar to permit their accurate separation. However, they do differ significantly in terms of their 3-D structure, and it is through the exploitation of this fact that CRM based classification schemes may be devised. A critical requirement for the successful extension of this research to landcover classification however, is the use of directional data within which the differences in 3-D structure between the different savanna types, will be expressed.

Although the estimation of LAI in this research was achieved via the inversion of a 1-D turbid medium (TM) model, which is specified in terms of only a few parameters, this research has also considered the use of more complex 3-D CRM, which take account of the 3-D structure of the vegetation. CRM based landcover classification will have to be pursued using a 3-D model, if the differences in vegetation structure are to be extracted. This could be achieved by implementing a knowledge based classification scheme, whereby groups of vegetation canopy properties (e.g. number of trees, crown height and width, tree height) which define a specific savanna type (e.g. shrub savanna, low tree-shrub savanna), are determined, and forward simulations run with the 3-D model, for each class. In so doing, each

landcover class could be associated with a set of forward simulations, and the spectral-directional data stored in a look-up-table (LUT), or used to train an ANN. The classification method would then be a model inversion using this LUT or ANN. Peddle *et al.* (2003, 2004), have demonstrated the effectiveness of such an approach using the 5-Scale model (Leblanc *et al.* 1999) to construct LUTs, and produce highly accurate (~80%) landcover maps for boreal forests in western Canada. This approach is deserving of further research to determine its effectiveness in classifying structurally distinct vegetation types in semi-arid savanna. An alternative approach, which has used the semi-empirical CRM described in § 2.6.2.5, has been developed by Chopping *et al.* (2002), and Su *et al.* (2005), whereby the weights on the geometric and volumetric kernels are used to extract information from AVHRR and MISR data, related to differences in vegetation community type, in desert grasslands of New Mexico, USA, and Autonomous Inner Mongolia, China, with classification accuracies of >90%. These methods also need to be demonstrated to be effective in the savanna vegetation communities studied in this research.

If such techniques can be developed and shown to be effective in savanna ecosystems then the potential for more accurate landcover classifications would be greatly enhanced. In so doing, the monitoring of landcover changes in these ecosystems would be aided considerably. In addition, the provision of more accurate landcover maps to ecosystem process models - used to calculate carbon fluxes, will also greatly improve the accuracy of carbon stock calculations. Taken together, the more accurate monitoring, and process level assessment of these ecosystems, would offer the potential for more scientifically informed management of these important ecosystems.

9.4 Conclusions

While canopy reflectance models have been used in semi-arid vegetation types before, to estimate tree size and canopy dimensions, the work presented in this thesis represents the first attempt to estimate LAI in semi-arid vegetation from a CRM inversion using satellite sensor data at a spatial resolution of <1km. This thesis has addressed the key issues associated with estimating vegetation properties in semi-arid ecosystems, where vegetation cover is less than 40%, such that the soil background

exerts a significant impact on the remotely sensed signal. The following conclusions are made:

- For the first time the scattering properties of Kalahari soils have been characterised, and shown to be highly non-Lambertian.
- In vegetation with two distinct canopy layers, the importance of the overstorey in generating shadow in the scene in these low LAI savanna vegetation types is insignificant over the conditions tested.
- A 1-D turbid medium modelling representation provides the closest fit to the ETM+ and MODIS data.
- Local and global SA have been compared and the importance of interaction effects between model parameters was shown to be relatively unimportant in these low LAI savanna vegetation types, such that reflectance is driven by first order effects.
- The visible and SWIR wavebands of ETM+ and MODIS display the greatest sensitivity to LAI. The NIR displays relatively little sensitivity to variation in LAI.
- Using the visible and SWIR wavebands as input to an artificial neural network, to invert the canopy reflectance model provided the highest accuracy. Inclusion of the VZA resulted in only marginal improvements in accuracy.
- The commonly used red/NIR combination in vegetation indices would appear to be sub-optimal in these low LAI savanna vegetation types, and similar vegetation types around the world.

The results of this research are likely to be applicable to other semi arid vegetation regions of the world, although it is unlikely that there will be such a homogeneous soil substrate, such that the importance of LAI in driving reflectance variability may not be as great, and consequently the potential for estimating LAI may be reduced. The use of canopy reflectance models to estimate leaf area index via a neural network inversion in semi-arid vegetation has been established. Extension of this work to incorporate non-Lambertian soil scattering, and improvements in modelling and

neural network inversions is likely to lead to improved accuracy, such that the exploitation of remotely sensed earth observation data will play a key role in improving the understanding, mapping and monitoring of these savanna ecosystems.

10 References

Ahl, D.E., Gower, S.T., Mackay, D.S., Burrows, S.N., Norman, J.M., and Diak, G.R., 2004, Heterogeneity of light use efficiency in a northern Wisconsin forest: implications for modeling net primary production with remote sensing, *Remote Sensing of Environment*, **93**, 168-178.

Ahl, D.E., Gower, S.T., Mackay, D.S., Burrows, S.N., Norman, J.M., and Diak, G.R., 2005, The effects of aggregated land cover data on estimating NPP in northern Wisconsin, *Remote Sensing of Environment*, **97**, 1-14.

Archer, S., 1994, Woody encroachment in southwestern grasslands and savannas: Rates, patterns, and proximate causes, In, *Ecological Implications of Livestock Herbivory in the West*, M.Vavra, W.A., Laycock, and R.D. Pieper Eds., Society for Range Management, Denver, pp. 13-68.

Archer, S., Schimel, D.S., and Holland, E.A., 1995, Mechanisms of shrubland expansion: Land use, climate or CO2?, *Climatic Change*, **29**, 91-99.

Arora, M.K., and Foody, G.M., 1997, An evaluation of variables affecting the accuracy of probabilistic, fuzzy, and neural network classifications with log-linear modelling, *International Journal of Remote Sensing*, **18**, 785-798.

Asner, G.P., 1998a, Biophysical and biochemical sources of variability in canopy reflectance, *Remote Sensing of Environment*, **64**, 234-253.

Asner, G.P., 1998b, Corrigendum, *Remote Sensing of Environment*, **65**, 225-226.

Asner, G.P., Bateson, C.A., Privette, J.L., ElSaleous, N., and Wessman, C.A., 1998a, Estimating vegetation structural effects on carbon uptake using satellite data fusion and inverse modeling, *Journal of Geophysical Research-Atmospheres*, **103**, d22, 28,839-28,853.

Asner, G.P., Wessman, C.A., and Archer, S., 1998b, Scale dependence of absorption of photosynthetically active radiation in terrestrial ecosystems, *Ecological Applications*, **8**, 4, 1003-1021.

Asner, G.P., Wessman, C.A., Schimel, D.S., and Archer, S., 1998c, Variability in leaf and litter optical properties: implications for BRDF model inversions using AVHRR, MODIS, and MISR, *Remote Sensing of Environment*, **63**, 243-257.

Asner, G.P., Braswell, B.H., Schimel, D.S., Wessman, C.A., 1998d, Ecological research needs from multiangle remote sensing data, *Remote Sensing of Environment*, **63**, 155-165.

Asner, G.P., Wessman, C.A., Bateson, C.A., and Privette, J.L., 2000, Impact of Tissue, Canopy, and Landscape factors on the hyperspectral reflectance variability of Arid ecosystems, *Remote Sensing of Environment*, **74**, 69-84.

Atkinson, P.M., and Tate, N.J., 1999, *Advances in Remote Sensing and GIS Analysis*. (John Wiley: Chichester).

Bacour, C., Jacquemoud, S., Tourbier, Y., Dechambre, M., and Frangi, J. -P., 2002, Design and analysis of numerical experiments to compare four canopy reflectance models, *Remote Sensing of Environment*, **79**, 72-83.

Baret, F., and Guyot, G., 1991, Potentials and limits of vegetation indices for LAI and APAR assessment, *Remote Sensing of Environment*, **35**, 161-173.

Baret, F., Clevers, J.G.P.W., and Steven, M.D., 1995, The robustness of canopy gap fraction estimates from red and near-infrared reflectances: A comparison of approaches, *Remote Sensing of Environment*, **54**, 141-151.

Barnsley, M.J., Allison, D., and Lewis, P., 1997, On the information content of multiple view angle (MVA) images, *International Journal of Remote Sensing*, **18**, 9, 1937-1960.

Barnsley, M.J., Lewis, P., O'Dwyer, S., Disney, M.I., Hobson, P., Cutter, M., and Lobb, D., 2000, On the potential of CHRIS/PROBA for estimating vegetation canopy properties from space, *Remote Sensing Reviews*, **19**, 171-189.

Bégué, A., Prince, S.D., Hana, N.P., and Roujean, J.L., 1996, Shortwave radiation budget of Sahelian vegetation. 2. Radiative transfer models, *Agricultural and Forest Meteorology*, **79**, 97-112.

Berk, A., Bernstein, L.S., Anderson, G.P., Acharya, P.K., Robertson, D.C., Chetwynd, J.H., and Adler-Golden, S.M., 1998, MODTRAN cloud and multiple scattering upgrades with application to AVIRIS, *Remote Sensing of Environment*, **65**, 367-375.

Bicheron, P., and Leroy, M., 1999, A method of biophysical parameter retrieval at global scale by inversion of a vegetation reflectance model, *Remote Sensing of Environment*, **67**, 251-266.

Bishop, C.M., 1995, *Neural Networks for Pattern Recognition*, Oxford University Press, Oxford, UK.

Borel, C.C., Gerstl, S.A.W., and Powers, B.J., 1991, The radiosity method in optical remote sensing of structured 3-d surfaces, *Remote Sensing of Environment*, **36**, 13-44.

Bowyer, P., and Danson, F.M., 2004, Sensitivity of spectral reflectance to variation in live fuel moisture content at leaf and canopy level, *Remote Sensing of Environment*, **92**, 297-308.

Bowyer, P., Danson, F.M., Trodd, N.M., 2003, Methods of sensitivity analysis in remote sensing: implications for model inversion, *IGARSS*, 21-26 July 2003, Toulouse, France.

Braswell, B.H., Schimel, D.S., Privette, J.L., Moore, B. III, Emery, W.J., Sulzman, E.W., and Hudak, A.T., 1996, Extracting ecological and biophysical information from

AVHRR optical data: an integrated algorithm based on inverse modeling, *Journal of Geophysical Research*, **101**, 23,335-23,348.

Breon, F.M., Maignan, F., Leroy, M., and Grant, Y., 2002, Analysis of hot spot directional signatures measured from space, *Journal of Geophysical Research*, **107**, D16, 10.1029/2001JD001094.

Buermann, W., Dong, J., Zeng, X., Myneni, R.B., and Dickinson, R.E., 2001, Evaluation of the utility of satellite-based vegetation leaf area index data for climate simulations, *Journal of Climate*, **14**, 3536-3550.

Bunnik, N.J.J., 1978, *The multispectral reflectance of shortwave radiation by agricultural crops in relation with their morphological and optical properties*, Pudoc, Wageningen, Netherlands.

Campbell, G.S., 1986, Extinction coefficients for radiation in plant canopies using an ellipsoidal inclination angle distribution, *Agricultural and Forest Meteorology*, **36**, 317-321.

Carter-Ingram, J., Dawson. T.P., and Whittaker, R.J., 2005, Mapping tropical forest structure in southeastern Madagascar using remote sensing and artificial neural networks, *Remote Sensing of Environment*, **94**, 491-507.

Ceccato, P., Flasse, S., and Gregoire, J.M., 2002, Designing a spectral index to estimate vegetation water content from remote sensing data Part 2. Validation and applications, *Remote Sensing of Environment*, **82**, 198-207.

Ceccato, P., Flasse, S., Tarantola, S., Jacquemoud, S., Gregoire, J-M., 2001, Detecting vegetation leaf water content using reflectance in the optical domain, *Remote Sensing of Environment*, **77**, 22-33.

Chan, K., Tarantola, S., and Saltelli, A., 2000, Variance-based methods, In, Saltelli, A., Chan, K., and Scott, E.M., (Eds.) *Sensitivity Analysis*, pp., 167-197, John Wiley & Sons Ltd, Chichester, England.

Chen, J., and Leblanc, S.G., 1997 A four-scale bidirectional reflectance model based on canopy architecture, *IEEE Transactions on Geoscience and Remote Sensing*, **35**, 1316-1337.

Chen, J.M., and Cihlar, J., 1995, Plant canopy gap-size analysis theory for improving optical measurements of leaf area index, *Applied Optics*, **34**, 27, 6211-6222.

Chen, J.M., Li, X., Nilson, T., and Strahler, A., 2000, Recent advances in geometrical optical modelling and its applications, *Remote Sensing Reviews*, **18**, 227-262.

Chen, J.M., Liu, J., Leblanc, S.G., Lacaze, R., Roujean, J.L., 2003, Multi-angular optical remote sensing for assessing vegetation structure and carbon absorption, *Remote Sensing of Environment*, **84**, 516-525.

Chen, J.M., Rich, P.M., Gower, S.T., Norman, J.M., and Plummer, S., 1997, Leaf area index of boreal forests: theory, techniques, and measurements, *Journal of Geophysical Research*, **102**, 29429-29443.

Chopping, M.J., 2000, Testing a LiSK BRDF model with in situ bidirectional reflectance factor measurements over semiarid grasslands, *Remote Sensing of Environment*, **74**, 287-312.

Chopping, M.J., Rango, A., and Ritchie, J.C., 2002, Improved semi-arid community type differentiation with the NOAA AVHRR via exploitation of the directional signal, *IEEE Transactions on Geoscience and Remote Sensing*, **40**, 5, 1132-1149.

Chopping, M.J., Rango, A., Havstad, K.M., Schiebe, F.R., Ritchie, J.C., Schmugge, T.J., French, A.N., Su, L., McKee, L., and Davis, M.R., 2003, Canopy attributes of desert grassland and transition communities derived from multiangular airborne imagery, *Remote Sensing of Environment*, **85**, 339-354.

Chopping, M.J., Su, L.H., Rango, A., and Maxwell, C., 2004, Modelling the reflectance anisotropy of Chihuahuan Desert grass-shrub transition canopy-soil complexes, *International Journal of Remote Sensing*, **25**, 14, 2725-2745.

Choudhury, B.J., and Tucker, C.J., 1987, Satellite observed seasonal and inter-annual variation of vegetation over the Kalahari, The Great Victoria Desert, and The Great Sandy Desert: 1979-1984, *Remote Sensing of Environment*, **23**, 233-241.

Cierniewski, J., 1987, A model for soil surface roughness influence on the spectral response of bare soils in the visible and near-infrared range, *Remote Sensing of Environment*, **23**, 97-115.

Cierniewski, J., and Verbrugghe, M., 1997, Influence of soil surface roughness on soil bidirectional reflectance, *International Journal of Remote Sensing*, **18**, 1277-1288.

Cohen, W.B., and Justice, C.O., 1999, Validating MODIS terrestrial ecology products: Linking In Situ and satellite measurements, *Remote Sensing of Environment*, **70**, 1-3.

Cohen, W.B., Maiersperger, T.K., Yang, Z., Gower, S.T., Turner, D.P., Ritts, W.D., Berterretche, M., and Running, S.W., 2003, Comparisons of land cover and LAI estimates derived from ETM+ and MODIS for four sites in North America: a quality assessment of 2000/2001 provisional MODIS products, *Remote Sensing of Environment*, **88**, 233-255.

Cole, M.M., 1963, Vegetation nomenclature and classification with particular reference to the savannas, *South African Geographical Journal*, **55**, 3-14.

Cole, M.M., 1986, *The Savannas: Biogeography and Geobotany*, Academic Press, London.

Combal, B, Baret, F., Weiss, M., Trubuil, A., Macé, D., Pragnère, A., Myneni, R., Knyazikhin, Y., and Wang, L., 2002a, Retrieval of canopy biophysical variables from

bidirectional reflectance using prior information to solve the ill-posed inverse problem, *Remote Sensing of Environment*, **84**, 1-15.

Combal, B., Baret, F., Weiss, M., 2002b, Improving canopy variables estimation from remote sensing data by exploiting ancillary information. Case study on sugar beet canopies, *Agronomie*, **22**, 205-215.

Coulson, K.L., Bouricius, G.M., and Gray, E.L., 1965, Optical reflection properties of natural surfaces, *Journal of Geophysical Research*, **70**, 4601-4611.

Crooks, T., 1992, Care and feeding of neural networks, *AI expert*, 37-41.

Cukier, R.I., Fortuin, C.M., Schuler, K.E., Petschek, A.G., and Schaibly, J.H., 1973, Study of the sensitivity of coupled reaction systems to uncertainties in rate coefficients, I. Theory, *Journal of Chemical Physics*, **59**, 3873-3878.

Cukier, R.I., Levine, H.B., and Schuler, K.E., 1978, Nonlinear sensitivity analysis of multiparameter model systems, *Journal of Computational Physics*, **26**, 1-42.

Curran, P.J. and Atkinson, P.M., 1998, Geostatistics and remote sensing, *Progress in Physical Geography*, **22**, 1, 61-78.

Danson, F.M., Steven, M.D., Malthus, T.J., and Clark, J.A., 1992, High-spectral resolution data for determining leaf water content, *International Journal of Remote Sensing*, **13**, 3, 461-470.

Daughtry, C.S.T., 1990, Direct measurements of canopy structure, *Remote Sensing Reviews*, **5**, 1, 45-60.

Dawson, M.S., Fung, A.K., and Manry, M.T., 1993, Surface parameter retrieval using fast learning neural networks, *Remote Sensing Reviews*, **7**, 1-18.

de Wit, C.T., 1965, *Photosynthesis of Leaf Canopies*, Agric. Res. Rep. Pudoc, Wageningen, Netherlands.

Deering, D.W., Eck, T.F., and Banerjee, B., 1999, Characterization of the reflectance anisotropy of three boreal forest canopies in spring-summer, *Remote Sensing of Environment*, **67**, 205-229.

Deering, D.W., Eck, T.F., Otterman, J., 1990, Bidirectional reflectance of selected desert surfaces and their three parameter soil characterisation, *Agricultural and Forest Meteorology*, **52**, 71-90.

Deschamps, P.Y., Bréon, F.M., Leroy, M., Podaire, A., Bricaud, A., Buriez, J.C., and Seze, G., 1994, The POLDER mission: instrument characteristics and scientific objectives, *IEEE Transactions on Geoscience and Remote Sensing*, **32**, 598-615.

Despan, D., Bedidi, A., and Cervelle, B., 1999, Bidirectional reflectance of rough bare soil surfaces, *Geophysical Research Letters*, **26**, 2777-2780.

Disney, M.I., Lewis, P., and North, P.R.J., 2000, Monte Carlo ray tracing in optical canopy reflectance modelling, *Remote Sensing Reviews*, **18**, 163-196.

Dougill, A.J., Thomas, D.S.G., and Heathwaite, A.L., 1999, Environmental change in the Kalahari: Integrated land degradation studies for nonequilibrium dryland environments, *Annals of the Association of American Geographers*, **89**, 3, 420-442.

Dowty, P., Frost, P., Lesolle, P., Midgley, G., Mukelabai, M., Otter, L., Privette, J., Ramontsho, J., Ringrose, S., Scholes, B., and Wang, Y., 2000, Summary of the SAFARI 2000 wet season field campaign along the Kalahari transect, *The Earth Observer*, **12**, 3, 29-34.

Drake, N.A., Mackin, S., and Settle, J., 1999, Mapping vegetation, soils, and geology in semiarid shrublands using spectral matching and mixture modeling of SWIR AVIRIS imagery, *Remote Sensing of Environment*, **68**, 12-25.

Duncan, J., Stow, D., Franklin, J., and Hope, A., 1993, Assessing the relationship between spectral vegetation indices and shrub cover in the Jornada Basin, New Mexico, *International Journal of Remote Sensing*, **14**, 3395-3416.

Edwards, M.C., Wellens, J., and Al-Eisawi, D., 1999, Monitoring the grazing resources of the Badia region, Jordan, using remote sensing, *Applied Geography*, **19**, 385-398.

Elmore, A.J., Mustard, J.F., Manning, S.J., and Lobell, D.B., 2000, Quantifying vegetation change in semiarid environments: precision and accuracy of spectral mixture analysis and the normalized difference vegetation index, *Remote Sensing of Environment*, **73**, 87-102.

Fang, H., and Liang, S., 2003, Retrieving leaf area index with a neural network method: Simulation and validation, *IEEE Transactions on Geoscience and Remote Sensing*, **41**, 9, 2052-2062.

Fang, H., and Liang, S., 2005, A hybrid inversion method for mapping leaf area index from MODIS data: experiments and application to broadleaf and needleleaf canopies, *Remote Sensing of Environment*, **94**, 405-424.

Fang, H., Liang, S., and Kuusk, A., 2003, Retrieving leaf area index using a genetic algorithm with a canopy radiative transfer model, *Remote Sensing of Environment*, **85**, 257-270.

Fassnacht, K.S., Gower, S.T., MacKenzie, M.D., Nordheim, E.V., and Lillesand, T.M., 1997, Estimating the leaf area index of North Central Wisconsin forests using the Landsat thematic mapper, *Remote Sensing of Environment*, **61**, 229-245.

Fensholt, R., Sandholt, I., and Rasmussen, M.S., 2004, Evaluation of MODIS LAI, FAPAR and the relation between FAPAR and NDVI in a semi-arid environment using in situ measurements, *Remote Sensing of Environment*, **91**, 490-507.

Foley, J.A., DeFries, R., Asner, G.P., Barford, C., Bonan, G., Carpenter, S.R., Chapin, F.S., Coe, M.T., Daily, G.C., Gibbs, H.K., Helkowski, J.H., Holloway, T., Howard, E.A., Kucharik, C.J., Monfreda, C., Patz, J.A., Prentice, I.C., Ramankutty, N., and Snyder, P.K., 2005, Global consequences of land use, *Science*, **309**, 570-574.

Fourty, T., and Baret, F., 1997, Vegetation water and dry matter contents estimated from top-of-the-atmosphere reflectance data, *Remote Sensing of Environment*, **61**, 34-45.

Franklin, J., and Strahler, A.H., 1988, Invertible canopy reflectance modeling of vegetation structure in semiarid woodland, *IEEE Transactions on Geoscience and Remote Sensing*, **26**, 809-825.

Franklin, J., and Turner, D.L., 1992 The application of a geometric optical canopy reflectance model to semiarid shrub vegetation, *IEEE Transactions on Geoscience and Remote Sensing*, **30**, 293-301.

Frost, P.G., Medina, E., Menaut, J.C., Solbrig, O., Swift, M., and Walker, B., (eds.) 1986, *Responses of savannas to stress and disturbance*. Biology International Special Issue No. 10, IUBS, Paris.

Gastellu-Etchegorry, J.P., Demarez, V., Pinel, V., and Zagolski, F., 1996, Modeling radiative transfer in heterogeneous 3-D vegetation canopies, *Remote Sensing of Environment*, **58**, 131-156.

Gastellu-Etchegorry, J.P., Gascon, F., and Esteve, P., 2003, An interpolation procedure for generalizing a look-up table inversion method, *Remote Sensing of Environment*, **87**, 55-71.

Gates, D.M., Keegan, H.J., Schleter, J.C., and Weidner, R., 1965, Spectral properties of plants, *Applied Optics*, **4**, 11-20.

Gemmell, F., and McDonald, A.J., 2000, View zenith angle effects on the forest information content of three spectral indices, *Remote Sensing of Environment*, **72**, 139-158.

Gerstl, S.A.W., 1990, Physics concepts of optical and radar reflectance signatures, *International Journal of Remote Sensing*, **11**, 1109-1117.

Gerstl, S.A.W., and Borel, C.C., 1992, Principles of the radiosity method versus radiative transfer for canopy reflectance modeling, *IEEE Transactions on Geoscience and Remote Sensing*, **30**, 2, 271-275.

Gobron, N., Pinty, B., and Verstraete, M.M., 1997, Theoretical limits to the estimation of the leaf area index on the basis of visible and near-infrared remote sensing data, *IEEE Transactions on Geoscience and Remote Sensing*, **35**, 6, 1439-1444.

Goel, N.S., 1988. Models of vegetation canopy reflectance and their use in estimation of biophysical parameters from reflectance data, *Remote Sensing Reviews*, **4**. 1-212.

Goel, N.S., 1989, Inversion of canopy reflectance models for estimation of biophysical parameters from reflectance data, In, Asrar, G. (Editor) *Theory and Applications of Optical Remote Sensing*, pp. 205-251., John Wiley & Sons, New York.

Goel, N.S., and Strebel, D.E., 1983, Inversion of vegetation canopy reflectance models for estimating agronomic variables. I., Problem definition and initial results using the Suits model, *Remote Sensing of Environment*, **13**, 487-507.

Goel, N.S., and Thompson, R.L., 1984a, Inversion of vegetation canopy reflectance models for estimating agronomic variables. III., estimation using only canopy reflectance data as illustrated by the Suits model, *Remote Sensing of Environment*, **15**, 223-236.

Goel, N.S., and Thompson, R.L., 1984b, Inversion of vegetation canopy reflectance models for estimating agronomic variables. IV. Total inversion of the SAIL model, *Remote Sensing of Environment*, **15**, 237-253.

Goel, N.S., and Thompson, R.L., 1984c, Inversion of vegetation canopy reflectance models for estimating agronomic variables. V. Estimation of leaf area index and average leaf angle using measured canopy reflectances, *Remote Sensing of Environment*, **16**, 69-85.

Goel, N.S., and Thompson, R.L., 2000, A snapshot of canopy reflectance models and a universal model for the radiation regime, *Remote Sensing Reviews*, **18**, 197-225.

Gong, P., Wang, D.X., Liang, S., 1999, Inverting a canopy reflectance model using a neural network, *International Journal of Remote Sensing*, **20**, 1, 111-122.

Goodchild, M.F., 1986, *Spatial autocorrelation*, CATMOG 47, GEOBOOKS, Norwich, U.K.

Gower, S.T., Kucharik, C.J., and Norman, J.M., 1999, Direct and indirect estimation of leaf area index, FAPAR, and net primary production of terrestrial ecosystems, *Remote Sensing of Environment*, **70**, 29-51.

Grace, J., 2004, Understanding and managing the global carbon cycle, *Journal of Ecology*, **92**, 189-202.

Graetz, R.D., and Gentle, M.R., 1982, The relationship between reflectance in the Landsat wavebands and the composition of an Australian semi-arid shrub rangeland, *Photogrammetric Engineering and Remote Sensing*, **148**, 1721-1730.

Graetz, R.D., Pech, R.P., and Davis, A.W., 1988, The assessment and monitoring of sparsely vegetated rangelands using calibrated Landsat data, *International Journal of Remote Sensing*, **9**, 1201-1222.

Grant, L., 1987, Diffuse and specular characteristics of leaf reflectance, *Remote Sensing of Environment*, **22**, 309-322.

Hanan, N.P., 2001, Enhanced two-layer radiative transfer scheme for a land surface model with a discontinuous upper canopy, *Agricultural and Forest Meteorology*, **109**, 265-281.

Hapke, B., 1986, Bidirectional reflectance spectroscopy 4: The extinction coefficient and the opposition effect, *Icarus*, **67**, 264-280.

Hapke, B., DiMucci, D., Nelson, R., and Smythe, W., 1996, The cause of the hot spot in vegetation canopies and soils: shadow-hiding versus coherent backscatter, *Remote Sensing of Environment*, **58**, 63-68.

Haykin, S., 1999, *Neural networks: a comprehensive foundation*, Second edition, Prentice Hall, New Jersey, USA.

Hibbard, K.A., Archer, S., Schimel, D.S., and Valentine, D.W., 2001, Biogeochemical changes accompanying woody plant encroachment in a subtropical savanna, *Ecology*, **82**, 7, 1999-2011.

Hosgood, B., Jacquemoud, S., Andreoli, G., Verdebout, J., Pedrini, G., and Schmuck, G., 1994, *Leaf optical properties experiment (LOPEX93)*, European Commission, Joint Research Centre, Institute for Remote Sensing Applications. Report EUR 16095 EN, p.21.

Hosgood, B., Sandmeier, St., Piironen, J., Andreoli, G., and Koechler, C., 1999, Goniometers, In *Encyclopedia of Electrical and Electronics Engineering*, Wiley and sons, New York, Vol.8, pp. 424-433.

House, J.I., Prentice, I.C., Ramankutty, N., Houghton, R.A., and Heimann, M., 2003, Reconciling apparent inconsistencies in estimates of terrestrial CO2 sources and sinks, *Tellus*, **55B**, 345-363.

Hu, B., Inannen, K., and Miller, J.R., 2000, Retrieval of Leaf Area Index and canopy closure from CASI data over the BOREAS flux tower sites, *Remote Sensing of Environment*, **74**, 255-274.

Huete, A., Didan, K., Miura, T., Rodriguez,E.P., Gao,X., and Ferreira, L.G., 2002, Overview of the radiometric and biophysical performance of the MODIS vegetation indices, *Remote Sensing of Environment*, **83**, 195-213.

Huete, A.R., 1988, A soil-adjusted vegetation index (SAVI), *Remote Sensing of Environment*, **25**, 295-309.

Huete, A.R., and Jackson, 1987, Suitability of spectral indices for evaluating vegetation characteristics on arid rangelands, *Remote Sensing of Environment*, **23**, 213-232.

Iaquinta, J., Pinty, B., and Privette, J.L., 1997 Inversion of a physically based bidirectional reflectance model of vegetation, *IEEE Transactions on Geoscience and Remote Sensing*, **35**, 687-698.

Irons, J.R., Campbell, G.S., Norman, J.M., Graham, D.W., and Kovalick, W.M., 1992, Prediction and measurement of soil bidirectional reflectance, *IEEE Transactions on Geoscience and Remote Sensing*, **30**, 2, 249-260.

Irons, J.R., Weismiller, R.A., and Petersen, G.W., 1989, Soil reflectance, In, Asrar, G. (Editor) *Theory and Applications of Optical Remote Sensing*, pp. 66-106., John Wiley & Sons, New York.

Jackson, R.B., Banner, J.L., Jobbagy, E.G., Pockman, W.T., and Wall, D.H., 2002, Ecosystem carbon loss with woody plant invasion of grasslands, *Nature*, **418**, 623-626.

Jacquemoud, S., and Baret, F., 1990, PROSPECT: A model of leaf optical properties spectra, *Remote Sensing of Environment*, **34**, 75-91.

Jacquemoud, S., Bacour, C., Poilve, H., and Frangi, J.-P., 2000, Comparison of four radiative transfer models to simulate plant canopies reflectance: Direct and inverse mode, *Remote Sensing of Environment*, **74**, 471-481.

Jacquemoud, S., Baret, F., and Hanocq, J.F., 1992, Modeling spectral and bidirectional soil reflectance, *Remote Sensing of Environment*, **41**, 123-132.

Jacquemoud, S., Baret, F., Andrieu, B., Danson, F.M., and Jaggard, K., 1995, Extraction of vegetation biophysical parameters by inversion of the PROSPECT + SAIL models on sugar beet canopy reflectance data. Application to TM and AVIRIS sensors, *Remote Sensing of Environment*, **52**, 163-172.

Jacquemoud, S., Ustin, S.L., Verdebout, J., Schmuck, G., Andreoli, G., and Hosgood, B., 1996, Estimating leaf biochemistry using the PROSPECT leaf optical properties model, *Remote Sensing of Environment*, **56**, 194-202.

Jeltsch, F., Milton, S.J., Dean, W.R.J., and van Rooyen, N., 1997, Simulated pattern formation around artificial waterholes in the semi-arid Kalahari, *Journal of Vegetation Science*, **8**, 2,177-188.

Justice, C. O., Townshend, J.R.G., Vermote, E.F., Masuoka, E., Wolfe, R.E., Saleous, N., Roy, D.P., and Morisette, J.T., 2002, An overview of MODIS land data processing and product status, *Remote Sensing of Environment*, **83**, 3-15.

Kaufman, Y.J., 1989, The atmospheric effect on remote sensing and its correction, In Asrar, G., (Editor), *Theory and Applications of Optical Remote Sensing*, pp. 336-428, John Wiley & Sons, New York.

Kaufman, Y.J., Karnieli, A., and Tanre, D., 2000, Detection of dust over deserts using satellite data in the solar wavelengths, *IEEE Transactions on Geoscience and Remote Sensing*, **38**, 525-531.

Kimes, D., Gastellu-Etchegorry, Esteve, P., 2002, Recovery of forest canopy characteristics through inversion of a complex 3D model, *Remote Sensing of Environment*, **79**, 320-328.

Kimes, D.S., 1983, Dynamics of directional reflectance factor distributions for vegetation canopies, *Applied Optics*, **22**, 1364-1372.

Kimes, D.S., Knyazikhin, Y., Privette, J.L., Abuelgasim, A.A., and Gao, F., 2000, Inversion methods for physically based models, *Remote Sensing Reviews*, **18**, 381-439.

Kimes, D.S., Nelson, R.F., Manry, M.T., and Fung, A.K., 1998, Attributes of neural networks for extracting continuous vegetation variables from optical and radar measurements, *International Journal of Remote Sensing*, **19**, 14, 2639-2663.

Kimes, D.S., Norman, J.M., and Walthall, C.L., 1985, Modeling the radiant transfers of sparse vegetation canopies, *IEEE Transactions on Geoscience and Remote Sensing*, **23**, 695-704.

Kimes, D.S., Ranson, K.J., and Sun, G., 1997, Inversion of a forest backscatter model using neural networks, *International Journal of Remote Sensing*, **18**, 10, 2181-2199.

Knyazikhin, Y., Glassy, J., Privette, J.L., Tian, Y., Lotsch, A., Zhang, Y., Wang, Y., Morisette, J.L., Votava, P., Myneni, R.B., Nemani, R.R., Running, S.W., 1999, MODIS leaf area index (LAI) and fraction of photosynthetically active radiation absorbed by vegetation (FPAR) product (MOD15) algorithm theoretical basis document, http://eospso.gsfc.nasa.gov/atbd/modistables.html. Last accessed 13 May 2002.

Knyazikhin, Y., Martonchik, J.V., Diner, D.J., Myneni, R.B., Verstraete, M., Pinty, B., and Gobron, N., 1998a, Estimation of vegetation canopy leaf area index and fraction of absorbed photosynthetically active radiation from atmosphere-corrected MISR data, *Journal of Geophysical Research*, **103**, d24, 32,239-32,256.

Knyazikhin, Y., Martonchik, J.V., Myneni, R.B., Diner, D.J., and Running, S.W., 1998b, Synergistic algorithm for estimating vegetation canopy leaf area index and fraction of absorbed photosynthetically active radiation from MODIS and MISR data, *Journal of Geophysical Research*, **103**, d24, 32,257-32,276.

Kremer, R.G., and Running, S.W., 1993, Community type differentiation using NOAA/AVHRR data within a sagebrush-steppe ecosystem, *Remote Sensing of Environment*, **46**, 311-318.

Kucharik, C.J., Norman, J.M., Gower, S.T., 1998, Measurements of branch area and adjusting leaf area index indirect measurements, *Agricultural and Forest Meteorology*, **91**, 69-88.

Kuusk, A., and Nilson, T., 2001, Testing directional properties of a forest reflectance model, *Journal of Geophysical Research*, **106**, D11, 12,011-12,021.

Lacaze, R., and Roujean, J-L., 2001, G-function and Hot SpoT (GHOST) reflectance model application to multi-scale airborne POLDER measurements, *Remote Sensing of Environment*, **76**, 67-80.

Lacaze, R., Chen, J.M., Roujean, J-L., and Leblanc, S.G., 2002, Retrieval of vegetation clumping index using hot spot signatures measured by POLDER instrument, *Remote Sensing of Environment*, **79**, 84-95.

Laliberte, A.S., Rango, A., Havstad, K.M., Paris, J.F., Beck, R.F., McNeely, R., and Gonzalez, A.L., 2004, Object-oriented image analysis for mapping shrub encroachment from 1937 to 2003 in southern New Mexico, *Remote Sensing of Environment*, **93**, 198-210.

Lancaster, I.N., 1978, The pans of the southern Kalahari, Botswana, *Geographical Journal*, **144**, 81-98.

Leblanc, S., Bicheron, P., Chen, J.M., Leroy, M., and Cihlar, J., 1999, Investigation of directional reflectance in Boreal forests with an improved four-scale model and airborne POLDER data, *IEEE Transactions on Geoscience and Remote Sensing*, **37**, 3, 1396-1414.

Lee, K-S., Cohen, W.B., Kennedy, R.E., Maiersperger, T.K., and Gower, S.T., 2004, Hyperspectral versus multispectral data for estimating leaf area index in four different biomes, *Remote Sensing of Environment*, **91**, 508-520.

Leprieur, C., Kerr, Y.H., and Pichon, J.M., 1996, Critical assessment of vegetation indices from AVHRR in a semi-arid environment, *International Journal of Remote Sensing*, **17**, 13, 2549-2563.

Leprieur, C., Verstraete, M.M., and Pinty, B., 1994, Evaluation of the performance of various vegetation indices to retrieve vegetation cover from AVHRR data, *Remote Sensing Reviews*, **10**, 265-284.

Levenberg, K., 1944, A method for the solution of certain non-linear problems in least squares, *Quarterly Journal of Applied Mathematics*, **II (2)**, 164-168.

Li, X., and Strahler, A.H., 1985, Geometric-Optical modeling of a conifer forest canopy, *IEEE Transactions on Geoscience and Remote Sensing*, **GE-23**, 705-721.

Li, X., and Strahler, A.H., 1992, Geometric-optical bidirectional reflectance modelling of the discrete crown vegetation canopy: effect of crown shape and mutual shadowing, *IEEE Transactions on Geoscience and Remote Sensing*, **30**, 2, 276-292.

Li, X., and Strahler, A.H., 1992, Geometric-optical bidirectional reflectance modelling of the discrete crown vegetation canopy: effect of crown shape and mutual shadowing, *IEEE Transactions on Geoscience and Remote Sensing*, **30**, 2, 276-292.

Li, X., Gao, F., Wang, J., and Strahler, A., 2001, A priori knowledge accumulation and its application to linear BRDF model inversion, *Journal of Geophysical Research*, **106**, D11, 11,925-11,935.

Li, X., Strahler, A.H., and Woodcock, C.E., 1995, A hybrid geometric optical-radiative transfer approach for modelling albedo and directional reflectance of

discontinuous canopies, *IEEE Transactions on Geoscience and Remote Sensing*, **33**, 2, 466-480.

Li, Z-J., Fung, A.K., Tjuatja, S., Gibbs, D.P., Betty, C.L., and Irons, J.R., 1996, A modeling study of backscattering from soil surfaces, *IEEE Transactions on Geoscience and Remote Sensing*, **34**, 1, 264-271.

Liang, S., Fang, H., and Chen, M., 2001, Atmospheric Correction of Landsat ETM+ Land Surface Imagery-Part I: Methods, *IEEE Transactions on Geoscience and Remote Sensing*, **39**, 11, 2490-2498.

Liang, S., Fang, H., Morisette, J.T., Chen, M., Shuey, C.J., Walthall, C., and Daughtry, C.S.T., 2002, Atmospheric correction of Landsat ETM+ land surface imagery - Part II: validation and applications, *IEEE Transactions on Geoscience and Remote Sensing*, **40**, 2736-2746.

Liang, S., Strahler, A.H., Jin, X., and Zhu, Q., 1996, Comparisons of radiative transfer models of vegetation canopies and laboratory measurements, *Remote Sensing of Environment*, **61**, 129-138.

Lindesay, J.A., 1988, South African rainfall, the Southern Oscillation and a Southern-Hemisphere semi-annual cycle, *Journal of Climatology*, **8**, 17-30.

Lu, H., Raupach, M.R., McVicar, T.R., and Barrett, D.J., 2003, Decomposition of vegetation cover into woody and herbaceous components using AVHRR NDVI time series, *Remote Sensing of Environment*, **86**, 1-18.

Lucht, W., and Roujean, J.L., 2000, Considerations in the parametric modelling of BRDF and albedo from multiangular satellite sensor observations, Remote Sensing Reviews, 18, 343-379.

Lyapustin, A.I., and Privette, J.L., 1999, A new method of retrieving surface bidirectional reflectance from ground measurements: Atmospheric sensitivity study, Journal of Geophysical Research, 104, 6257-6268.

Maignan, F., Breon, F.M., and Lacaze, R., 2004, Bidirectional reflectance of Earth targets: evaluation of analytical models using a large set of spaceborne measurements with emphasis on the hot spot, Remote Sensing of Environment, 90, 210-220.

Malthus, T.J., Andrieu, B., Danson, F.M., Jaggard, K.W., and Steven, M.D., 1993, Candidate high spectral resolution infrared indices for crop cover, *Remote Sensing of Environment*, **46**, 204-212.

Marquardt, D.W., 1963, An algorithm for least-squares estimation of non-linear parameters, *Journal of the Society of Industrial and Applied Mathematics*, **11**, 2, 431-441.

Martonchik, J. V., Bruegge, C. J., Strahler, A. H., 2000, A Review of Reflectance Nomenclature Used in Remote Sensing, Remote Sensing Reviews, 19, 9-20.

Mason, S.J., and Jury, M.R., 1997, Climatic variability and change over southern Africa: a reflection on underlying processes, *Progress in Physical Geography*, **21**, 23-50.

Mather, P.M., 1999, *Computer Processing of Remotely-Sensed Images*, Wiley and Sons, UK.

Matthews, E.A., 1983, Global vegetation and land use: New high-resolution databases for climate studies, *Journal of Applied Meteorology*, **22**, 474-487.

Melillo, J.M., Borchers, J., Chaney, J., Fisher, H., Fox, S., Haxeltine, A., Janetos, A., Kicklighter, D.W., Kittel, T.G., F. McGuire, A.D., McKeown, R., Neilson, R., Nemani, R., Ojima, D.S., Painter, T., Pan, Y., Parton, W.J., Pierce, L., Pitelka, L., Prentice, C., Rizzo, B., Rosenbloom, N.A., Running, S., Schimel, D.S., Sitch, S. et al., 1995, Vegetation ecosystem modelling and analysis project - comparing biogeography and biogeochemistry models in a continental scale study of terrestrial ecosystem responses to climate change and co2 doubling, *Global Biogeochemical Cycles*, **9**, 407-437.

Meroni, M., Colombo, R., and Panigada, C., Inversion of a radiative transfer model with hyperspectral observations for LAI mapping in poplar plantations, *Remote Sensing of Environment*, **92**, 195-206.

Merzlyak, M.N., Chivkunova, O.B., Melø, T.B. and Razi Naqvi, K., 2002, Does a leaf absorb radiation in the near infrared (780-900nm) region? A new approach to quantify optical reflectance, absorption and transmission of leaves, *Photosynthesis Research*, **72**, 263-270.

Moran, S., Jackson, R.D., Slater, P.N., and Teillet, P.M., 1992, Evaluation of simplified procedures for retrieval of land surface reflectance factors from satellite sensor output, *Remote Sensing of Environment*, **41**, 169-184.

Mueller-Dombois, D., and Ellenberg, H., 1974, *Aims and Methods of Vegetation Ecology*, Wiley and Sons, London.

Musick, H.B., 1984, Assessment of Landsat multispectral scanner spectral indexes for monitoring arid rangeland, *IEEE Transactions on Geoscience and Remote Sensing*, **22**, 6, 512-519.

Myneni, R.B., and Ross, J., 1991, *Photon-Vegetation Interactions*, New York: Springer-Verlag.

Myneni, R.B., and Williams, D.L., 1994, On the relationship between FAPAR and NDVI, *Remote Sensing of Environment*, **49**, 200-211.

Myneni, R.B., Asrar, G., Tanre, D., and Choudhury, B.J., 1992, Remote sensing of solar radiation absorbed and reflected by vegetated land surfaces, *IEEE Transactions on Geoscience and Remote Sensing*, **30**, 302-314.

Myneni, R.B., Hall, F.G., Sellers, P.J., and Marshak, A.L., 1995a, The interpretation of spectral vegetation indexes, *IEEE Transactions on Geoscience and Remote Sensing*, **33**, 2, 481-486.

Myneni, R.B., Hoffmann, S., Knyazikhin, Y., Privette, J.L., Glassy, J., Tian, Y., Wang, Y., Song, X., Zhang, Y., Smith, G.R., Lotsch, A., Friedl, M., Morisette, J.T., Votava, P., Nemani, R.R., and Running, S.W., 2002, Global products of vegetation leaf area and fraction absorbed PAR from year one of MODIS data, *Remote Sensing of Environment*, **83**, 214-231.

Myneni, R.B., Keeling, C.D., Tucker, C.J., Asrar, G., and Nemani R.R., 1997, Increased plant growth in the northern high latitudes from 1981-1991, *Nature*, **386**, 698-702.

Myneni, R.B., Ross, J., Asrar, G., 1989, A review on the theory of photon transport in leaf canopies, *Agriculture, Forestry, Meteorology*, **45**, 1-153.

Ni, W, and LI, X., 2000, A coupled vegetation-soil bidirectional reflectance model for a semiarid landscape, *Remote Sensing of Environment*, **74**, 113-124.

Ni, W., Li, X., Woodcock, C., Caetano, M.R., and Strahler, A.H., 1999, An analytic hybrid GORT model for bidirectional reflectance over discontinuous plant canopies, *IEEE Transactions on Geoscience and Remote Sensing*, **37**, 2, 987-999.

Nicholson, S.E., and Kim, J., 1997, The relationship of the El Nino-Southern Oscillation to African rainfall, *International Journal of Climatology*, **17**, 117-135.

Nicodemus, F.E., 1970, Reflectance nomenclature and directional reflectance and emissivity, *Applied Optics*, **9**, 6, 1474-1475.

Nilson, T., 1971, A theoretical analysis of the frequency of gaps in plant stands, *Agricultural and Forest Meteorology*, **8**, 25-38.

Nilson, T., and Peterson, 1991, A forest canopy reflectance model and a test case, *Remote Sensing of Environment*, **37**, 131-142.

Norman, J.M., and Campbell, G.S., 1989, Canopy structure, In, Pearcy, R.W., Ehleringer, J., Mooney, H.A., and Rundel, P.W., 1989, *Plant Physiological Ecology Field Methods and Instrumentation*, Chapman Hall, London U.K., pp.301-325.

Norman, J.N., Welles, J.M., and Walter, E.A., 1985, Contrasts among bidirectional reflectance of leaves, canopies, and soils, *IEEE Transactions on Geoscience and Remote Sensing*, **23**, 659-667.

North, P.R.J., 1996, Three-dimensional forest light interaction model using a Monte Carlo method, *IEEE Transactions on Geoscience and Remote Sensing*, **34**, 4, 946-956.

North, P.R.J., 2002, Estimation of FAPAR, LAI, and vegetation fractional cover from ATSR-2 imagery, *Remote Sensing of Environment*, **80**, 114-121.

Numerical Algorithms Group, 1990, *The NAG Fortran Library*, Mark 14, Volume 3, NAG Inc., Downers Grove, Illinois.

Oreskes, N., Schrader-Frechette. K., and Belitz, K., 1994, Verification, validation, and confirmation of numerical models in the earth sciences, Science, 263, 641-646.

Ouaidrari, H., and Vermote, E.F., 1999, Operational atmospheric correction of Landsat TM data, *Remote Sensing of Environment*, **70**, 4-15.

Pacala, S.W., Hurtt, G.C., Baker, D., Peylin, P., Houghton, R.A., Birdsey, R.A., Heath, L., Sundquist, E.T., Stallard, R.F., Ciais, P., Moorcroft, P., Caspersen, J.P., Shevliakova, E., Moore, B., Kohlmaier, G., Holland, E., Gloor, M., Harmon, M.E., Fan, S.-M., Sarmiento, J.L., Goodale, C.L., Schimel, D., and Field, C.B., 2001, Consistent land- and atmosphere-based U.S. carbon sink estimates, *Science*, **292**, 2316-2320.

Palmer, A.R., and van Rooyen, 1998, Detecting vegetation change in the southern Kalahari using Landsat TM data, *Journal of Arid Environments*, **39**, 143-153.

Peddle, D.R., Franklin, S.E., Johnson, R.L., Lavigne, M.A., and Wulder, M.A., 2003, Structural change detection in a disturbed conifer forest using a geometric optical reflectance model in multiple-forward-mode, *IEEE Transactions on Geoscience and Remote Sensing*, **41**, 1, 163-166.

Peddle, D.R., Johnson, R.L., Cihlar, J., and Latifovic, R., 2004, Large area forest classification and biophysical parameter estimation using the 5-Scale canopy reflectance model in multiple-forward-mode, *Remote Sensing of Environment*, **89**, 252-263.

Peñuelas, J., Piñol, J., Ogaya, R., and Filella, I., 1997, Estimation of plant water concentration by the reflectance Water Index WI (R900/R970), *International Journal of Remote Sensing*, **18**, 13, 2869-2875.

Perkins, J.S., and Thomas, D.S.G., 1993, Spreading deserts or spatially confined environmental impacts? Land degradation and cattle ranching in the Kalahari desert of Botswana, *Land Degradation and Rehabilitation*, **4**, 179-194.

Pielke, R.A., and Avissar, R., 1990, Influence of landscape structure on local and regional climate, *Landscape Ecology*, **4**, 133-155.

Pinty, B., Gobron, N., Widlowski, J-L., Gerstl, S.A., Verstraete, M.M., Antunes, M., Bacour, C., Gascon, F., Gastellu-Etchegorry, J-P., Goel, N., Jacquemoud, S., North. P., Qin, W., and Thompson, R., 2001, Radiation transfer model intercomparison (RAMI) exercise, *Journal of Geophysical Research*, **106**, D11, 11,937-11,956.

Pinty, B., Verstraete, M.M., and Dickinson, R.E., 1990, A physical model of the bidirectional reflectance of vegetation canopies. 2. Inversion and validation, *Journal of Geophysical Research*, **95**, 11767-11775.

Pinty, B., Verstraete, M.M., and Gobron, N., 1998, The effect of soil anisotropy on the radiance field emerging from vegetation canopies, *Geophysical Research Letters*, **25**, 6, 797-800.

Pinty, B., Widlowski, J-L., Taberner, M., Gobron, N., Verstraete, M.M., Disney, M., Gascon, F., Gastellu-Etchegorry, J-P., Jiang, L., Kuusk, A., Lewis, P., Li, X., Ni-Meister, W., Nilson, T., North, P., Qin, W., Su, L., Tang, S., Thompson, R., Verhoef, W., Wang, H., Wang, J., Yan, G., Zang, H., 2004, Radiation transfer model intercomparison (RAMI) exercise: results from the second phase, *Journal of Geophysical Research*, **109**, D06210, doi:10.1029/2003JD004252.

Potter, C.S., Randerson, J.T., Field, C.B., Matson, P.A., Vitousek, P.M., Mooney, H.A., Klooster, S.A., 1993, Terrestrial ecosystem production: a process model based on global satellite and surface data, *Global Biogeochemical Cycles*, **7**, 811-841.

Prentice, I.C., Heimann, M., and Sitch, S., 2000, The carbon balance of the terrestrial biosphere: ecosystem models, and atmospheric observations, *Ecological Applications*, **10**, 1553-1573.

Press, W.H., Flannery, B.P., Teukolsky, S.A., and Vetterling, W.T., 1986, *Numerical Recipes*, Cambridge University Press, New York, pp. 274-312.

Preston-Whyte, R.A., and Tyson, P.D., 1989, *The Atmosphere and Weather of Southern Africa*, Oxford University Press, Cape Town, 374 pp.

Price, J., and Bausch, W.C., 1995, Leaf area index estimation from visible and near infrared reflectance data, *Remote Sensing of Environment*, **52**, 55-65.

Prince, S.D., and Astle, W.L., 1986, Satellite remote sensing of rangelands in Botswana I. Landsat MSS and herbaceous vegetation, *International Journal of Remote Sensing*, **7**, 1533-1553.

Prince, S.D., and Tucker, C.J., 1986, Satellite remote sensing of rangelands in Botswana II. NOAA AVHRR and herbaceous vegetation, *International Journal of Remote Sensing*, **7**, 1555-1570.

Privette, J.L., Asner, G.P., Conel, J., Huemmrich, K.F., Olson, R., Rango, A., Rahman, A.F., Thome, K., and Walter-Shea, E.A., 2000, The EOS prototype validation exercise (PROVE) at Jornada: overview and lessons learned, *Remote Sensing of Environment*, **74**, 1-12.

Privette, J.L., Emery, W.J., and Schimel, D.S., 1996a, Inversion of a vegetation reflectance model with NOAA AVHRR data, *Remote Sensing of Environment*, **58**, 187-200.

Privette, J.L., Myneni, R.B., Emery, W.J., and Hall, F.G., 1996b, Optimal sampling conditions for estimating grassland parameters via reflectance model inversions, *IEEE Transactions on Geoscience and Remote Sensing*, **34**, 1, 272-283.

Privette, J.L., Myneni, R.B., Emery, W.J., and Pinty, B., 1995, Inversion of a soil bidirectional reflectance model for use with vegetation reflectance models, *Journal of Geophysical Research*, **100**, d12, 25,497-25,508.

Privette, J.L., Myneni, R.B., Knyazikhin, M., Mukelabai, M., Roberts, G., Tian, Y., Wang, Y., and Leblanc, S.G., 2001, Early spatial and temporal validation of MODIS LAI product in Africa, *Remote Sensing of Environment*, **83**, 232-243.

Privette, J.L., Myneni, R.B., Tucker, C.J., and Emery, W.J., 1994, Invertibility of a 1-D discrete ordinates canopy reflectance model, *Remote Sensing of Environment*, **48**, 89-105.

Privette, J.L., Tian, Y., Roberts, G., Scholes, R.J., Wang, Y., Caylor, K.K., Frost, P., and Mukelabai, M., 2004, Vegetation structure characteristics and relationships of Kalahari woodlands and savannas, *Global Change Biology*, **10**, 281-291.

Qi, J., Kerr, Y.H., Moran, M.S., Weltz, M., Huete, A.R., Sorooshian, S., and Bryant, R., 2000, Leaf area index estimates using remotely sensed data and BRDF models in a semiarid region, *Remote Sensing of Environment*, **73**, 18-30.

Qin, W., and Gerstl, A.W., 2000, 3-D scene modelling of semidesert vegetation cover and its radiation regime, *Remote Sensing of Environment*, **74**, 145-162.

Qin, W., and Liang, S., 2000, Plane-parallel canopy radiation transfer modelling: recent advances and future directions, *Remote Sensing Reviews*, **18**, 281-305.

Quaife, T., and Barnsley, M.J., 1999, Comparison of SMAC and 6S for atmospheric correction of multi-angle image data sets, 811-818, *RSS 1999*, 8-10 September, University of Wales. RSS University of Nottingham, Nottingham, UK.

Rahman, H., 2001, Influence of atmospheric correction on the estimation of biophysical parameters of crop canopy using satellite remote sensing, *International Journal of Remote Sensing*, **22**, 7, 1245-1268.

Rahman, H., and Dedieu, G., 1994, SMAC: a simplified method for the atmospheric correction of satellite measurements in the solar spectrum, *International Journal of Remote Sensing*, **15**, 123-143.

Rahman, H., Pinty, B., and Verstraete, M.M., 1993, Coupled surface atmosphere reflectance (CSAR) model, 2., Semiempirical surface model usable with NOAA advanced very high resolution radiometer data, *Journal of Geophysical Research*, **98**, 20791-20801.

Rautiainen, M., Stenberg, P., Nilson, T., and Kuusk, A., 2004, The effect of crown shape on the reflectance of coniferous stands, *Remote Sensing of Environment*, **89**, 41-52.

Reason, C.J.C., and Rouault, M., 2002, ENSO-like decadal variability and South African rainfall, *Geophysical Research Letters*, **29**, 987-990.

Richter, R., 1996, A spatially adaptive fast atmospheric correction algorithm, *International Journal of Remote Sensing*, **17**, 1201-1214.

Ringrose, S., and Matheson, W., 1987, Spectral assessment of indicators of range degradation in the Botswana Hardveld environment, *Remote Sensing of Environment*, **23**, 379-396.

Ringrose, S., and Matheson, W., 1991, A Landsat analysis of range conditions in the Botswana Kalahari drought, *International Journal of Remote Sensing*, **12**, 1023-1051.

Ringrose, S., Matheson, W., and Vanderpost, C., 1998, Analysis of soil organic carbon and vegetation cover trends along the Botswana Kalahari Transect, *Journal of Arid Environments*, **38**, 379-396.

Ringrose, S., Matheson, W., Wolski, P., & Huntsman-Mapila, P., 2003, Vegetation cover trends along the Botswana Kalahari transect, *Journal of Arid Environments*, **54**, 297-317.

Rollin, E.M., Milton, E.J., and Emery, D.R., 2000, Reference panel anisotropy and diffuse radiation - some implications for field spectroscopy, *International Journal of Remote Sensing*, **21**, 15, 2799-2810.

Rosema, A., Verhoef, W., Noorbergen, H., and Borgesius, J.J., 1992, a new forest light interaction model in support of forest monitoring, *Remote Sensing of Environment*, **42**, 23-41.

Ross, J.K., 1981, *The Radiation Regime and Architecture of Plant Stands*, W. Junk, The Hague, Netherlands.

Rowell, D.L., 1994, *Soil Science: methods and applications*, Longman Group, UK Limited.

Rumelhart, D.E., Hinton, G.E., and Williams, R.J., 1986, Learning representations by back-propagating errors, *Nature*, **323**, 533-536.

Running, S.W., and Coughlan, J.C., 1988, A general model of forest ecosystem processes for regional applications I. Hydrologic balance, canopy gas exchange and primary production processes, *Ecological Modelling*, **42**, 125-154.

Saltelli, A., 1999, Sensitivity analysis: Could better methods be used?, *Journal of Geophysical Research*, **104**, 3789-3793.

Saltelli, A., 2000, What is sensitivity analysis? In, Saltelli, A., Chan, K., and Scott, E.M., (Eds.) *Sensitivity Analysis*, pp., 3-13, John Wiley & Sons Ltd, Chichester, England.

Saltelli, A., Tarantola, S., and Chan, K.P.S., 1999, A quantitative model-independent method for global sensitivity analysis of model output, *Technometrics*, **41**, 1, 39-56.

Sandmeier, S.R., and Strahler, A.H., 2000, BRDF laboratory measurements, *Remote Sensing Reviews*, **18**, 481-502.

Sandmeier, St., Müller, Ch., Hosgood, B., and Andreoli, G., 1998, Sensitivity analysis and quality assessment of laboratory BRDF data, *Remote Sensing of Environment*, **64**, 176-191.

Schimel, D.S., House, J.I., Hibbard, K.A., Bousquet, P., Ciais, P., Peylin, P., Braswell, B.H., Apps, M.J., Baker, D., Bondeau, A., Canadell, J., Churkina, G., Cramer, W., Denning, A.S., Field, C.B., Friedlingstein, P., Goodale, C., Heimann, M., Houghton, R.A., Melillo, J.M., Moore III, B., Murdiyarso, D., Noble, I., Pacala, S.W., Prentice, I.C., Raupach, M.R., Rayner, P.J., Scholes, R.J., Steffen, W.L., and Wirth, C., 2001, Recent patterns and mechanisms of carbon exchange by terrestrial ecosystems, *Nature*, **414**, 169-172.

Schlesinger, W.H., Reynolds, J.F., Cunningham, G.L., Huenneke, L.F., Jarrell, W.M., Virginia, R.A., Whitford, W.G., 1990, Biological feedbacks in global desertification, *Science*, **247**, 1043-1048.

Schmidt, H., and Karnieli, A., 2000, Remote sensing of the seasonal variability of vegetation in a semi-arid environment, *Journal of Arid Environments*, **45**, 43-59.

Scholes, R. J., Dowty, P. R., Caylor, K., Parsons, D. A. B., Prost, P. G. H., Shugart, H. H., 2002, Trends in savanna structure and composition along an aridity gradient in the Kalahari, *Journal of Vegetation Science*, **13**, 3, 419-428.

Scholes, R.J., 1997, Savanna, In, Cowling, R.M., Richardson, D.M., Pierce, S.M., and Huntley, B.J., (Editors), *Vegetation of Southern Africa*, Cambridge, Cambridge University Press, pp. 258-277.

Scholes, R.J., and Archer, S.J., 1997, Tree-grass interactions in savannas, *Annual Review of Ecology and Systematics*, **28**, 517-544.

Scholes, R.J., and Parsons, D.A.B., 1997, The Kalahari Transect: research on global change and sustainable development in southern Africa, *IGBP Report 42*, IGBP Secretariat, Royal Swedish Academy of Sciences, Stockholm, Sweden.

Scholes, R.J., Frost, P.G.H., and Tian, Y., 2004, Canopy structure in savannas along a moisture gradient on Kalahari sands, *Global Change Biology*, **10**, 292-302.

Sellers, P.J., Dickinson, R.E., Randall, D.A., Betts, A.K., Hall, F.G., Berry, J.A., Collatz, G.J., Denning, A.S., Mooney, H.A., Nobre, C.A., Sato, N., Field, C.B., and Henderson-Sellers, A., 1997, Modelling the exchanges of energy, water, and carbon between continents and the atmosphere, *Science*, **275**, 502-509.

Shaw, P.A., and Thomas, D.S.G., 1997, Pans, playas and salt lakes. In, Thomas, D.S.G. (Editor), *Arid zone geomorphology: process, form, and change in drylands*, Second edition, pp., 293-317, John Wiley & Sons, Chichester, U.K.

Shugart, H.H., Macko, S.A., Lesolle,P., Szuba, T.A., Mukelabai, M.M., Dowty, P., and Swap, R.J., 2004, The SAFARI 2000 - Kalahari transect wet season campaign of year 2000, *Global Change Biology*, **10**, 273-280.

Sietsma, J., and Row, R.J.F., 1991, Creating artificial neural networks that generalize, *Neural Networks*, **4**, 67-79.

Skarpe, C., 1990a, Shrub layer dynamics under different herbivore densities in an arid savanna, Botswana, *Journal of Applied Ecology*, **27**, 873-885.

Skarpe, C., 1990b, Structure of the woody vegetation in disturbed and undisturbed arid savanna, Botswana, *Vegetatio*, **87**, 11-18.

Smith, J.A., 1993, LAI inversion using a backpropagation neural network trained with a multiple scattering model, *IEEE Transactions on Geosciences and Remote Sensing*, **31**, 1102-1106.

Smith, M.O., Ustin, S.L., Adams, J.B., Gillespie, A.R., 1990, Vegetation in deserts: I. A regional measure of abundance from multispectral images, *Remote Sensing of Environment*, **31**, 1-26.

Solbrig, O.T., 1991, Savanna modelling for global change, *Biology International Special Issue No. 24*, IUBS, Paris.

Strahler, A. H., 1997, Vegetation Canopy Reflectance Modeling - Recent Developments and Remote Sensing Perspectives, *Remote Sensing Reviews*, **15**, 179-194.

Strahler, A.H., Jupp, D.L.B., 1990, Modeling bidirectional reflectance of forests and woodlands using boolean models and geometric optics, *Remote Sensing of Environment*, **34**, 153-166.

Su, L., Chopping, M.J., Rango, A., Martonchik, J.V., and Peters, D.P.C., 2005, Recognition of semi-arid vegetation types based on MISR multi-angular observations and surface anisotropy patterns inversed by bidirectional reflectance models, *The 9th International Symposium on Physical Measurements and Signature in Remote Sensing* (ISPMSRS), Beijing, China, October 17-19, 2005, published on CD.

Suits, G.H., 1972, The calculation of the directional reflectance of a vegetative canopy, *Remote Sensing of Environment*, **2**, 117-125.

Swap, R.J., Annegarn, H.J., Suttles, J.T., King, M.D., Platnick, J.L., Privette, J.L., and Scholes, R.J., 2003, Africa burning: a thematic analysis of the southern African regional science initiative (SAFARI 2000), *Journal of Geophysical Research*, **108**, D13, 8465, doi:10.1029/2003JD003747.

Tanre, D., Deroo, C., Duhaut, P., Herman, M., Morcrette, J.J., Perbos, J., and Deschamps, P.Y., 1990, Description of a computer code to simulate the satellite signal in the solar spectrum: 5S code, *International Journal of Remote Sensing*, **11**, 659-668.

Teillet, P.M., and Fedosejevs, 1995, On the dark target approach to atmospheric correction of remotely sensed data, *Canadian Journal of Remote Sensing*, **21**, 374-387.

Thomas, D.S.G. and Shaw, P.A., 1991: *The Kalahari Environment*, Cambridge University Press, Cambridge.

Thomas, D.S.G., Sporton, D., and Perkins, J.S., 2000, The environmental impact of livestock ranches in the Kalahari, Botswana: natural resource use, ecological change and human response in a dynamic dryland system, *Land Degradation and Development*, **11**, 327-341.

Tian, Y., Woodcock, C.E., Wang, Y., Privette, J.L., Shabanov, N.V., Zhou, L., Zhang, Y., Buermann, W., Dong, J., Veikkanen, B., Häme, T., Andersson, K., Ozdogan, M., Knyazikhin, Y., and Myneni, R.B., 2002, Multiscale analysis and validation of the MODIS LAI product I. Uncertainty assessment, *Remote Sensing of Environment*, **83**, 414-430.

Trodd, N.M., and Dougill, A.J., 1998, Monitoring vegetation dynamics in semi-arid African rangelands: use and limitations of Earth observation data to characterise vegetation structure, *Applied Geography*, **18**, 315-330.

Tucker, C.J., 1979, Red and photographic infrared linear combinations for monitoring vegetation, *Remote Sensing of Environment*, **8**, 127-150.

Turner, D.P., Cohen, W.B., Kennedy, R.E., Fassnacht, K.S., and Briggs, J.M., 1999, Relationships between leaf area index and Landsat TM spectral vegetation indices across three temperate zone sites, *Remote Sensing of Environment*, **70**, 52-68.

Tyson, P.D., 1986, *Climatic change and variability over Southern Africa*, Oxford University Press, Cape Town, 220 pp.

Tyson, P.D., and Crimp, S.J., 1998, The climate of the Kalahari Transect, *Transactions of the Royal Society of South Africa*, **53**, 93-112.

Tyson, P.D., Dyer, T.G.J., and Mametse, M.N., 1975, Secular changes in South African rainfall: 1880 to 1972, *Quarterly Journal of the Royal Meteorological Society*, **101**, 817-833.

van Leeuwen, W.J.D., and Huete, A.R., 1996, Effects of standing litter on the biophysical interpretation of plant canopies with spectral indices, *Remote Sensing of Environment*, **55**, 123-134.

van Leeuwen, W.J.D., Huete, A.R., Walthall, C.L., Prince, S.D., Bégué, A., Roujean, J.L., 1997, Deconvolution of remotely sensed spectral mixtures for retrieval of LAI, fAPAR and soil brightness, *Journal of Hydrology*, **Vol.189**, No.1-4, pp.697-724.

van Rooyen, N., and van Rooyen, M.W., 1998, Vegetation of the south-western arid Kalahari: an overview, Transactions Royal Society of South Africa, 53, 113-140.

Verhoef, W., 1984, Light scattering by leaf layers with application to canopy reflectance modelling: the SAIL model, *Remote Sensing of Environment*, **16**, 125-141.

Vermote, E.F., and Vermeulen, A., 1999, Atmospheric correction algorithm: spectral reflectances (MOD09), Algorithm Theoretical Background Document, (http://modarch.gsfc.NASA.gov/MODIS/ATBD/atbd_mod09.pdf (Last accessed: 21 February 2003)

Vermote, E.F., El Saleous, N., Justice, C.O., Kaufman, Y.J., Privette, J.L., Remer, L., Roger, J.C., and Tanré, D., 1997b, Atmospheric correction of visible to middle-infrared EOS-MODIS data over land surfaces: background operational algorithm and validation, *Journal of Geophysical Research*, **102**, D14, 17,131-17,141.

Vermote, E.F., El Saleous, N.Z., and Justice, C.O., 2002, Atmospheric correction of MODIS data in the visible to middle infrared: first results, *Remote Sensing of Environment*, **83**, 97-111.

Vermote, E.F., Tanre, D., Deuze, J.L., Herman, M., and Morcrette, J-J., 1997a, Second simulation of the satellite signal in the solar spectrum, 6S: An Overview, *IEEE Transactions on Geoscience and Remote Sensing*, **35**, 675-686.

Verstraete, M. M., and Pinty, B., 1996, Designing optimal spectral indices for remote sensing applications, *IEEE Transactions on Geoscience and Remote Sensing*, **34**, 1254-1265.

Verstraete, M.M., Pinty, B., and Myneni, R.B., 1996, Potential and limitations of information extraction on the terrestrial biosphere from satellite remote sensing, *Remote Sensing of Environment*, 58, 201-214.

Walthall, C., Dulaney, W., Anderson, M., Norman, J., Fang, H., and Liang, S., 2004, A comparison of empirical and neural network approaches for estimating corn and soybean leaf area index from Landsat ETM+ imagery, *Remote Sensing of Environment*, **92**, 465-474.

Walthall, C.L., Kim, M., Williams, D.L., Meeson, B.W., Agbu, P.A., Newcomer, J.A., and Levine, E.R., 1993, Data sets for modelling: A retrospective collection of bidirectional reflectance and forest ecosystem dynamics multisensor aircraft campaign data sets, *Remote Sensing of Environment*, **46**, 340-346.

Walthall, C.L., Roujean, J.L., and Morisette, J., 2000, Field and landscape BRDF optical wavelength measurements: experience, techniques and the future, *Remote Sensing Reviews*, **18**, 503-531.

Wang, Y., Tian, Y., Zhang, Y., El-Saleous, N., Knyazikhin, Y., Vermote, E., and Myneni, R.B., 2001, Investigation of product accuracy as a function of input and model uncertainties, *Remote Sensing of Environment*, **78**, 3, 299-313.

Wang, Y., Woodcock, C.E., Buermann, W., Stenberg, P., Voipio, P., Smolander, H., Häme, T., Tian, Y., Hu, J., Knyazikhin, Y., and Myneni, R.B., 2004, Evaluation of the

MODIS LAI algorithm at a coniferous forest site in Finland, *Remote Sensing of Environment*, **91**, 114-127.

Wang, Y.P., and Jarvis, P.G., 1988, Mean leaf angles for the ellipsoidal inclination angle distribution, *Agricultural and Forest Meteorology*, **43**, 319-321.

Wanner, W., Li, X., and Strahler, A.H., 1995, On the derivation of kernels for kernel-driven models of bidirectional reflectance, *Journal of Geophysical Research*, **100**. d10, 21,077-21,089.

Wanner, W., Strahler, A.H., Hu, B., Lewis, P., Muller, J-P., Li, X., Barker-Schaaf, C.L., and Barnsley M.J., 1997, Global retrieval of BRDF and albedo over land from EOS MODIS and MISR data: theory and algorithm, *Journal of Geophysical Research*, **102**, 17143-17162.

Weare, P.R., and Yalala, A., 1971, Provisional vegetation map of Botswana, *Botswana Notes and Records*, **3**, 131-147.

Weiss, M., Baret, F., Myneni, R.B., Pragnere, A., and Knyazikhin, Y., 2000, Investigation of a model inversion technique to estimate canopy biophysical variables from spectral and directional reflectance data, *Agronomie*, **20**, 3-22.

Welles, J.M., 1990, Some indirect methods of estimating canopy structure, *Remote Sensing Reviews*, **5**, 31-43.

White, M.A., Asner, G.P., Nemani, R., Privette, J.L., and Running, S.W., 1999, Measuring fractional cover and leaf area index in arid ecosystems: digital camera, radiation transmittance, and laser altimetry methods, *Remote Sensing of Environment*, **74**, 45-57.

Wofsy, S.C., 2001, Where has all the Carbon gone?, Science, 292, 2261-2263.

Wohlfahrt, G., Sapinsky, S., Tappeiner, U., and Cernusca, A., 2001, Estimation of plant area index of grasslands from measurements of canopy radiation profiles, *Agricultural and Forest Meteorology*, **109**, 1-12.

Wolfe, R.E., Nishihama, M., Fleig, A.J., Kuyper, J.A., Roy, D.P., Storey, J.C., and Patt, F.S., 2002, Achieving sub-pixel geolocation accuracy in support of MODIS land science, *Remote Sensing of Environment*, **83**, 31-49.

Wood, J., 1996, LAI theory, In, Potter, E., Wood, J., and Nicholl, C., *SunScan Canopy Analysis System User Manual*, SS1-UM-1.05, pp.54-62.

Woodcock, C.E., Collins, J.B., Jakabhazy, V.D., Li, X., Macomber, S.A., , and Wu, Y., 1997, Inversion of the Li-Strahler canopy reflectance model for mapping forest structure, *IEEE Transactions on Geoscience and Remote Sensing*, **35**, 2, 405-414.

Woodcock, C.E., Strahler, A.H. and Jupp, D.L.B. (1988a) The use of variograms in remote sensing. I. Scene models and simulated images. *Remote Sensing of Environment*, **25**, 323-48.

Woodcock, C.E., Strahler, A.H., and Jupp, D.L.B. (1988b) The use of variograms in remote sensing: II. Real digital images. *Remote Sensing of Environment*, **25**, 349-379.

Woolley, J.T., 1971, Reflectance and transmittance of light by leaves, *Plant Physiology*, **47**, 656-662.

Wu, Y., and Strahler, A.H., 1994, Remote estimation of crown size, stand density, and biomass of the Oregon transect, *Ecological Applications*, **4**, 2, 299-312.

Yang, J., and Prince, S.D., 2000, Remote sensing of savanna vegetation changes in eastern Zambia 1972-1989, *International Journal of Remote Sensing*, **21**, 2, 301-322.

Zhou, L., Kaufman, R.K., Tian, Y., Myneni, R.B., and Tucker, C.J., 2003, Relation between interannual variations in satellite measures of northern forest greenness and climate between 1982 and 1999, *Journal of Geophysical Research*, **108**, D1, doi:10.1029/2002JD002510.

11 WWW References

Chapter 2

www 2.1
http://www.soton.ac.uk/~epfs/methods/nat-env.shtml
Last accessed 23. march 2003

www 2.2
http://www.geog.utoronto.ca/info/facweb/Chen/Chen%27s%20homepage/home.htm
Last accessed 10 January 2005

Chapter 3

www 3.1
(http://iridl.ldeo.columbia.edu/SOURCES/.NOAA/.NCDC/.DAILY/.STATION.cuf/IWMO/682260/683280/VALUES/)
Last accessed 21 September 2002

www 3.2
http://ltpwww.gsfc.nasa.gov/IAS/handbook/handbook_htmls/chapter11/chapter11.html
Last accessed 17 March 2005

Chapter 6

www 6.1
http://www.geog.utoronto.ca/info/facweb/Chen/jxie1/PolderPaper/Figure5.html.
Last accessed 2 January 2005

Chapter 8

www 8.1
Earth observing data gateway http://edcimswww.cr.usgs.gov/pub/imswelcome/
Last accessed 14 February 2005

www 8.2
Myneni, R.B., Knyazikhin, Y., Glassy, J., Votava, P., and Shabanov, N., 2005, Users Guide, FPAR, LAI (ESDT: MOD15A2) 8-day composite NASA MODIS land algorithm (cliveg.bu.edu/modismisr/products/modis/userguide.pdf)
Last accessed 10 January 2005